University of Southampton

Faculty of Engineering and Physical Sciences

Chemistry

Evaluation of metal nitrides as the negative electrode in sodium-ion batteries and as a protective coating in lithium metal batteries

by

Samuel David Scott Fitch

Supervisors

Dr. Nuria Garcia-Araez

Prof. Andrew L. Hector

Thesis for the degree of Doctor of Philosophy

September 2020

University of Southampton

Abstract

Faculty of Engineering and Physical Sciences

Chemistry

Doctor of Philosophy

Evaluation of metal nitrides as the negative electrode in sodium-ion batteries and as a protective coating in lithium metal batteries

By

Samuel David Scott Fitch

In this project, an experimental study of the application of Sn_3N_4 as a high capacity negative electrode material is assessed in sodium-ion batteries, using a new synthesis method to make Sn_3N_4 microcrystalline and nanocrystalline powders. The underlying mechanism is interrogated using ex situ experimental characterisation (X-ray diffraction, extended X-ray absorption fine structure and X-ray absorption near edge structure).

The project also assesses the suitability of Li_3N as a protective layer on the surface of lithium metal negative electrodes; for secondary lithium metal battery and lithium-sulfur applications. a method was developed for nitriding electrodeposited lithium electrodes that were characterised by scanning transmission X-ray microscopy and X-ray photoelectron spectroscopy. The electrochemical performance of nitrided electrodes was also assessed by galvanostatic cycling techniques. Finally, the stability of the nitrided lithium electrode towards polysulfide species was assessed by X-ray photoelectron spectroscopy and scanning transmission X-ray microscopy. This study offers a unique assessment for the stability of unmodified and modified electrodeposited lithium electrodes towards polysulfide intermediates formed within a Li-S battery.

Table of Contents

Table of Figures

Table of Equations

Table of Tables

Research Thesis: Declaration of Authorship

Print name:	Samuel David Scott Fitch

Title of thesis:	Evaluation of metal nitrides as negative electrode in sodium-ion batteries and protective coating in lithium metal batteries

I declare that this thesis and the work presented in it are my own and has been generated by me as the result of my own original research.

I confirm that:

1. This work was done wholly or mainly while in candidature for a research degree at this University;
2. Where any part of this thesis has previously been submitted for a degree or any other qualification at this University or any other institution, this has been clearly stated;
3. Where I have consulted the published work of others, this is always clearly attributed;
4. Where I have quoted from the work of others, the source is always given. With the exception of such quotations, this thesis is entirely my own work;
5. I have acknowledged all main sources of help;
6. Where the thesis is based on work done by myself jointly with others, I have made clear exactly what was done by others and what I have contributed myself;
7. Parts of this work have been published as:

    - S. D. S. Fitch, G. Cibin, S. P. Hepplestone, N. Garcia-Araez and A. L. Hector, *J. Mater. Chem. A*, 2020, **8**, 16437–16450

Signature:		Date:	

Acknowledgements

I would like to thank both of my academic supervisors Professor Andrew Hector and Dr Nuria Garcia-Araez for giving me the opportunity to work with them and for guiding me throughout the past four years. I am greatly indebted to both of them for their support through difficult times and for making me a better researcher. I would also like to thank the University of Southampton – Chemistry department for providing a fantastic environment in which to make the most of your research experience.

I would like to thank the past and present members of both Andrew Hector and Nuria Garcia-Araez research groups for their support both inside and outside the lab. This support was offered from the electrochemistry group as a whole. In particular, I would like to thank Dr Joshua Whittam, Dr Min Zhang, Dr James Frith, Shao Li, Dr Thomas Homewood, Dr Nina Meddings, Dr Daniel Wright, Dr Hang Cheng, Dr Vivek Padmanabham, Dr Liam Furness, Dr Samantha Soule and Dr Andrew Lodge. My special thanks goes to Gilles Moehl who has provided the greatest help and entertainment in many challenging situations.

I would also like to thank the Diamond Light Source synchrotron research facility for the opportunity on the following beamtimes:

- SP14239 - With many thanks to Dr Giannantonio Cibin of B18 and Professor Alan Chadwick for their support.
- SP17860 and SP20639 - With many thanks to Dr Burkhard Kaulich, Dr Tohru Araki and Dr Majit Kazemian of I08 for their long nights and continued support.
- S122619 –With many thanks to Dr Tien-Lin Lee of I09 for his expertise and support with the experiment.

My Additional thanks goes to those who helped with the beamtime and data analysis, Dr Samantha Soule, Joe Fear, Nina Meddings, Rachel Lear, Gilles Moehl and Andrew Hector.

Finally, I would like to offer a huge thanks to my parents David and Kate and my sister Verity who have provided support and encouragement in all aspects of my life. To my Grandma Dylis Heeley who offered me the most important piece of advice “Don’t get too cocky” and lastly, to Hannah for everything, without you this would not have been possible.

Definitions and Abbreviations

General abbreviations

CE	Coulombic efficiency
DCA	differential capacity analysis
DEC	diethyl carbonate
DMC	dimethyl carbonate
DME	1,2-dimethoxyethane
DOL	1,3-dioxolane
EC	ethylene carbonate
EIS	electrochemical impedance spectroscopy
EXAFS	extended X-ray absorption fine structure
FEC	fluoroethylene carbonate
FEP	fluorinated ethylene propylene
FWHM	full width at half maximum
GCPL	galvanostatic cycling with potential limitation
HOMO	highest occupied molecular orbital
IMFP	inelastic mean free path
$LiAsF_6$	lithium hexafluoroarsenate
LIBs	lithium-ion batteries
LPS	lithium polysulfides
Li-S	lithium-sulfur
LiTFSI	bis(trifluoromethanesulfonyl)imide lithium salt
LMBs	lithium metal batteries
LUMO	lowest unoccupied molecular orbital
$NaPF_6$	sodium hexafluorophosphate
NIBs	sodium-ion batteries
OCV	open circuit voltage
PFA	polyfluoroalkoxy alkane

SEI	solid electrolyte interphase
SEM	scanning electron microscopy
SHE	standard hydrogen electrode
SS	stainless steel
STXM	scanning transmission X-ray microscopy
TBA	tributylamine
TEM	transmission electron microscopy
T_{sc}	time to short circuit
XANES	X-ray absorption near-edge structure
XPS	X-ray photoelectron spectroscopy
XRD	X-ray diffraction

Chapter 1 Introduction

1.1 Overview of batteries

1.1.1 A brief history of batteries

Electrical energy powers our lives and with the development of high capacity energy storage devices, we can mobilise this source with ease and efficiency to run our laptops, mobile phones, cars, tools etc. Rechargeable Li-ion cells are now ubiquitous in the portable electronic market.[1,2] The development of electrochemical energy storage devices has a rich history, spanning over two centuries involving great scientists from all over the world, overcoming key challenges to maximise the performance and safety of the current systems we benefit from today.

In march 1800, Alessandro Volta at the University of Pavia, Italy, reported on the first electrochemical cell.[3] He proposed that the difference in metals was the source of "metallic energy", and demonstrated this theory by alternating two different metals (zinc and copper) separated by a cloth soaked in a sodium chloride solution (**Figure 1.1**), a design that is widely known as the Voltaic pile.

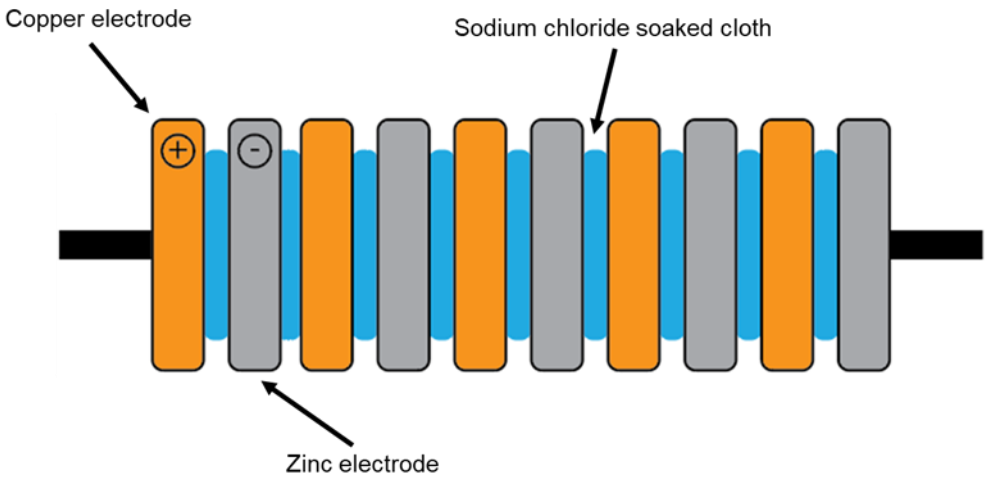

Figure 1.1 – Schematic diagram of a voltaic pile.

This pioneering work in electrochemistry was later expanded on by Michael Faraday. He determined that the electromotive force generated from a Voltaic pile was the extent of a chemical reaction at the metal electrodes with the passage of electricity, permitted by the conductive salt solution which was recognised as the electrolyte.[4]

In 1836, John Daniell developed an electrochemical cell that contained a zinc anode (negative electrode) immersed in a zinc sulfate solution which was housed in a porous pot, the pot was placed inside a copper can (cathode, positive electrode) filled with copper sulfate solution (**Figure 1.2**).[5]

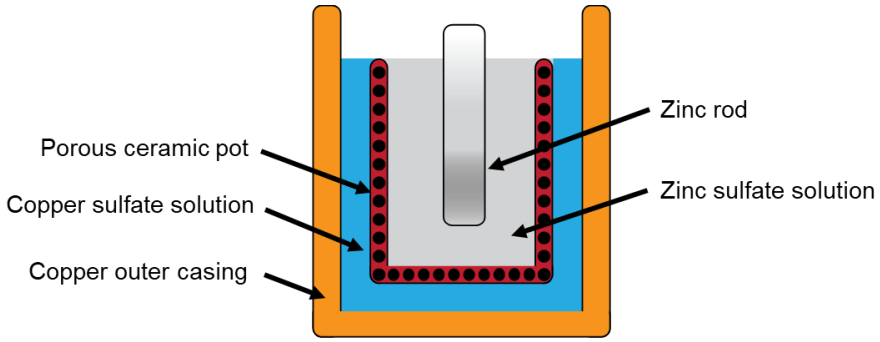

Figure 1.2 – Schematic diagram of a Daniell cell.

In 1866, French engineer Georges-Lionel Leclanché designed the first electrochemical cell that would go into mass production.[6] The Leclanché cell was initially comprised of a manganese dioxide/carbon composite positive electrode, a zinc rod as a negative electrode and an aqueous ammonium chloride solution as the electrolyte medium. Development of the cell saw the replacement of liquid electrolytes with a paste forming the basis of alkaline cells (**Figure 1.3**).

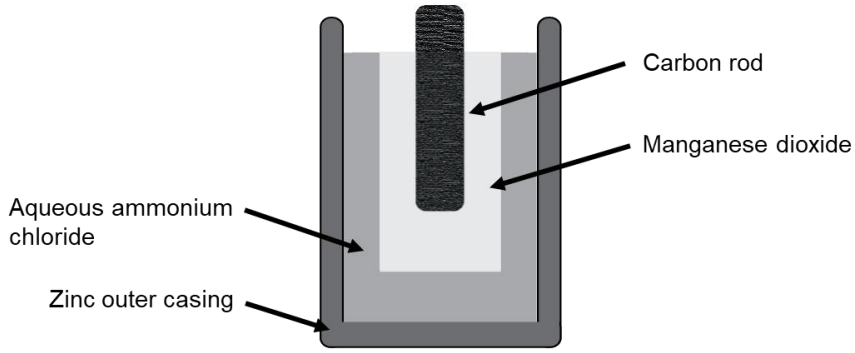

Figure 1.3 – Schematic diagram of the Leclanché cell.

The successful production of Leclanché cells was the catalyst for the inventions of the lead-acid rechargeable battery by Gaston Plantè in 1859 and the rechargeable nickel-cadmium battery by the Swedish engineer Waldmar Junger, who developed the cell in 1901.[7,8]

1.1.2 Development of lithium ion batteries

Lithium ion batteries are usually comprised of multiple electrochemical cells, which are connected in parallel/series that define the overall voltage and capacity of the battery.

Each cell contains a positive/negative electrode separated by an ion-conducting electrolyte. The electrolyte enables the transfer of charged Li-ions between the two electrodes. The cell is connected externally, allowing the flow of electrons to occur in tandem with the internal flow of ions giving overall electroneutrality within the cell.

Lithium-based batteries account for 63% of global sales for portable energy storage devices.[9] The initial attraction to develop batteries with Li metal as the negative electrode (LMBs) is attributed to lithium being the lightest (equivalent weight of 6.94 g mol^{-1}) and most electropositive metal available (-3.04 V vs. SHE (standard hydrogen electrode)).[10,11] The physico-chemical properties of lithium allow for superior specific energy per weight storage systems over other metals. Li-based batteries were first demonstrated in the 1970's with the assembly of primary cells (non-rechargeable) with variable discharge rates.[12]

During the same period, various inorganic compounds were heavily researched as potential positive electrode materials due to reversible reactions with lithium ions. Intercalation-based materials emerged as a crucial discovery for battery technology.

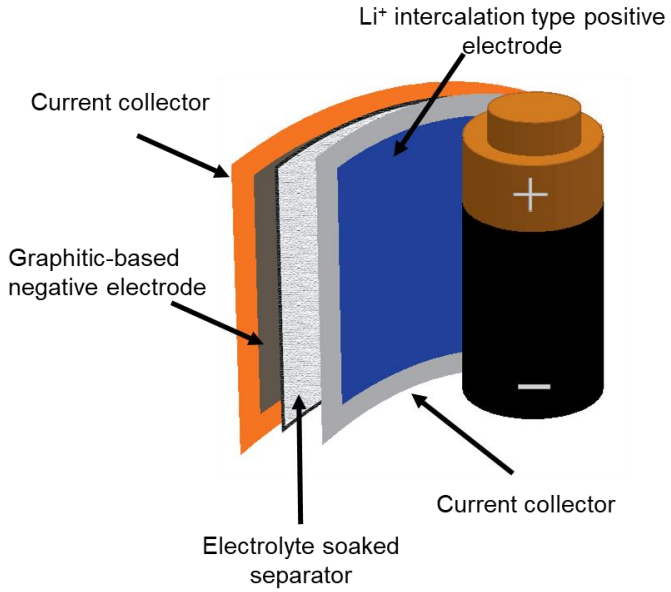

Figure 1.4 – Schematic diagram of current Li-ion battery design (cylindrical cell).

Exxon developed the first recognised secondary lithium cell (rechargeable) in the 1980's. The cell comprised of layered TiS_2 (intercalation) as the positive electrode, lithium metal as the negative electrode and lithium perchlorate salt dissolved in 1-3 dioxolane as the electrolyte.[12] The performance of the battery gained interest from industry, which drew considerable attention to the reversible performance of the layered TiS_2 positive electrode. The cell also highlighted the shortcomings of a lithium metal electrode/organic electrolyte combination. The main drawback of cells that employed lithium metal as an electrode is the formation of dendritic lithium that can bridge the two electrodes; short-circuiting the cell. Ohmic heat generated from the chemical exothermic reactions between dendritic lithium and the positive electrode, in the presence of a combustible electrolyte, can lead to thermal runway and in some instances, ignite the cell.[13] Dendrites occur at higher currents where the depletion of lithium ions near the electrode surface triggers the preferential deposition of lithium on the top of lithium

projectiles, which then triggers the fast growth of very large needle structures, which are called lithium dendrites.

The discovery of intercalation compounds in the form of lithiated metal oxides revolutionised the energy storage field. The most notable class of oxides demonstrated that sufficient ion diffusion could occur in three-dimensional materials with electronic structures that catered for greater operational voltages.[14] In the mid-1980's, John Goodenough presented a family of compounds based on Li_xMO_2 (where M= Co, Ni,), where lithium ions could intercalate into the crystal lattice of trivalent cobalt or nickel oxides to form the lithiated metal oxide. These positive electrode materials are still commercialised today.[15,16]

The research focus shifted to finding a replacement for lithium metal as the negative electrode. Murphy et al. first proposed the concept of employing a second insertion material to replace lithium metal.[17] Further developments saw graphitic-based layered compounds become the favoured insertion material due to their low operational voltages and relative safety record.[18,19] This gave rise to the "rocking-chair" battery and laid the foundation for Li-ion host negative electrode materials, that are still widely employed in LIBs technology today (**Figure 1.5**).[11]

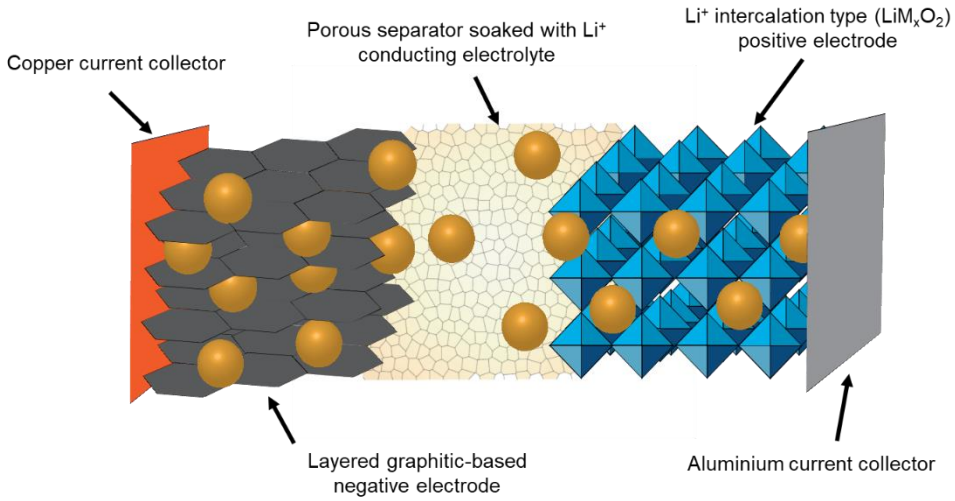

Figure 1.5 - Schematic diagram of a typical LIB ("rocking-chair") utilising graphitic carbon as a negative electrode, and a Li^+ intercalation type (Li_xMO_2) as the positive electrode. Adapted from reference.[11]

Within the "rocking chair" model, lithium ions intercalate/deintercalate between a positive electrode (e.g. Li_xMO_2) and a negative electrode (e.g. graphite). Li-ions diffuse through the electrolyte as the battery is charged and discharged. Because the lithium is in its ionic state, the possibility for metallic dendrite growth is significantly reduced and these cells are in principle much safer than the lithium metal electrode.

The majority of current commercial lithium-ion battery systems still employ $LiCoO_2$ (first commercialised by SONY®) as the positive electrode, graphitic carbon as the negative electrode and a gel polymer electrolyte encapsulated within a porous separator to give a defined distance between the two electrodes.[20]

The electrochemical redox reaction at the battery's positive electrode:

$$Li_{1-x}CoO_2 + xLi^+ + xe^- \leftrightarrow LiCoO_2 \qquad \textbf{Equation 1}$$

Negative electrode:

$$Li_xC_6 \leftrightarrow C_6 + xLi^+ + xe^- \qquad \textbf{Equation 2}$$

Gives an overall cell reaction:

$$Li_{1-x}CoO_2 + Li_xC_6 \leftrightarrow LiCoO_2 + C_6 \qquad \textbf{Equation 3}$$

Li-ion batteries dominate the portable electronic market but there is a constant drive to optimise the current performance of existing battery materials, in conjunction with developing new materials for the next generation of Li-ion batteries. The popularisation of electric vehicles and plug-in hybrid electric vehicles has seen the demand for high-energy density battery systems (500 W h kg^{-1} or higher) with a particular focus on systems "beyond LIBs", with current commercial cells offering ~ 150 W h kg^{-1}.[21]

Energy density is the energy normalised per unit volume, but often the term energy density is used to refer to the specific energy, which is the energy normalised per unit mass. The amount of electrical energy a battery delivers to a system per unit weight is expressed in W h kg^{-1} (specific energy). This value is related to the cell voltage (V) and specific capacity (A h kg^{-1}):

$$E = \int V dQ \qquad \textbf{Equation 4}$$

where E is the capacity, V is the battery terminal voltage (potential difference) and dQ denotes infinitesimal changes of specific capacity. By increasing the operating potential window and capacity of a cell, there is scope to develop batteries with greater specific energies.

In this report, the terms anode and cathode are replaced with negative and positive electrodes respectively, this is to minimise confusion over the role each electrode has in secondary (rechargeable) cells. In battery research, the positive and negative electrodes are defined by the redox potential of which they operate, the electrode with the more positive redox potential is defined as the positive electrode and vice versa.

1.1.3 Solid electrolyte interphase in lithium-ion batteries

A fundamental understanding of the reaction mechanisms involved at the electrode-electrolyte interface is essential for the development of next generation rechargeable lithium ion batteries. Research into the solid electrolyte interphase (SEI) has spanned over four decades but there is still limited understanding on how the SEI is initially formed and how the chemical composition and mechanical properties of the interfacial layer affects the electrochemical performance of an electrode. LIBs operate by shuttling Li-ions between positive and negative electrode host structures. The electrodes are separated by a defined space in the form of a separator filled with an aprotic electrolyte.

During the first charge of the Li-ion battery, the electrolyte undergoes reduction at the surface of the negatively polarised graphite electrode. The reduction products form a passivating layer comprised of inorganic and organic compounds that form the SEI. In current Li-ion battery technology, cyclic alkyl carbonate solvents are commonly employed with dissolved Li-ion salts as the liquid electrolyte (**Figure 1.6**). The reduction products of these electrolytes promote effective SEI layers with good cycling stability towards the negative electrode.[22]

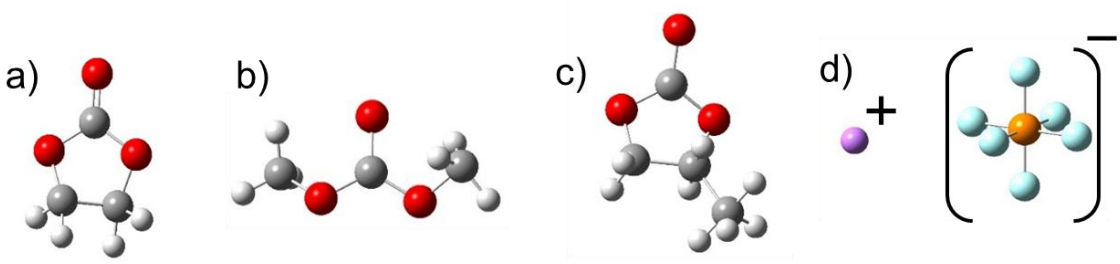

Figure 1.6 - Common Li-ion electrolyte components including aprotic solvents; (**a**) ethylene carbonate, (**b**) dimethyl carbonate, (**c**) propylene carbonate and the common Li^+ salt; (**d**) lithium hexafluorophosphate.

The formation of a stable SEI is important, since negative electrode materials operate at much lower potentials than the electrochemical stability window of the organic electrolytes. The decomposition of the electrolyte on the surface of the electrode in the initial formation of an SEI should be passivating in nature, i.e. prevent electron transport whilst maintaining sufficiently high Li-ion transport through the interphase.[23] Issues arise

when continued consumption of electrolyte occurs due to reduction at stresses and defect sites formed in the initial SEI layer which continues over subsequent cycles. Hence, understanding the formation and tailoring the SEI, is crucial in designing an interphase that enhances the overall performance of a cell.

There are thermodynamic considerations that give some insight into why the SEI formation occurs during cycling. Positive electrodes usually operate at potentials greater than 3 V vs. Li^+/Li. Consequently, there will be a driving force for electrolyte oxidation if the Fermi level of the electrode is lower in energy than the HOMO (highest occupied molecular orbital) of the electrolyte (**Figure 1.7**).

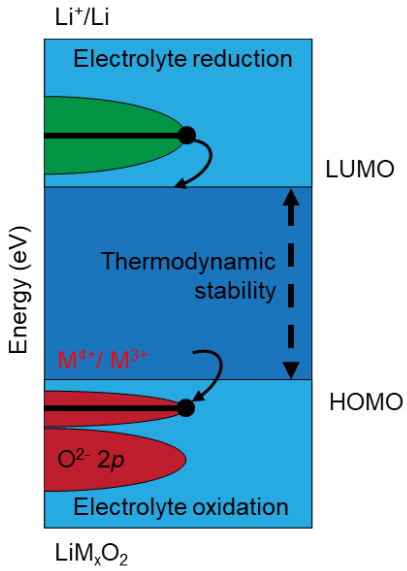

Figure 1.7 - HOMO and LUMO energy levels associated with electrolyte reduction/oxidation reactions at the negative and positive electrodes.

Negative graphitic electrodes operate at potentials close to 0 V vs. Li^+/Li, storing lithium near the valence state. If the negative electrode has a Fermi level higher in energy than the LUMO (lowest unoccupied molecular orbital) of the electrolyte, then there will be a driving force for electrolyte reduction. [16,24,16,25,26]

Aprotic electrolytes are known to be thermodynamically unstable to reduction at the negative electrode; the reduction products form an SEI layer on the electrode surface. The ideal SEI should be ionically conductive to Li-ions, electronically insulating, have no

detrimental effect on electrochemical performance and act as a protective barrier to prevent further electrolyte decomposition.

Numerous reaction mechanisms have been proposed for the formation mechanisms associated with the SEI within battery research. Progress in understanding the SEI has been greatly enhanced by characterisation techniques such as X-ray photoelectron spectroscopy (XPS), Fourier transform infrared spectroscopy (FTIR), Raman scattering and X-ray diffraction (XRD).[27,28,29,30] SEI composition in lithium-ion systems is well studied through these characterisation techniques.

As lithiated carbon materials are not stable in air; Li-ion cells are assembled in a discharged state with a graphitic negative electrode and a lithiated positive electrode. 1 M $LiPF_6$ in EC/DMC (1:1) is a commonly employed electrolyte solution in Li-ion technology, where EC (ethylene carbonate) and DMC (dimethyl carbonate) are the co-solvents chosen for their combined properties of viscosity, volatility and fairly large electrochemical stability window.[31] $LiPF_6$ (lithium hexafluorophosphate) is the dissolved salt that gives high Li-ion conductivity to the solution. The electrolyte solution is thermodynamically unstable at low potentials vs. Li^+/Li. A widely accepted model for the reduction process of this electrolyte suggests EC reduction via. a two-step electron process starting at ~ 0.85 V vs. Li^+/Li:[32]

(1) $$EC + 2e^- + Li^+ \rightarrow C_2H_4 + CO_3Li^-$$

(2) $$CO_3Li^- + Li^+ + EC \rightarrow 2(CH_2OCO_2Li)$$

Equation 5

1.2 Sodium-ion negative electrodes

1.2.1 Sodium ion batteries

Advancements in the electronics industry coupled with rapid population growth has increased the demand for energy storage devices. As previously discussed, lithium-ion batteries are considered the primary choice for electrochemical energy storage applications. However, there are growing concerns over the availability of battery-grade lithium resources especially with the popularisation of plug-in electric and hybrid-electric vehicles. Approximately 1.4 kg of lithium carbonate is required per hybrid vehicle, with an estimated 50% of all vehicles powered electrically by 2030.[33] It is clear that other battery systems need to be introduced to meet expected energy storage demands.

Table 1.1 - Summary of key characteristics for lithium and sodium

Metal	Atomic weight (g mol^{-1})	Standard electrode potential / V (vs. SHE)	Theoretical capacity (mA g^{-1})	Cost ($ per kg)	Ionic radius / Å	Percentage in Earth's crust
Li	6.94	-3.05	3862	6.5[34]	0.69	0.01%[35]
Na	22.99	-2.71	1166	0.50[34]	0.98	2.83% [35]

Renewed interest in sodium-ion batteries (NIBs) has seen >3900 journal papers published in 2019, this is in part, attributed to sodium sharing similar physico-chemical properties to lithium and so similar battery systems can be explored.[36] The global availability of the alkali metal within seawater and the Earth's crust could lead to a lower economic and geopolitical impact on sourcing battery grade sodium. Aluminium can also be employed as the current collector (no alloying with sodium ions) on the negative electrode side in place of the more expensive copper metal, further reducing the overall costs of NIBs.[37] The main drawback of this system is the increased atomic mass and larger ionic radius of the Na-ion, effectively resulting in NIBs offering intrinsically lower gravimetric and volumetric capacities over their lithium counterpart.[38]

Sodium-ion batteries share fundamental principles with LIBs, where Na-ions shuttle back and forth within a suitable electrolyte between a negative and positive electrode during charge/discharge processes. This allows current LIBs materials to be tested in their sodium form. There has been great success in the development of suitable positive electrode materials, including layered transition metal oxides ($NaCoO_2$ and $NaMnO_2$ etc.), and polyanionic compounds ($NaFePO_4$, $NaCoPO_4$).[39,40,41,42,43]

For Na-ion batteries, the negative electrode is still a considerable challenge. Graphite is the material of choice for LIBs, however the larger ionic radius of sodium ions (1.02 Å for Na^+, 0.76 Å for Li^+) leads to sluggish reaction kinetics, lower capacities and poor cycle stability in sodium ion cells. Attention in developing suitable negative electrode materials that can accommodate larger sodium ions fall primarily into three categories; Amorphous "hard carbon" electrodes with larger interlayer spacing than graphite, that can allow insertion of Na-ions into the carbon structure. (**Figure 1.8**)

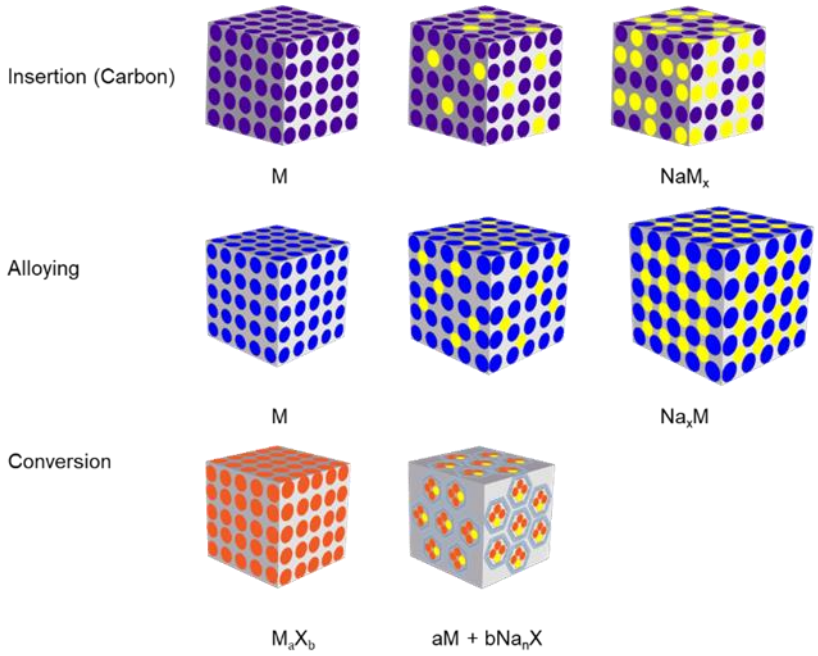

Figure 1.8 - Illustration of the different mechanisms of charge storage for popular sodium-ion negative electrodes.

Alloying of metallic and non-metallic elements with Na-ions can deliver high specific capacities but are subjected to large volume variations during cycling causing severe capacity fade. Conversion-alloying attempts to improve on the cyclability of alloying materials by forming matrix "buffers" within the electrode material during the initial reduction, that can withstand large volume variations during cycling whilst maintaining high specific capacities.

1.2.2 Carbon-based materials

Carbon-based materials have been investigated as negative electrode materials for sodium-ion battery devices. They offer several important advantages, such as low cost, abundance of raw materials, renewability and moderate conductivity.[44,45,46] During recent years, the development of carbonaceous negative electrode materials for NIBs have been dominated by hard carbon materials. Dahn et al. first reported on hard carbon materials derived from pyrolysed glucose with a reversible capacity around 300 mA h g^{-1}, however capacity fading greatly affected the overall performance of the electrode.[47] Hard carbon has a "house of cards" structure where graphite-like microcrystallites are interspersed in amorphous carbon regions. During sodiation, Na-ions adsorb onto surface active sites of the hard carbon, intercalation proceeds into stacked parallel graphene sheets of the microcrystallite material that have sufficiently large *d*-spacing which can accommodate Na-ions (**Figure 1.9**).

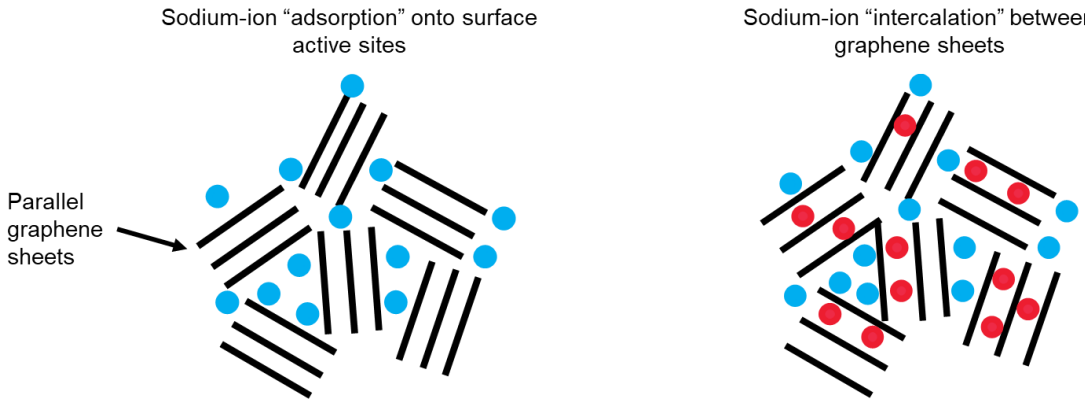

Figure 1.9 - Schematic illustration of the mechanism for Na-ion storage in hard carbon.

More recently, nano-structuring and the introduction of defects sites for hard-carbon materials including nanofibers, nanospheres and nanosheets have seen improvements in the conductivity and structural stability of the material during cycling.[48,49,50] A large number of defect sties allow for more sodium adsorption on the carbon structure and can improve sodium diffusion pathways during deeper sodiation of the anode.[51,52,53]

1.2.3 Alloying-based materials

Group 14 (Si, Ge, Sn and Pb) and Group 15 (P, As, Sb and Bi) metallic and non-metallic elements have been considered as sodium alloying negative electrode materials.[54,55,56,57,58,59] The interest stems from the high theoretical capacities these materials could achieve at sufficiently low operational voltages (< 1.0 V vs. Na^+/Na). In particular, P, Pb, Sn and Sb have shown promising experimental performance as reversible sodium negative electrode materials operating at room temperature.

Table 1.2 - Summary of the electrochemical properties for various sodium-alloying elements

Element	Sodiated phase	Theoretical gravimetric capacity (mA h g^{-1})	Average Potential *vs.* Na^+/Na (V)	Volume expansion (%)
P[60,61]	Na_3P	2596	~ 0.5	500
Pb[62]	$Na_{3.75}Pb$	1482	0.5	400
Sn[63,64]	$Na_{3.75}Sn$	847	0.6	420
Sb[65,66,67]	Na_3Sb	660	~ 0.8	393

The main drawback of these negative electrode materials is the large volume variations associated with the Na-ion alloying process. Constant volume changes of metallic particles lead to pulverisation, delamination, and loss of conduction pathways.[68] Mechanical variations within the negative electrode put a considerable strain on the SEI layer, cracking at the interfacial region of the electrode promotes further electrolyte reduction on the surface which leads to capacity fading, poor cell cycling and reduced Coulombic efficiency.[69]

The sodium-tin alloying mechanism has been extensively studied. Sn alloys with sodium at relatively low potentials (~0.2 V vs. Na^+/Na) to form crystalline $Na_{15}Sn_4$, the final phase formation. The full sodiation of tin yields a high theoretical capacity of 847 mA h g^{-1}.[60,61] Tin exhibits a volume expansion of 420% when alloyed with the larger sodium ion. Datta et al. cycled pure microcrystalline tin in a sodium-ion cell to study the performance.[70] The first charge produced a specific capacity of 856 mA h g^{-1}, of which 280 mA h g^{-1} was recovered on the first discharge, which gave an initial irreversible capacity loss of 67%. The large hysteresis of charge can be attributed to the breakdown of the SEI on the surface of the electrode, which prevented a fully passivated layer to form and inhibited the movement of sodium ions from the electrolyte into the electrode.

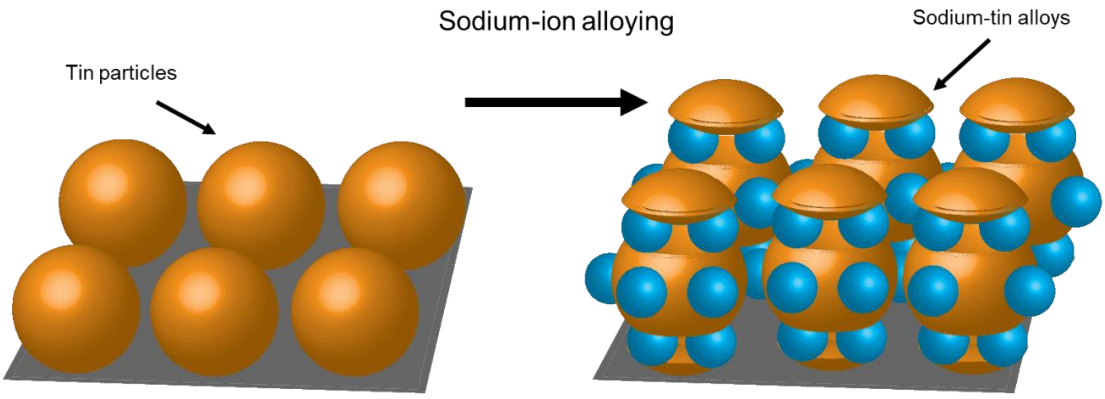

Figure 1.10 - Schematic illustration of the mechanism for Na-ion storage in tin electrodes.

To alleviate the problems associated with volume expansion, modifying the particle size of Sn has been explored to improve the dimensional stability of the bulk material during cycling.[71,72] If the metallic host particles are small, the *absolute* volume change of the electrode can be minimised. Sn-based nanostructured electrodes have been designed to improve cycling stability.[73,33] Nanomaterials are structures with dimensions within the 1-100 nm range, they offer unique mechanical and electrical properties compared to their bulk form. Wang et al. reported in situ transition electron microscopy (TEM) to study the sodiation of tin nanoparticles (NPs) during cycling, they observed the initial formation of an amorphous Na-poor phase (Na_xSn, $x < 0.5$), which consumed Sn nanoparticles.[74] On subsequent sodiation, the final crystalline $Na_{15}Sn_4$ phase formed with an overall lower volumetric expansion than the expected value (420%). This highlighted

the potential benefit of nanostructuring Sn particles to withstand the stresses imposed by volume change on cycling.

Despite improvements in the mechanical properties of small tin particles, the cycling stability is still not sufficient compared to Li-ion systems. More recently the development of Sn-based conversion materials has shown promising signs for improving the cyclability of alloying electrodes whilst still delivering high capacities.

1.2.4 Tin-based conversion materials

Conversion-based materials have been studied in LIBs as negative electrodes since the late 1970's. Poizot et al. was recognised for highlighting the performance of nano-sized transition metal oxides as conversion electrodes, however other binary metal compounds have since been studied (M_aX_b, M = transition metal, X = H, F, S, N, O, P).[75]

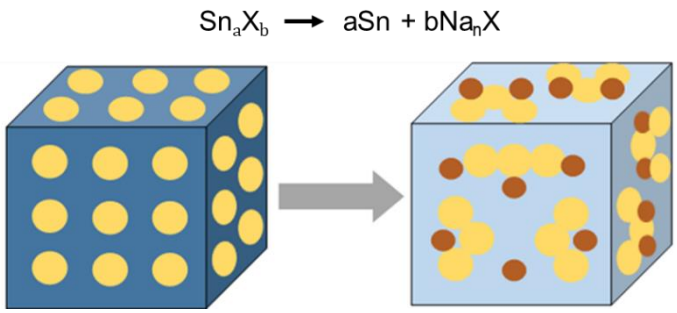

Figure 1.11 - Schematic illustration of the mechanism for Na-ion storage in tin-based conversion materials. Yellow circles indicate conversion material (Sn_aX_b) and orange circles indicate sodium ions.

Tin-based conversion electrodes (SnO_2, SnS, Sn_4P_3, etc.) are designed to mitigate the stresses imposed on the electrode by the formation of a matrix structure during initial reduction (Sn + Na_xM_y).[76,77,78,79,80,81] The formed structure should accommodate and reduce the agglomeration of tin nanoparticles embedded within the electrode.

1.2.5 SnO_2 conversion electrode

SnO_2 has been widely reported as a viable conversion sodium electrode, owing to its high theoretical capacity (1378 mA h g^{-1}), low redox potential and ease of synthesis.[82,83] Studies of SnO_2 conversion electrodes in LIBs have reported the formation of Sn particles embedded in an Li_2O matrix on first lithium reduction.[84,85,86] Further reduction of the metal particles proceeds via lithium-alloying intermediate phases until full lithiation of the metal is achieved. It is understood that the inert Li_2O forms a robust, buffering matrix within the electrode, that can alleviate the stresses imposed on the negative electrode during large volume variations of the electrochemically active Sn particles. A similar process occurs in SnO_2 negative electrodes for sodium cells whereby a Na_2O matrix is formed irreversibly on first reduction. However, bare SnO_2 materials show limited reversibility of conversion and alloying reactions on subsequent oxidation.[87,88] This leads to a large irreversible capacity hysteresis for charge passed during the initial reduction/oxidation process. The irreversibility is in part, due to the low electronic/ionic conductivities of the oxide matrix.[89,90,88]

Nano-structuring of conversion materials and the incorporation of carbon structures have shown significant improvements in the electrochemical performance of SnO_2 as a sodium negative electrode. A study into the kinetics of Na-ion storage into SnO_2 determined that slow Na-ion diffusion into the oxide limited the overall electrochemical reactions of the material.[91] A synthesised amorphous SnO_2/carbon nanotube composite electrode, enhanced the diffusion rate of Na-ions through the reduced particle size of amorphous SnO_2, which delivered a capacity of 590 mA h g^{-1} after 50 cycles at a rate of 100 mA g^{-1}. Wang et al. used a hydrothermal synthesis method to produce ultrafine SnO_2 nanoparticles (~ 5nm diameter) loaded onto a reduced graphene oxide framework. The framework enhanced the electronic conductivity of the electrode and allowed for "buffering space" due to the change in volume as the cell was cycled. The composite achieved reversible capacities of 330 mA h g^{-1} at a rate of 100 mA g^{-1} after 150 cycles in sodium half-cells.[92] SnO_2 nanospheres coated with nitrogen-doped carbon and graphene have also been reported. The composite-conversion negative electrode

material delivered reversible capacities of 420 ma h g^{-1} after 30 cycles at a specific current of 100 mA g^{-1}.[93]

1.2.6 Sn_4P_3 conversion electrode

Recent studies into Sn_4P_3 aimed to combine the advantages of Sn (high capacity) with P (High conductivity, low redox potential). Yi et al. synthesised Sn_4P_3 nanoparticles supported on reduced graphene oxide sheets via a low temperature solution-based phosphorisation reaction.[94] Galvanostatic cycling was performed on the composite negative electrode in sodium half-cells, which yielded a capacity of 640 mA h g^{-1} after 100 cycles at 100 mA g^{-1}. Another Sn_4P_3 composite with carbon yolk-shell nanocubes delivered reversible capacities of 700 mA h g^{-1} after 50 cycles at 100 mA g^{-1}.[95]

1.2.7 Sn_3N_4 conversion electrode

Tin nitride was first assessed as a conversion electrode material for lithium-ion batteries.[96] Sn_3N_4 thin films were prepared by radio-frequency sputtering with varied layer thickness (50-500 nm). Lithium half-cells were constructed with tin nitride as the working electrode, lithium foil as the counter electrode and 1 M $LiClO_4$ in PC as the electrolyte. It was determined that the conventional conversion reaction (**Equations 6** and **7**) proposed for Sn_3N_4 was incomplete based on the capacities achieved from the initial cycle.

Conversion reaction:

$$Sn_3N_4 + 12Li^+ + 12e^- \leftrightarrow 4Li_3N + 3Sn \qquad \textbf{Equation 6}$$

Alloying reaction:

$$Sn + 4.4Li^+ + 4.4e^- \leftrightarrow Li_{4.4}Sn \qquad \textbf{Equation 7}$$

Previously, our group reported a method to synthesise bulk nanocrystalline Sn_3N_4 by ammonolysis of a tin dialkylamide at various temperatures between 300 and 400 °C. Tin nitride electrodes demonstrated a reversible (de-sodiation) capacity of 270 mA h g^{-1} after 50 cycles at 50 mA g^{-1} with a Coulombic efficiency

close to 95%.[36] Ex situ diffraction measurements on cycled electrodes suggested that a significant fraction of the material was not involved in the electrochemical processes. Consequently, it was envisioned that smaller crystallite sizes could deliver larger capacities. Nano-structuring can increase the surface area of the tin nitride particle, increasing the availability of active sites for Na-ions to adsorb onto the surface. Nano-structuring can introduce defect sites which offer additional active sites for sodium adsorption and can potentially increase the specific capacity of the tin nitride material. This is now demonstrated in this work, with a new synthesis route and an ex situ experimental study of the reaction mechanism.

1.3 Lithium-sulfur battery

1.3.1 Overview

Interest into the development of lithium-sulfur (Li-S) batteries has significantly increased over recent years, owing to the attractive characteristics of sulfur. Li-S electrochemical systems have a high theoretical specific capacity (1675 mA h g^{-1}) and a high energy density (2600 W h kg^{-1}) which could meet the demands set for energy-storage devices in long-range vehicle applications.[97,98,99] Other attractive properties for developing Li-S systems include the high abundance, nontoxicity and low cost of elemental S ($0.6 kg^{-1}), in comparison with metal cobalt oxides currently utilised as positive electrode materials in commercial LIBs ($23 kg^{-1} for nickel manganese cobalt oxide (NMC)).[100,101,102]

Conventional Li-S cells in research settings consist of a lithium metal negative electrode, an organic liquid electrolyte and a sulfur composite (usually elemental sulfur, carbon additive and PTFE binder) positive electrode.[103,104] In principle, elemental sulfur (S_8) will be fully reduced to lithium sulfide (Li_2S) on discharge and re-oxidised to sulfur reversibly on the subsequent charge. The overall redox reaction can be given as:

$$S_8 + 16Li^+ 16e^- \leftrightarrow 8Li_2S \qquad \textbf{Equation 8}$$

However, the actual discharge and charge processes are exceedingly complex and the exact mechanisms by which the reactions proceed by remain unclear. Lithium-sulfur batteries discharge (reduction) by the transformation of solid sulfur to solid lithium sulfide via the formation of lithium polysulfides (LPS) of variable chain length at the positive electrode, whilst Li-ions are continuously stripped from the lithium metal negative electrode (**Figure 1.12**).[105,106,107] Sulfur is electrically insulating so unlike Li-ion battery systems, the electrochemical reactions do not occur in the solid-state but proceed by electron-transfer between the conductive carbon framework of the positive electrode interface and the various intermediate sulfur species dissolved in the surrounding encapsulated electrolyte.[108,109] During discharge, the polysulfide chain length is shortened, with the final reduction process forming insoluble Li_2S in what is sometimes referred to as a solid-liquid-solid transformation.[110] Li_2S_2 has also been considered as a final insoluble discharge product, however, no experimental crystallographic data has been reported to support Li_2S_2 as a final reduction compound.[111,112,113] This multistep process is reversed on subsequent oxidation (charge).

Despite decades of research, the discharge mechanism with respect to LPS formation remains controversial, with differing views over the intermediate species that could be formed during the redox process. Reported polysulfide anions and radicals include: S_8^{2-}, S_6^{2-}, S_4^{2-}, S_3^{2-}, $S_3^{\bullet-}$ S_2^{2-} which arise from various proposed electrochemical and chemical reduction reactions.[114,115,116,117,118] An additional complexity in determining the intermediate products is that LPS are known to disproportionate/comproportionate in solution to form an equilibria of various polysulfides, due to the close Gibbs free-energies of the various polysulfide species.[119,108,120] [116,105,117] The role of the electrolyte could also affect the composition of intermediate species during cycling. It has been reported that electron-pair donor solvents including dimethylacetamide and dimethylformamide could stabilise the S_3^- radical during discharge.[121,122]

A typical discharge curve for a Li-S cell is presented in **Figure 1.12**. The profile has been illustrated with a simplistic mechanistic pathway, which demonstrate the key regions discussed during reduction.

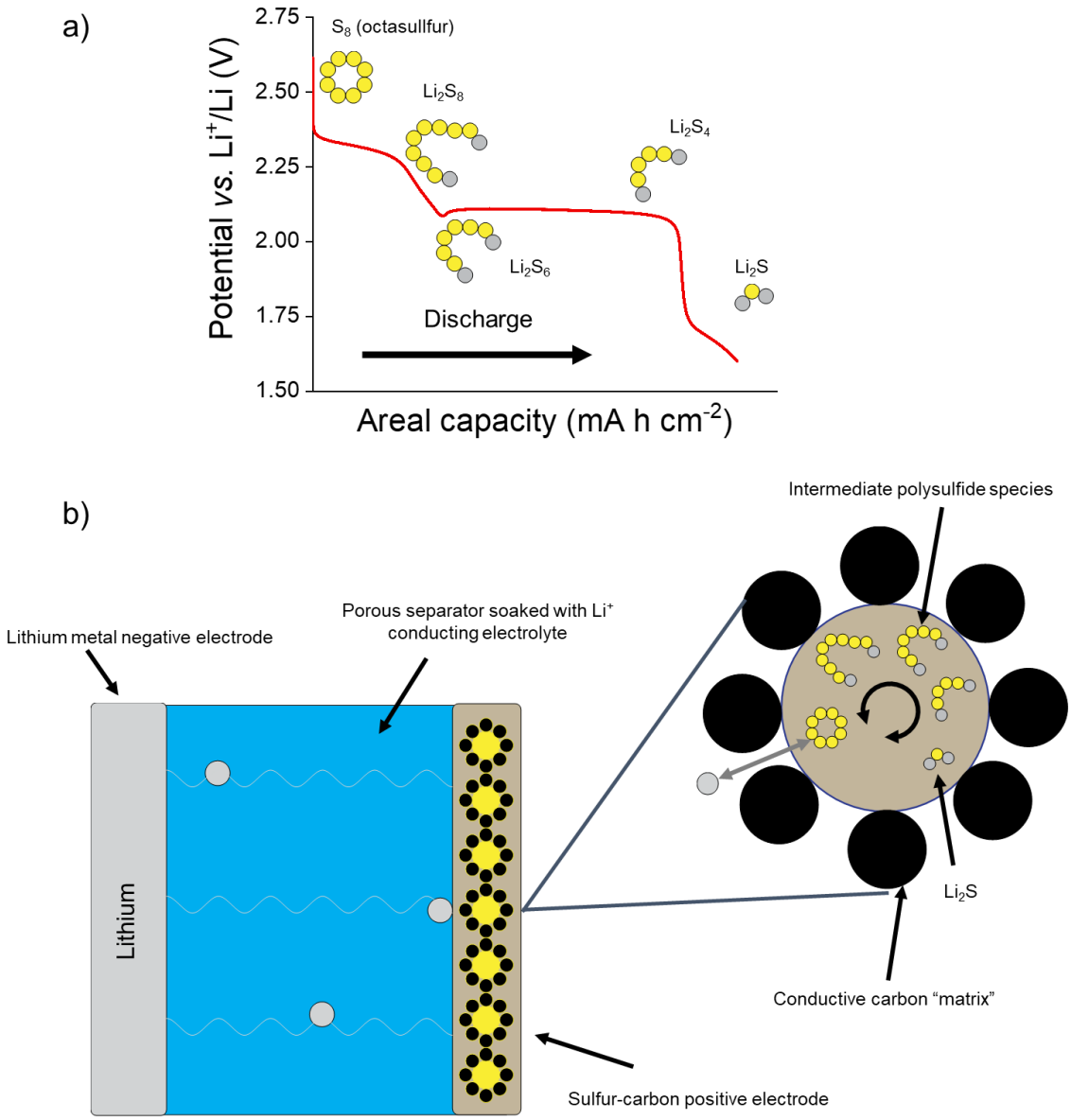

Figure 1.12 - (**a**), Typical discharge curve for a Li-S cell when plotting potential vs. capacity. (**b**), Generalised schematic diagram of a Li-S cell during operation. Adapted from references.[123,124]

1.3.2 Key challenges

Octasulfur (cyclo-S_8) is the most abundant form of elemental sulfur and is the most stable allotrope at room temperature.[125,126] During discharge, this cyclic structure undergoes multiple structural and morphological changes as it is reduced to form polysulfides (Li_2S_x, $8 \leq x \leq 3$). These structural changes coupled with the insulating properties of sulfur cause electrochemical contact issues within the composite electrode. This limits the electrochemical performance of the cell, as not all the available sulfur is utilised during cycling.[97,127,128] An additional challenge for Li-S battery research to overcome, is the intermediate polysulfide species formed during discharge/charge can diffuse away from the positive electrode. Due to the strong nucleophilic reactivity of polysulfide anions, the choice of solvents for Li-S electrolytes are largely limited to cyclic and linear ethers (1,3-dioxolane and 1,2 dimethoxyethane). However, polysulfide species are highly soluble in both dioxolane and glyme-based electrolyte systems.[129,130,131] This allows for polysulfide species to travel between the two electrodes during operation which is conventionally described as the shuttle mechanism.[132,133]

In this mechanism, high-order polysulfides (Li_2S_8 or Li_2S_6) diffuse through the porous separator towards the lithium metal negative electrode, where they are reduced to form insoluble Li_2S on the lithium negative electrode.[134,135,136] This parasitic reaction proceeds until full coverage of the lithium metal electrode has been achieved. The reduction of high-order polysulfide species continues on contact with the Li_2S layer to form low-order polysulfide species which remain highly soluble in the electrolyte.[137,138] Over time there is an increase in concentration of these polysulfide species at the lithium negative electrode which leads to the species diffusing back towards the positive electrode and are, in-turn, re-oxidised back into high-order polysulfide chains. This process is autocatalytic and will continue throughout the duration of cell operation (**Figure 1.13**).

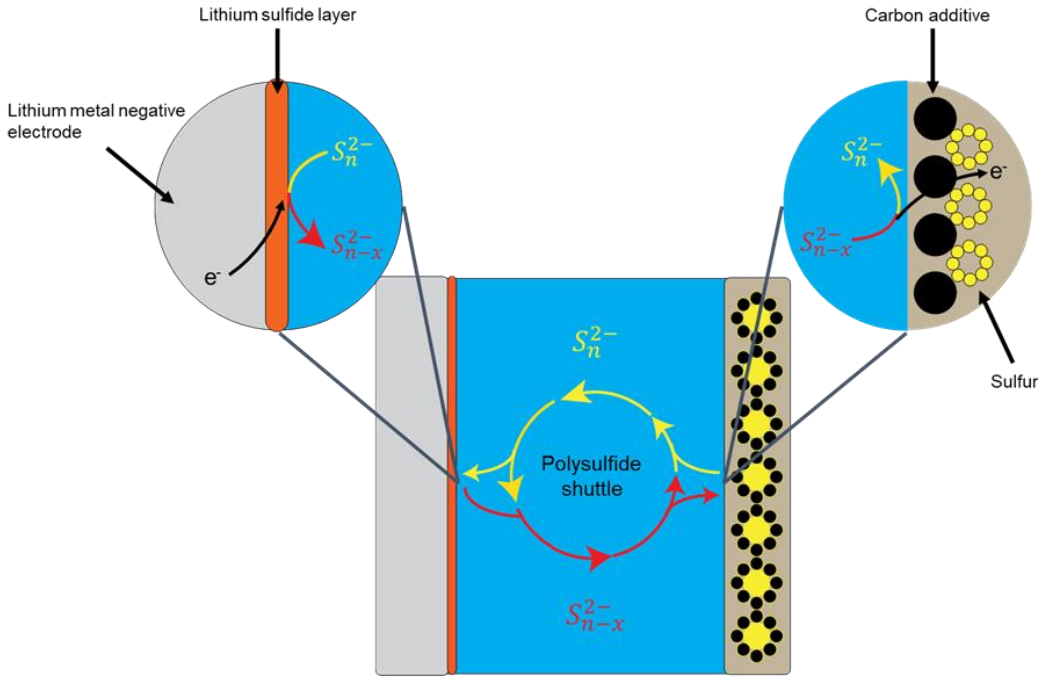

Figure 1.13 - Generalised schematic diagram of the shuttle mechanism, where $\boldsymbol{S_n^{2-}}$ represents high-order polysulfide species and $\boldsymbol{S_{n-x}^{2-}}$ represents low-order polysulfide species. Adapted from reference.[124]

This process has a profound effect on the cyclability of Li-S cells, as active sulfur species are consumed from the positive electrode, limiting the practical capacities that can be achieved during operation. One might look at this problem pragmatically and suggest tuning the electrolyte to limit the solubility of LPS species. However, the solubility and reactivity of LPS is the driving force for the overall cell reaction, so attempts to suppress the solubility will likely limit the overall power density the cell can achieve.

One promising strategy to ameliorate the effects of the shuttle mechanism is to design positive sulfur composite electrode structures in a way that confine the dissolved polysulfide species locally and minimise LPS diffusion away from the positive electrode. Various conductive carbon frameworks have been proposed based on carbon nanospheres, carbon nanotubes and graphene.[139,140,141,142] Metal oxide/nitride/sulfide frameworks for composite sulfur positive electrodes have also been studied for LPS trapping, with additional catalytic properties than can accelerate the transformation of lithium polysulfides to lithium sulfide.[143,144,145,146]

As previously stated, corrosion of the lithium metal negative electrode is also an unwanted by-product of the shuttle mechanism.[147,108] Strategies to protect the metal electrode from the shuttle mechanism include: Developing ion selective separators which restrict lithium polysulfides to the positive electrode side and prevent diffusion of LPS towards the lithium metal electrode.[148,149,150,151] Screening of electrolyte additives which aid in the formation of a favourable solid electrolyte interphase.[152,153,154 149,150,151] $LiNO_3$ has been studied comprehensively as an electrolyte additive in Li-S cells where the reduction of the nitrate passivates the lithium metal surface with a compact layer consisting of LiN_xO_y, Li_3N and Li_2O.[155,156,157] Improvements in the Coulombic efficiency in Li-S batteries with $LiNO_3$ additive can be ascribed to the synergetic effect of the co-presence of $LiNO_3$ and polysulfides, where the reduction products on the lithium electrode promote planar lithium growth morphology whilst preventing further lithium sulfide formation.[158] Lastly, the design of protective layers (also known as an artificial SEI layer) on the metal electrode surface prior to electrochemical cycling in a Li-S cell. This approach allows for greater control over the formation of interphasial layers from a wide range of compounds/materials which cannot be regulated through electrolyte additives.[159,160,161]

Lithium metal is considered the negative electrode material of choice for Li-S applications. However, the issues of low Coulombic efficiency from the formation of inactive ("dead") lithium and dendritic growth are universal where organic liquid electrolytes and lithium negative electrodes are employed and are directly correlated to electrode-electrolyte (electro)chemical reactions. Developing strategies to improve the Li metal-electrolyte interactions for improved cyclability has to be considered alongside the prevention of lithium corrosion by parasitic Li_2S formation.

1.4 Lithium metal negative electrode

The focus on tuning the reactivity of the lithium metal electrode is key to unlocking high energy density batteries systems including secondary lithium metal batteries, Li-O_2 and Li-S. The metallic electrode itself is considered the "Holy Grail" due to its low density (ρ = 0.59 g cm^{-3}) and exceptionally negative electrochemical potential (-3.04 V vs. Li^+/Li).[162] Due to the highly reactive nature of lithium, there has been great difficulty in finding suitable electrolytes that are thermodynamically stable. Research into lithium-based batteries began after W.S. Harris discovered that lithium metal is kinetically stable against cyclic esters (ethylene carbonate etc.), after an initial passivating layer had formed.[11] Further insight into the phenomenon revealed the well described concept of the solid electrolyte interphase (SEI), which serves a necessary function for any electrode material that operates outside the thermodynamic stability window of the electrolyte. Rechargeable (secondary) lithium metal batteries were extensively researched in the 1980's, however, growing safety concerns with the reactivity of lithium through dendritic growth combined with poor cyclability, saw the research focus shift to lithium ion batteries (LIBs) when Sony commercialised a battery that replaced lithium metal with a graphitic negative electrode. The popularisation of electric vehicles and plug-in hybrid electric vehicles has seen the demand for high-energy density batteries systems (500 Wh kg^{-1} or higher) with a particular focus on making lithium metal negative electrodes viable to deliver capacities "beyond LIBs".

1.4.1 Lithium dendrite formation and growth

One aspect as to why lithium forms dendrites is that it has relatively low surface tension. Hence, there is a low energy penalty in forming a high surface area, roughening the electrode surface.[163,164]

Lithium deposition is usually kinetically controlled. Under these conditions, it has been demonstrated that lithium deposition takes place preferentially at regions with higher conductivity at the SEI, such as defects, stresses in the metal etc. The growth mechanism of lithium electrodeposition at the electrode surface proceeds in the formation of "mossy" lithium through the formation of whiskers.[165,166] Further Li-ion electrodeposition proceeds at the base of these projectile structures (rather than from the tip), as the newly formed SEI at the base of the whiskers is more conductive than the SEI-protected tips.[167] Acceleration of large branched whiskers then proceeds under the Li-ion plating regime (**Figure 1.14**).

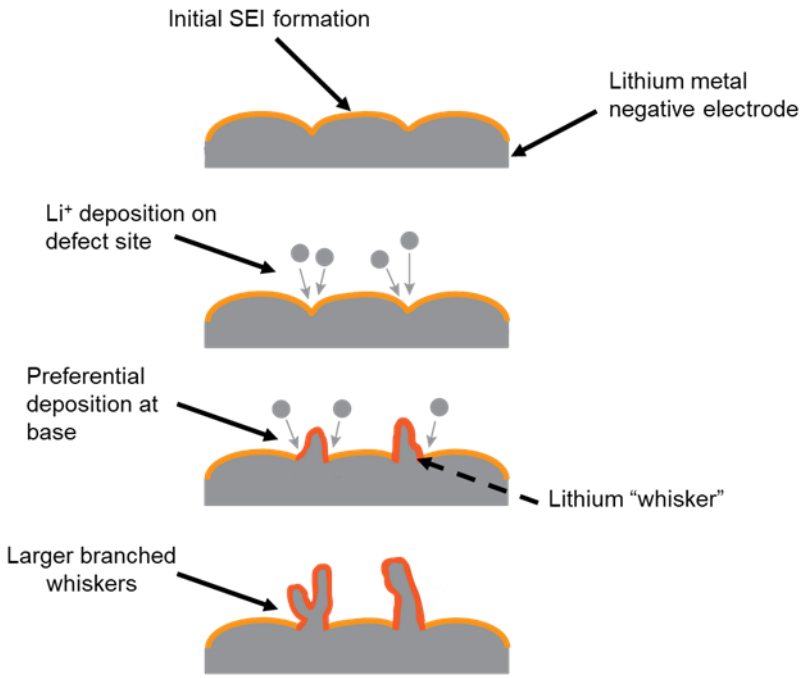

Figure 1.14 - Generalised schematic of Li-ion deposition and the formation of lithium "whiskers". Deposition continues at the base of these projectiles as larger branched whiskers proceed.

The continuous fracture and repair of the SEI has long since considered to be the determining factor for low Coulombic efficiency (CE), where both electrolyte and active Li metal are continuously consumed during cycling. There are two processes which contribute to low CE. The reaction of the electrolyte with metallic lithium is a necessary process for the formation of an SEI and irreversibly consumes lithium. Additionally, unreactive ("dead") metallic Li^0 contributions occur where structures of lithium are detached from the Li surface during stripping and are electrically isolated by the surrounding SEI.[168,169] Similar to plating, the stripping process (oxidation), preferentially takes place at the base of the whiskers, which can lead to the formation of "dead lithium" on the metal surface. This occurs when lithium whiskers are disconnected from the metal electrode, becoming electrically isolated for the duration of cell cycling (**Figure 1.15**).

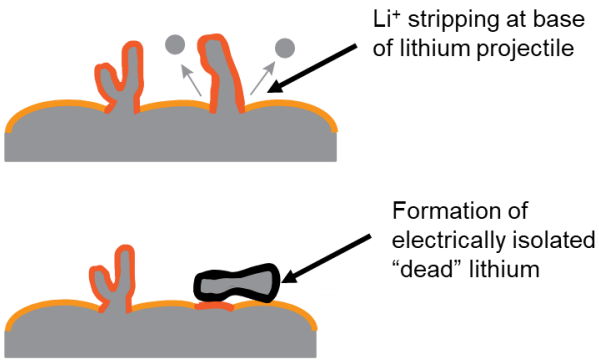

Figure 1.15 - Generalised schematic diagram of Li-ion stripping and the formation of inactive "dead" lithium on the interface of the metal electrode.

An additional consideration can be made for higher current values associated with lithium plating reactions. At higher currents, the process of lithium plating is affected by the rate of mass transport of lithium ions from the electrolyte towards the surface. The depletion of lithium ions near the electrode surface triggers the preferential deposition of lithium on the top of the lithium deposits, which then triggers the fast growth of very large needle structures, which are called lithium dendrites. Formation of lithium dendrites is an important safety issue as they can cause the cell to "short-circuit."

1.4.2 Solid Electrolyte Interphase on lithium metal electrodes

The solid electrolyte interphase (SEI) has become a key critical component of lithium metal battery research since the breakthrough studies performed by Peled and Aurbach.[170,171,172] They reported on the composition of reduction layers formed through different electrolyte solutions on contact with the surface of lithium electrodes. Owing to the highly negative electrode potential of Li^+/Li, virtually all known organic electrolyte systems will be reduced at the Li surface.[173] Passivation of Li-ions through the SEI makes it possible to still operate a cell that employs Li metal as a negative electrode. Certain properties are required for the successful formation of an SEI on Li metal electrodes. On top of having ion-conducting and electron insulating properties, the SEI for Li metal needs to be fully homogenous in composition, morphology and ionic conductivity. [174,175] A "routine" SEI formed on Li metal was found to have a Li^+ ionic conductivity of 3.1 $x10^{-7}$ S cm^{-1}.[176] SEI layers are commonly fragile, non-uniform and unstable. There is a demand for the SEI to have flexible/elastic mechanical properties to accommodate volume variations from the plating/stripping processes at the electrodes' surface.[177] Any inhomogeneities in the composition and morphology will lead to uneven electrodeposition. On lithium-based electrodes in organic electrolytes, there is a mixture of Li alkyl carbonates (ROCOOLi) and large molecular-weight polymers throughout the entire SEI which are "spongy" in composition.[178] In contrast, more stable, "harder" inorganic compounds of Li_2O, Li_2CO_3 and Li halides dominate the inner layer of the SEI closest to the metal electrode which is best represented through the "mosaic model" (**Figure 1.16**).

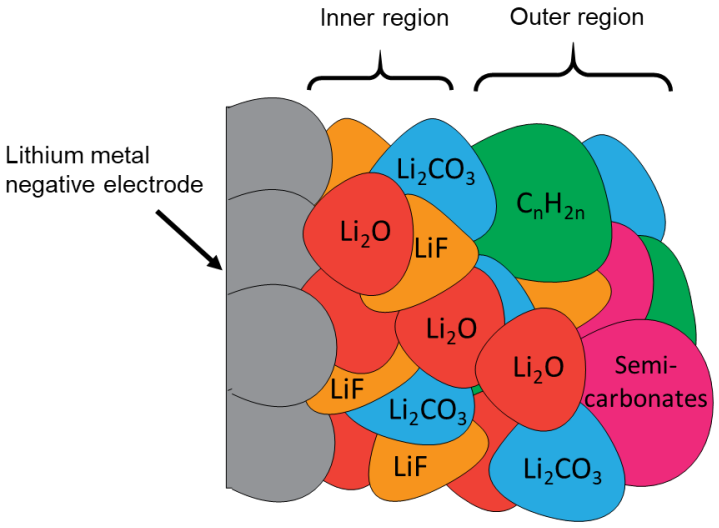

Figure 1.16 – The "mosaic model" of the SEI on lithium metal electrodes, formed in an organic liquid electrolyte . Inorganic species of LiF and Li_2O are present towards the inner region of the SEI, with the more "spongy" organic species located towards the bulk electrolyte. Adapted from reference.[173]

The mosaic model was first presented by Peled et al., which incorporated electrochemical impedance spectroscopy (EIS) and XPS spectra performed by Aurbach and Kanamura for a reaction mechanism that described the varied composition of the SEI in terms of decomposition and location to the electrode.[179,172,180,171]

As previously stated, organic carbonates are the electrolyte of choice for almost all commercial Li-ion batteries available today, but when tested in LMBs there has been a significant drop in electrochemical performance. This is attributed to the lack of flexibility associated with the "mosaic model" SEI making them vulnerable to interfacial variations at the interface due to the large volume change associated with the Li plating/stripping processes.[181,182,183]

Ethers have proven better electrolyte solvents for Li negative electrodes, demonstrating high Coulombic efficiencies (>98%) with signs of dendrite suppression in several reports.[184,185,173] The decomposition of ethers on contact with the lithium electrode leads to the formation of oligomers, which show good flexibility and a strong affinity to the lithium metal surface (**Figure 1.17**).

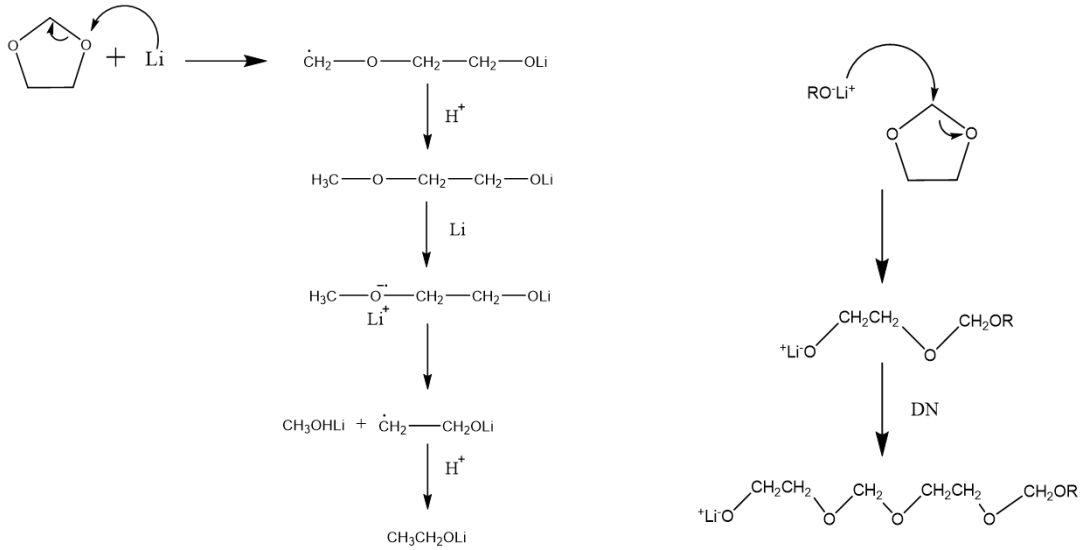

Figure 1.17 - Proposed reaction mechanism for the formation of oligomers from the reduction of 1,3 dioxolane.

Selecting an appropriate electrolyte system that can withstand the large volume variations during plating/stripping processes is an important consideration for lithium metal electrodes. However, issues over dendrite formation still remain and require additional strategies to overcome the inherent safety risk.

1.4.3 Chemical and engineering approaches to suppress dendrite formation

1.4.3.1 High salt concentration

Multiple chemical and engineering routes have been considered for the suppression of branched lithium growth in cells with Li metal electrodes. Jeong et al. reported that a highly concentrated (3.3 molal) LiTFSI salt in propylene carbonate solution inhibited the growth of mossy lithium.[186] However, the current density was limited to 0.5 mA cm^{-2} for the plating/stripping study in Li||Li symmetrical cells which yielded a low Coulombic efficiency of 80% after 50 cycles. The effect of high salt concentration electrolyte solutions on the morphology of deposited lithium has also been reported.[187] Smooth nodule-like lithium structures were electrodeposited in a 4 molal LiTFSI-ether electrolyte solution, at lower salt concentrations the morphology of the electrodeposited lithium changed to needle-like structures.

1.4.3.2 3D current collectors

Designing 3D current collectors with a high surface area can effectively reduce the local current density at the metal surface and minimise uncontrollable mossy lithium formation.[188,189] Lui et al. reported dendrite free and stable cycling of a lithium metal negative electrode with a 3D porous copper current collector against a $LiFePO_4$ positive electrode in a full cell configuration.[190] SEM images revealed smooth deposits after 100 plate/strip cycles, however the current density applied during testing was limited to 1 mA cm^{-2}.

1.4.3.3 Self-healing electrostatic shield

Dendrite-free Li deposition was recently achieved in carbonate electrolytes that contained Cs^+ and Rb^+.[191,192] The addition of these cations act as a "self-healing electrostatic shield" mechanism. Cs and Rb were chosen as metals as their reduction potential is just below Li. During lithium deposition, the additive cation in low concentrations formed a positively charged electrostatic shield around any lithium

protrusions that have formed from uneven electrodeposition. This directed further lithium deposition away from the protrusion, which inhibited further branched growth.

1.4.3.4 Electrolyte additives

Various electrolyte additives have been considered to facilitate preferential surface deposition morphology. Lithium iodide (LiI) has been studied as a functional additive in ether-based electrolyte solutions performed in Li||Li symmetrical cells.[193] The presence of LiI helped induce the polymerisation of the ether-solvents to form an ion conductive flexible oligomer layer on the surface of the lithium metal electrode. The surface layer inhibited the formation of branched lithium growth and promoted uniform Li deposition during plating/stripping. However, the current densities applied in this study were limited to <4 mA cm^{-2}, so branched lithium growth/dendrites could still occur at higher rates.

Winter et al. reported that the addition of fluorethylene carbonate (FEC) to 1 M lithium bis(trifluoromethanesulfonyl)imide (LiTFSI) in tetraethylene glycol dimethyl ether (TEGDME), enabled the formation of a stable SEI on lithium metal electrodes.[194] 3% of FEC electrolyte additive was tested in Li||Li symmetrical cells and the Coulombic efficiency of Li plating/stripping remained around 95% for more than 100 cycles. XPS analysis carried out on ex situ cycled Li electrodes revealed a strong presence of LiF in the SEI, which originated from the decomposition of FEC and is known to aid in lithium deposition across the SEI.[195] An alternative route for LiF formation in the SEI of lithium metal electrodes has also been reported, trace amounts of water (25-50 ppm) are used as an electrolyte additive in lithium hexafluorophosphate ($LiPF_6$) containing electrolytes.[196] The presence of water induced the formation of a trace amount of hydrogen fluoride (HF) from the hydrolytic decomposition of the $LiPF_6$ salt, which in turn was electrochemically reduced to form a dense LiF-rich layer on the lithium metal surface.

1.4.3.5 Artificial solid electrolyte interphase

One promising strategy to promote uniform lithium deposition during plating is to stabilise the lithium metal surface with an artificial layer that acts as an SEI (sometimes referred to as a protective layer) or aids in the production of favourable electrolyte-electrode interphases. It is essential that these artificial layers possess the same key criteria as previously described for an ideal SEI on the lithium metal electrode. The pre-treated layer should cover the entire Li surface prior to cycling, the layer should also be electrically insulating, as-well as providing a strong physical barrier against branched lithium formation whilst being flexible enough to accommodate the volume expansion of the lithium electrode during plating/stripping. Monroe and Newman have suggested that dendrite growth during the plating process could be effectively suppressed if the organic electrolyte was replaced with a conducting solid electrolyte that has a shear modulus which is twice that of lithium.[163,164] The coatings should also be chemically stable at the operating potentials of the lithium metal electrode and promote good Li-ion conductivity across the layer during cycling.

A common approach to forming artificial SEI layers is by controlled exposure of lithium metal electrodes with chosen chemicals. An example of this is the reaction between substituted-silanes and the natural hydroxyl groups that are present in the native layer on lithium foil. Dunn et al. exposed lithium foil to tetraethoxysilane to form a thin silicate layer on the metal surface, this protective coating was electrochemically stable and exhibited a low initial impedance.[197] The layer was stable over 100 cycles in treated Li||treated Li symmetrical cells, with smooth lithium deposits observed in ex situ SEM images. A thin (~50-nm) uniform layer of lithium phosphate (Li_3PO_4) was achieved by the reaction of polyphosphoric acid with a lithium metal electrode prior to cycling.[198] The artificial SEI layer displayed good Li-ion conductivity and a high Young's modulus which are ideal qualities for the passivation layer. The modified lithium electrode demonstrated stable cycling for 200 cycles in Li_3PO_4 treated Li||$LiFePO_4$ cells. Recently, Hou et al. developed an artificial multi-phase protective film for the lithium metal electrode.[199] The composite film consisted of a Li_xSi alloy, Si-linked oligomers and LiCl. The modified lithium was electrochemically assessed in symmetric cells which showed

stable cycling for 2200 hours. However, the current density was limited to just 1 mA cm^{-2}.

1.5 Aims and objectives

Sodium-ion batteries are limited by the lack of sufficient negative electrode materials that can deliver competitive energy densities for the energy storage market. Li-S applications too, need to address key issues with the Li metal negative electrode if the potential of Li-S as a high energy density battery system is to be realised. The primary focus of this research project is to develop novel synthetic methods to investigate different metal nitrides as candidates for negative electrode materials or protective coatings in sodium-ion and secondary lithium metal battery applications.

In this thesis there are three main sections:

1. **Evaluation of tin nitride (Sn_3N_4) as a negative electrode in sodium-ion batteries** - Solvothermal synthesis of crystalline Sn_3N_4 has not been previously reported in the literature. This project aims to find the optimum reaction conditions to produce a single phase crystalline powder of Sn_3N_4. The synthesis is also tailored towards the galvanostatic cycling performance of the metal nitride in Na half-cells. By varying the temperature of the solvothermal synthesis, Sn_3N_4 with varying particle size can be obtained. The comparison between nanocrystalline and microcrystalline Sn_3N_4 electrodes was performed in Na half-cells. Nano-structuring cam increase the surface area of the tin nitride particle, increasing the availability of active sites for Na-ions to adsorb onto the surface. Nano-structuring can introduce defect sites which offer additional active sites for sodium adsorption and can potentially increase the specific capacity of the tin nitride material.

   The reaction mechanisms of charge storage for Sn_3N_4 were explored during cycling. The nitride has previously been reported as a conversion-alloying material, however the extent of these reaction processes is relatively unknown.[36] The reaction mechanisms were assessed by a combined ex situ mechanistic study of Sn_3N_4 electrodes in sodium half-cells by X-ray absorption spectroscopy (XAS)

and X-ray diffraction (XRD), to follow the electrochemical reactions of the metal nitride during reduction (charging) and oxidation (discharging).

2. **Evaluation of lithium nitride as a protective layer for lithium metal batteries** – This section aims to utilise lithium nitride (Li_3N) as an artificial SEI layer for the lithium metal electrode, that will facilitate the even passivation of lithium ions from the liquid electrolyte through the interface onto the metal electrode surface. Lithium nitride is formed under ambient conditions when the metal is in direct contact with nitrogen.[200] It has a unique crystal structure that allows for superior Li-ion conductivity (~10^{-3} s cm^{-1}) even at room temperature.[201] It is expected that the nitride layer acting as a protective layer will facilitate the even deposition of Li ions through its highly conductive and ordered structure. The shear modulus of Li_3N (150 GPa) should be adequate to suppress dendritic growth.[202]
   Scanning transmission X-ray microscopy data was collected on unmodified and nitrided lithium structures to provide information about the distribution of chemical species during electrodeposition and nitridation. XPS was also performed to analyse the surface of these materials. To determine whether the formed Li_3N layer affects the electrochemical performance of the lithium metal electrode, unidirectional galvanostatic polarisation and plate/strip measurements were carried out on both the unmodified and nitrided lithium electrodes.

3. **Evaluation of lithium nitride as a protective layer for lithium-sulfur batteries** - This section assesses the nitrided lithium electrodes as a protective layer against a polysulfide-containing electrolyte solution. The stability of the Li_3N protected lithium compared to unmodified lithium electrodes was assessed by optical microscopy, STXM and XPS, with particular attention to the different sulfur environments which can adversely affect the performance of the lithium metal electrode in Li-S cells.

Chapter 2 Instrumental methods

2.1 Electrochemical testing

In this section, the general electrochemical testing and cell preparation procedures that are mentioned throughout this report are described. Any additional description to electrochemical conditions or cell preparation that is unique to one particular chapter will be reported in the experimental part of that section.

2.1.1 General experimental procedure

2.1.1.1 Preparation of electrolyte solutions

The electrolyte solution used for the electrodeposition of lithium onto copper or nickel current collectors (**Chapters 4** and **5**) was 4 M bis(trifluoromethanesulfonyl)imide lithium salt (LiTFSI) in 1,3 DOL. The LiTFSI (99.95%, Aldrich) salt was dried under vacuum (>0.2 mbar) at 140 °C for 48 hours before use. After drying, the LiTFSI salt was stored in an argon-filled glovebox (Mbraun, oxygen and water content < 5 ppm) prior to use. 1,3 DOL (99.8%, anhydrous, ~75 ppm butylated hydroxytoluene (BHT) as inhibitor, Aldrich) was opened in the glovebox and dried over molecular sieves (4 Å,8-12 mesh bead size, Aldrich) for 48 hours prior to use. The electrolyte solution was prepared in an argon-filled glovebox by dissolving the appropriate amount of solid into the 1,3 DOL solvent. Electrolyte solutions were generally used within four weeks.

2.1.1.2 Separator preparation

Two different types of separator have been used throughout this thesis. Glass-fibre sheets (Whatman, glass microfiber filters, grade GF/F) were punched into discs (12 mm ϕ) and dried under vacuum (< 0.2 mbar) at 150 °C for 48 hours). After drying, the glass-fibre separators were stored in an argon-filled glovebox. Monolayer polypropylene separators (Celgard 2400) were punched into discs (12 mm ϕ) and dried under vacuum

(< 0.2 mbar) at 60 °C for 48 hours. After drying, the polypropylene separators were stored in an argon-filled glovebox.

2.1.1.3 Cell setup

In this thesis, two-electrode Swagelok cells (**Figure 2.1**) were constructed for all the electrochemical measurements reported. However, the material for the individual components varied due to the different chemical compatibility requirements between chapters. The cell housing and nuts were either stainless steel (316) or polyfluoroalkoxy alkane (PFA) with a ½″ internal diameter, the ferrules were also made from PFA. Current collectors and caps were made from either copper or stainless steel (316l).

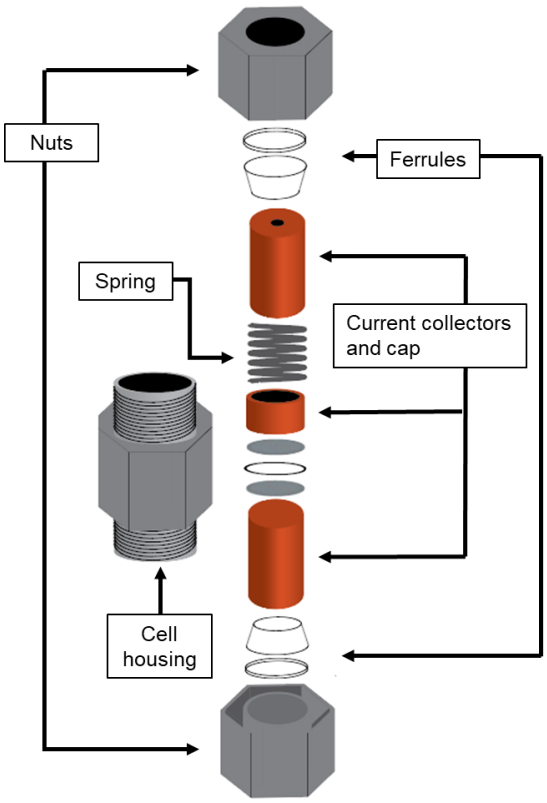

Figure 2.1 - Schematic of a Swagelok cell used throughout this report.

To prepare the cell for construction, Swagelok cell components (housing, nuts spring and ferrules) were placed in a vacuum oven at 80 °C for 24 hours. If stainless steel cells were used, the housing was first lined with fluorinated ethylene propylene (FEP, 0.127 mm thickness, RS components) to prevent short circuiting. Stainless steel current collectors and caps were mechanically polished to a mirror finish using alumina suspensions of decreasing particle size (25, 3.0 and 0.3 µm) with polishing pads (Buehler). The polished current collectors and caps were then sonicated in isopropanol (IPA) for 30 minutes before drying in the vacuum oven at 80 °C for 24 hours.

Copper bars and caps were polished using the same procedure for stainless steel however the copper parts were dried under vacuum at room temperature for 1 hour before being transferred to the glovebox (oxygen and water content < 5 ppm) to minimise the formation of a native oxide layer. Once all parts have been transferred to the glovebox, the cell components were allowed to cool to ambient temperature before cell construction. One side of the cell is first constructed by placing ferrules onto one current collector from the top and one nut from the bottom, the cell housing is then screwed in place. The respective electrodes and electrolyte-soaked separators are then stacked inside the housing for the required experiment, the cap is then placed on top followed by a spring to generate stack pressure in the cell and to ensure electrical connectivity is maintained during measurement. Finally, an additional bar is screwed into place to complete the cell.

2.1.2 Galvanostatic cycling

Galvanostatic cycling (constant current chronopotentiometry) is used to simulate the charge and discharge conditions expected for an operational battery. During galvanostatic cyling, a constant current is applied to the working electrode whilst the potential is measured until a potential/time limit is reached, the direction of current is then reversed to achieve one full cycle. All galvanostatic cycling data reported in this thesis were cycled with potential limitations (GCPL) that were suitable for the working electrode (**Figure 2.2**).

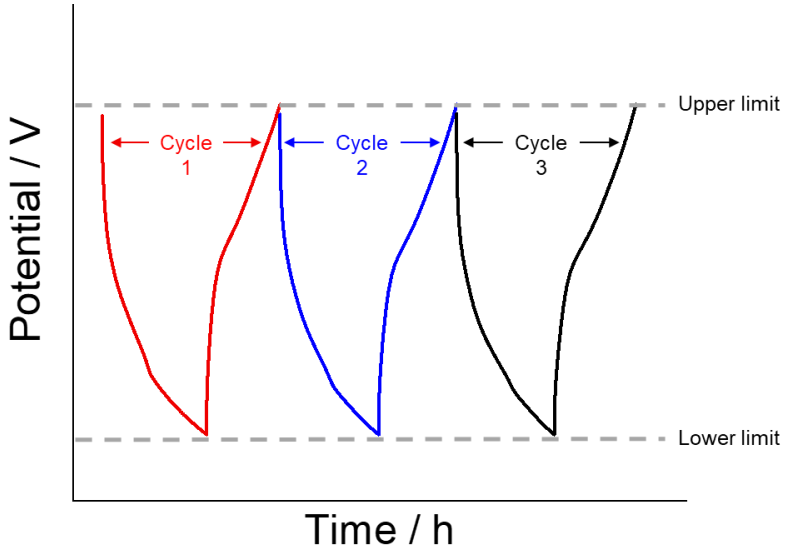

Figure 2.2 - Example of GCPL. A fixed current is applied to a working electrode and the potential is recorded until the lower and upper potential limits are reached, the direction of current is then reversed.

The terms charge and discharge will be defined in each section as reduction and oxidation depending on the type of working electrode and the electrochemical reactions that are being evaluated.

2.1.2.1 Galvanostatic cycling instrumentation

All electrochemical measurements were recorded using a multichannel potentiostat (VMP2 or MPG, Bio-Logic) using EC-Lab software (Bio-Logic). The specific details of GCPL will be presented at the beginning of each chapter.

2.1.3 Differential capacity analysis

Differential capacity analysis (DCA) is an analytical tool that is primarily applied to constant current (galvanostatic cycling) datasets. DCA can aid the interpretation of constant current measurements by monitoring electrochemical processes during multiple cycles and can serve as an indicator for cell failure.[203,204] DCA tracks the rate of change of capacity for an electrochemical system during reduction/oxidation as a function of terminal voltage. The curves are obtained by differentiating the capacity vs. voltage of constant current datasets:

$$\frac{dQ}{dE}$$ **Equation 9**

The curves of DCA plots highlight voltage plateaus in reduction/oxidation curves as peaks (**Figure 2.3**). Each individual peak can represent a different (electro)chemical process or structure variance of the studied electrode.

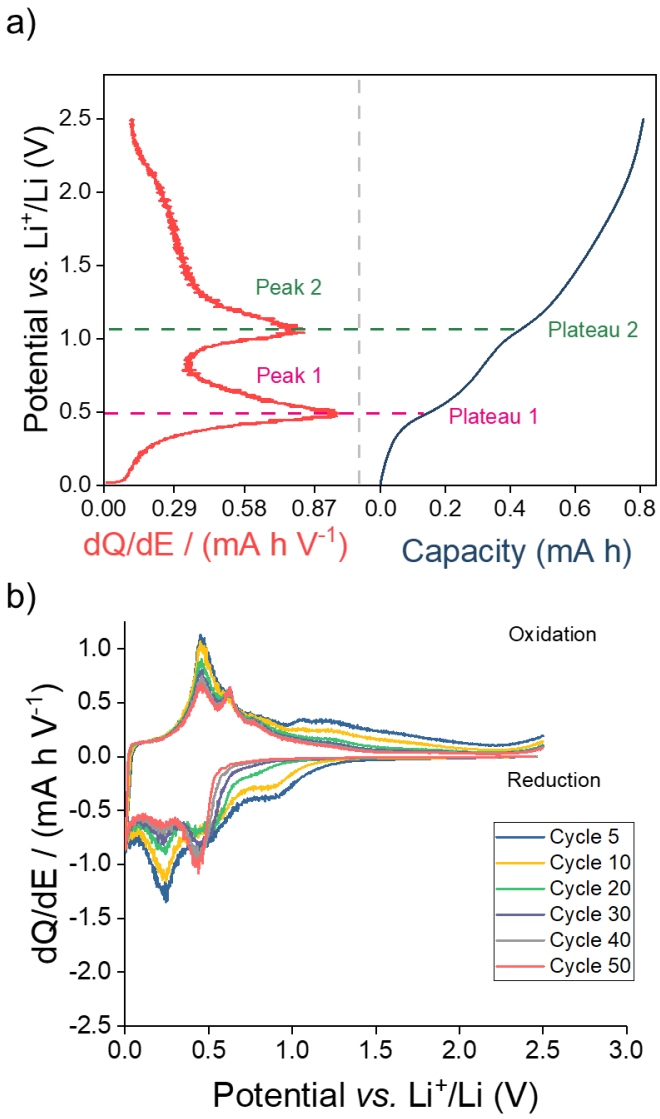

Figure 2.3 – (**a**), Example of a constant current oxidation profile (blue) and corresponding DCA curve (red) highlighting the two sloping plateaus as peaks. (**b**), Example of a DCA plot displaying multiple cycles of reduction/oxidation curves.

Similar to cyclic voltammetry (CV), the area under the peak represents the capacity of a particular process. The y-axis in CV tends to be current (*I*), which can be converted to $\frac{dQ}{dE}$ by dividing by the sweep rate.[205] DCA plots tend to produce more defined, sharper peaks than CV as constant current experiments are usually carried out over greater time periods. This allows electrochemical processes to proceed closer to equilibrium whereas the applied potential scan rates set for CV's may neglect the extent of some electrochemical processes. An additional benefit to studying DCA plots over CV is that the *IR* drop remains constant throughout constant current measurements but varies through a CV sweep which can alter peak shapes.[206]

2.1.3.1 Differential capacity analysis instrumentation

The differential plots presented in this thesis have been generated from galvanostatic cycling data collected on multichannel potentiostats (VMP2 or MPG, Bio-Logic). The DCA plots were generated using EC-Lab software (Bio-Logic) by differentiating the constant current curves with 3 mV intervals. It is important to note that DCA was performed on cells cycled in two-electrode configuration as half-cells vs. lithium or sodium metal foils. As a result, the working and counter electrode processes are not decoupled. In principle the foils should provide a constant electrochemical response, but polarisation effects may alter the electrochemical response.

It is sometimes necessary to perform smoothing of the raw experimental data to produce satisfactory DCA curves without excessive noise. Excessive noise is usually the result of systematic and random error, if the noise is significant during collection of constant current cycling measurements, it can be exaggerated in the corresponding DCA plots which could be mistaken as a true electrode process. Attempts to minimise noise generated from systematic error have been made. Cells are cycled in climatic controlled chambers to reduce temperature fluctuation and potentiostats are connected to electrical line filters to deliver appropriate frequency characteristics for the electrochemical measurement. Any remaining noise contributions can be minimised by smoothing. Repeating the data can also account for any random errors collected upon cycling.

EC-Lab software provides a list of smoothing methods with the Savatzky-Golay and moving average filters being the preferred choice. The degree of smoothing can be varied by altering the main parameters: the smoothing window, iterations and the degree of polynomial curve being fitted. This is an imprecise process as the ideal goal is to minimise the noise for suitable interpretation of DCA without suppressing "real" contributions and introducing smoothing artefacts.[203,207] Smoothing artefacts and suppression of true data can include reducing peaks heights, introducing new features to the curves and the removal of features altogether. The DCA plots presented in this thesis were smoothed by a 3 point moving average function.

2.1.4 Electrochemical impedance spectroscopy

Electrical resistance is well known and can be defined as the ability of a circuit element to resist the flow of electrical current. For an ideal resistor, Ohm's law describes the relationship between resistance, potential and current as:

$$R = \frac{V}{I} \qquad \textbf{Equation 10}$$

This relationship is limited to the behaviour of an ideal resistor. In reality an electrochemical cell will contain multiple resistive and capacitive elements and so AC impedance spectroscopy techniques are employed.

For electrical circuits that contain capacitor elements, the fundamental relationship between charge and voltage is given as:

$$C = \frac{dQ}{dV} \qquad \textbf{Equation 11}$$

where Q is the charge stored in the capacitor in coulombs and C is the capacitance in farads.

Electrochemical impedance spectroscopy (EIS) is a powerful analytical technique due to the range of informative information that can be extracted from the data. To understand the impedance of electrochemical systems, it is useful to understand the behaviour of simple electrical circuits that contain linear electrical elements such as

resistance and capacitance. The technique involves applying a small amplitude AC potential (Potentio, PEIS) or current (Galvano, GEIS) perturbation across a cell and measuring the corresponding current or potential response respectively.

If a small amplitude, sinusoidal potential (<25 mV) is superimposed upon an applied potential, the response will be a (pseudo)linear AC current at the same frequency, however the phase and amplitude will be shifted in phase.

In the most common experiments, the impedance across a cell, (Z), is analysed as a function of the potential perturbation, frequency (f) and phase shift (ϕ) in the current response:

$$Z = \frac{\Delta E sin(\omega t)}{\Delta I sin(\omega t + \phi)} \qquad \textbf{Equation 12}$$

where ΔE is the maximum amplitude of the applied sinusoidal potential (mV) and angular frequency ((ω) ω is the radial frequency described as $\omega = 2\pi f$). The response will be a current with a maximum amplitude (ΔI) which is also shifted in phase from the signal (ϕ). The impedance is therefore expressed in terms of a magnitude (Z) and phase shift (ϕ).

Complex notation is used to facilitate processing impedance data. Using complex notation, the potential perturbation is described as:

$$E = |E|(cos(\omega t) + isin(\omega t) \qquad \textbf{Equation 13}$$

Current response:

$$i = i_0\,[cos(\omega t + \phi) + i\,sin(\omega t + \phi)\,] \qquad \textbf{Equation 14}$$

Then from Euler's theorem:

$$E = E_0\,exp(i\omega t) \qquad \textbf{Equation 15}$$

and:

$$i = i_0\,exp(i\omega t + i\phi) \qquad \textbf{Equation 16}$$

Impedance can now be expressed in complex notation:

$$Z = \frac{E}{I} = \frac{-i}{\omega C} \qquad \textbf{Equation 17}$$

where i is an imaginary number ($i = \sqrt{-1}$). The complex notation removes the time dependence which facilitates processing.

EIS is generally interpreted through complex analysis in the form of a Nyquist plot. In complex analysis, a projection on the x-axis is termed the real part ((*Z*) = *Z*'), and a projection on the y-axis is called the imaginary part (-Im(*Z*)=*Z''*, y axis), giving a complex plane impedance plot. In simplistic terms, resistive values are read on the real x −axis and capacitive values are read on the imaginary y −axis.

EIS is commonly reported in battery research, however the fitting and interpretation of EIS spectra is complex. Multiple modified versions of equivalent circuits have been suggested to quantify and comment on the stability of an electrode before, during and after cycling. As a result of this uncertainty, EIS presented in **Chapter 4** will be qualitatively assessed as useful insights can still be obtained from the shape of the spectra.

2.1.4.1 Electrochemical impedance spectroscopy instrumentation

Potentiostatic impedance spectroscopy (PEIS) was recorded before and after the plate/strip measurements (**Chapter 4**) on a multichannel potentiostat (VMP3, Bio-Logic). A sinusoidal potential with 10 mV amplitude was applied to the OCV at frequencies from 1 MHz to 10 mHz, with 3 points averaged at each frequency.

2.2 X-ray diffraction

X-ray diffraction (XRD) is a powerful, versatile, non-destructive technique that can reveal the chemical composition and the crystallographic structure of a sample.[208]

X-rays are generated in a cathode ray tube by heating a filament to produce electrons, the electrons are accelerated towards a target anode (i.e. copper) by applying a high voltage (~40 kV). The accelerated electrons bombard the target, incoming electrons that have sufficient energy to eject an electron from the inner shell will produce radiation characteristic of the target material (photoelectric effect).[209] The generated radiation usually consists of several characteristic wavelengths of X-rays with the most common being K_α and K_β. Monochromators are used to remove unwanted wavelength contributions (usually. K_β). However, K_α consists of $K_{\alpha1}$ and $K_{\alpha2}$ lines which are sufficiently close in wavelength that the monochromator cannot discriminate between them and so a weighted average of the two is applied when collecting data.[210] The monochromated beam is then collimated which concentrates and directs the X-rays towards the sample.

For samples to be characterised by this technique they must possess a crystalline structure. Crystal structures have a periodic array of atoms in long-range order. The wavelength of X-rays is similar to the distance between atoms in a crystal. When the monochromated beam strikes a series of parallel planes in a crystal, the incoming X-rays can strike and scatter from the sample's electrons in atoms (elastic scattering). If the scattered angle of incidence is equal to the angle between the scattered beam and the normal, a Bragg reflection is produced (**Figure 2.4**).

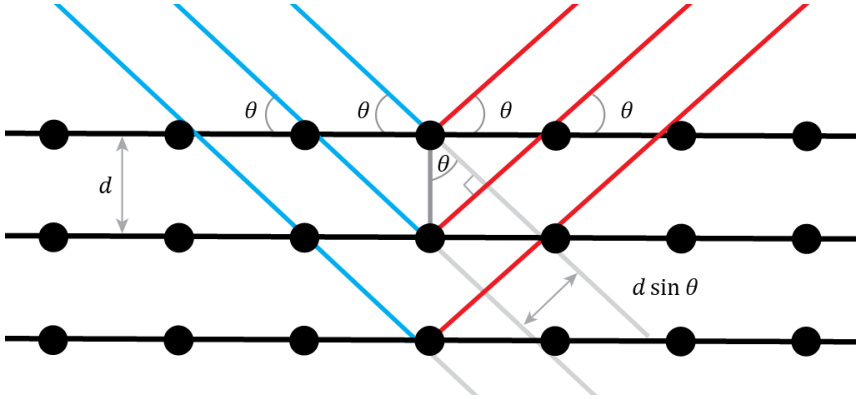

Figure 2.4 - Generalised schematic of an allowed Bragg reflection in a crystal.

The angle at which constructive interference will occur is shown by the Bragg equation:

$$n\lambda = 2d_{hkl}sin(\theta_{hkl}) \qquad \textbf{Equation 18}$$

where λ is the incident X-ray wavelength, d_{hkl} is the crystal spacing and θ_{hkl} is the Bragg angle.

2.2.1 Powder X-ray diffraction

The majority of diffractometers designed for powder X-ray diffraction (PXD) employ the Bragg-Brentano parafocusing geometry (**Figure 2.5**).[211] In this setup, the incident angle of the X-rays (ω), is defined between the X-ray source and the sample and is always ½ of the detector angle. The diffraction angle (2θ), is defined between the incident beam and the detector. In Bragg-Brentano geometry, the diffraction vector (s) is always normal to the surface of the sample.

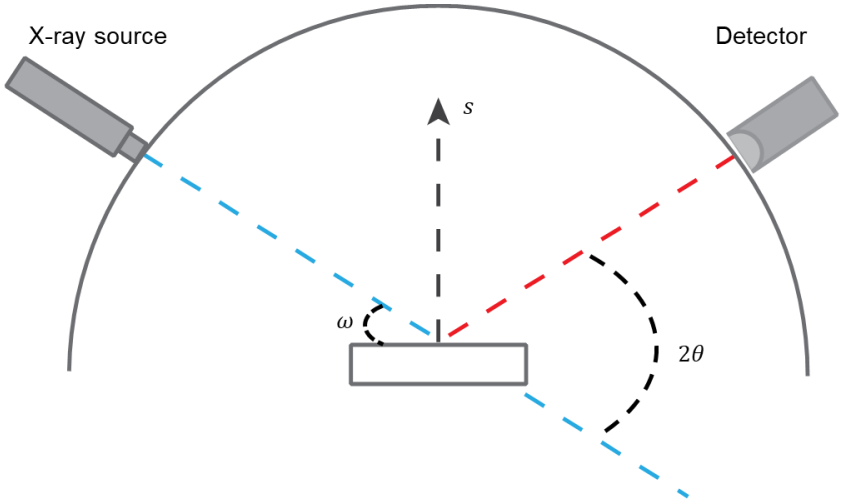

Figure 2.5 - Generalised schematic of PXD in Bragg-Brentano geometry.

The crystal structure describes the atomic arrangement of a material; crystals adopt a range of lattice planes that determine at which angle a Bragg reflection is allowed. The planes where the smallest Bragg angle is observed must have the largest separation (*d*-spacing). In a primitive cubic system, the (100) plane will have the largest d_{hkl} spacing and will give rise to the first reflection (**Figure 2.6**).

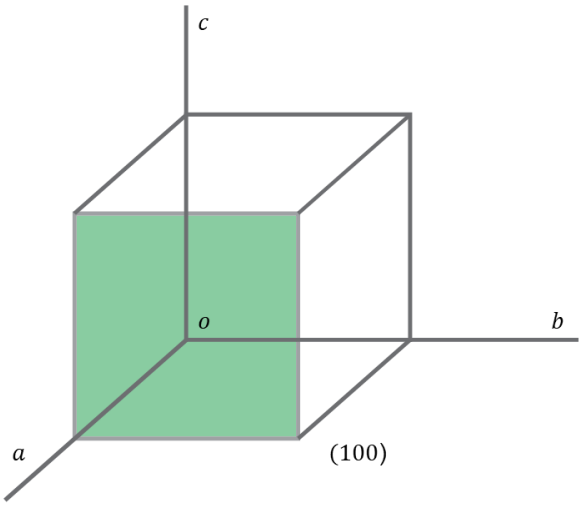

Figure 2.6 - Schematic of the (100) lattice plane in a cubic system.

2.2.1.1 Rietveld refinement

Rietveld refinement is an analytical tool used to validate the structure of crystalline materials by analysing the diffraction patterns collected from PXD. Diffraction

patterns usually consist of many overlapping peaks which are also influenced by instrumental factors. The process of Rietveld refinement employs a least squares fitting method to minimise the difference between the collected diffraction data and the calculated data from a model obtained from the ICSD database.[212]

$$M = \sum_i w_i \left(y_i^{obs} - y_i^{calc}\right)^2 \qquad \textbf{Equation 19}$$

where w_i is a weighting factor, y_i^{obs} is the observed intensity and y_i^{calc} is the calculated intensity.

The calculated profile term y_i^{calc}, is determined from the structural model which is the sum of the calculated contributions from neighbouring Bragg reflections (k) and the background contribution.

$$y_i^{calc} = s \sum_i L_k \, |F_k|^2 \, \Phi(2\theta_i - 2\theta_k) \, P_k \, A + y_{bi} \qquad \textbf{Equation 20}$$

where s is the scale factor, i is the Miller indices for a Bragg reflection, L_k is the Lorentz polarisation and multiplicity factors, F_k is the structure factor for the k^{th} Bragg reflection, Φ is the reflection profile function, P_k is the preferred orientation function, A is the absorption factor and y_{bi} is the background intensity at the i^{th} step.

For Rietveld refinements of PXD, a pseudo-Voigt type peak profile function is usually applied to model the peak profile and to describe accurately the peak shape for the generation of the calculated profile. The pseudo-Voigt function is a contribution of Gaussian and Lorentzian components.

The Gaussian contribution to the peak shape can be described as:

$$C_G = \frac{(4ln2)^{\frac{1}{2}}}{H_k\sqrt{\pi}} \exp\left[\frac{-4ln2(2\theta_i - 2\theta_k)^2}{H_k^2}\right] \qquad \textbf{Equation 21}$$

And the Lorentzian contribution to the peak shape can be described as:

$$C_L = \frac{2}{\pi H_k} \Big/ \left[1 + 4\frac{(2\theta_i - 2\theta_k)^2}{H_k^2}\right] \qquad \textbf{Equation 22}$$

where $H_k$is the full width at half maximum (FWHM) of the k^{th} Bragg reflection and $2\theta_k$ is the calculated position for the k^{th} Bragg reflection corrected for the zero point origin.

To determine the quality of fit between the calculated and experimental pattern, a series of reliability factors (R-factors) are defined:

$$R_{profile} = 100 \sum_{i}^{n} \frac{y_i^{obs} - y_i^{calc}}{y_i^{obs}} \qquad \textbf{Equation 23}$$

The most mathematically significant reliability factor is the $R_{weighted\ profile}$:

$$R_{weighted\ profile} = 100 \sum_{i}^{n} \frac{y_i^{obs} - y_i^{calc}}{y_i^{obs}} \qquad \textbf{Equation 24}$$

The $R_{expected}$ is a measure of the data quality:

$$R_{expected} = 100 \left[\frac{(N - P + C)^2}{\sum_i w_i \left(y_i^{obs} - y_i^{calc}\right)^2} \right]^{\frac{1}{2}} \qquad \textbf{Equation 25}$$

where N is the total number of observations, P is the number of refinable parameters and C is the number of constraints used in the refinement. The ratio of the two R-factors gives the chi-squared value for the fit:

$$\chi^2 = \left[\frac{R_{weighted\ profile}}{R_{expected}} \right]^2 \qquad \textbf{Equation 26}$$

2.2.1.2 Scherrer equation

Information about average crystallite size can also be extracted from the peak broadening of X-ray diffraction patterns (FWHM), this analysis was developed by Paul Scherrer in 1918. If crystallite sizes of the target sample are sufficiently small, the maxima of diffraction patterns are broadened by an amount inversely proportional to the crystallite size. To accurately measure crystallite size, the broadening contribution from the instrument (diffractometer) must be accounted for prior to calculation, this is usually determined from collecting a pattern from a highly crystalline standard under the same

optical conditions as the target sample. An average crystallite size can then be calculated from the Scherrer equation:

$$\tau = \frac{K\lambda}{\left(\sqrt{\beta_0^2 - \beta_s^2}\right)} cos(\theta) \qquad \textbf{Equation 27}$$

where τ is the "true" crystallite size, K is the Scherrer constant, a dimensionless shape factor which value depends on the shape of the crystallite (typically ~0.9), λ is the incident X-ray wavelength, β_0 is the FWHM for the target sample, β_s is the FWHM for the highly crystalline standard and θ is the Bragg angle.

An external technique such as transmission electron microscopy (TEM) can be used to compare the average crystallite size in a sample.

2.2.1.3 Powder X-ray diffraction instrumentation

Powder X-ray diffraction measurements reported in this thesis were recorded on a Bruker D2 Phaser using Cu-Kα radiation (λ = 1.5418 Å) in Bragg-Brentano geometry. The reflections present were identified by comparison with the ICSD database and patterns refined using the GSAS package.[213]

GSAS is a refinement software package that employs a "pseudo-Voigt" type peak profile function, which combines Gaussian and Lorentzian components.[210] The Gaussian shape is described by the Cagliotti function, the Lorentzian shape involves many factors but the main two contributions are the size and strain broadening terms. The refinement fitting is considered finished when no further significant changes are witnessed to unit cell dimensions, instrument or sample parameters over multiple cycles on the software, whilst maintaining a high quality fit to the data. From the refinement, a crystallite size of the material can be determined using an adaption of the Scherrer formula described in the GSAS manual.[214]

An LaB_6 standard collected in the same geometry was used to define the Gaussian instrumental peak shape, with the crystallite size obtained from the Lorentzian crystallite size broadening terms of the GSAS refinement and calculated from a modified Scherrer formula:

$$\rho = \frac{18000K\lambda}{\pi X} \qquad \textbf{Equation 28}$$

where K is the Scherrer constant, λ is the incident X-ray wavelength and X is the Lorentzian profile coefficient determined from the GSAS Rietveld refinement.

2.2.2 Grazing incidence X-ray diffraction

Grazing incidence X-ray diffraction (GIXD) is an X-ray technique where the incident angle is fixed at a very small angle (ω < 5°) which allows the X-rays to be scattered mainly at the top-most surface of the sample where the beam length and penetration depth is fixed (**Figure 2.7**).

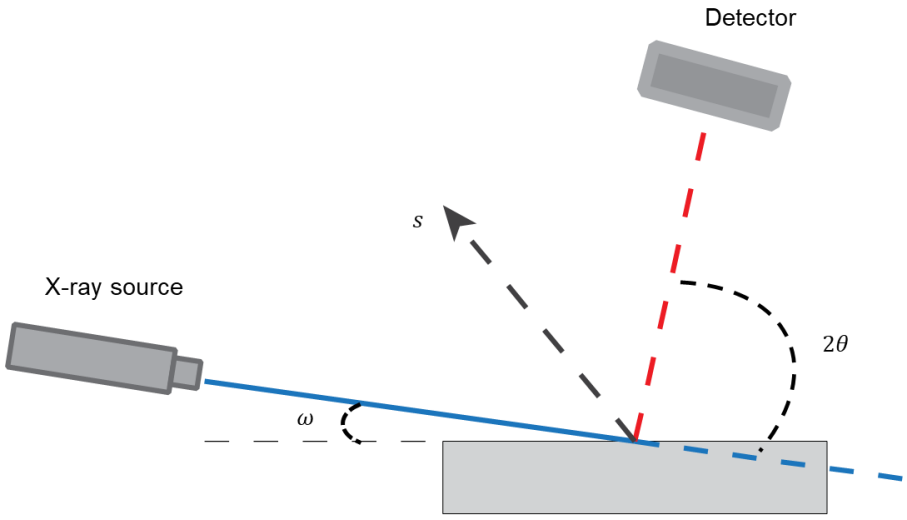

Figure 2.7 - Generalised schematic of GIXD geometry.

2.2.2.1 Grazing incidence X-ray diffraction instrumentation

Ex situ X-ray diffraction patterns reported in **Chapter 3** were carried out in an air-sensitive XRD sample holder (Bruker) and were collected in grazing incidence geometry (1° incidence angle) with Cu-Kα radiation (λ = 1.5418 Å) using a Rigaku Smartlab with Hypix 2D detector.

2.3 Optical microscopy

Optical microscopy itself is a general term that encompasses a range of techniques including, bright field, dark field, phase contrast, confocal and fluorescence microscopy. The optical microscope is a type of microscope that employs visible light with a series of lenses to generate magnified images of a sample. Objects are typically mounted on a stage and viewed through eyepieces or captured as a digital image. Solid samples can be

illuminated in a variety of ways; bright field imaging is where light goes directly through the sample and dark field imaging is where light passes around the sample.

2.3.1 Optical microscopy instrumentation

Optical images reported in this thesis were captured with an Olympus BH2 microscope with both light field and dark field imaging. The Olympus BH2 microscope is equipped with an episcopic microscope wafer inspection station and a built in halogen light transformer for varying the light intensity to accommodate for a variety of samples.

Due to the air sensitive nature of the samples, they were first sealed inside a modified glass-slide chamber inside an argon-filled glovebox before being transferred to the optical microscope for imaging (**Figure 2.8**).

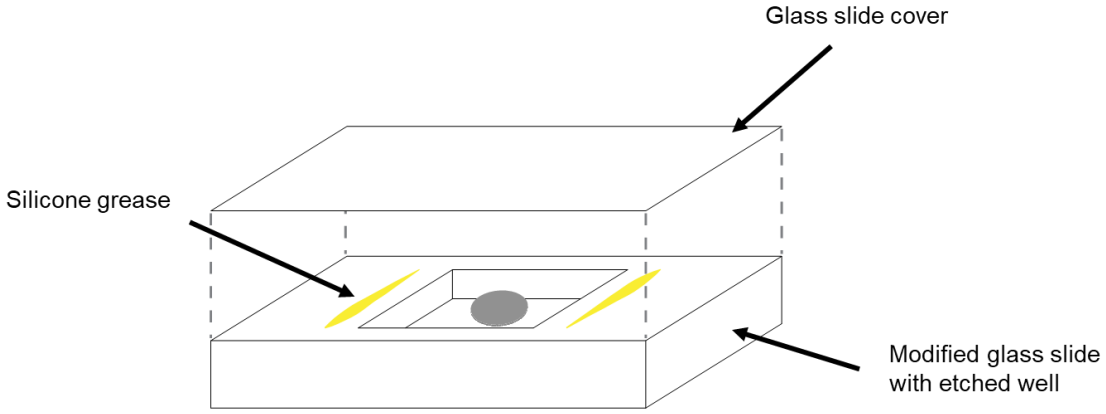

Figure 2.8 - Schematic of sample loaded into glass-chamber for optical microscopy.

2.4 Transmission electron microscopy

Whilst optical microscopy offers an effective route to image samples under standard conditions, the resolution is limited by the wavelength of light. Resolution is defined as the minimum distance by which two structures can be separated and still appear as two distinct objects, this can be described mathematically by Abbe's equation:

$$d = \frac{0.612\lambda}{n \sin \theta} \qquad \textbf{Equation 29}$$

where d is resolution, λ is the wavelength of imaging radiation, n is the index of refraction of medium between source and lens relative to free space and θ is half the aperture angle in radians. $n \sin \theta$ can be considered as the numerical aperture of the lens and is a measure of the light gathering capacity of the lens.

Consequently, other microscopy techniques need to be considered when measuring samples at high magnification. As the wavelength of an electron can be up to 100 000x shorter than that of visible light, electron microscopes are a preferred option to resolve structures on the nanometre scale.

Transmission electron microscopy (TEM) operates through the same basic principles as an optical microscope, with the electron beam passing directly through the sample (transmission) to a detector. In a typical TEM an electron beam is focused into a small, coherent beam through a series of condenser lenses (**Figure 2.9**).

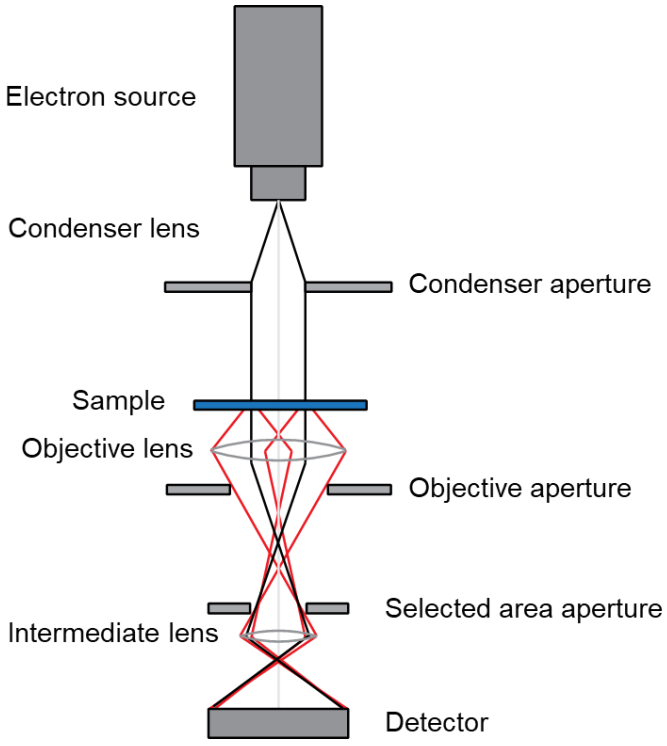

Figure 2.9 - Generalised schematic of a TEM microscope.

The beam is shaped by the condenser aperture by excluding high angle electrons. The concentrated beam strikes the sample and depending on the sample thickness and composition, a portion of the electrons are transmitted through the sample. The

transmitted electrons are refocused by an objective lens before passing optional apertures and lenses before an image is generated on the detector.

TEM samples must be thin enough to allow sufficient electron transfer through the sample. Solid inorganic materials are typically suspended on a metal TEM grid with a very thin carbon film which can be mounted directly into the instrument.

2.4.1 Transmission electron microscopy instrumentation

Transmission electron microscopy (TEM) was carried out with a FEI Technai12 (120 kV) on samples that were dispersed into isopropanol with ultrasound and dropped onto TEM carbon grids.

2.5 Scanning electron microscopy

Scanning electron microscope (SEM) allows the electron imaging of samples that would be considered too thick for TEM. Instead of measuring samples in transmission mode, SEM constructs images from electrons that interacted with the sample surface.

In a typical SEM, electrons are thermionically emitted from an electron gun, equipped with a tungsten filament cathode. The electron beam (typically 0.2 to 40 keV) is focussed by one or two condenser lenses to produce a spot size (typically < 5 nm) on the sample. Scanning coils are used to deflect the beam so it can scan the sample surface along the x or y axis. Several detectors are used to detect different signals ejected from the interaction of the sample with the electron beam.

The interaction of the electron beam with a sample occurs within an excitation volume on and below the sample surface. The contribution of this volume is dependent on the angle and energy of the incident electron beam as-well as the composition of the sample (**Figure 2.10**).

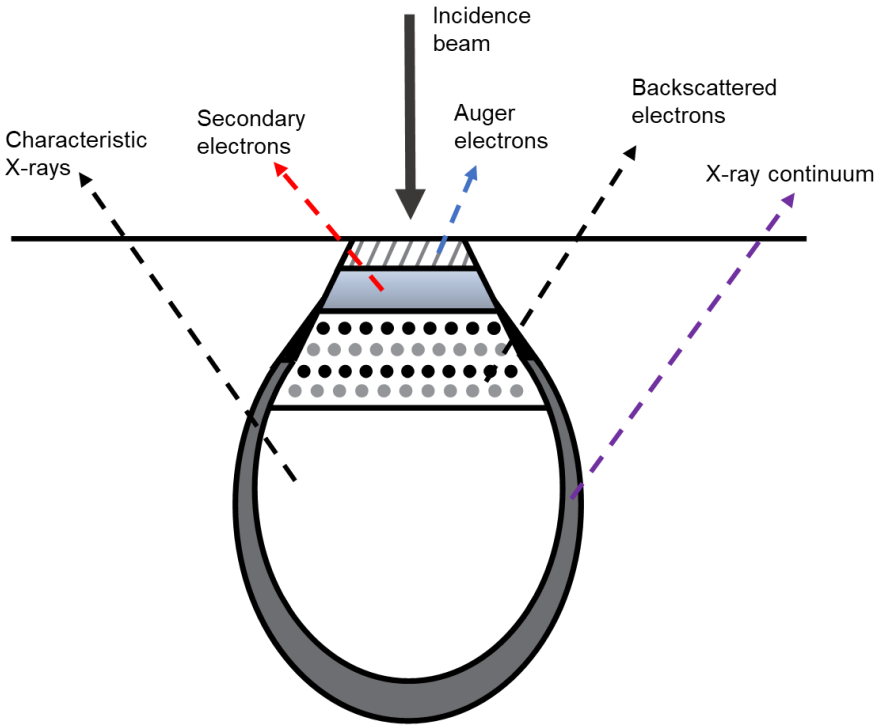

Figure 2.10 - Schematic illustration of the interaction volume from a target sample at a given energy of incident beam electrons which combined with the escape depths defines the spatial resolution of each signal.

Both elastic and inelastic scattering processes in the sample are considered for SEM. Elastic scattering of atoms deeper into the sample (10-100 nm) result in the generation of backscattered electrons (BSE) that travel back to the specimen surface and into the vacuum. Inelastic scattering occurs from interactions at the sample surface (1 nm mean escape depth) where low energy electrons (≤ 50 eV) can escape into the vacuum and are referred to as secondary electrons (SE). Both BSE and SE are detected for image processing, however the ejection of characteristic X-rays holds information on the chemical composition unique to the elements present in the sample.

2.5.1 Scanning electron microscopy instrumentation

Both surface topography and cross-section SEM images reported in **Chapter 4** were collected on a JEOL JSM6500F microscope. Due to the air sensitive nature of the electrode samples, the electrodes were mounted on SEM stubs inside an argon glovebox before transferring to the instrument inside a modified glass chamber. The mounted

samples were quickly loaded onto the SEM specimen stage with minimal air exposure (≤ 4 seconds) to reduce the reactions of electrode with air.

2.6 Synchrotron-based techniques

Additional characterisation techniques reported in this thesis were measured using the synchrotron radiation facility at Diamond Light Source (DLS). X-ray absorption spectroscopy (XAS), scanning transmission X-ray microscopy (STXM) and hard X-ray photoelectron spectroscopy (HAXPES) were performed on dedicated beamlines that can best utilise the high intensity and photon flux that is generated from a synchrotron source.

2.6.1 Synchrotron radiation

The use of synchrotron radiation (SR), has enabled the characterisation of battery materials reported in this thesis, that would not be possible in lab-based settings. It is important to recognise the intrinsic properties of SR; however, the full description of formulation is outside the scope of this research. Instead a brief overview of third generation synchrotrons is presented.

Diamond Light Source U.K is an example of a third generation synchrotron; an overview of the facility is presented in **Figure 2.11**. Electrons are generated by thermionic emission by heating a high voltage cathode under vacuum, the liberated electrons are accelerated out of the electron gun by earthed anodes and guided into the linear accelerator (linac).

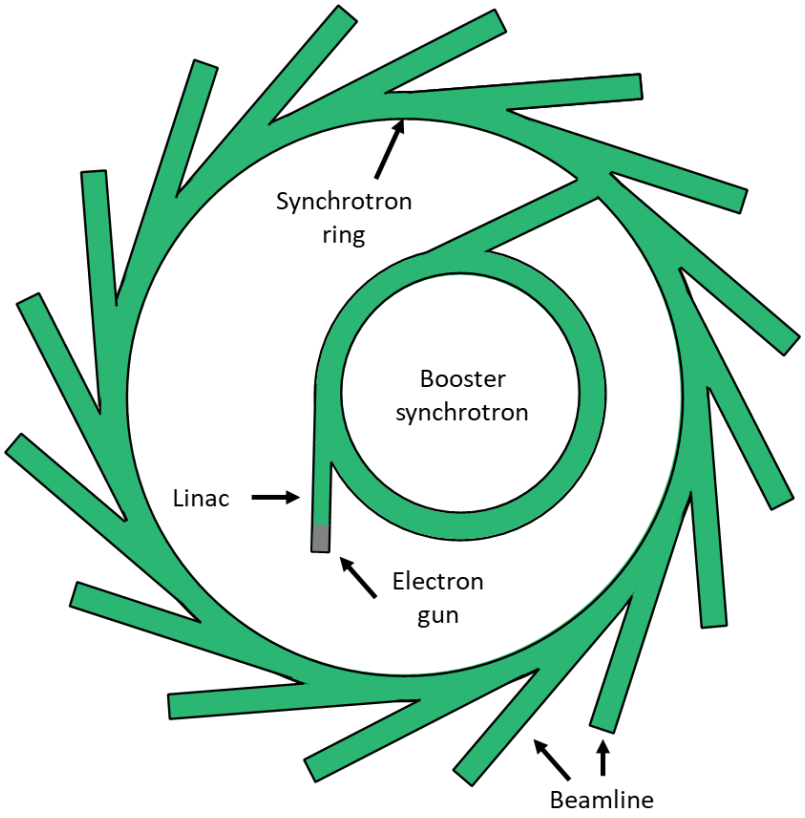

Figure 2.11 - Schematic representation of the Diamond Light Source synchrotron.

The linac has a series of radio frequency (RF) cavities which fields accelerate the electrons to ultra-relativistic speeds. The energy of the electron travelling at high velocity can be derived from the famous expression:[215]

$$E = \frac{mc^2}{\sqrt{1 - {v^2}/{c^2}}} = \gamma mc^2 \qquad \textbf{Equation 30}$$

where γ is the Einstein relativistic factor of an electron, v is the velocity of the electron and c is the velocity of light in free space. At Diamond the electrons have an energy of 3000 MeV and so the relativistic factor γ can be calculated as:[216]

$$\gamma = \frac{E}{mc^2} \qquad \textbf{Equation 31}$$

where the energy at rest of a particle is the mass of a particle multiplied by the velocity of light in free space squared (mc^2). The energy at rest for an electron is 0.5

MeV. At DLS electrons have a relativistic factor of 6000, hence the electrons are travelling at 99.97% the speed of light.

These high energy electrons are then injected into the booster synchrotron where they are shaped and stabilised to 3 GeV and can be used to top up the main synchrotron ring to provide a stable current. The synchrotron ring is not a true ring, rather it is shaped like a many sided polygon. At DLS there are 25 straight sections that are angled together to form a closed loop. Synchrotron light (radiation) at DLS is generated in two ways. The first is from changing the trajectory of the electron through bending magnets, this change in momentum causes a release of broad spectral radiation which is focussed down one of the straight sections along the initial direction of an electron. At the end of each straight section is an experimental hutch that will tune the beam to whatever specification is necessary for that beamline. These "bending'' beamlines are denoted with the letter B (e.g. B18).

The other source of synchrotron radiation is an insertion device positioned in the straight sections of the main storage ring. An undulator is an example of an insertion device which is a series of vertical dipole magnets with alternating polarity (**Figure 2.12**).

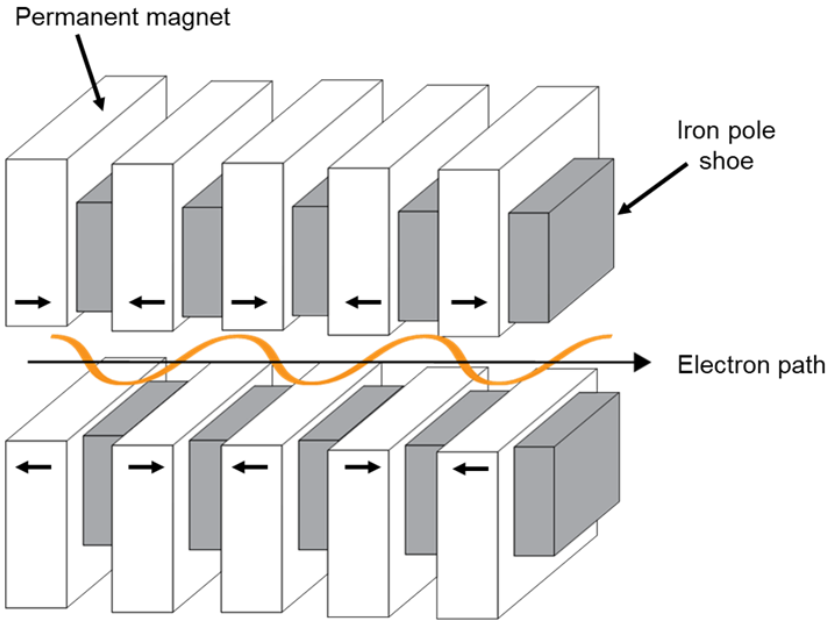

Figure 2.12 - Schematic diagram showing the electron trajectory between the opposing magnetic poles of an insertion device (undulator). The polarity of the magnets forces the electrons to oscillate leading to an emission of radiation. Adapted from reference.[217]

As the electrons path travels through these magnets, its trajectory oscillates from the opposing magnetic fields, causing synchrotron radiation to be emitted at the maxima of the peaks and troughs of the oscillations. The polarity and spacing of the magnets can be varied so the emitted radiation undergoes constructive interference at the desired wavelengths for that beamline (denoted with the letter I, (e.g. I08, I09)). The resulting narrow energy band of radiation is highly collimated in the horizontal and vertical directions.

2.7 X-ray absorption spectroscopy

X-ray absorption spectroscopy (XAS) is a powerful spectroscopic technique that can be utilised to study the local atomic geometry and chemical state of a particular element within a material. As XAS probes short range order, it is not limited to crystalline and highly ordered materials. Measurements can be collected on disordered systems including gases, liquids and amorphous crystal structures.[218] This can be particularly advantageous to battery material characterisation as some crystalline electrode materials will undergo structural transformations to an amorphous phase during discharge/charge.[219]

Generally, the intensity of X-ray absorption is determined from the relationship between the incident and transmitted intensity as described by Beer-Lambert Law:[220]

$$I_t = I_0 e^{-\mu t} \qquad \textbf{Equation 32}$$

where the incoming X-ray photons with incident intensity (I_0), pass through the sample. The transmitted X-ray photons intensity (I_t) will be reduced by an amount determined by the absorption properties of the sample. The thickness (t) and the absorption coefficient (μ) of the material will determine the transmitted intensity.

The absorption coefficient is a function of the photon energy with a value that is determined by the probability that absorption will take place, this is governed by Fermi's golden rule:[221,222]

$$\lambda_{if} = \frac{2\pi}{\hbar}\left|M_{if}\right|^2 P_f \qquad \textbf{Equation 33}$$

where λ_{if} is the transition probability, M_{if} is the matrix element for the interaction and P_f is the density of the final states.

The rule states that the likelihood of a photon being absorbed is dependent on the difference between the initial and proposed final state of the absorbing atom. If they are similar in energy, then absorption is more likely to occur.

A change in absorbance of a material is measured over a defined range of x-ray energies. As the incident X-rays probe with increasing energy, the photons are able to penetrate the sample further. At specific energies, a sharp rise in absorbance will occur in the form of an absorption edge. The occurrence of these edges is due to the photoelectric effect:[223]

$$E_k = h_f - E_b \qquad \textbf{Equation 34}$$

where the incoming X-ray (h_f), is absorbed by a core electron of lower binding energy (E_b) and a photon is emitted with kinetic energy equal to E_k with the characteristic absorption edge.

A simple mechanism is presented in **Figure 2.13**. Where an incident X-ray photon is absorbed by an electron in the core 1s (K) orbital of the target atom. The absorption is simultaneously followed by an excitation of an electron from the 1s orbital to the continuum (photoelectron), leaving a core hole at the 1s level.[224] This vacancy leads to different types of relaxation processes which lower the overall energy of the atom, either by emission of an X-ray fluorescence photon (**Figure 2.13**) or emission of an Auger electron.

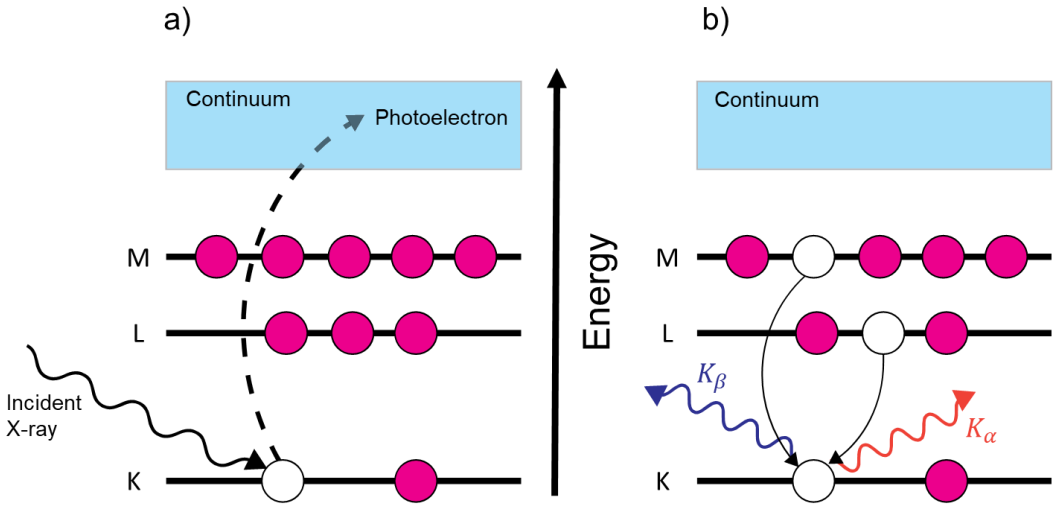

Figure 2.13 - Generalised schematic depicting (**a**), the absorption and emission of a core electron (photoelectric effect). (**b**), Relaxation of a higher electron to fill the core hole, that leads to fluorescence X-ray emission.

For X-ray fluorescence, a higher energy electron relaxes to fill the core hole, ejecting a photon of well-defined energy. The energy of the fluorescence photon emitted during relaxation is characteristic of the target atom.

The term XAS consists of both the X-ray Absorption Near Edge Structure (XANES) and Extended X-ray Absorption Fine Structure (EXAFS) which can be identified as two separate regions on an XAS spectrum (**Figure 2.14**).

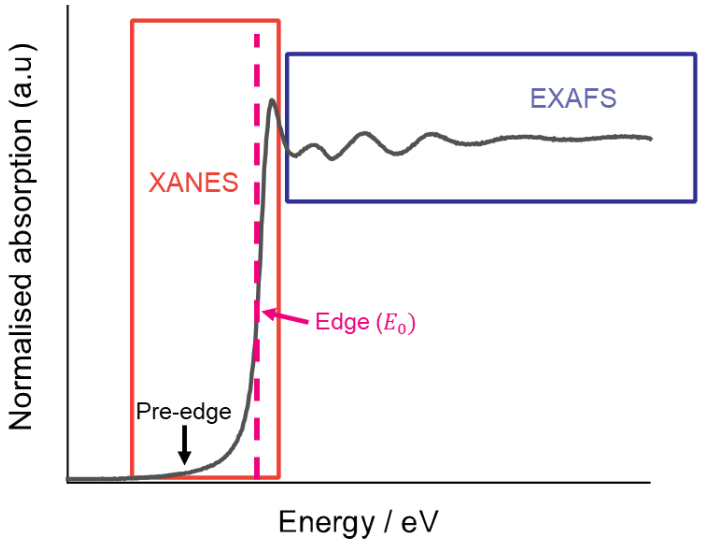

Figure 2.14 - XAS spectrum highlighting the different regions of XAS.

The absorption spectrum in **Figure 2.14** highlights the key spectral features that can be interpreted from XAS. The XANES region is usually defined as ± 10 eV from the absorption edge and includes the pre-edge. The oscillatory structure at higher energies above the edge is referred to as the EXAFS region.

2.7.1 X-ray absorption near-edge structure

The X-ray absorption near-edge structure (XANES) region is very sensitive to the chemical environment and oxidation state of the absorbing atom. The transitions that gives rise to the absorption edge is governed by the dipole selection rule ($\Delta L = \pm 1$) that is derived from Fermi's golden rule. For example the allowed K-edge transitions are $s \rightarrow p$.[225] The region consists of the pre-edge, where energy of the incoming X-rays is not sufficient to promote an excitation of a core electron followed by the absorption edge itself. Atoms in a higher oxidation state require more energy to promote a photoelectric transition. This is due to the core electron requiring more energy to be emitted, as the nucleus of the atom is less shielded and carries a higher effective charge. Oxidation states of a sample of interest can be determined by comparison with standards of known oxidations states.

2.7.2 Extended X-ray absorption fine structure

The extended X-ray absorption fine structure (EXAFS) region is ~50 to 1000 eV above the edge energy (E_0). The atomic arrangement of the neighbouring atoms give rise to oscillation in the absorption coefficient.[226] EXAFS then, provides structural information including radial (bond) distances with neighbouring atoms and their geometries. At energies greater than the absorption edge, the core electron can be ejected as a photoelectron. The ejected photoelectron can be described as a wave. As it propagates out of the absorbing atom, it gets scattered by the outer shell electrons of the next neighbour atoms, creating constructive/destructive interference patterns between the outgoing/incoming scattered pathways of the photoelectron wave **(Figure 2.15**).

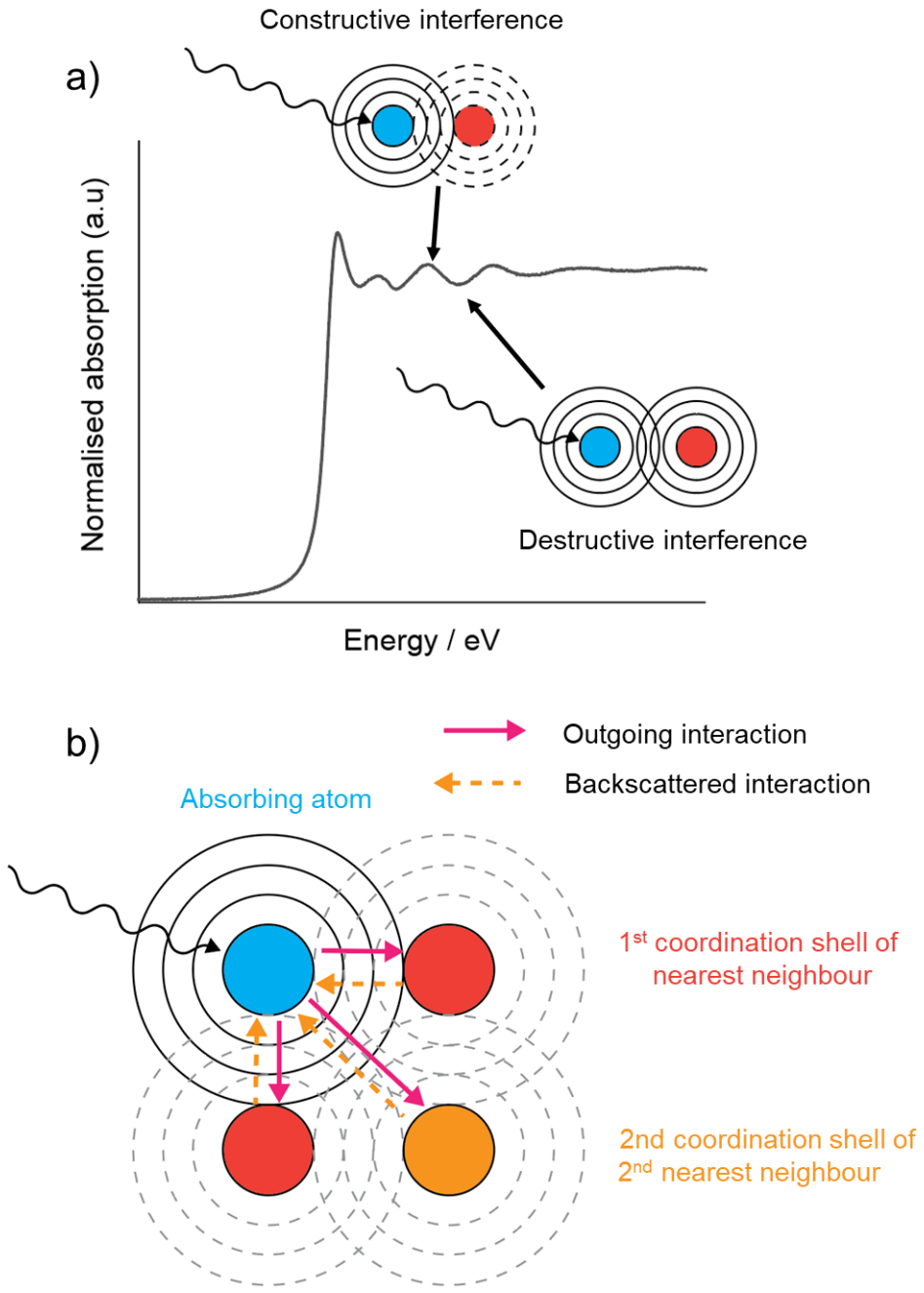

Figure 2.15 – (**a**), XAS spectrum illustrating the origins of EXAFS oscillations. (**b**), Generalised schematic of the outgoing/backscattered interactions with the ejected photoelectron.

2.7.3 XAS data acquisition and processing

For ex situ measurements collected before and after galvanostatic cycling reported in **Chapter 3**, Swagelok cells were taken apart in an argon-filled glovebox, and electrodes were rinsed with DEC solvent and allowed to dry. The electrodes were sealed inside polyfoil pouches and transferred to the synchrotron. X-ray absorption measurements were collected at the B18 beamline of Diamond Light Source across the Sn K-edge region from 28.8 to 30.0 keV. Tin standards were produced by preparing inks with Sn, SnO, SnO_2 (Aldrich) and Na_4Sn powders diluted with acetylene black to match the respective mass loadings of the tin nitride electrodes. The Na_4Sn standard was prepared in a nitrogen-filled glovebox where a slight excess of Na (4.4 equiv, Aldrich, 99% purity) and Sn (Aldrich) was loaded into a furnace tube and sealed, following a previously reported synthesis method for Na_4Sn.[227] The tube was placed into a furnace at 300 °C and heated for 1 hour under flowing N_2. After heating, the sample was transferred to the glovebox before diluting with acetylene black to produce the Na_4Sn standard.

Due to the dilute nature of the absorbing material in the electrode, XAS spectra were collected in fluorescence mode, where the incident photon energy was calibrated to that of Sn foil (29200 eV) for the Sn K-edge. In fluorescence mode, the intensity of the incident beam (I_0), is measured using an ion chamber whilst an energy dispersive solid-state detector collects the intensity of the fluorescence signal (I_f). The absorption coefficient in fluorescence measurements is given as:

$$\mu(E) \propto {I_f}/{I_0} \qquad \textbf{Equation 35}$$

Beamline B18 at the Diamond Light Source U.K has an energy range of 2-35 keV.[228] XAS measurements at the Sn K-edge were carried out using a Si (311) crystal monochromator, with a Pt coated mirror to reject the higher harmonics. B18 is equipped with a nine-element germanium detector that is positioned at 90° to the incident beam, with the sample orientated at 45°in fluorescence mode (**Figure 2.16**).

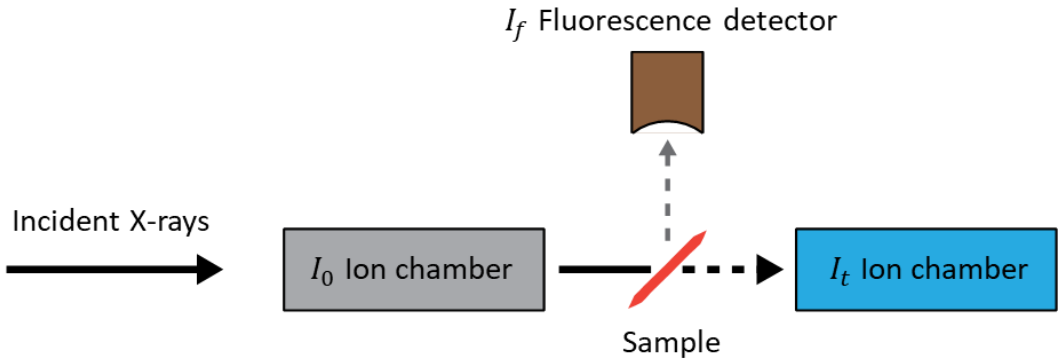

Figure 2.16 - Experimental setup for XAS data acquisition in fluorescence mode on B18.

Collected XAS measurements were processed using the ATHENA and ARTEMIS software programmes, as part of the IFEFFIT software package.[229] XAS spectra were collected in triplicate for each sample. The files were merged in $\mu(E)$ prior to data processing to improve the statistics of the data. The merged XAS spectra were then normalised to set the absorption edge jump to 1 by fitting a linear pre-edge function extrapolated to maximum energy, followed by fitting a quadratic post-edge function to maximum energy through the body of the EXAFS region. Both the pre and post edge functions are subtracted from the data (**Figure 2.17)**.

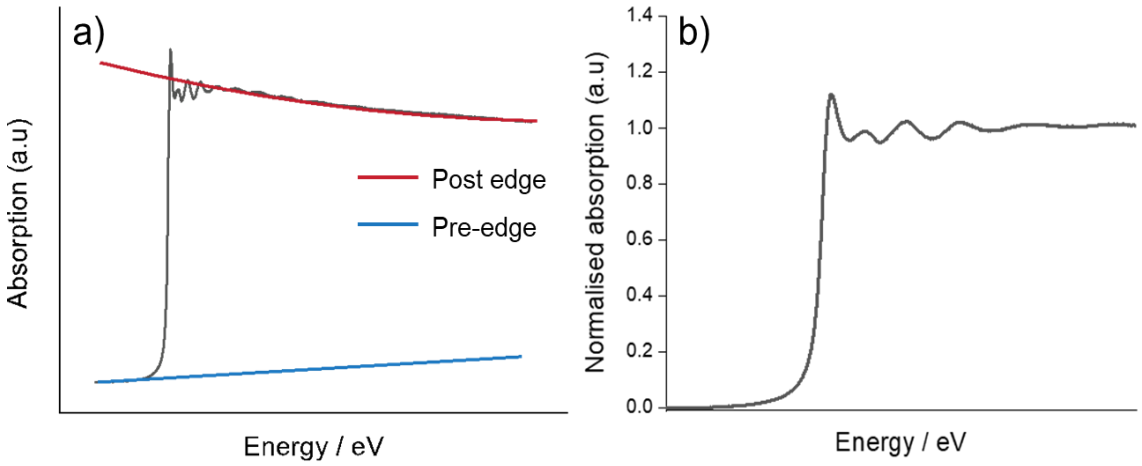

Figure 2.17 - (**a**), Fitting the pre and post edge functions to the XAS spectrum in $\mu(E)$ for the Sn K-edge collected on the Sn reference foil. (**b**), Normalised XAS spectrum where the edge jump is set to 1.

The processing of XAS spectra in ATHENA is sufficient for XANES analysis, however EXAFS requires additional processing in the ARTEMIS programme.

EXAFS is best understood in terms of the wave behaviour of the emitted photoelectron from the absorption process. Because of this, it is common to convert the X-ray energy to k when presenting EXAFS data. k is the wave number of the photoelectron, that has dimensions of 1/distance and can be expressed as:

$$k = \sqrt{\frac{2m(E - E_0)}{\hbar^2}} \qquad \textbf{Equation 36}$$

where E_0 is the edge energy, m is the electron mass and $\hbar$ is Plancks constant. The EXAFS equation focuses on the oscillations above the absorption edge. Therefore the generalised definition for the EXAFS function $x(k)$, is the oscillatory portion of the absorption coefficient:

$$x(k) = \frac{\mu(k) - \mu_0(k)}{\Delta\mu} \qquad \textbf{Equation 37}$$

where $\mu(E)$ is the measured absorption coefficient and $\mu_0(E)$ is the atom absorption coefficient of the isolated atom. The difference in these values is normalised by the measured jump in the absorption $\Delta\mu$, at the threshold energy.

As the oscillatory signal decays quickly with increasing k, it is sometimes necessary to multiply $x(k)$ by a power of k (typically $k^2 or k^3$) to best interpret the spectrum. **Figure 2.18** presents an isolated EXAFS spectrum of the Sn K-edge for the tin reference foil weighted by k^2. The different frequencies present in the oscillations of EXAFS ($x(k)$) represent different near-neighbour coordination shells around the absorbing atom. A Fourier transform to the data converts k to radial distance R which is a more meaningful value to interpret the atomic distances. **Figure 2.18** also presents the k^2 weighted Fourier transform of the EXAFS spectrum from the Sn K-edge of the tin reference foil.

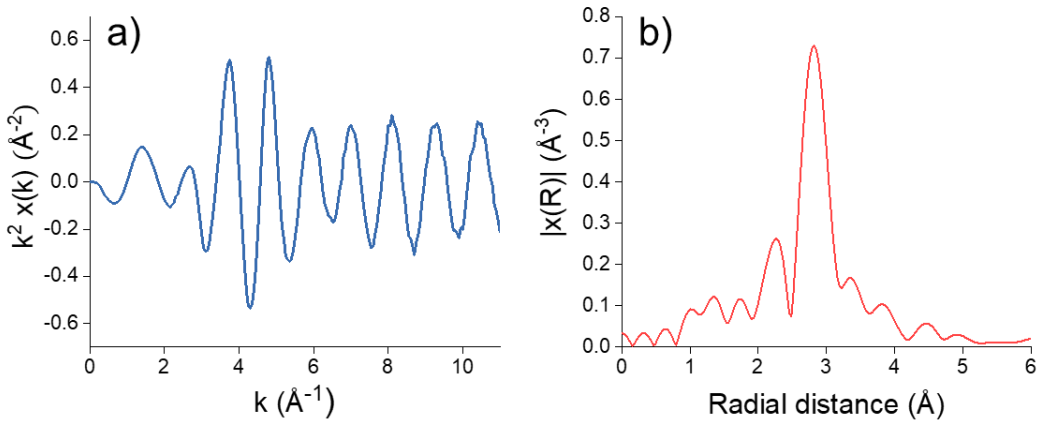

Figure 2.18 - (**a**), Isolated EXAFS spectrum of the Sn K-edge for the tin reference foil weighted by k^2. (**b**), k^2 weighted fourier transform of the EXAFS spectrum.

The EXAFS equation, derived by Stern, Sayers and Lytle, is an extremely useful expression for EXAFS ($x(k)$) that is used to quantify EXAFS data, which includes the scattering from different neighbouring atoms.[226,230,231,232] Artemis programming software was used to carry out fits from experimental EXAFS data to a known system in k and R-space. The calculated spectrum is generated from the EXAFS equation. In the ARTEMIS software, the EXAFS equation is used to calculate the fit of experimental data to a known standard, the equation that is used in the software package is given as:

$$\chi(k,\Gamma) = \sum \frac{(NrS_0^2)F\Gamma(k)}{2kR_\Gamma^2}\, sin\big(2kR_\Gamma + \phi_r(k)\big)e^{-2\sigma_\Gamma^2 k^2} e - 2R_\Gamma/\lambda(k) \qquad \textbf{Equation 38}$$

And:

$$R_r = R_{cif} + \Delta R_\Gamma \qquad \textbf{Equation 39}$$

where Γ is the total number of parameters involved, Nr is the number of photoelectron scattering pathways in the calculation, S_0^2 is the amplitude reduction factor, σ_Γ^2 is the mean square disorder of the pathway, ΔR_Γ is the change in half-path length and E_0 is an energy correction term that shifts the theory and experimental data in eV. The other functions involved are calculated from the FEFF6 code which runs within the ARTEMIS software package.

2.8 Scanning transmission X-ray microscopy

Scanning transmission X-ray microscopy (STXM) is a spectromicroscopy technique that combines near edge X-ray absorption fine structure (NEXAFS) in the soft X-ray energy range (~100 to 2500 eV) with X-ray microscopy.[233,234,235]The primary regions of XANES and EXAFS have been defined for XAS previously. NEXAFS however, is an additional feature typically localised to the region ~50 eV above the absorption edge. This region is very sensitive to the bonding environment of the absorbing atom. Fine structure features arise from the excitation into unoccupied molecular orbitals of the bonds associated with the absorbing atom.[236] Spectral information is extracted from a series of image sequences (stacks) that are acquired at increasing photon intervals over the NEXAFS region of interest (**Figure 2.19**). At one incident photon energy, the sample is raster scanned and the transmitted X-ray intensity is recorded for each pixel. STXM then, is a combination of spatially resolved spectroscopy and high spatial resolution imaging with heterogeneous spectral sensitivity.

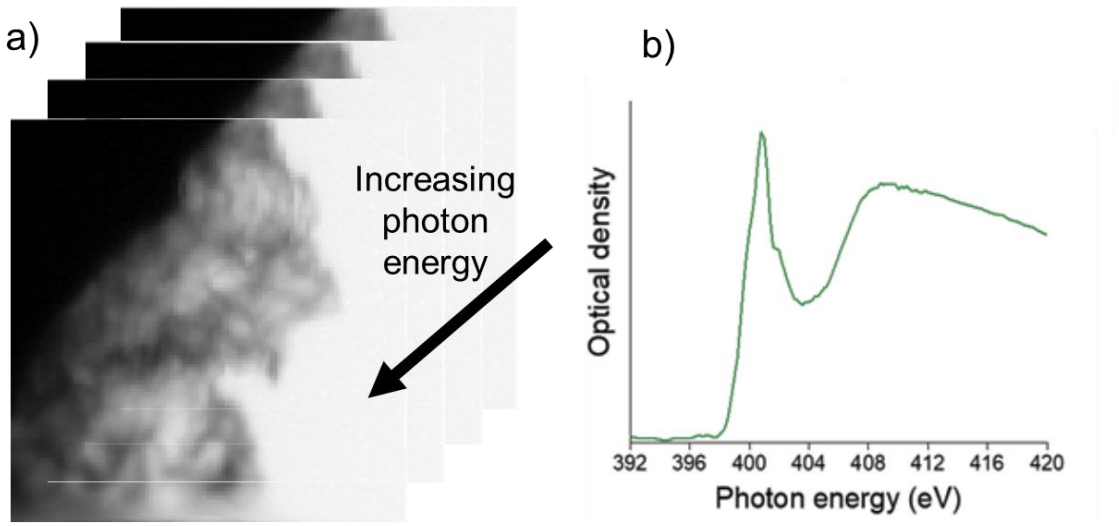

Figure 2.19 – (a), Stack of STXM images with increasing photon energy. (**b**), Corresponding NEXAFS spectroscopic response.

In STXM, a coherent, monochromatic soft X-ray beam (defined by the undulator and monochromator downstream) is micro-focused onto the sample by a Fresnel zone plate. The beam illuminates the sample and the transmitted X-rays are detected. The transmission images are generated by a raster scan of the sample, which is mounted on a scanning stage (**Figure 2.20)**. STXM data presented in this thesis was collected on the I08 beamline at DLS.

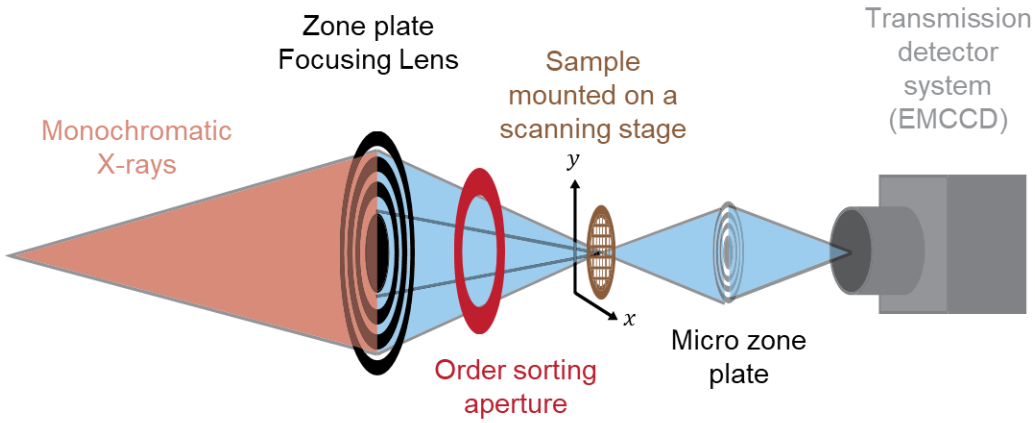

Figure 2.20 - Schematic of a STXM end-station which is utilised on I08.

The fundamentals of scanning transmission X-ray microscopy are still governed by the same principles as for any microscope. The Fresnel zone plate serves as the objective lens, and so determines the limit of resolution that can be acquired for STXM (**Figure 2.21**). The zone plate focuses a coherent beam to a small spot on the sample (spot size). The sample is then scanned in the x and y directions. The focal length (f) of a zone plate at a given photon energy (λ) is expressed as:[237]

$$f = \frac{D \cdot \delta_{rN}}{\lambda} \qquad \textbf{Equation 40}$$

where D is the zone plate diameter and δ_{rN} is the width of the outermost zone. A zone plate with diameter (D) = 480 µm and δ_{rN} = 25 nm was used at I08 to collect images on the samples. For images collected at the N K-edge (λ = 400 eV), The focal length would be 3.874 mm.

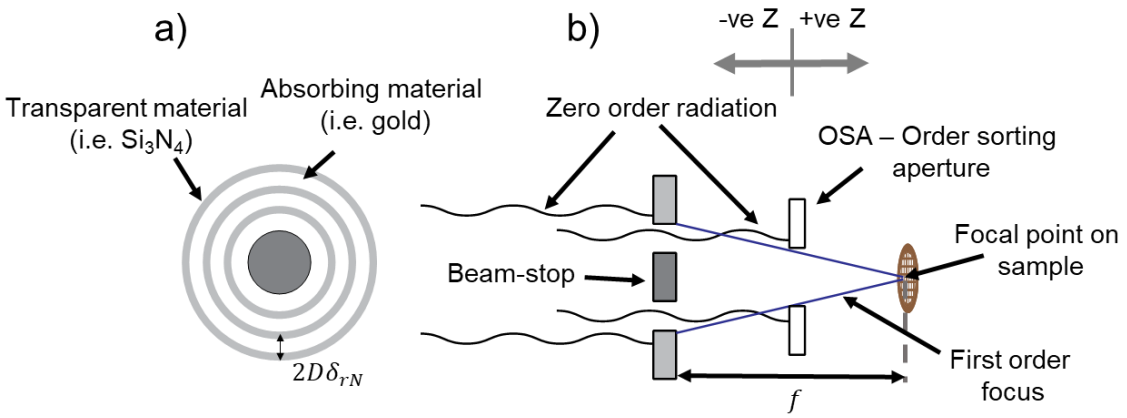

Figure 2.21 – Schematic diagram of a Fresnel zone plate. (**a**), Front view. (**b**), Side view showing first order focus and rejecting all other orders.

A Fresnel zone plate consists of concentric absorbing rings (gold) and thin transparent zones (Si_3N_4). The zone plate focuses monochromatic X-rays with circular diffractive grating (**Figure 2.21**). Combined with a central beam-stop and order sorting aperture (OSA). All orders of focus are absorbed except for first.[238]

The diffracted limited spatial resolution (Δr) or Rayleigh resolution is given by:[239]

$$\Delta r = 1.22 \cdot \delta_{rN} \qquad \textbf{Equation 41}$$

This equation states that the spatial resolution is determined by the outermost zone width of the zone plate. So for δ_{rN} = 25 nm, a spatial resolution of 31 nm can be achieved. However, the practical resolution is limited by the optics setup and is discussed later.

2.8.1 STXM data acquisition and processing

Samples were prepared by electrodepositing lithium onto uncoated nickel and copper TEM grids (Alfa Aesar). The electrodepositing procedure is discussed in greater detail in **Chapter 4**. To produce lithium structures that were mechanically stable but were not too thick to block the beam, the plating time was restricted to 15 minutes (**Figure 2.22**).

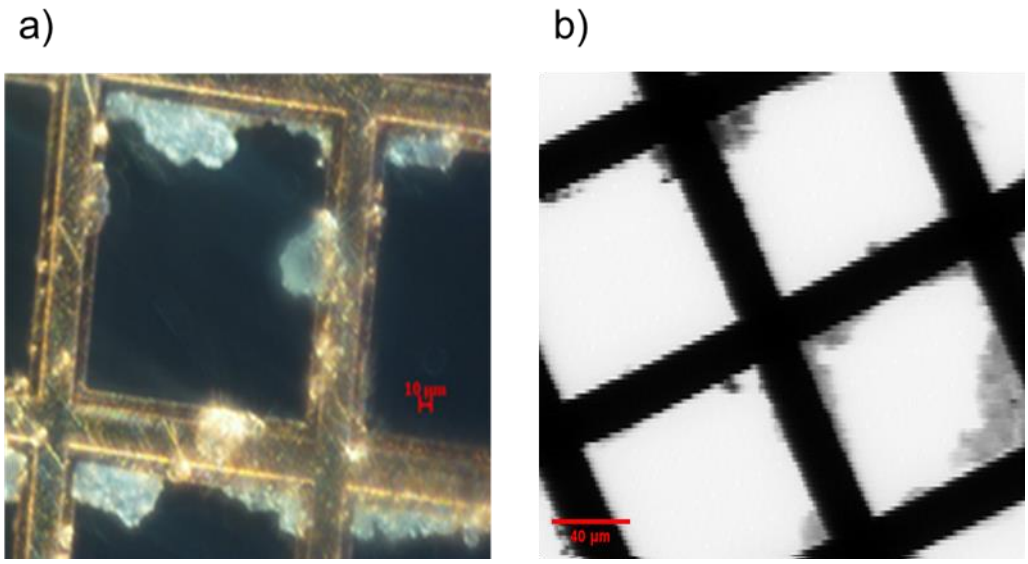

Figure 2.22 - (**a**), Optical microscope image at 20x magnification of electrodeposited lithium structures on a copper TEM grid. Scale bar = 10 µm. (**b**), 200 x 200 µm (pixel size = 500 nm) STXM image of electrodeposited lithium on a copper TEM grid. Scale bar = 40 µm.

After electrodeposition, the TEM grids were rinsed with 1,3 dioxolane to remove any residual salt and then exposed to various chemical treatments outlined in **Chapters 4** and **5**. The TEM grid was further washed with 1,3 dioxolane to remove any residual salt and then sealed in a glass vial under argon. The vials were placed inside an air-tight Schott glass bottle, filled with 4 Å molecular sieves before transporting to the I08 beamline at DLS. On arrival the samples were transferred into an argon-filled glovebox (**Figure 2.23**).

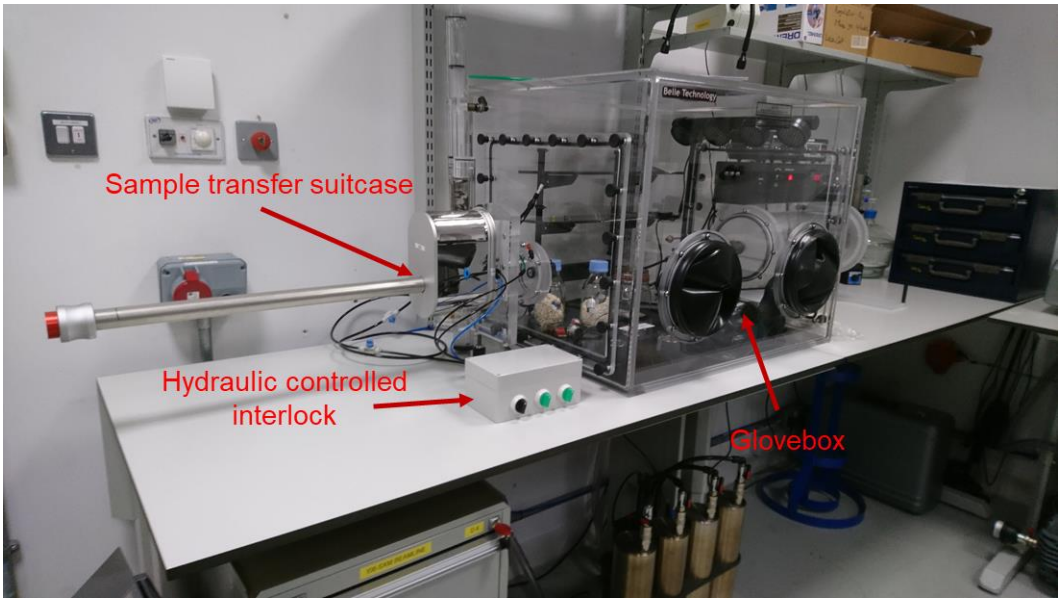

Figure 2.23 - Air-sensitive glovebox and sample transfer system used on the I08 beamline.

Prior to data collection, the TEM grid was mounted on a stage in the glovebox and transferred via a vacuum suitcase to the instrument under argon (**Figure 2.24**).

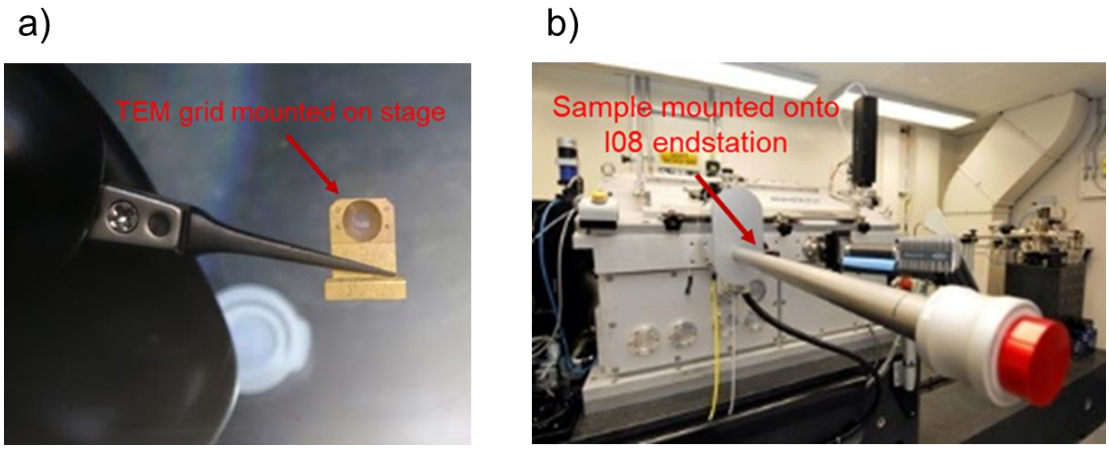

Figure 2.24 - (**a**), Sample TEM grid mounted on stage for data acquisition. (**b**), Sample transfer suitcase mounted onto I08 end-station. The suitcase is opened to ultra-high vacuum prior to inserting the sample into the instrument.

STXM was performed on a sample size typically 15x15 µm. **Equation 41** determined the diffraction spatial resolution based on a zone plate with δ_{rN} = 25 nm to be 31 nm. However, the true resolution is also determined by the optics, specifically the size of the exit slit and the demagnification factor of the optics geometry.

The exit slits are positioned upstream from the Fresnel zone plate and have a gap size of 30 µm. Demagnification is calculated from the source distance (distance between exit slit and zone plate) divided by the focal length (f).

The optics geometry at I08 has a source distance of 2.6 metres, so the spatial resolution for photon energies of the N K-edge will be 44 nm. From calculating the spatial resolution, a suitable pixel size can be selected. So for a sample size of 15 x 15 µm, a pixel size of 50 nm was chosen for the N K-edge.

In STXM, a series of transmission images are acquired at each pixel location (x, y) over a series of incremental photon energies. As previously discussed, X-rays are attenuated by $I_t = I_0 e^{-\mu t}$**.** Converting transmission intensity to optical density can be determined by:

$$OD = \mu t = -ln\left[\frac{I(x,y,E)}{I_0(E)}\right] \qquad \textbf{Equation 42}$$

where OD is the optical density and $I(x, y, E)$ is a stack of transmission images which are normalised by the incident intensity of the beam (I_0).

Before converting a stack of transmission images to optical density, a series of pre-processing steps are carried out. First, the dark current contribution (noise from the environment and instrument) is subtracted from the stack in the MaNTiS software package prior to processing.[240] Secondly, each image is individually checked for "top up" features where the topping up of the synchrotron by injection of electrons from the booster ring causes saturation of an array of pixels **(Figure 2.25**). The saturation of pixels is represented as artefacts in the spectral response of that edge energy, and so are deleted from the stack. Aligning the stack of images by pixel is carried out in the Axis 2000 software which accounts for any lateral movement during the focusing of the sample over the course of data collection.

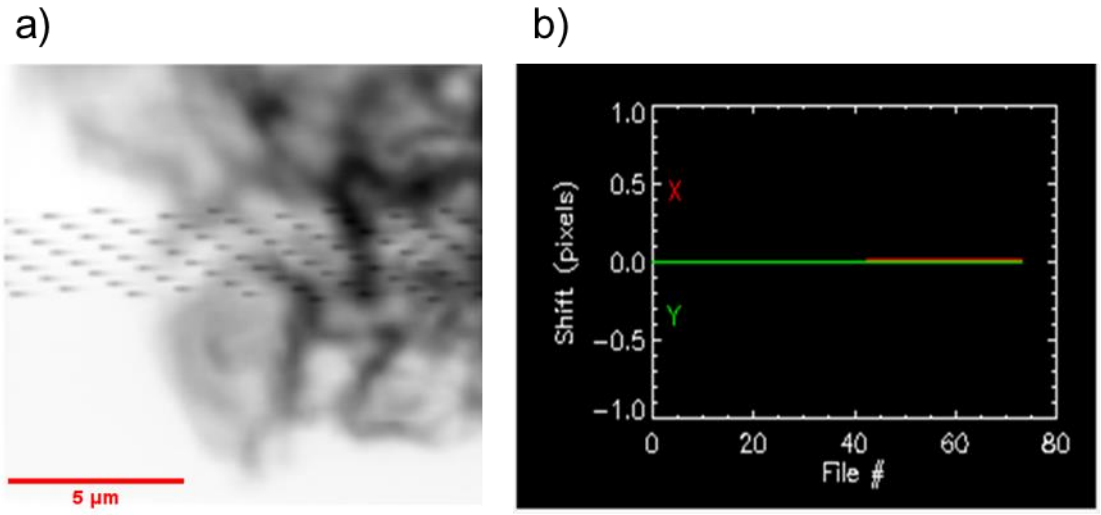

Figure 2.25 - (**a**), Example of an STXM image with the top up effect. (**b**), Corrected pixel shifts at the end of alignment performed in Axis 2000. Scale bar = 5 µm.

The aligned data stack is loaded back into MANTiS and can now be converted from transmission images to optical density. A region on the stack of images is chosen for the incident intensity I_0, where the beam has not been attenuated by the sample and the stack is converted to optical density (**Figure 2.26**).

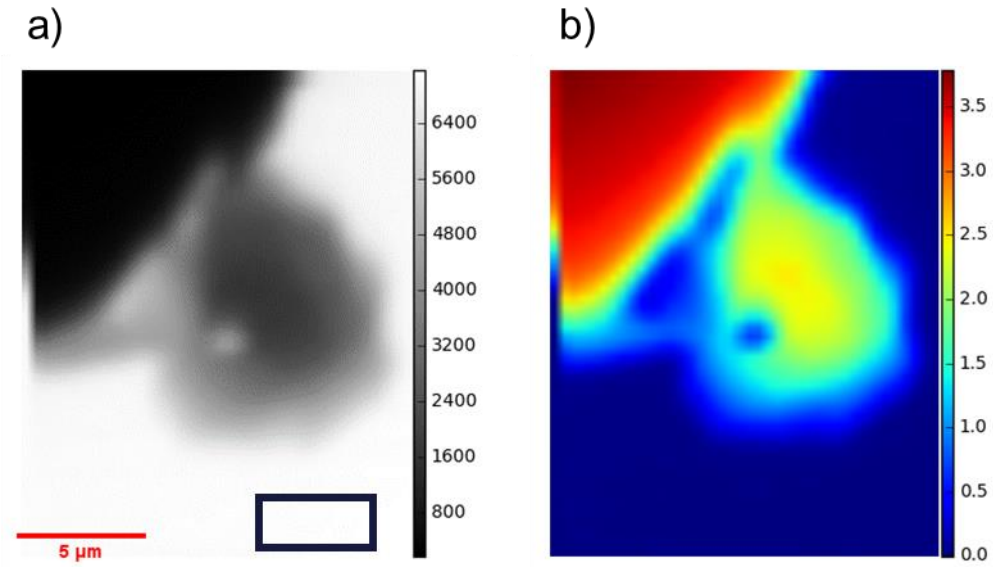

Figure 2.26 - (**a**), STXM transmission image of the LiTFSI standard at 2848 eV (S K-edge). Scale bar represents flux of photons. Blue rectangle highlights a region suitable for I_0 where the beam has not been attenuated by the sample. (**b**), Corresponding image converted to optical density. Scale bar = 5 µm. Intensity scale represents OD.

Maps of arbitrary specimen regions can be obtained by creating cluster maps where pixels containing a similar spectral response are grouped together. Principle component analysis (PCA) is performed on the OD data stack, of which a number of significant spectral components is calculated for the stack. It is assumed that the minimum number of significant spectral components needed to describe the entire dataset through a number of regions, is representative for presenting the spectral response of a sample cluster map. Principle component analysis obtains a set of significant eigenimages and significant eigenspectra from the data's covariance matrix. **Figure 2.27** presents the 1st principle component eigenimage and corresponding spectrum for the LiTFSI standard STXM stack over the S K-edge energies.

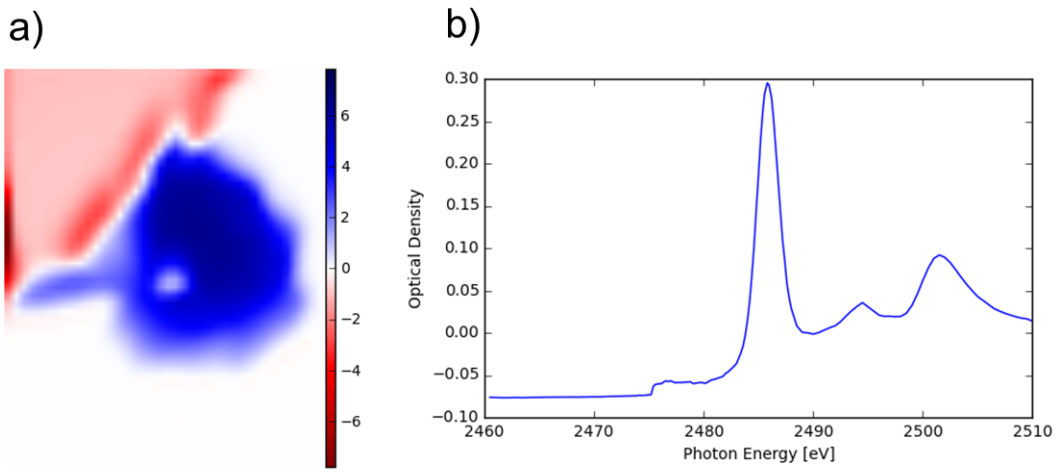

Figure 2.27 – (**a**), Eigenimage for the for the 1st principle component of the LiTFSI standard STXM stack of the S K-edge energies. (**b**), Corresponding eigenspectrum for the 1st principle component.

MANTiS software automatically detects the smallest subset of these images and spectra which is sufficient to represent all the non-noise variations in the data set. In short, PCA finds pixels within the dataset with a similar spectral response, this is evaluated further in cluster analysis. Cluster analysis groups pixels with similar weightings of eigenspectra from the results of PCA. The software package automatically produces a set of regions with grouped pixels termed clusters. The number of clusters is adjustable by the user with knowledge of the experiment to determine how many significant different

regions are representative of the sample. An example of PCA and cluster analysis for the LiTFSI standard STXM stack over the S K-edge energies is presented in **Figure 2.28**.

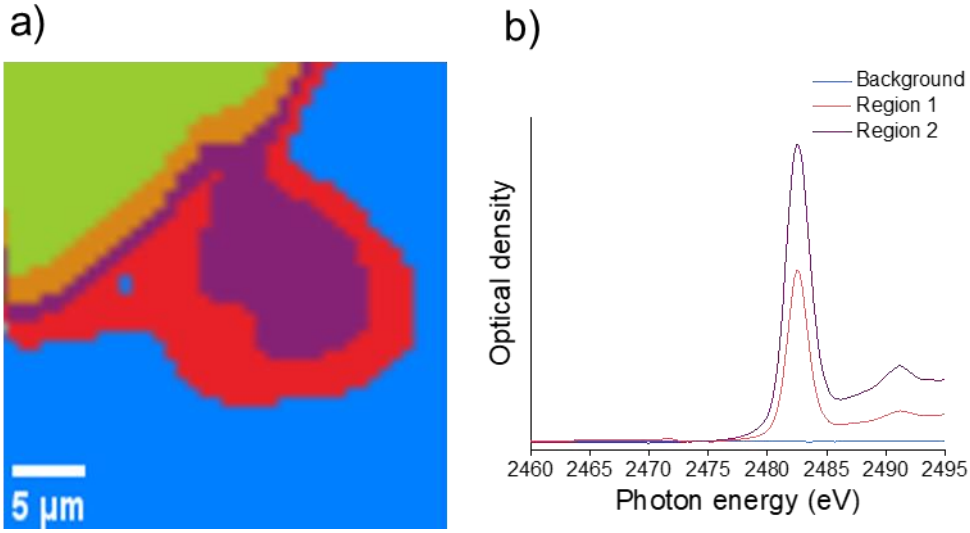

Figure 2.28 – (**a**), LiTFSI standard STXM cluster map over the sulfur K-edge energies. (**b**), Corresponding NEXAFS spectra which show the different S environments determined from PCA.

The background (blue) shows no absorption. 2 different regions were determined from PCA which fully describes the different S-containing environments present for the sample. As the salt is homogenous, the absorbing positions were the same, however the intensities of the peaks differ between the bulk (purple) and outer regions of the salt. The green and orange regions represent the TEM grid. As the grid is strongly absorbing, there is no meaningful optical density data that can be extracted from these regions.

2.9 X-ray photoelectron spectroscopy

Photoelectron spectroscopy (PES) is a powerful technique for investigating the chemical composition, bonding and electronic structures of surfaces and interfaces.[241,242]

X-ray photoelectron spectroscopy (XPS) is a common application of PES, where a sample is irradiated by monochromatic soft X-ray photons that excite inner shell electrons. The underlying principle of XPS is based on the photoemission process previously discussed for X-ray absorption spectroscopy. Instead of measuring absorbance of the incident photon, XPS resolves the kinetic and binding energies of the emitted photoelectron:

$$E_k = \hbar\omega - E_b \qquad \textbf{Equation 43}$$

where an incident photon of energy ($\hbar\omega$) is absorbed by an electron with binding energy (E_b) below the vacuum level. As a result, a photoelectron is ejected into the vacuum with kinetic energy (E_k) and can be detected by an electron analyser.

The work presented in this thesis focuses on the binding energy (E_b) of the emitted photoelectron which can be approximated by Bohr's atomic model.[243]

$$E_b \approx -\frac{Z_a^2}{n^2} \cdot 13.6\ eV \qquad \textbf{Equation 44}$$

where Z_a is the atomic number and n is the quantum number of the target atom. The binding energy then, is characteristic for individual elements. Whilst valence electrons contain information about chemical bonds, inner shell electrons deliver information on the chemical composition. Measuring the binding energy distributions of core electrons reveals a chemical fingerprint for identifying single atoms.

For a single atom system, the binding energy is conventionally measured with respect to the Fermi level rather than the vacuum level (**Figure 2.29**) and is expressed as:

$$E_k = \hbar\omega - E_b - \Phi_{sample} \qquad \textbf{Equation 45}$$

where Φ_{sample} is the work function of the material, which represents the energy barrier that ejected electrons need to overcome in order to escape from the surface and into the vacuum.[244,245,246] This term must be included since the binding energy is referenced to the Fermi level rather than the vacuum level, defining the Fermi levels as the zero point of the energy scale.

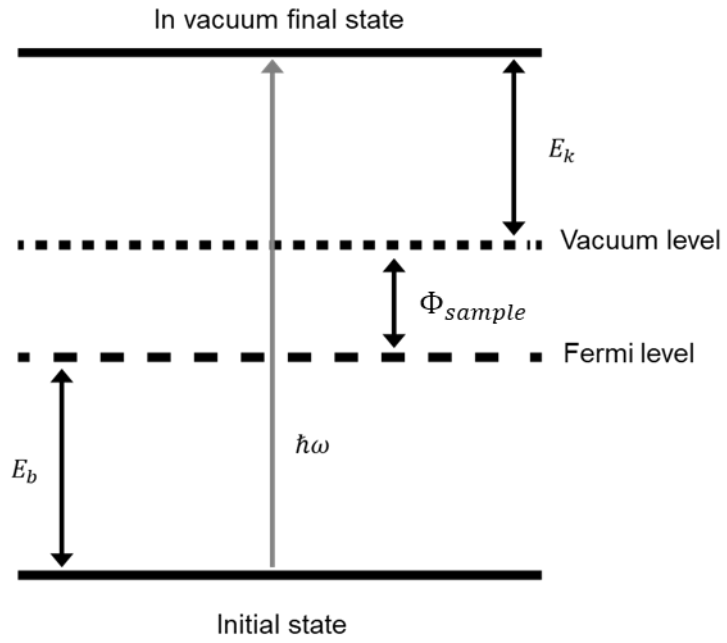

Figure 2.29 – Schematic energy level diagram within the framework of a single emitted photoelectron.

The work function then, is defined as the minimum energy required to eject an electron from the Fermi level of a material into vacuum with no further interactions. The incident photon therefore must be sufficiently higher than the work function of the sample (Φ_{sample}) to liberate a photoelectron.[246,247]

XPS relies on an X-ray source and electron analyser to observe core levels and chemical shifts of target materials. **Figure 2.30** presents a typical photoemission experiment with a photon source, input lens and a concentric hemispherical analyser (CHA). There are different variations of electron analysers designed for PES experiments,

however the CHA is most commonly used in modern XPS instruments, including the experiments reported in this thesis.

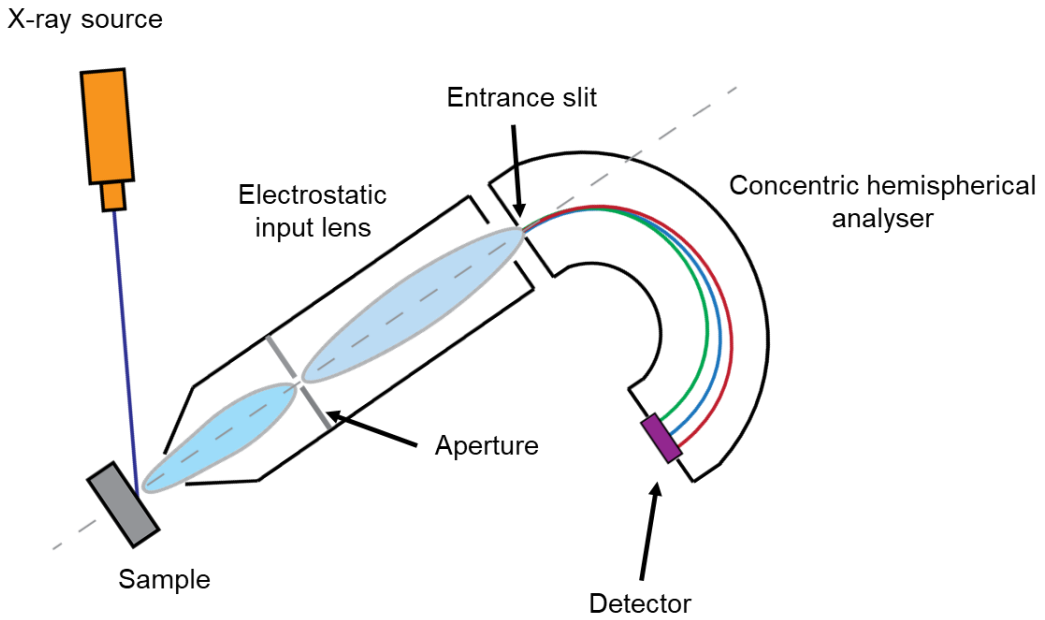

Figure 2.30 – Schematic illustration of an XPS experiment outlining the key components. Adapted from references.[248,249]

The optical layout and voltage applied to the electrostatic lens determines the operating mode, with the aperture defining the area and acceptance angle.[250,251] The lens also has the ability to accelerate or retard the emitted electrons by manipulating a voltage (V), allowing a kinetic energy (E_k) spectrum to be obtained for the sample. The electrostatic 180° hemispherical analyser consists of two metallic hemispheres concentrically arranged to disperse the emitted electrons as a function of their kinetic energy. The hemisphere also acts as an energy filter, so only emitted electrons with a chosen pass energy (PE) will continue their trajectory along the central path of the hemisphere.[252,253,246] The choice of pass energy during experimental setup, determines the energy resolution of the analyser (resolve peaks shapes that have small changes in energy).

Experimentally, the sample and analyser are both connected to ground so the Fermi levels are aligned with each other. This acts as a known reference point in the energy diagram for an XPS experiment (**Figure 2.31**).

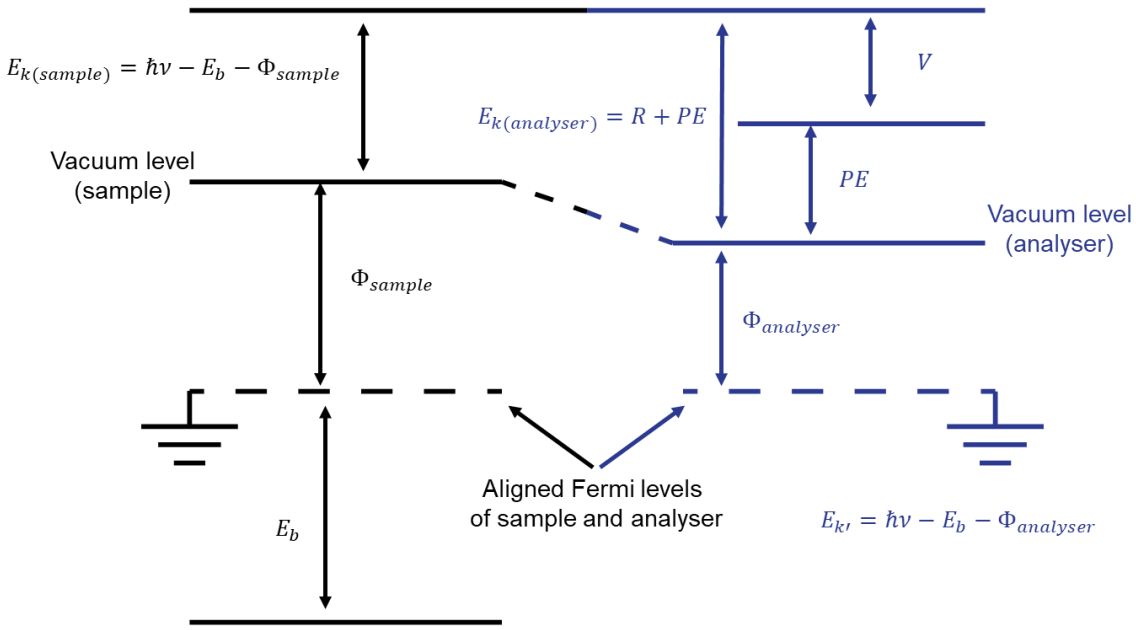

Figure 2.31 - Energy level diagram of an XPS experiment for the sample and instrument. The Fermi levels of the sample and analyser are aligned by connecting both to ground.

The work function of the analyser defines the vacuum level ($\Phi_{analyser}$).[245,246,244] Consequently, as an electron enters the analyser, it is either accelerated or decelerated to the vacuum level of the analyser according to the difference in work functions. The spectrometer records the total number of electrons at increasing kinetic energy ($E_{k'}$). Data collected at the analyser can be presented on a binding energy scale by:

$$E_{k'} = \hbar\omega - E_b - \Phi_{analyser} \qquad \textbf{Equation 46}$$

2.9.1 XPS data acquisition and processing

XPS data reported in **Chapters 4** and **5** were collected on the I09 beamline at the Diamond Light Source synchrotron. Samples were prepared by electrodepositing lithium onto nickel current collectors (4 mm diameter, Advent materials 99.98%) to produce lithium electrodes. The electrodepositing procedure is discussed in greater detail in **Chapter 4**. After electrodeposition, the lithium electrodes were rinsed with 1,3 dioxolane to remove any residual salt, and then exposed to various chemical treatments outlined in **Chapters 4** and **5**. After chemical treatment, the electrodes are further washed with 1,3 dioxolane and then sealed in a glass vial under argon. The vials are placed inside an air-tight Schott glass bottle, filled with 4 Å molecular sieves before transporting to the I09 beamline at DLS. On arrival the electrodeposited lithium electrodes are transferred inside an argon-filled glovebox (Mbraun, oxygen and water content < 5 ppm).

Prior to XPS data collection, lithium electrodes are mounted onto a 12 x12 mm copper stage inside an argon-filled glovebox with conductive carbon tape. To maximise the amount of samples loaded onto to the I09 end-station, the electrodes were arranged onto the copper stage as presented in **Figure 2.32**. Some of the 4 mm diameter electrodes were carefully cut in two inside the glovebox.

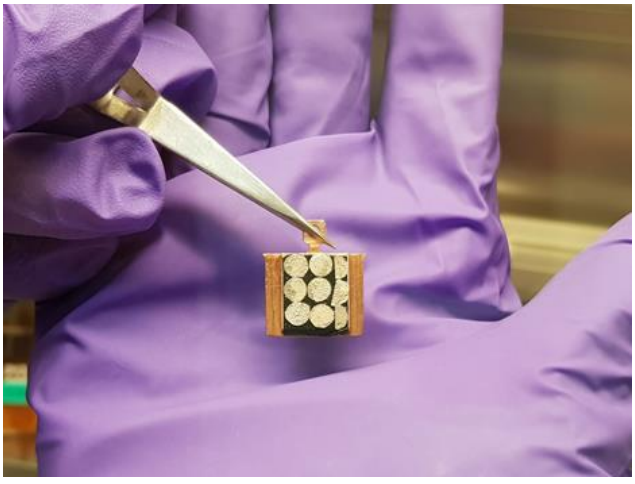

Figure 2.32 - Lithium electrodes mounted onto a copper stage for XPS measurements on the I09 beamline.

The mounted samples are transferred from the glovebox via a vacuum suitcase and attached to the I09 end-station (**Figures 2.33** and **2.34**).

a) b)

Figure 2.33 – (**a**), Front and (**b**), side-view of samples loaded into the vacuum suitcase.

a) b)

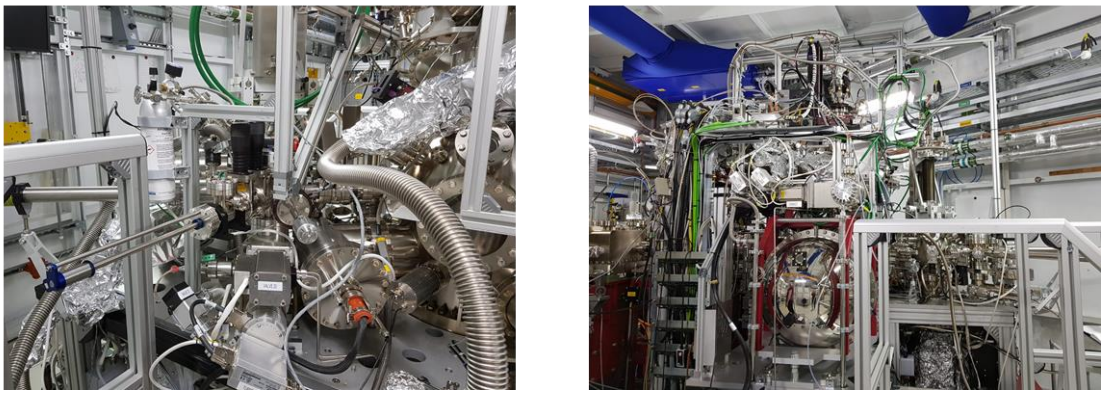

Figure 2.34 - (**a**), Sample transfer suitcase mounted onto the I09 end-station. The suitcase is opened to ultra-high vacuum prior to inserting the sample into the instrument. (**b**), I09 end-station.

The I09 beamline is uniquely equipped to provide incident photon energies from the soft (100 - 2100 eV) and hard (2.1 – 20 keV) energy regimes, by utilising two canted undulators (**Figure 2.35**).

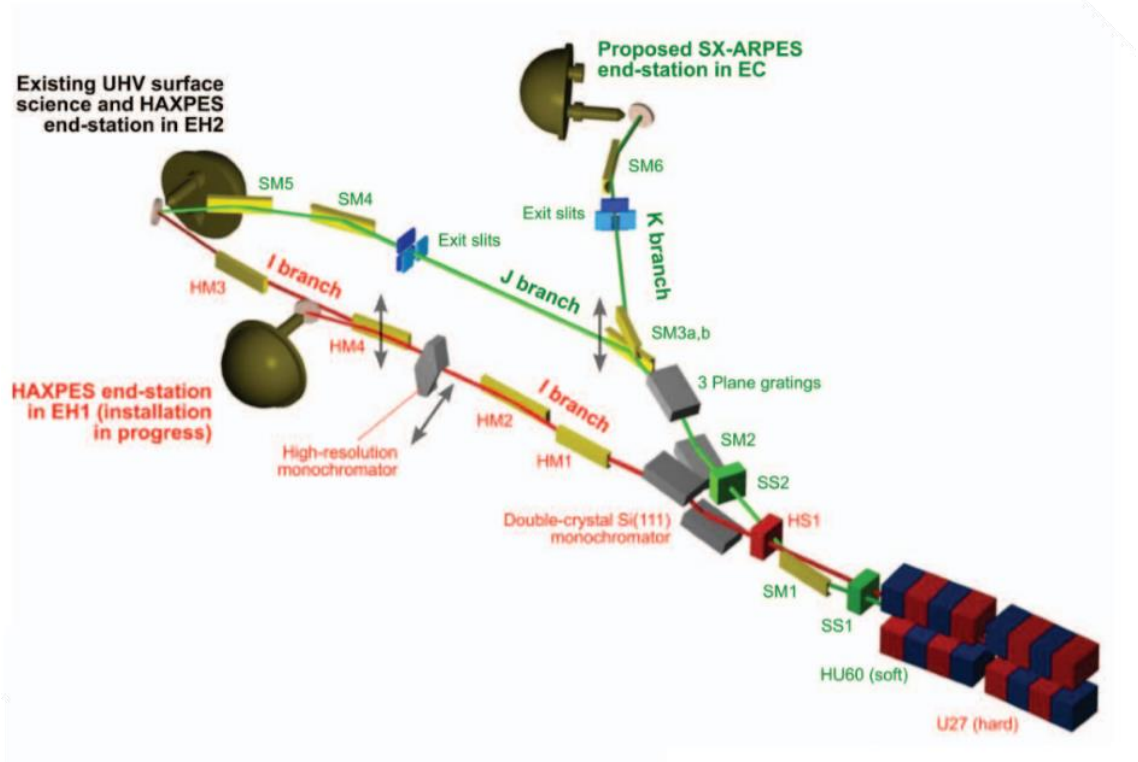

Figure 2.35 - Schematic of the beamline layout for I09. Reproduced from reference.[254]

Photoelectrons emitted from a sample are detected using a CHA VG Scienta EW 4000 electron analyser equipped with a 2D detector. This spectrometer has a wide acceptance angle lens ($\sim \pm 30°$) allowing a sufficient amount of photoelectrons to be collected at high incident photon energies, where the photo-ionisation cross-sections are typically much smaller, which reduces the probability of a photoemission event to take place.[255] **Figure 2.36** presents the experimental geometry of the sample and analyser at the I09 end-station.

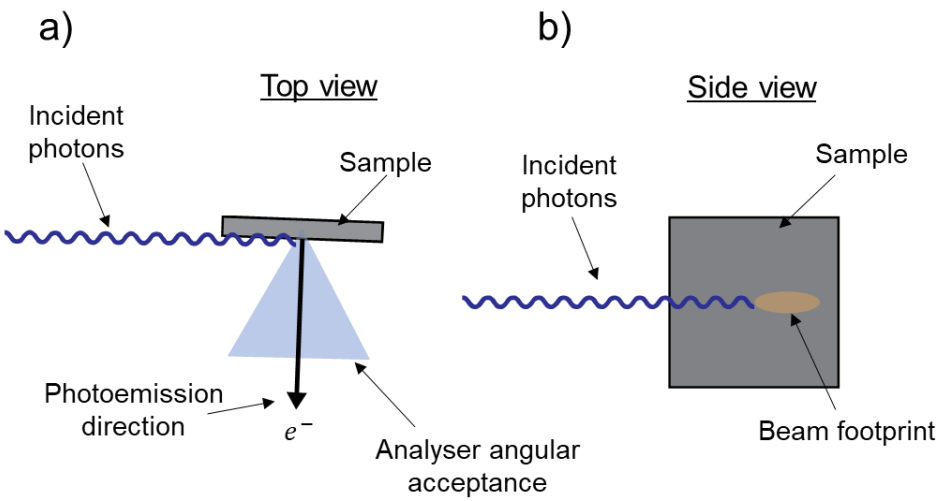

Figure 2.36 - Schematic of the experimental geometry at the I09 end-station. (**a**), Top view of sample in grazing incidence geometry with the analyser orientated for an angular acceptance ($\sim \pm 30°$) around the photoemission direction. (**b**), Side view of sample indicating the beam footprint as a result of grazing incidence.

The incident X-rays are perpendicular to the analyser, which allows XPS to be collected in grazing incidence geometry (1° incidence angle). The resulting beam footprint (0.4 mm) increases the amount of photoelectrons emitted from the sample at higher photon energies. The pass energy was set to 370 eV and the resolution of the CHA VG Scienta EW 4000 electron analyser was 0.25 eV.

The surface sensitivity of XPS experiments is determined by the small escape depth of photoelectrons (Typically < 10 nm for Al k_α source) which arises from the inelastic mean free path (IMFP) of electrons in organic and inorganic compounds. The IMFP can be defined as the average distance that an electron can travel through a material without energy loss. The intensity of emitted electron decay is a function of the distance (I_d), that the electron has to travel as described by Beer lambert's law:

$$I_d = I_0\, e^{-d/\lambda_e} \qquad \textbf{Equation 47}$$

where I_0 is the intensity of the emitted electron at depth d and λ_e is the inelastic mean free path of an electron in a solid.

The ratio of $\frac{I_d}{I_0}$ then, can be seen as the probability that a photoelectron, emitted at depth d, can escape to the vacuum without energy loss from any inelastic processes. The mean free path of electrons (λ_e), is dependent on the kinetic energy of the emitted electrons. Experimental values of the mean free path of various materials are presented in **Figure 2.37**.

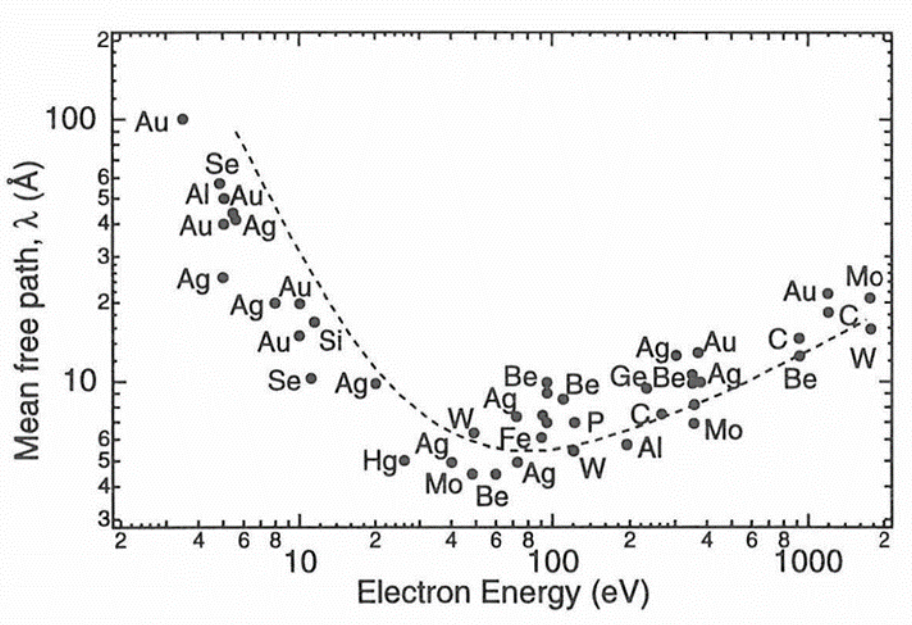

Figure 2.37 - Plot of the mean free path vs. the kinetic energy for a diverse range of materials. Reproduced from reference.[256]

Depth profiling of the lithium electrodes was achieved by varying the incident photon energies available on the I09 beamline. By increasing the incident photon energy, the kinetic energies of the emitted photoelectrons are also increased which improves the probability of a photoemission event to occur at a higher escape depth. Two "soft" (1 and 2.15 keV) and one "hard" (6.45 keV) X-ray energies were chosen to increase the depth sensitivity at greater energies, with higher energies being able to probe deeper into the sample. An approximation on the probing depth for each of the different core levels can be calculated from the IMFP by the TPP-2M approach.[257]

The intensity of the incident X-rays was optimised by opening the gap of the exit slits to minimise beam damage on the sample. To monitor beam damage, the F 1s signal was recorded at regular intervals where significant damage would reduce the intensity of the CF_3 signal to LiF (**Figure 2.38**). There is an obvious increase in intensity of the LiF signal at 686 eV before optimisation of the incident X-rays for XPS measurements.

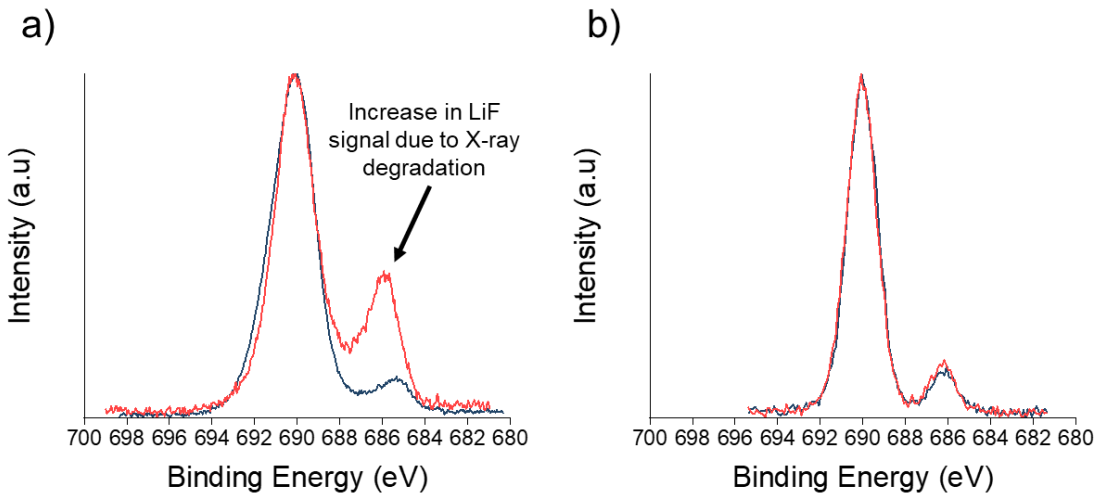

Figure 2.38 - XPS spectra of the F 1s signal from a lithium electrode before **(a)**, and after (**b**), optimisation of the incident X-ray beam.

The F 1s, C 1s, N 1s, O 1s and S 2p core levels were investigated at each incident photon energy. The peak fitting procedure was carried out with the CasaXPS software package. The background under the XPS spectra was subtracted using the Shirley-type function. The photoelectron peak positions were obtained by fitting model curves (70% Gaussian, 30% Lorentzian) with peaks positions calibrated to the adventitious carbon. In the photoemission from the S 2p subshells, the spectral lines are split into two component peaks (**Figure 2.39**). This splitting arises from the spin-orbit coupling effects in the final state.[258] Whilst the initial state of the inner shell of sulfur is filled (S 2p), after a photoemission process in the final state, one electron has been removed and an unpaired spin is left behind, where the spin can be orientated either up or down. The 2p orbital has a non–zero orbital angular momentum ($l < 0$) which gives rise to a peak doublet representing the two possible states having different energies (S $2p_{1/2}$ and S $2p_{3/2}$).

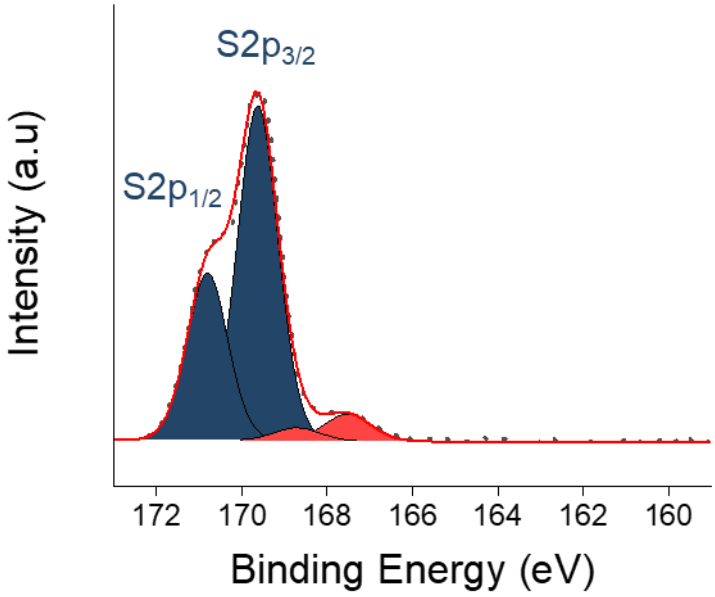

Figure 2.39 - Example of the spin-orbit splitting in the S2p XPS spectrum.

The peaks have a defined ratio of 1:2 which corresponds to 2 electrons in the S $2p_{1/2}$ and 4 electrons in the S $2p_{3/2}$ level. The S 2p peak doublet has closely spaced spin-orbit components that are separated by 1.18 eV.

Chapter 3 Tin nitride as a negative electrode material

3.1 Introduction

The utilisation of lithium-ion batteries (LIBs) as electrical energy storage devices has undergone rapid growth due to their outstanding high energy density and long cycling stability. However, even state of the art LIBs are not able to meet the demand for higher energy density storage devices (electric vehicles etc.), as they are limited by the specific capacity of the graphitic negative electrode (372 mA h g-^{1}).[259] The renewed interest in sodium-ion batteries (NIBs) is in part due to the high abundance, low cost and wide geographical distribution of the alkali metal. Sodium is the sixth most abundant element and is found both in sea water and in various mineral forms.[260,261] The metal shares similar physico-chemical properties with lithium. Sodium analogues of LIB positive electrode (cathode) materials have already been developed, including layered transition metal oxides (Na_xMO_2 where M = Ni, Co, Mn etc.) and polyanionic compounds such as $NaFePO_4$.[39,40,41,42,43]

For NIBs, the negative electrode is still a considerable challenge. For LIBs, the standard negative material is graphite, however the larger ionic radius of sodium ions (1.02 Å for Na^+, 0.76 Å for Li^+) leads to sluggish reaction kinetics, lower capacities and poor cycling stability in sodium-ion cells. Other carbon materials in the form of amorphous and hard carbon are able to accommodate sodium ions, delivering reversible capacities of up to ~350 mA h g^{-1}.[262,263,264]

Sn-based alloying materials have been studied as negative electrodes for NIBs. The full sodiation of Sn to $Na_{15}Sn_4$ has a theoretical capacity of 847 mA h g^{-1}.[63,64] However, Sn undergoes a volume variation of 420% during alloying/dealloying with Na. This large volume change imposed on the metallic Sn particles leads to pulverization, delamination and loss of conduction pathways, although nanostructuring does improve stability. Tin-based binary materials (e.g. SnO_2, SnS, Sn_4P_3) can mitigate the stresses imposed on the electrode by the formation of a matrix structure during initial reduction ($Sn + Na_xM_y$),[76,77,78,79,80,81] as well as offering possible extra capacity by the combination of conversion and alloying processes. The most studied of these systems is SnO_2, owing

to its high theoretical capacity (1378 mA h g^{-1}), low redox potential and ease of synthesis. [82,83] However, the material suffers from a large initial irreversible capacity loss, low electronic conductivity and poor cyclability.[89,90,88] Nano-structuring of conversion materials and formation of composites with ordered carbon structures has yielded significant improvements in their electrochemical performance.

Table 3.1 - Selection of high-performing tin-based materials for sodium-ion negative electrodes

Material	Current (mA g^{-1})	First sodiation capacity (mA h g^{-1})	First de-sodiation capacity (mA h g^{-1})	Final capacity (mA h g^{-1}) / no. of cycles
Sn/graphite composite[265]	50	580	410	360/20
C-SnO_2-C hollow core/shell/shell[93]	100	1200	620	420/30
Amorphous SnO_2 on C nanotubes[91]	100	1110	630	590/50
SnS-acetylene black composite[266]	100	760	500	530/80
Sn_4P_3 nanoparticles on reduced graphene oxide[267]	100	1600	780	640/100
Sn_4P_3 nanoparticles in a cube-shaped carbon shell[95]	100	1430	750	700/50

Even higher capacities are, in principle, obtainable with tin nitride (Sn_3N_4). Sn_3N_4 is a metastable semiconducting material that assumes the spinel structure. The structure has a tuneable band gap and applications in photocatalysis, chemical sensing and solid state LIBs have been suggested.[268,269,270,96] As a negative electrode material in NIBs, the conversion of Sn_3N_4 to Sn and Na_3N followed by full alloying of Sn to $Na_{15}Sn_4$ would result in a capacity of 1512 mA h g^{-1}. Previously our group produced bulk nanocrystalline Sn_3N_4 by ammonolysis of a tin dialkylamide and demonstrated a reversible (de-sodiation) capacity of 270 mA h g^{-1} after 50 cycles at 50 mA g^{-1} with a Coulombic efficiency close to 95%.[36] Ex situ diffraction measurements on cycled electrodes suggested that a significant fraction of the material was not involved in the electrochemical processes. Consequently, it was envisioned that smaller crystallite sizes could deliver larger

capacities. The spinel phase of tin nitride has a large number of nitrogen sites in the atomic structure which increases the probability of introducing defects during nano-structuring onto the surface of the crystal structure. These defects can serve as additional sodium ion adsorption sites on the surface of metal nitride.

Tin (IV) nitride (Sn_3N_4) adopts the spinel structure and crystallises with the cubic spinel structure (*Fd-3m*) with a reported lattice parameter of ~9.037(3) Å.[271] There are two different Sn sites in the metal nitride where an $^1/_8$ of the tetrahedral vacancies are filled with Sn(1)-ions and a $^1/_2$ of all octahedral vacancies are occupied by Sn(2)-ions (**Figure 3.1**).

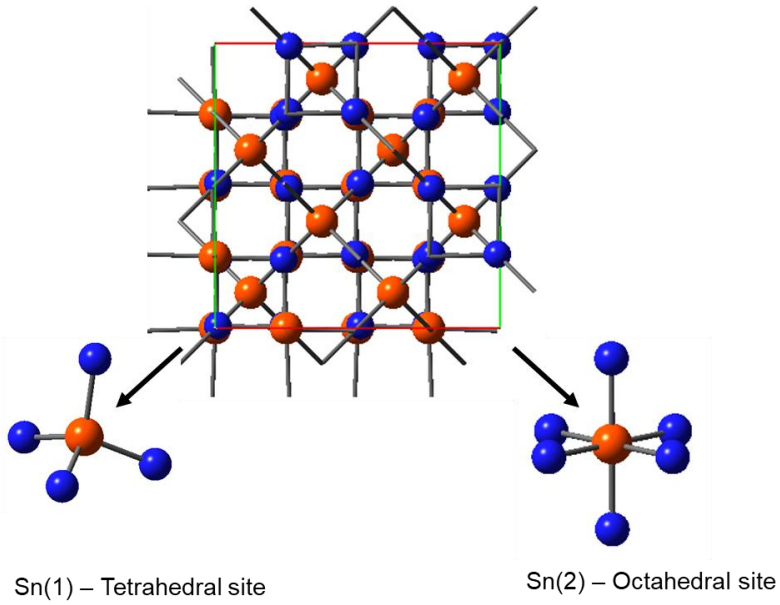

Figure 3.1 - Spinel crystal structure of Sn_3N_4 highlighting the tetrahedral and octahedral coordination sites of the metal atom.

The first documented preparation of the metal nitride was published by Fischer and Iliovoci using an electrical discharge method in 1909.[272] First bulk preparation of an amorphous Sn_3N_4 powder was performed by Maya in 1991, via an amide-imide intermediate.[273] Crystalline Sn_3N_4 was first characterised with powder X-ray diffraction (XRD) by Scotti et al. in 1999.[212] The process involved reacting tin-halide (SnI_4) with KNH_2 in liquid ammonia at 243 K. Sn_3N_4 thin films have also been produced by chemical vapour deposition (CVD) using $Sn(NMe_2)_4$ as a precursor in the presence of ammonia.[96] Tin nitride has been formed by reactive magnetron sputtering followed by annealing

under nitrogen.[274] The thin film was stable under vacuum up to 450 ºC; over this temperature; decomposition occurs producing beta-tin and SnO_2. High temperature and pressure synthesis of a pure phase tin nitride has also been achieved by Shemkunas et al. following a solid-state-metathesis reaction between tin tetraiodide (SnI_4), Li_3N and ammonium chloride (NH_4Cl).[275] Typical high pressures of ~2.5 GPa were employed using a piston cylinder at a temperature of 623 K.

3.2 Experimental

3.2.1 Solvothermal synthesis and characterisation

Synthesis of Sn_3N_4 was carried out under anaerobic conditions using either a nitrogen-filled glovebox or Schlenk line techniques. Benzene (Aldrich) was refluxed over sodium for 8 h, distilled and stored under nitrogen. $SnCl_4$ (Aldrich) was short-path distilled. $LiNH_2$ was obtained by reacting *n*-BuLi (1.6 mol dm^{-3} in hexane, 500 cm^3, Aldrich) with ammonia (distilled from a ~100 cm^3 sodium/liquid ammonia solution) at 0 °C, filtering the white solid product and drying in vacuo. Solvothermal synthesis was performed in a 75 cm^3 autoclave (Parr 4740CH), with a quartz liner reducing the internal volume to ~60 cm^3. $SnCl_4$ (0.60 g, 2.3 mmol) was placed in the silica liner and covered by 30 cm^3 of benzene. $LiNH_2$ (0.21 g, 9.2 mmol) was added and stirred. The autoclave was sealed and heated for 12 hours at temperatures (300 to 430 °C) as discussed later. Typically, ~30 Atm. pressure was developed during heating. After cooling to room temperature, the autoclave was opened and the solid was washed with deionised water (50 mL) and MeOH (20 mL) to remove the LiCl by-product. The powder was further washed with HCl (3 mol dm^{-3}, 30 mL) to remove any tin metal contributions that could have formed by decomposition of the metal nitride. Powder X-ray diffraction (XRD) measurements were recorded on a Bruker D2 Phaser using Cu-K_α radiation (λ = 1.5418 Å) in Bragg-Brentano geometry. The reflections were identified by comparison with the ICSD database and patterns refined using the GSAS package.[276] An LaB_6 standard collected in the same geometry was used to define the Gaussian instrumental peak shape, with the crystallite size obtained from the Lorentzian crystallite size broadening terms.[277]

Rietveld refinement of the XRD patterns of Sn_3N_4 samples were done by refining the scale factor, background, lattice parameter, zero point correction, thermal displacement parameters, Sn atom positions, crystallite size broadening and isotropic strain. In two-phase fits containing two crystallite sizes, the tin thermal displacement parameters were constrained to a single value and the nitrogen thermal displacements were fixed. Transmission electron microscopy (TEM) was carried out with a FEI Technai12 (120 kV) on samples that were dispersed into propanol with ultrasound and dropped onto carbon grids. Bulk elemental CHN combustion analysis was obtained from Medac Ltd, and the values are reported in weight percentages. ~10 mg of sample were loaded into tin capsules with WO_3 oxidising agent, the sample undergoes flash combustion and the relative contributions of C, H and N in the sample are recorded through several analysers.

3.2.2 Electrode preparation and cell setup

Electrode preparation involved homogenising the Sn_3N_4 active material (75%) with acetylene black (20%, Shawingan black, 100%-compressed, Chevron) and sodium alginate (5%, Aldrich) dissolved in deionised water with an IKA T 25 disperser. The slurry was cast onto Cu foil (17.5 µm thick, 99.9 % purity, Goodfellow Ltd) using a K-bar (wet thickness of 200 µm) and dried at room temperature. The coated foil was punched into circular discs (11 mm diameter) and pressed at 10 tonnes to obtain the Sn_3N_4 electrode. Typical mass loadings of electrodes prepared in this way were 0.5-1.0 mg cm^{-2}. Swagelok cells were assembled in an argon-filled glove box. Sodium half-cells were prepared by cutting a fresh face of sodium metal (Aldrich, 99% purity) and rolling to produce sodium foil counter-electrodes, with two microfiber filter (Whatman, GF/F grade) separators soaked in 120 µL of 1 mol dm^{-3} $NaPF_6$ (Aldrich, anhydrous) in a 47.5: 47.5: 5 by wt. mixture of ethylene carbonate (EC), diethyl carbonate (DEC) and fluoroethylene carbonate (FEC) (all Aldrich, 99%, anhydrous or vacuum distilled before use).

3.2.3 Electrochemical measurements

Galvanostatic cycling with potential limitation measurements were recorded using a BioLogic MPG multi-channel potentiostat. Galvanostatic cycling was carried out at 25 °C at various rates of charge/discharge within the voltage range of 10 mV to 2.5 V vs. the sodium metal counter-electrode.

3.2.4 Ex situ measurements

Ex situ X-ray diffraction patterns were collected in a sealed XRD sample holder (Bruker, loaded in the glove box) and were collected in grazing incidence geometry (1° incidence angle) with Cu-K_α radiation (λ = 1.5418 Å) using a Rigaku Smartlab with Hypix 2D detector. X-ray absorption near edge structure (XANES) and extended X-ray absorption fine-structure (EXAFS) measurements of cycled Sn_3N_4 electrodes (handled in polyfoil pouches), were collected at the B18 beamline of Diamond Light Source across the Sn K-edge region from 28.8 to 30.0 keV. Tin standards were produced by preparing inks with Sn, SnO_2, SnO (Aldrich) and Na_4Sn powders diluted with acetylene black to match the respective mass loadings of the tin nitride electrodes. The Na_4Sn standard was prepared in a nitrogen-filled glovebox where a slight excess of Na (4.4 equiv, Aldrich, 99% purity) and Sn (Aldrich) was loaded into a furnace tube and sealed, following a previously reported synthesis method for Na_4Sn.[227] The tube was placed into a furnace at 300 °C and heated for 1 hour under flowing N_2. After heating, the sample was transferred to the glovebox before diluting with acetylene black to produce the Na_4Sn standard. The Sn edge positions were obtained as the first inflection point of the respective XANES absorption spectra, and the EXAFS data has been fitted using two independent Sn-N coordination shells, similar to previous studies of Sn_3N_4.[278]

3.3 Results and discussion

3.3.1 Solvothermal synthesis of Sn_3N_4

Solvothermal synthesis has become an effective, well-controlled route for the preparation of crystalline metal nitrides.[279,94,280] By heating reactants in a solvent medium inside a sealed autoclave, metathesis reactions can proceed at mild temperatures due to the solvent absorbing heat produced in the exothermic reactions.[281,282,283] Thermal decomposition of the formed metal nitrides is also significantly reduced under solvothermal conditions, and the products are usually crystalline.[284,285] Sn_3N_4 was synthesised via a simple and scalable solvothermal method with defined particle size by a solvothermal metathesis reaction, with benzene employed as the solvent owing to its stability under solvothermal conditions:[286,287]

$$3SnCl_4 + 12LiNH_2 \rightarrow Sn_3N_4 + 12LiCl + 8NH_3 \qquad \textbf{Equation 48}$$

XRD and TEM were employed to characterise the product of the solvothermal reaction. Sn_3N_4 crystallises with the cubic spinel structure (Fd-3*m*) with a reported lattice parameter of ~9.037(3) Å.[278] Powder X-ray diffraction (PXD) patterns of the brown powders produced in solvothermal reactions at 300, 350 and 430 °C are presented in **Figure 3.2.**

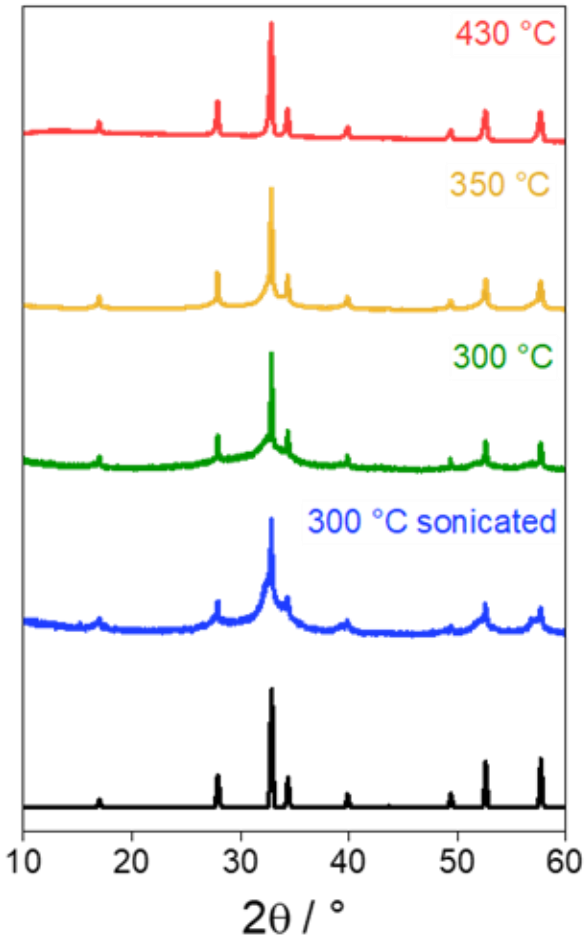

Figure 3.2 - Powder XRD patterns for the products of solvothermal synthesis at various temperatures. The black pattern denotes the literature Sn_3N_4 reflection positions and intensities.[212]

Peak reflections of the Sn_3N_4 reference were observed in all XRD patterns. A single defined phase was observed at 430 °C corresponding to a microcrystalline structure, and this material will be referred to as microcrystalline Sn_3N_4 in the following text. In the XRD data for samples prepared at lower temperatures, broad asymmetric peaks are present at similar position towards lower angles of 2θ in relation to the sharper peaks resembling the microcrystalline phase obtained at 430 °C. This contribution indicates the presence of an additional nanocrystalline Sn_3N_4 phase. The asymmetric broadening feature was accentuated in the sample sonicated in HCl, indicating a greater contribution from the smaller crystallite size phase. The material obtained by heating at 300 °C followed by sonication will be referred to as nanocrystalline Sn_3N_4. Only the

microcrystalline (430 °C) and nanocrystalline (300 °C + sonication) will be discussed hereafter.

A Rietveld fit to the microcrystalline Sn_3N_4 (430 °C) XRD pattern (**Table 3.2**, R_{wp} = 5.0%, R_p = 3.4%) yielded a lattice parameter of 9.0549(2) Å and an average crystallite of 310(40) nm (**Figure 3.3**). TEM micrographs confirm crystallites of similar size (**Figure 3.4**).

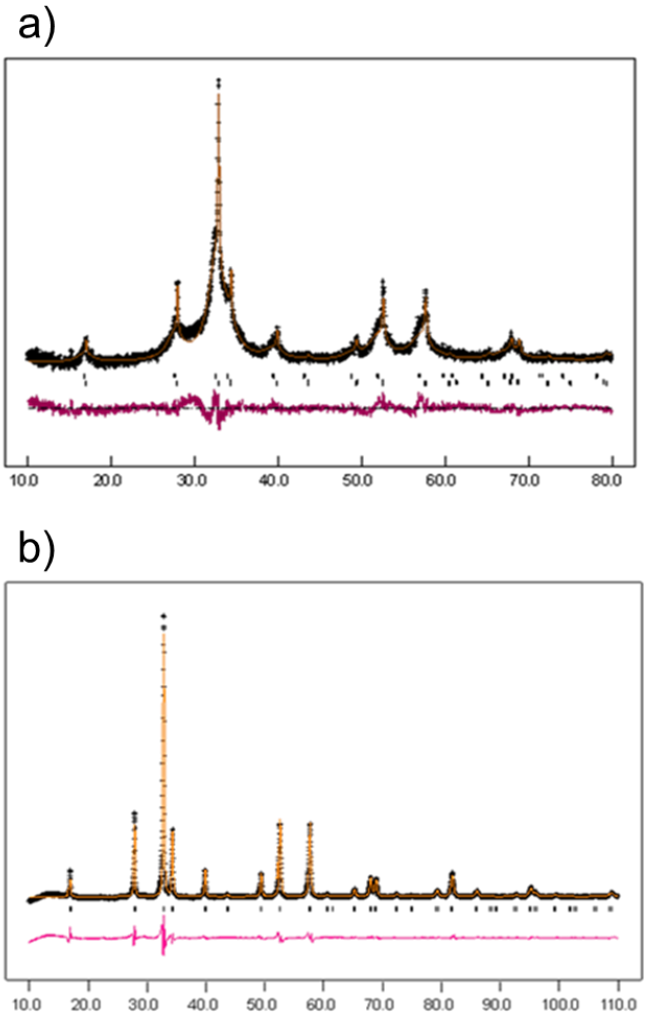

Figure 3.3 – (**a**), Rietveld fit for nanocrystalline Sn_3N_4 (two phases) and (**b**), microcrystalline Sn_3N_4 (one phase). (+) Indicate collected data points. Upper continuous line is the calculated profile and lower continuous line is the difference. Tick marks show allowed reflection positions for Sn_3N_4.

Careful inspection of the XRD pattern reveals that the nanocrystalline Sn_3N_4 contains two components, and a two-phase Rietveld fit (**Table 3.2,** R_{wp}= 9.4%, R_p = 7.4%)

confirmed the presence of two distinct phases, both fitting well as Sn_3N_4 (lattice parameters of the two phases were 9.0514(4) (minor component) and 9.139(2) (major component) Å, with average crystallite sizes of 137 nm (13.2% of the minor component) and 5.95 nm (86.8% of the major component), respectively. TEM shows crystallites around both of these sizes, with a greater number of nanocrystalline particles present (**Figure 3.4**). Nitrogen content determined by combustion analysis was 8.2%, thus lower than the expected 13.6% for pure Sn_3N_4, which could be explained by the presence of N-deficient phases or the incomplete combustion of the sample in the elemental analysis.

Table 3.2 - Reliability profile factor (R_p), reliability weighted profile factor (R_{wp}), lattice parameters for the two phases (Å), average crystallite size of each phase (nm) and relative contribution of each phase in the sample (%).

Material	**"Microcrystalline" Sn_3N_4**	**"Nanocrystalline" Sn_3N_4**	
Parameter		Minor component	Major Component
R_{wp} / %	5.0	9.4	
R_p / %	3.4	7.4	
Wt %	100	13.2(4)	86.8(2)
a / Å	9.0549(2)	9.0514(4)	9.139(2)
Crystallite size / nm	310(40)	137(13)	5.950(9)
Sn1 multiplicity	8	8	8
Sn1 (x,x,x) x-value	0.125	0.125	0.125
Sn1 ($^1/_8$,$^1/_8$,$^1/_8$) U_{iso} / Å^2	0.0231(6)	0.0102(10)	0.0102(10)
Sn2 multiplicity	16	16	16
Sn2 (x,x,x) x-value	0.5	0.5	0.5
Sn2 (½,½,½) U_{iso} / Å^2	0.0234(5)	0.0102(10)	0.0102(10)
N multiplicity	32	32	32
N (x,x,x) x-value	0.2600(6)	0.263(3)	0.261(2)
N (x,x,x) U_{iso} / Å^2	0.008(2)	0.02	0.02

The microcrystalline and nanocrystalline Sn_3N_4 samples were also characterised by EXAFS, **Figure 3.4** presents the magnitudes of the Fourier transforms of the k^3-weighted EXAFS data.

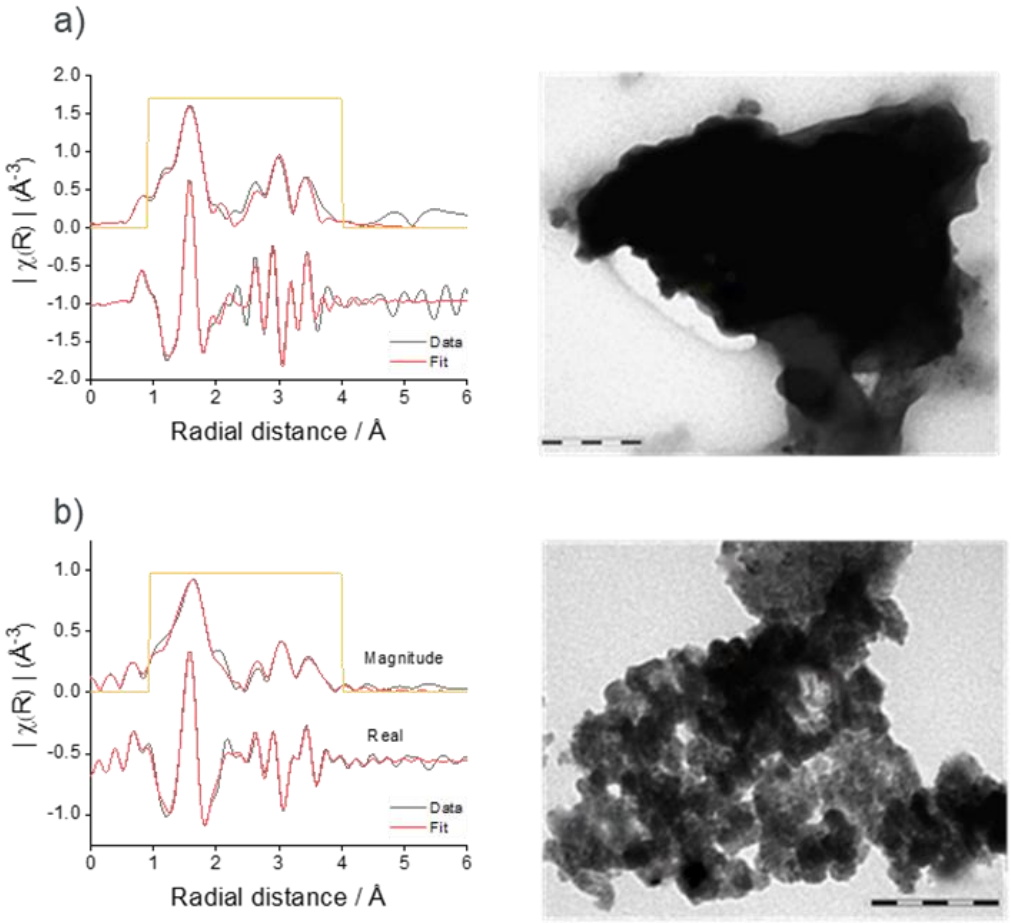

Figure 3.4 - Magnitude and real part of the Fourier transforms of k^3-weighted Sn K-edge EXAFS and TEM images of microcrystalline (**a**) and nanocrystalline (**b**) Sn_3N_4. The scale bar in (**a**) is 200 nm and in (**b**) it is 100 nm.

Figure 3.4 presents the magnitudes of the Fourier transforms of the k^3-weighted EXAFS data. A peak doublet at ~1.5 Å radial distance is present in both samples and corresponds to the tetrahedral tin site (Sn_{tet}-N) and octahedral tin site (Sn_{oct}-N) distances at 2.05 and 2.20 Å, as expected for the spinel Sn_3N_4 structure and in agreement with previous studies.[278] Peaks between 2.5 and 4 Å are attributed to other Sn-Sn interactions within the structure.[278] While XRD is suitable to characterise the composition of the microcrystalline sample, the nanocrystalline sample gives broad diffraction peaks. However, EXAFS shows that both samples have a very similar set of correlations with similar intensities (**Table 3.3**), confirming structural similarities of Sn_3N_4 in both samples. In addition, the analysis of the Sn K-edge XANES data enables the evaluation

of the Sn oxidation state (more detail **in Section 3.3.3**), which were found to be 3.7 and 3.3 for the Sn_3N_4 micro and nanocrystalline samples, respectively.

Table 3.3 - EXAFS results for the fits to the tetrahedral and octraheal Sn-N shells of microcrystalline and nanocrystalline Sn_3N_4. Model crystallographic values are given as reference.[212]

Coordination	Microcrystalline EXAFS data analysis		Nanocrystalline EXAFS data analysis		Model crystallographic data
Sn(1)-N (tetrahedral)	R_r / Å	2.03 ± 0.02	R_r / Å	2.08 ± 0.04	2.105
	σ_Γ^2 / Å	0.003 ± 0.002	σ_Γ^2 / Å	0.004 ± 0.003	-
Sn(2)-N (octahedral)	R_r / Å	2.14 ± 0.02	R_r / Å	2.18 ± 0.02	2.177
	σ_Γ^2 / Å	0.007 ± 0.003	σ_Γ^2 / Å	0.007 ± 0.006	-

The estimation of the nitrogen content of the Sn_3N_4 samples by combustion analysis gives values (10.1% and 8.2% for the microcrystalline and nanocrystalline samples) that are lower than expected for pure, stoichiometric Sn_3N_4 (13.6%). This can be ascribed, in part, to the presence of nitrogen vacancies, which is supported by the fact that the Sn K-edge XANES analysis provides values of the oxidation state of tin lower than 4 (**Section 3.33**). The elemental analysis also shows that the samples contain carbon and hydrogen (12.4% C and 2.0% H for the microcrystalline sample and 1.0% C and 2.0% H for the nanocrystalline sample). The lower content of carbon in the nanocrystalline sample is expected, since less decomposition of the solvent (benzene) will take place at the lower temperature used for the solvothermal synthesis method.[281,282] Taking into account the presence of carbon and hydrogen residues and the nitrogen vacancies (calculated from the tin oxidation number), the expected values of the nitrogen content are 10.9% and 11.1% for the microcrystalline and nanocrystalline samples. The experimental values of the nitrogen content are somewhat lower (10.1% and 8.2% for the microcrystalline and nanocrystalline samples). The process of washing the samples in a HCl solution after synthesis could induce a hydrolysis reaction producing a partial oxygen substitution of nitrogen sites at particle surfaces, forming a tin oxy-nitride. This effect

will be more severe for the nanocrystalline sample since it has a higher surface area. The XRD and EXAFS results show that the spinel structure is preserved after the oxygen-nitrogen substitution. Incomplete combustion of the samples, as observed in other metal nitride studies, could also contribute to the lower than expected nitrogen content obtained from the elemental analysis.[288]

3.3.2 Electrochemistry of tin nitride in sodium half-cells

Sn_3N_4 exhibits good stability in deionised water, hence water processable binders can be employed in electrode preparation, avoiding toxic organic solvents. In a previous study of tin nitride within our group, electrodes prepared with sodium alginate as a binder demonstrated the best electrochemical stability during cycling and so this study continued with sodium alginate as the binder.[36] The binder is comparatively more rigid than the commonly used PVDF, a property that increases the electrode's ability to withstand large volume changes during cycling.[289,290,291] Na half-cells were initially constructed with 1 mol dm^{-3} $NaPF_6$ in EC/DEC (1:1 by wt.) electrolyte.

The theoretical capacity for tin nitride (Sn_3N_4) materials was calculated from the electrochemical reactions considered for a tin-based conversion material. Previously, it was suggested that complete conversion of Sn_3N_4 to $Na_{15}Sn_4$ could result in a capacity of up to 1512 mA h g^{-1} based on the following reactions.[36]

Conversion reaction:

$$Sn_3N_4 + Na^+ + 12e^- \leftrightarrow 4Na_3N + 3Sn \qquad \textbf{Equation 49}$$

Alloying reaction:

$$4Sn + 15Na^+ + 15e^- \leftrightarrow Na_{15}Sn_4 \qquad \textbf{Equation 50}$$

Using these theoretical capacities as a method to calculate "C-rates" (1C represents a current designed to fully charge or discharge a cell in one hour) would be unreliable as the extent of these electrochemical processes is unknown. Instead specific currents are quoted in this report with 200 mA g^{-1}, giving an equivalent C-rate of (C/7.6) based on the conversion-alloying reactions.

To improve the cyclability, 5% fluoro-ethylene carbonate (FEC) was used as an electrolyte additive, which aids the formation of a stable solid electrolyte interphase, accommodating the reaction mechanisms associated with conversion-alloying type electrodes as reported in previous studies.[292,293,294]

Initial galvanostatic cycling of microcrystalline Sn_3N_4 in Na half-cells was investigated at 200 mA g^{-1} with 1 mol dm^{-3} $NaPF_6$ in EC/DEC (1:1 by wt.) electrolyte with 5% FEC additive (**Figure 3.5**). The cycling data indicated that successful Sn_3N_4 electrodes had been produced. However, the Sn_3N_4 displayed a significant irreversible capacity loss on the initial cycle. At 200 mA g^{-1}, 672 mA h g^{-1} of charge was passed on first reduction (discharge, negative current) to 10 mV, of which 215 mA h g^{-1} was recovered on the first oxidation (charge, positive current) to 2.5 V. This large initial capacity loss (CE=32%) is tentatively attributed to the decomposition of electrolyte and formation of an SEI.[78,36] Subsequent cycles demonstrated appreciable cycling stability with a capacity fade of 6% between the 10th (268 mA h g^{-1}) and 50th (250 mA h g^{-1}) oxidations (**Table 3.4**). The Coulombic efficiency was 98% after the 50th cycle, indicating a stable, reversible electrochemical process.

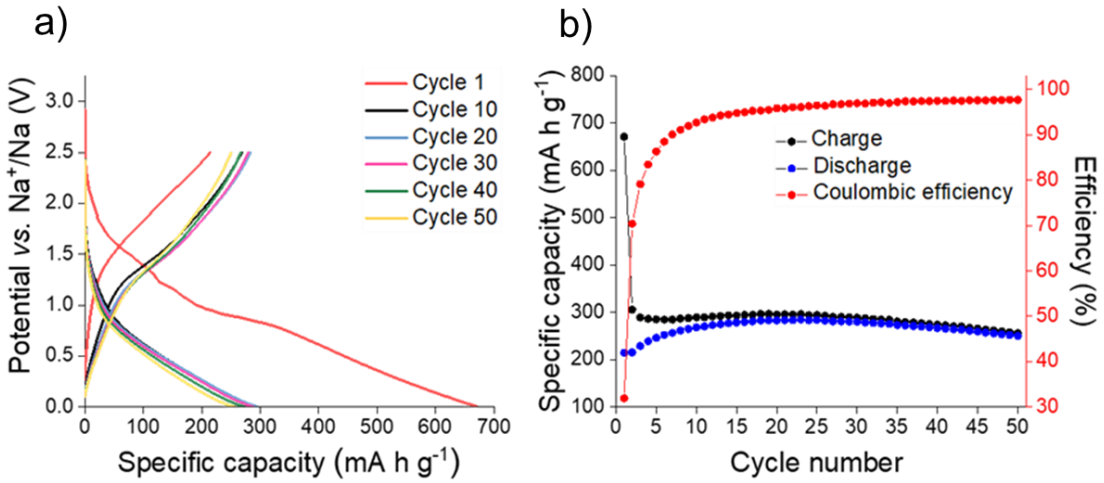

Figure 3.5 – (**a**), Galvanostatic cycling of Sn_3N_4 (micro) vs. Na^+/Na (V) with 5% FEC at 200 mA g^{-1} between 2.5 V and 10 mV over 50 cycles. (**b**), Corresponding specific capacity of Sn_3N_4 vs. cycle number.

Table 3.4 - Specific capacity values obtained from galvanostatic cycling of microcrystalline Sn_3N_4 at 200 mA g^{-1} with 5% FEC and the corresponding Coulombic efficiency.

Cycle number	Capacity-Reduction (mA h g^{-1})	Capacity-Oxidation (mA h g^{-1})	Coulombic efficiency (%)
1	672	215	32
10	290	268	93
20	296	281	96
30	289	281	97
40	274	267	98
50	256	250	98

Galvanostatic cycling of microcrystalline Sn_3N_4 in Na half-cells with 5% FEC showed appreciable capacity achieved after 50 cycles (250 mA h g^{-1}). The issue of a large initial irreversible capacity loss still remains, which could be related to intrinsic changes in the tin nitride materials' structural/(electro)chemical properties through the initial electrochemical reduction process.

Galvanostatic cycling of microcrystalline Sn_3N_4 with 5% FEC was also investigated at 50 mA g^{-1} (**Figure 3.6**, **Table 3.5**). The capacities achieved were greatly improved upon compared to microcrystalline electrodes cycled at the faster current of 200 mA g^{-1}.

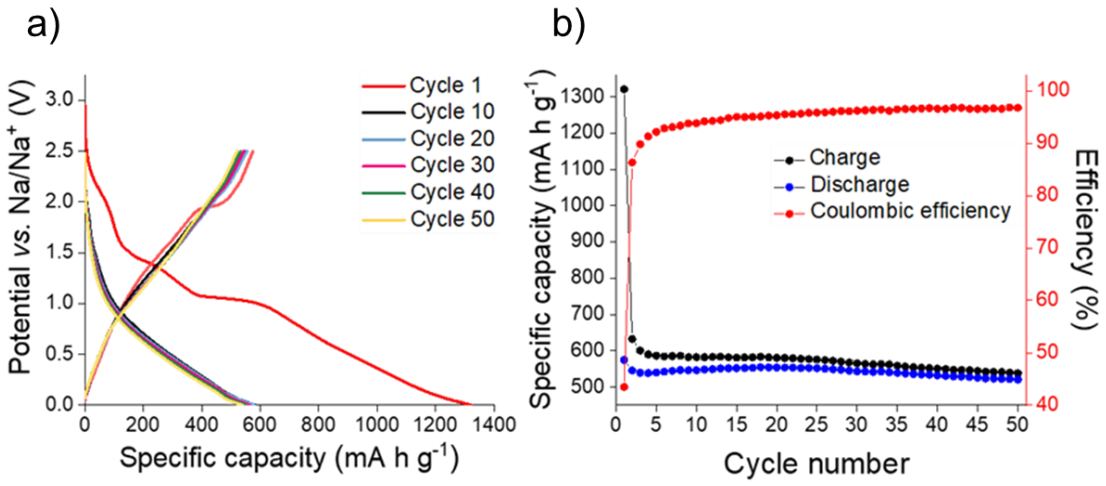

Figure 3.6 – (a), Galvanostatic cycling of Sn_3N_4 (micro) vs. Na^+/Na V with 5% FEC at 50 mA g^{-1} between 2.5 V and 10 mV, over 50 cycles. (**b**), Corresponding specific capacity of Sn_3N_4 vs. cycle number.

Table 3.5 – Specific capacity values obtained from galvanostatic cycling of microcrystalline Sn_3N_4 at 50 mA g^{-1} with 5% FEC and the corresponding Coulombic efficiency.

Cycle number	Capacity-Reduction (mA h g^{-1})	Capacity-Oxidation (mA h g^{-1})	Coulombic efficiency (%)
1	1320	574	44
10	582	546	94
20	581	554	95
30	565	544	96
40	551	532	97
50	539	521	98

There was a slight improvement in the initial irreversible capacity loss with a Coulombic efficiency of 44% (32% at 200 mA g^{-1}). However, at both rates the initial reduction capacity observed is still lower what would be expected for conversion-alloying processes with Na-ions (1512 mA h g^{-1}). One explanation is that not all the tin nitride material has been accessible for electrochemical processes, and that the reduction/oxidation processes are confined to the surface. The increased capacities observed at 50 mA g^{-1} may be due to diffusion-controlled processes (insertion, conversion, alloying etc.) which are more accessible at slower rates.[295,296,297]

Galvanostatic cycling of nanocrystalline Sn_3N_4 was also investigated in Na half-cells **(Figure 3.7**, **Table 3.6**).

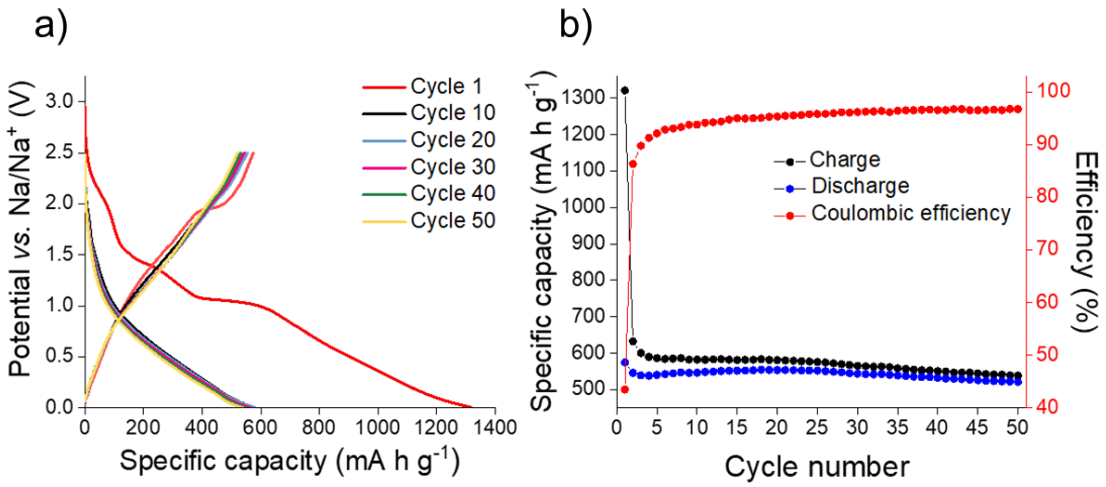

Figure 3.7 – (**a**), Galvanostatic cycling of Sn_3N_4 (nano) vs. Na^+/Na (V) with 5% FEC at 200 mA g^{-1} between 2.5 V and 10 mV, over 50 cycles. (**b**), Corresponding specific capacity of Sn_3N_4 vs. cycle number.

Table 3.6 - Specific capacity values obtained from galvanostatic cycling of nanocrystalline Sn_3N_4 at 200 mA g^{-1} with 5% FEC and the corresponding Coulombic efficiency.

Cycle number	Capacity-Reduction (mA h g^{-1})	Capacity-Oxidation (mA h g^{-1})	Coulombic efficiency (%)
1	1382	450	35
10	446	421	94
20	453	435	96
30	449	439	98
40	438	427	98
50	424	416	98

At 200 mA g^{-1}, after the initial irreversible capacity loss, a reversible capacity of ~420 mA h g^{-1} was achieved. Capacity fade from the 10^{th} (421 mA h g^{-1}) to the 50^{th} (416 mA h g^{-1}) oxidation was only ~1%. In addition, the Coulombic efficiency rose to 98%, demonstrating favourable reversibility of the charge/discharge reactions on cycling.

Galvanostatic cycling of nanocrystalline Sn_3N_4 in Na half-cells at 200 mA g^{-1} showed greater capacities obtained compared to the microcrystalline electrodes. Almost double the capacity was recovered on first oxidation (nano, 450 mA h g^{-1}, micro 215 mA h g^{-1}) with a slight improvement in the reversibility of the first cycle (CE = 35%). The capacities achieved of these nanocrystalline Sn_3N_4 electrodes is remarkable, considering that other high capacity tin-based materials all incorporate a carbon architecture material such as graphene sheets, hollow spheres or nanotubes (**Table 3.1**). In other Sn-based conversion systems without a secondary support, capacity fading over multiple cycles is a problem. Wang et al. cycled SnO_2 at 50 mA g^{-1} with a capacity of 200 mA h g^{-1} achieved after 50 cycles.[298] Ma et al. compared Sn_4P_3/hollow C core-shell composites with unsupported Sn_4P_3, and cycling the unsupported material delivered a capacity of just 104 mA h g^{-1} after the 20^{th} cycle at 100 mA g^{-1}.[93] The cycling of unsupported SnS electrodes was reported by Yu et al. with ~200 mA h g^{-1} achieved after 50 cycles at 100 mA g^{-1}.[299]

Galvanostatic cycling of nanocrystalline Sn_3N_4 with 5% FEC was also investigated at 50 mA g^{-1} (**Figure 3.8**, **Table 3.7**). As expected, more charge was passed

at the lower current of 50 mA g^{-1}. Reversible capacities of ~850 mA h g^{-1} were obtained during cycling. The Coulombic efficiency after the 50th cycle was 94%.

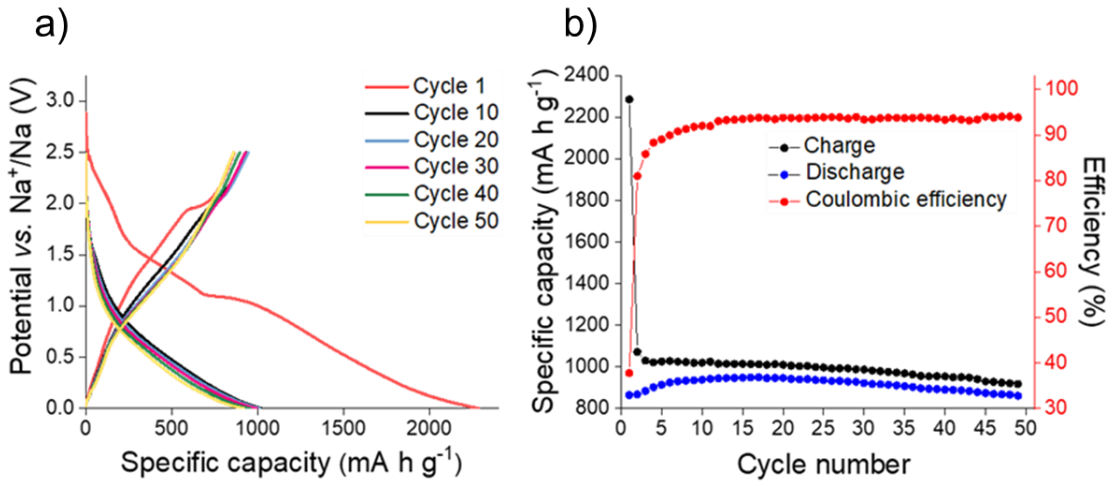

Figure 3.8 - Galvanostatic cycling of Sn_3N_4 (nano) vs. Na^+/Na V with 5% FEC at 50 mA g^{-1} between 2.5 V and 10 mV, over 50 cycles. (**b**), Corresponding specific capacity of Sn_3N_4 vs. cycle number.

Table 3.7 – Specific capacity values obtained from galvanostatic cycling of nanocrystalline Sn_3N_4 at 50 mA g^{-1} with 5% FEC, and the corresponding Coulombic efficiency.

Cycle number	Capacity-Reduction (mA h g^{-1})	Capacity-Oxidation (mA h g^{-1})	Coulombic efficiency (%)
1	2286	864.4	38
10	1020	939	92
20	1010	947	94
30	988	922	94
40	955	891	94
50	918	861	94

3.3.3 Structural and chemical change during cycling of tin nitride in sodium half-cells

In order to elucidate the reactions undergone by Sn_3N_4 materials in Na half-cells, electrodes were extracted from the cell at potentials chosen from features observed in the voltage profile (**Figure 3.9**). These were 1.6, 1.2, 1.0, 0.5 and 0.01 V vs. Na^+/Na during reduction and 0.1, 0.75, 1.5 and 2.5 V vs. Na^+/Na during oxidation. Samples were then characterised ex situ by XRD, XANES and EXAFS. These experiments utilised microcrystalline Sn_3N_4 in order to obtain more useful diffraction data, although it is recognised that the nanocrystalline material has the larger capacity. On first reduction, there is a sloping plateau over 1.6 V followed by a small plateau at 1 V.

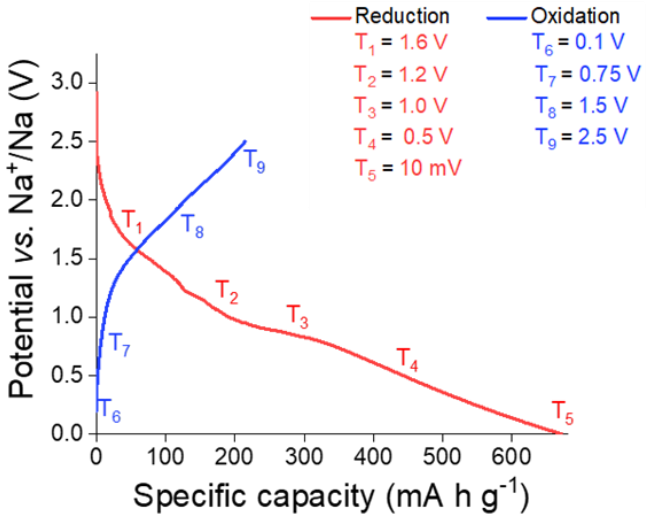

Figure 3.9 - Initial galvanostatic cycle of microcrystalline Sn_3N_4 depicting where samples were taken for ex situ XRD, XANES and EXAFS studies.

If following the reaction mechanisms of well described conversion materials (SnO_2,Sn_4P_3), the initial reduction would likely be attributed to the conversion of tin nitride to metallic tin and sodium nitride ($Sn_3N_4 \rightarrow Sn^0$ and Na_3N). At lower potentials the formation of Na_xSn_y phases is expected, which likely requires some Sn to have already formed. A large, sloping plateau is observed at 0.5 V, that could be ascribed to the alloying reaction ($Sn \rightarrow Na_xSn$). This alloying process continues to 10 mV, as described in SnO_2 and Sn_4P_3 systems.[300,301,302] Since the sodiation of Sn produces a series of Na_xSn_y

compounds at potentials in between 0.5 V and 0 V vs. Na^+/Na, these final processes have been assigned to the Sn alloying reactions ($Sn \rightarrow Na_xSn_y$).[303,304,305,306,74]

Sn K-edge XANES analysis was performed to probe changes in the oxidation state of Sn in the cycled electrodes. For that purpose, prior to the measurements, Sn-K edges were calibrated against Sn standards with defined oxidation states (Sn, SnO_2, SnO and Na_4Sn with oxidation states of 0, +4, +2 and -4, respectively, (**Figure 3.10, Table 3.8**). The edge energy positions were defined at the first inflection point, taken as the maximum in the first derivative. The edge energies of the reference compounds are plotted against their oxidation state and then fitted with a 2nd order polynomial regression (with standard deviation determined from the fit). An interpolation of the measured absorption edge energies of the samples under investigation to the regression line yields an average oxidation state for the sample.

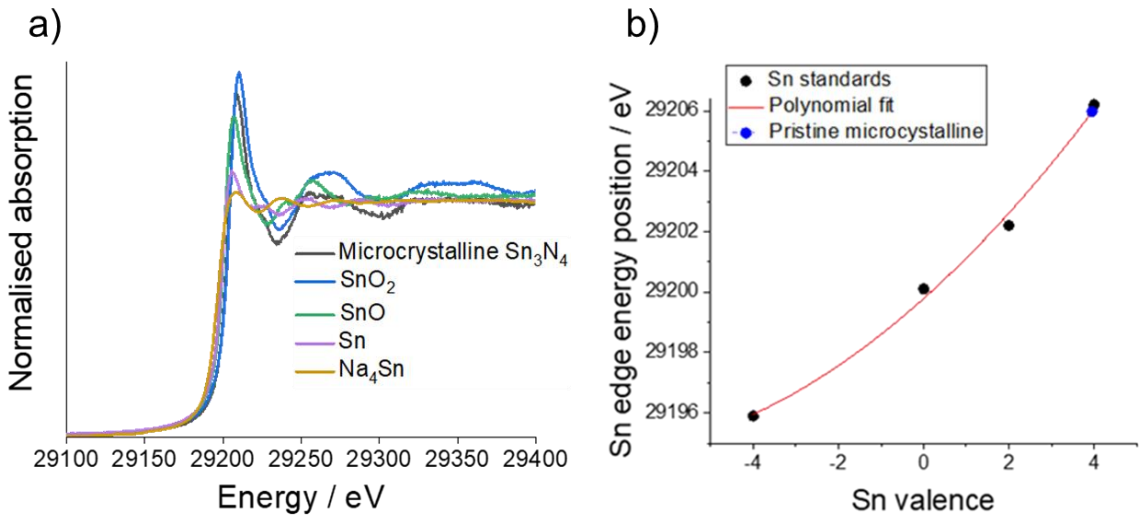

Figure 3.10 – (**a**), Sn-K edge XANES of known Sn standards and pristine microcrystalline Sn_3N_4 electrode. **(b)**, Calibration of Sn-K edge energies vs. oxidation state with a 2nd order polynomial.

Table 3.8 – Sn K-edge energies calibrated to the oxidation state of known Sn standards.

Reference sample	Oxidation state (Sn)	Sn K-edge energy
Na_4Sn	-4	29195.9
Sn	0	29200.1
SnO	2	29202.2
SnO_2	4	29206.2

The calculated oxidation state of the Sn ions in the solvothermally prepared microcrystalline Sn_3N_4 electrode was 3.7 ± 0.3, whose value agrees well with a previous EXAFS study of chemically prepared Sn_3N_4 ($SnBr_2$ and KNH_2 in liquid NH_3) which obtained a value of 3.5. Scotti et al. determined an oxidation state of +4 for the Sn ions, the result for microcrystalline Sn_3N_4 in this report is slightly lower and is likely attributed to the formation of a N-deficient material. The estimation of the nitrogen content of the Sn_3N_4 samples by combustion analysis gave values (10.1% for microcrystalline Sn_3N_4) that are lower than expected for pure, stoichiometric Sn_3N_4 (13.6%).

The XANES spectra (**Figure 3.11**) show the edge energy shifting to lower energy values during the first reduction and a decrease in the intensity of the white line position at the fully reduced state (10 mV vs. Na^+/Na), corresponding to an average oxidation state of -0.1 ± 0.3 (**Table 3.9**). Whilst a negative oxidation state implies that Na-Sn alloying has taken place, it also suggests incomplete conversion of Sn_3N_4 to Na-Sn alloys, as full conversion would yield a much lower oxidation state (-1.25) for the fully sodiated $Na_{15}Sn_4$ phase. **Figure 3.11** also shows an increase in the edge energy shift and intensity of the white line position in the XANES spectra during the first oxidation of the Sn_3N_4 electrode. The average oxidation state of Sn was 3.5 ± 0.3 (**Table 3.9**) in the fully charged state (2.5 V vs. Na^+/Na), very close to the average oxidation of the pristine sample (3.7 ± 0.3). This strongly suggests that reformation of Sn_3N_4 has occurred.

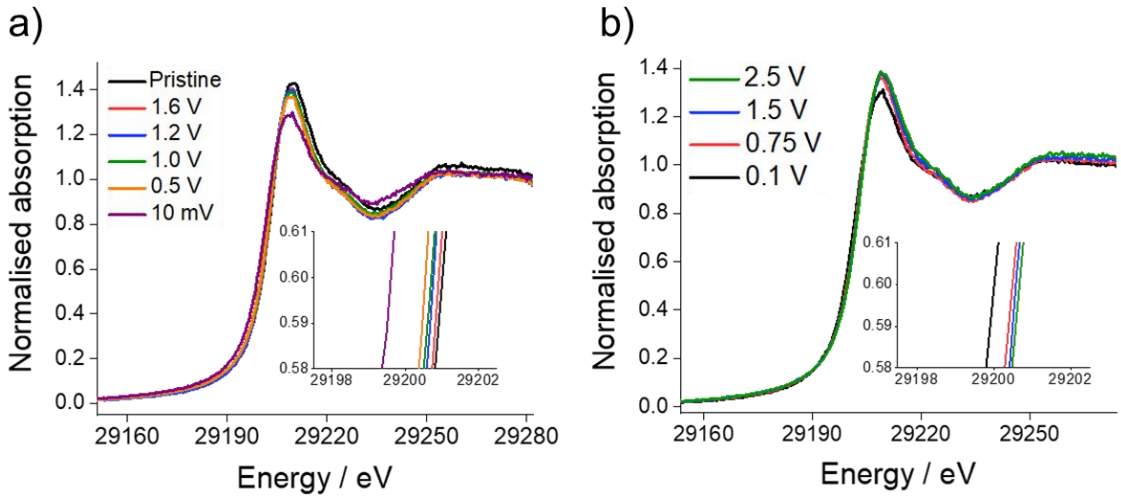

Figure 3.11 - Sn K-edge XANES spectra during: (**a**), first reduction and (**b**), first oxidation of microcrystalline Sn_3N_4 as a function of cell potential. The insets show the central part of the absorption edge, magnified for clarity.

Table 3.9 - Average oxidation state and standard deviation as evaluated from the Sn K-edge energies of microcrystalline Sn_3N_4 electrodes cycled to various potentials during initial reduction and oxidation.

Sample *vs.* (Na^+/Na)		Oxidation state (Sn)	Sn K-edge energy
Pristine		3.7 ± 0.3	29205.5
Reduction	**1.6 V**	3.1 ± 0.3	29204.4
	1.2 V	2.9 ± 0.3	29203.8
	1.0 V	2.5 ± 0.3	29203.4
	0.5 V	1.3 ± 0.3	29201.2
	10 mV	-0.1 ± 0.3	29199.6
Oxidation	**0.1 V**	0.9 ± 0.3	29200.7
	0.75 V	1.5 ± 0.3	29301.3
	1.5 V	2.8 ± 0.3	29203.9
	2.5 V	3.5 ± 0.3	29205.2

Figure 3.12 presents the ex situ XRD data of Sn_3N_4 electrodes cycled to the same set of potentials as in the XANES measurements in **Figure 3.11**. It is observed that the reflections corresponding to Sn_3N_4 become sharper on reduction of the electrode, this suggests that the smaller crystallites are reacting more readily and hence the average crystallite size increases. At 0.5 V, clear reflections for Sn metal appear in the pattern.

Formation of Na-Sn alloys is not clearly visible in the XRD data, indicating poor crystallinity or small particle size of the Na-Sn alloys. During the initial stages of the re-oxidation, the intensity of the Sn metal reflections diminishes but small Sn diffraction peaks are still visible at the end of charge (2.5 V), suggesting incomplete reversibility of the conversion process. The Sn_3N_4 peaks are broader after cycling, suggesting a decrease in the crystallinity (e.g. decrease in average particle size). This is attributed to the effect of the Na-Sn alloying process.

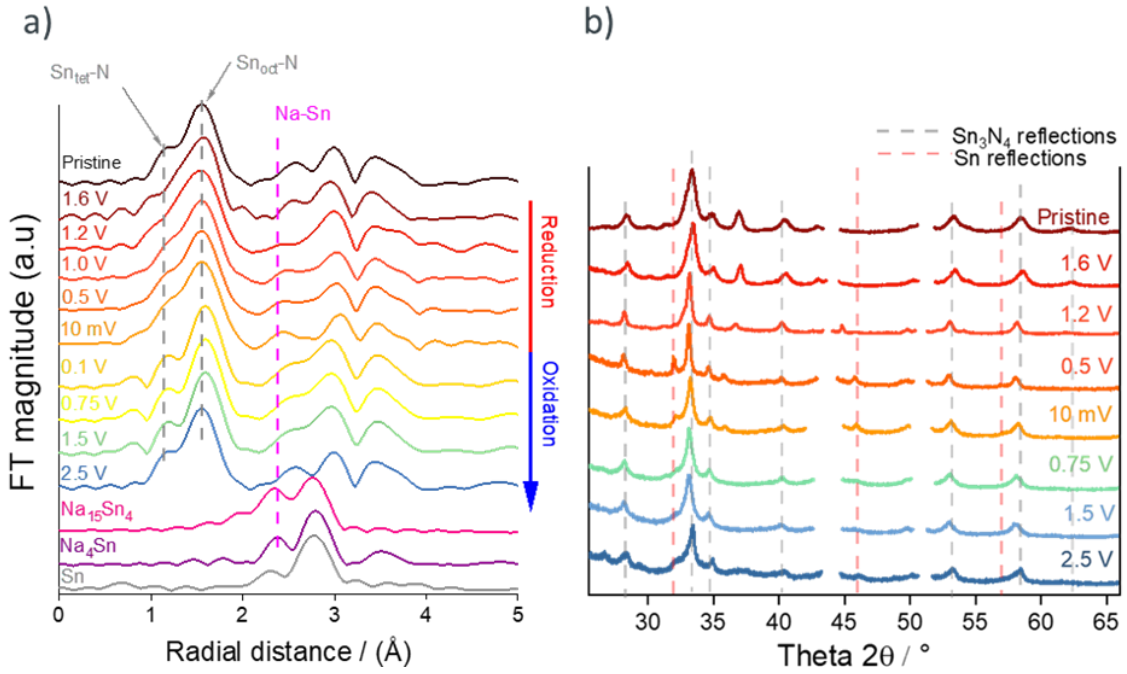

Figure 3.12 – (**a**). Fourier transforms of k ^{3}-weighted Sn K-edge EXAFS during initial reduction and oxidation of microcrystalline Sn_3N_4. The data of $Na_{15}Sn_4$, Na_4Sn and Sn from the ICSD database is also included for comparison. (**b**), Corresponding ex situ XRD patterns, with peaks due to the Cu current collector are omitted from the pattern.

The EXAFS spectra collected on samples during the first cycle (**Figure 3.12**) show a peak doublet at 1.5 Å radial distance corresponding to Sn-N bonds. The intensity of the lower radial distance peak within the doublet, corresponding to the tetrahedral Sn(1)-N bond distance, decreases greatly during reduction compared to the octahedral Sn(2)-N site. For a true conversion-alloying process, a more obvious change is expected in the XRD, where Sn_3N_4 reflections are reduced in intensity whilst also expecting to see stronger Sn or Na_xSn_y phases. The assumed consumption of smaller crystallites in the

XRD patterns coupled with the preferential reduction of the tetrahedral Sn(1)-N bond distance, could suggest an initial insertion process with Na is favoured over conversion at the surface of the tin nitride, with the bulk crystallites remaining chemically unchanged. The insertion process could displace Sn which can subsequently go on to form Na_xSn_y phases. The decrease in the intensity of the peak related to the tetrahedral Sn(1)-N bond distance starts at very high potentials (1.6 V), which is much higher than the observed potentials of conversion in SnO_2 studies.[92,307,308] A previous study into the reaction mechanism of tin nitride thin films with lithium ions by ^{119}Sn Mössbauer spectroscopy suggested that the Li-ions preferentially inserted into the tetrahedral sites of the spinel structure.[309] The study also suggested that on further insertion the Sn was likely extracted from the structure which could go on to form Li_xSn_y alloys.

A recent study has suggested sodium insertion into Sn_4P_3 proceeds at higher potentials during the initial reduction, before conversion/alloying processes take place.[310] However, this was performed on Sn_4P_3-P nanocomposite electrode where Na-insertion into black phosphorus is a known mechanism and so de-coupling insertion processes between Sn_4P_3 and P may be complex.[311]

As the potential is further reduced, a new Sn chemical environment starts to emerge from 1 V to 10 mV which is highlighted in greater detail in the difference plot of **Figure 3.13**. This could be assigned to the formation of Na-Sn alloys. The intensity of the Sn(1)-N tetrahedral peak increases in the EXAFS spectra during the subsequent re-oxidation of the tin nitride electrode suggesting that Sn_3N_4 is reforming, which is in agreement with the results from XANES analysis.

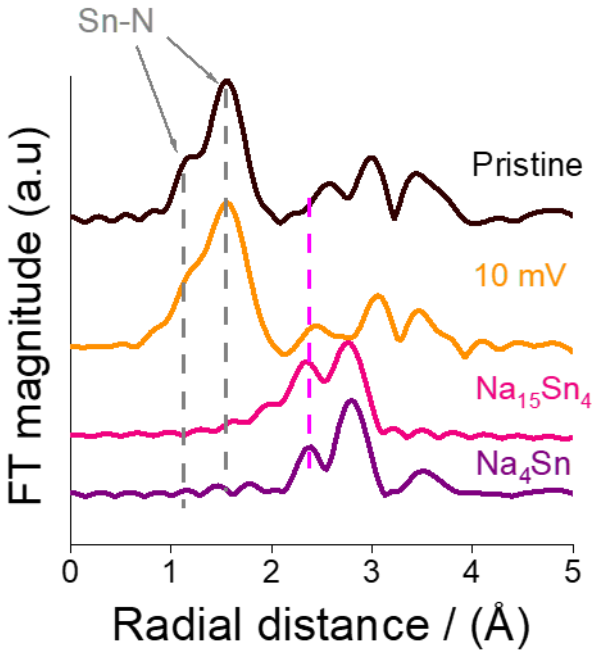

Figure 3.13 – Difference plot of Fourier transforms of k^3-weighted Sn K-edge EXAFS during initial and final states of the first reduction of microcrystalline Sn_3N_4. Arrows indicate the radial distance of Sn-N first and second nearest neighbours.

With greater insight into the structural and (electro)chemical processes occurring during the initial cycling of a microcrystalline Sn_3N_4 electrode; derivative capacity plots were compared between the first cycle of micro and nano electrodes at 50 mA g^{-1} (**Figure 3.14**).

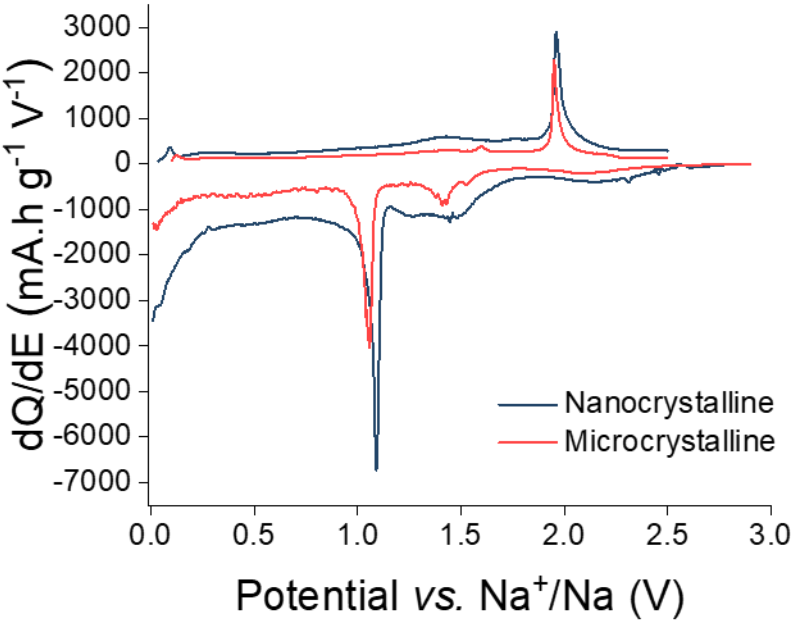

Figure 3.14 - Derivative capacity plot computed from the initial galvanostatic cycle of microcrystalline and nanocrystalline Sn_3N_4 at a specific current of 50 mA g^{-1} between 2.5 V and 10 mV.

The derivative capacity plots are very similar for both the microcrystalline and nanocrystalline Sn_3N_4 electrodes, demonstrating that the electrodes undergo similar electrochemical reactions during cycling. The main difference is that the magnitudes of the peaks is higher for the nanocrystalline electrode, which is in agreement with the higher specific capacities achieved for that material. The differential capacity plots also suggest that the processes occurring at 2 V on oxidation (charging) is the reverse of the processes at 1.5 or 1.2 V.

3.4 Conclusions

Microcrystalline and nanocrystalline Sn_3N_4 were successfully prepared using solvothermal conditions at 430 °C, or at 300 °C followed by ultrasound treatment in aqueous HCl. Sn_3N_4 electrodes of both materials were cycled in Na half-cells with 5 % FEC electrolyte additive, with the nanocrystalline electrode providing a higher capacity and good cycling stability over 50 cycles. Indeed, the capacity exceeds those reported for other tin-based materials, and good cycling stability with other tin-based materials has only been achieved with carbon supports or composite structures. The results presented here bring a deeper understanding of the Sn_3N_4 reaction mechanism in Na-ion cells. They provide evidence of the formation of Na-Sn alloys at the end of discharge and of reformation of Sn_3N_4 at the end of charge. Ex situ X-ray diffraction and X-ray absorption spectroscopy studies indicate that there is initial Na insertion into the Sn_3N_4 nanoparticles, ejecting some Sn which forms Sn_xNa_y phases on the surface, which is also consistent with the observed changes in the Sn-N and Na-Sn bond distances obtained from EXAFS spectra and with the change in the oxidation state obtained from XANES. The new solvothermal synthesis developed here is a simple and low cost synthesis route that enables control of the Sn_3N_4 particle size, which is critical to achieve full utilisation of Sn_3N_4 and thus higher capacity.

Chapter 4 Evaluation of lithium nitride as protective layer for lithium metal batteries

4.1 Introduction

This work assesses the effect of modifying the lithium metal electrode by forming a stable artificial interface layer of lithium nitride (Li_3N) between the metal and the liquid electrolyte. Li_3N has been studied as a solid-state material, however, the nitride's low decomposition potential (~0.6 V vs. Li^+/Li) has hindered its advancement.[312,313] The nitride has also been considered as a protective layer, owing to the very high conductivity of Li^+ ($2\times10^{-4}\Omega^{-1}cm^{-1}$), this layer will facilitate the even deposition of the lithium ions through the interface onto the metal surface (**Figure 4.1**).[314,315] A nitride layer has also been reported to limit the reactivity of the lithium metal electrode, which can facilitate the formation of a stable SEI.[316]

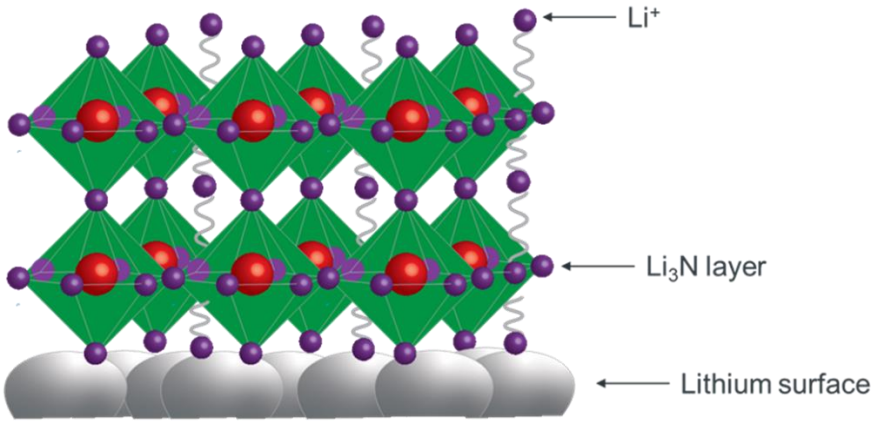

Figure 4.1 - Li_3N crystal structure comprised of layered Li_2N sheets between Li atoms on the lithium metal electrode surface.

The formation of heavier alkali metal binary nitrides has proven difficult. Lattice energy calculations demonstrate that the energies of formation for alkali binary nitrides become significantly less favourable going down group 1. In contrast lithium nitride (Li_3N) has a sufficiently negative value for the Gibbs free energy of formation

(ΔGf_f = -128.64 kJ mol^{-1}) leading to the formation of the metal nitride under standard conditions upon the reaction of lithium with nitrogen.[317]

Under these standard conditions, the alpha polymorph crystal structure of lithium nitride is formed (α-Li_3N), with a space group of *P6/mmm* where *a* =3.655 Å and *c*= 3.874 Å. The metal nitride can be described as a layered structure of Li_2N perpendicular to the *c* axis. Li atoms that occupy sites between the N atoms connect these Li_2N layers. Within the lithium nitride planes there are cationic vacancies (1-2% Li^+ vacancies) which help facilitate the intraplanar hopping mechanism of lithium ions within the crystal structure, this process becomes more significant at elevated temperatures.[318] The electrochemical performance of lithium nitride has been investigated as a bulk active material. Desjardins et al. reported a lithium-lithium nitride (linode) electrode, which consisted of 11 mol % Li_3N homogenised with lithium metal.[319] They reported two major advantages to this material: The operating potential is identical to that of metallic lithium and consequently has no effect on the cell voltage. The capacities reported were close to that of metallic lithium (90% corresponding to ~3400 Ah kg^{-1}). Secondly, the linode was found to be less reactive towards common electrolytes leading to a decrease in electrolyte decomposition on the surface of the electrode.

Studies into Li_3N as a protective layer on the lithium metal surface have also been reported. Modified lithium metal electrodes with a Li_3N layer have been prepared by exposing battery-grade lithium foil under a nitrogen atmosphere in a sealed container.[316] Under these conditions (Flowing N_2, 2 hours, 20 °C) two isomorphs of Li_3N with a hexagonal structure are formed (α- Li_3N [*P6/mmm*] and α′-Li_3N [*P3m1*]). Zhang et al. further expanded on these conditions by varying the N_2 gas flow rate and reaction temperature.[320] Polycrystalline Li_3N synthesised at room temperature for 2 hours with a constant N_2 flow rate of 100 mL/min delivered the best electrochemical performance. Cui et al. acknowledged the difficulties of forming defined Li_3N layers with complete coverage on lithium foil in direct contact with N_2 gas.[321] The presence of a native surface film (mainly oxide) on the as-received battery-grade lithium foil, inhibited the formation of a uniform nitride layer.

In these studies, where lithium foil is exposed to nitrogen gas at a raised temperature, the resulting nitride layer is very thick (< 200 nm). To form well-defined

thin Li_3N layers on the surface of electrodes, an experimental set-up was designed to reduce air and moisture exposure during nitridation, whilst maintaining N_2 flow at an elevated temperature to form crystalline Li_3N. The suitability of battery-grade lithium foil and electrodeposited lithium was also assessed as the lithium source for nitridation.

4.2 Experimental

4.2.1 Electrode preparation

The electrolyte solution used for the electrodeposition of lithium onto nickel discs was 4 M bis(trifluoromethanesulfonyl)imide lithium salt (LiTFSI) in 1,3 DOL. LiTFSI (99.95%, Aldrich) was dried under vacuum (>0.2 mbar) at 140 °C for 48 hours before use. After drying, the LiTFSI salt was stored in an argon-filled glovebox (Mbraun, oxygen and water content < 5 ppm). 1,3 DOL (99.8%, anhydrous, ~75 ppm butylated hydroxytoluene (BHT) as inhibitor, Aldrich) was opened in the glovebox and dried over molecular sieves (4 Å,8-12 mesh bead size, Aldrich, dried under vacuum at 180° C for 48 hours) for 2 days prior to use. The electrolyte solution was prepared in an argon-filled glovebox by dissolving the appropriate amount of solid into the 1,3 DOL solvent. Electrolyte solutions were typically used within four weeks.

Two sources of lithium are reported for nitrogen treatment. Battery grade-lithium (Rockwood lithium) was used-as is, with 11 mm diameter electrodes punched from the foil. Electrodeposited lithium electrodes were prepared in two-electrode cells (SS cell housing lined with FEP with polished Cu current collectors). A Ni disc (Advent materials 99.8%, 11 mm diameter) was used as the working electrode against a lithium foil counter electrode (Rockwood lithium, 12 mm diameter). Two Celgard 2400 discs (12 mm diameter, dried under vacuum at 60 °C for 28 hours) were used as separators, wetted with 80 µL of electrolyte. Electrodeposition of lithium onto Ni was performed on a BioLogic MPG multi-channel potentiostat. An initial rest period of 30 minutes was used to record the open circuit potential. 3 plate/strip cycles followed, at a current density of 0.25 mA cm^{-2} with a 5-minute rest between each change in current direction. A final 16-hour plate was carried out at 0.5 mA cm^{-2}. The cells are then disassembled inside an argon-filled

glovebox, washed with 1,3 DOL (99.95%, Aldrich) to remove any salt and stored in the glovebox for nitrogen treatment or electrochemical testing (plated lithium electrodes were typically used within one week).

4.2.2 Synthesis of lithium nitride layers

Dedicated glassware (**Figure 4.2**) was designed in-house for nitrogen treatment of lithium electrodes.

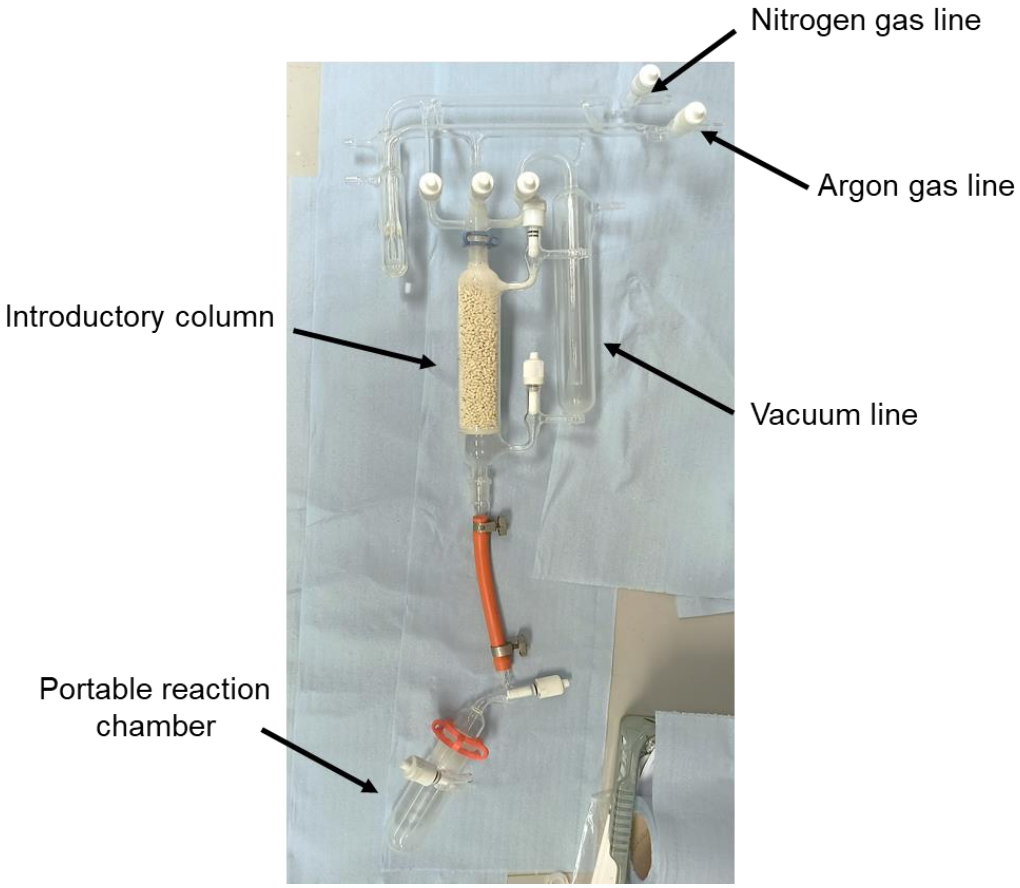

Figure 4.2 -.Dedicated glassware for the nitridation of lithium electrodes.

The glassware has two dedicated gas-lines for nitrogen argon which are controlled by Young's taps that join a single inlet alongside a vacuum line. An introductory column filled with regenerated molecular sieves is attached to the inlet and can also be individually isolated. The portable reaction chamber houses a copper stage to improve heat transfer to the samples. The chamber was designed to be able to enter a glovebox

under vacuum and exit the glovebox filled with argon, to minimise the sample's exposure moisture/air during transfer. The reaction chamber is attached to the introductory column for evacuation and refilling of gases. The dedicated glassware was designed to minimise the exposure of lithium electrodes to air/water.

Lithium electrodes (foil or electrodeposited) are loaded onto a copper stage inside an argon-filled glovebox (Mbraun, oxygen and water content < 5 ppm) and are transported under argon in a sealed portable reaction chamber. The reaction chamber was attached to the introductory column filled with molecular sieves (dried at 200 °C, 24 h) under a positive flow of argon (BOC Pureshield, 99.998%), the reaction chamber was then immersed in an oil bath at 90 °C for the duration of the nitridation reaction. The entire system was then evacuated for 20 minutes to remove the argon gas. Nitrogen (BOC, 99.998% minimum) gas was carefully back-filled to first fill the introductory column where trace water was removed by molecular sieves. The flow of N_2 was then set to 50 $cm^3\,min^{-1}$ before carefully back-filling the heated reaction chamber. N_2 gas was kept at a constant flow (50 cm^3/min) for a reaction time of 2 hours, afterwards the entire system was again evacuated for 20 minutes to stop the nitridation reaction. The evacuated reaction chamber was reopened inside an argon-filled glovebox, where the nitrogen-treated lithium electrodes are stored for electrochemical testing or characterisation (electrodes are typically used within 1 week). A reaction time of 2 hours was chosen after an initial set of reactions were carried at increasing times of nitridation to optimise the procedure. The N_2 gas was kept at a constant flow (50 cm^3/min) for all the different measurements as this ensured a constant supply of nitrogen was reaching the lithium. There was no noticeable change in appearance of the lithium electrode after one hour of nitridation. After two hours, the electrode surface started turning a rosy red, which is attributed to Li_3N formation on the surface of the electrode. After 5 hours the lithium electrode had turned black and was brittle to handle, this indicated that the nitridation reaction had gone too far and had reacted with the majority of the available lithium.

4.2.3 Electrochemical measurements

The electrolyte solution used for unidirectional galvanostatic polarisation and lithium plating/stripping measurements was 1 M lithium hexafluoroarsenate ($LiAsF_6$) in 1,3 DOL with 100 ppm tributylamine (TBA) as a stabiliser. $LiAsF_6$ (98 %, Aldrich) was dried under vacuum (>0.2 mbar) at 140 °C for at least 48 hours before use. After drying, the $LiAsF_6$ salt was stored in an argon-filled glovebox (Mbraun, oxygen and water content < 5 ppm) prior to use. 1,3 DOL (99.8%, anhydrous, ~75 ppm butylated hydroxytoluene (BHT) as inhibitor, Aldrich) was opened in the glovebox and dried over molecular sieves (4 Å,8-12 mesh bead size, Aldrich, dried at 200 °C for 2 days under vacuum) for 48 hours prior to use. TBA (99.5%, Aldrich) was opened in the glovebox and dried over molecular sieves (4 Å,8-12 mesh bead size, Aldrich, dried at 200 °C for 2 days under vacuum) for 48 hours prior to use. The electrolyte solution was prepared in an argon-filled glovebox by dissolving the appropriate amount of solid into a stock solution of 100 ppm TBA in 1,3 DOL solvent. Electrolyte solutions were generally used within four weeks.

Unidirectional galvanostatic polarisation measurements were recorded using a multichannel potentiostat (VMP2 or MPG, Bio-Logic). Two-electrode Swagelok cells (SS cell housing lined with FEP with polished Cu current collectors) were constructed with either unmodified (electrodeposited lithium without N_2 exposure) or nitrogen-treated (electrodeposited lithium, nitrided for 2 hours at 90 °C) electrodes against a battery-grade lithium foil (Rockwood lithium) counter electrode. A gasket (1 mm diameter hole, Viton, fluoropolymer elastomer) was used as a spacer and filled with 15 µL of electrolyte. A constant negative current was applied to the working electrode (constant plating of Li onto the working electrode) and the potential response vs. time was recorded. Great care should be taken when dissembling the Swagelok cells, as dendritic lithium is extremely reactive to moisture in the air and can ignite. The risk was minimised as the area of dendritic lithium on the electrode was limited to 1 mm by the gasket. Cells were taken apart in a fumehood and the lithium electrodes were destroyed in IPA.

Lithium plating/stripping measurements were recorded using GCPL settings on a multichannel potentiostat (VMP2 or MPG, Bio-Logic). Symmetric cells (unmodified or

nitrogen-treated electrode, 11 mm diameter) were constructed with 2x Celgard 2400 separators, wetted with 80 µL of electrolyte. Galvanostatic cycling was performed at a fixed current density of 2 mA cm^{-2} over 1.5-hour charge (plate) and discharge (strip) intervals for 25 cycles. Potentiostatic electrochemical impedance spectroscopy (PEIS) was recorded before and after the plate/strip measurements on a multichannel potentiostat (VMP3, Bio-Logic). A sinusoidal potential with a 10 mV amplitude was applied to the OCV at frequencies from 1 MHz to 10 mHz, with 3 points averaged at each frequency.

4.3 Results and discussion

4.3.1 Synthesis and characterisation of lithium nitride protective layers

Initial attempts to synthesise lithium nitride as a protective layer were carried out on battery-grade lithium foil (Rockwood lithium). The purity of as-received lithium-metal is usually specified as > 99.99% (trace metal basis). Common industrial methods for processing high purity lithium include, melting extracted lithium at high temperatures under vacuum or fused salt electrolysis followed by distillation and collection in cast-iron enclosures.[322,323,324] Whilst great efforts go into manufacturing lithium foil with trace amount of impurities, several contaminants have been identified (Li_2CO_3, Li_2O, LiOH, LiN_2O_2 and Li_3N), that are primarily located at the metal surface as part of the native film.[325,326,327,328]

X-ray photoelectron spectroscopy was performed on the as-received lithium foil to determine any chemical species present in the native passivation layer on the metal surface. Depth profiling on the native film was achieved by varying the incident photon energy using synchrotron radiation (Diamond Light Source). Two "soft" (1 and 2.15 keV) and one "hard" (6.45 keV) X-ray energies were chosen to increase the depth sensitivity at greater energies, with higher energies being able to probe deeper into the sample. An approximation of the probing depth for the different core levels can be calculated from the inelastic mean free path for the three different photon energies.

Figure 4.3 presents the evolution of the O 1s, N 1s, C 1s and Li 1s spectra of the battery-grade lithium foil with increasing incident energy. The approximated escape depth for each core level is also highlighted for the different incident energies. The Li 1s core-level spectra is difficult to analyse due to multiple species that can be present under a broad convoluted peak. However, the metallic Li^0 signal is easy to detect as a sharp peak at 54.5 eV. The Li^0 signal can be used as a reference for estimating where the incident photons are probing the native layer with respect to the lithium surface.[329,180] From this, an interpretation of the XPS analysis can be made of the chemical environments present on the surface of the lithium foil with respect to the native passivation layer as a function

of incoming incident energies (**Figure 4.4**). **Table 4.1** summarises the XPS analysis and peak assignments for the observed spectral lines.

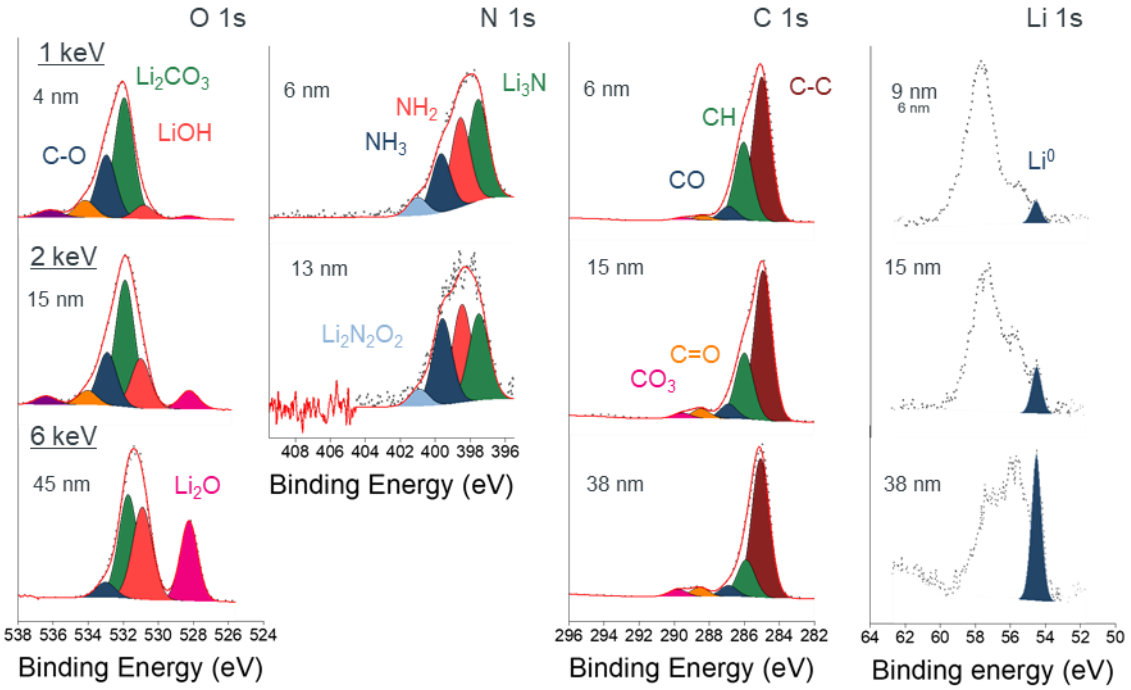

Figure 4.3 – XPS spectra for the O 1s, N 1s, C 1s and Li 1s regions of the surface of the lithium foil with native passivation layer as a function of increasing excitation energies, with the resulting probing depth calculated for each element.

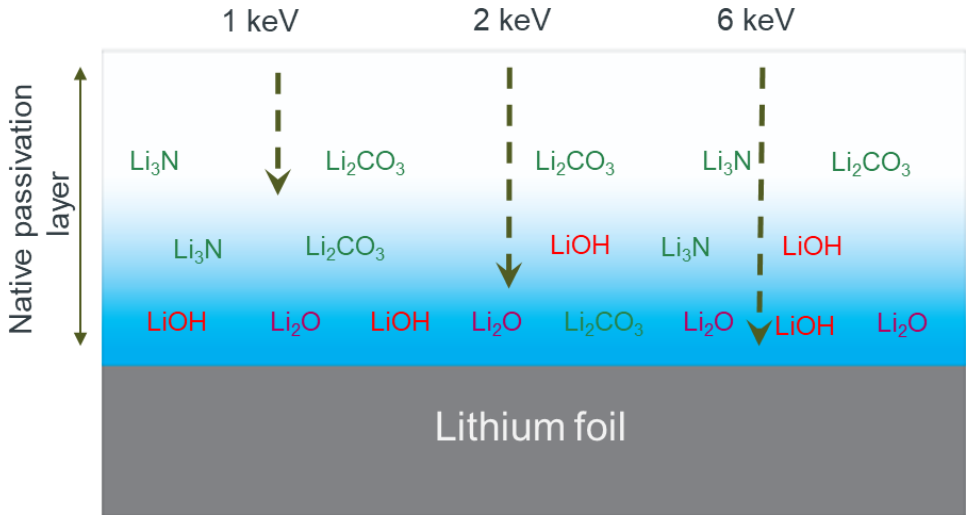

Figure 4.4 – Resulting schematic from the interpretation of XPS analysis of the lithium foil with native passivation layer.

Table 4.1 – Summary of XPS analysis and assignements for the surface characterisation of the battery-grade lithium foil with native passivation layer.

Orbital	Binding energy (eV)	FWHM	Peak assignments
O 1s	528.3	1.2	Li_2O[325,330,331]
	530.8	1.3	LiOH[325,331,332,333]
	531.9	1.3	Li_2CO_3[325,331,333,334]
	532.9	1.3	C-O[333,335,336,337]
	534.2	1.3	Unassigned
	536.2	1.6	Na Auger[338,339]
N 1s	397.5	1.3	Li_3N[332,340,341,342]
	398.5	1.3	Potential NH_2[343,344,345]
	399.6	1.3	Potential NH_3[339,340,341]
	401	1.3	$Li_2N_2O_2$[346,347,348,349]
C 1s	285	1.2	C-C[168,330,350]
	285.9	1.2	CH[155]
	286.8	1.2	C-O[155,168,350,351,352]
	288.3	1.2	C=O[168,330,350,351]
	289.4	1.2	CO_3[155,168,330,350,352]
Li 1s	54.5	0.8	Li^0 [353,354,355,356]

Deconvolution of the broad peak observed in the O 1s spectra at 1 keV, reveals three signals corresponding to LiOH, Li_2CO_3 and C-O species. At higher energies, an additional peak emerges at 528.3 eV corresponding to Li_2O, grows in intensity with increasing photon energy, indicating that the contribution of lithium oxide increases on proximity to the metallic lithium surface buried underneath the native layer.[325,328,331,357]

The C 1s spectra confirm the presence of carbonate species at 2 and 6 keV. Previous studies have also reported the presence of carbonates on the surface of pristine lithium foil which originate from the extraction/purification of battery grade lithium.[325,358]

The N 1s spectra reveal that 4 different nitrogen-containing environments are present in the native layer of the battery-grade lithium foil. A signal for Li_3N (397.5 eV) is observed at 1 keV which can be considered a contaminant from the lithium foil reacting with air, forming part of the native layer on the surface.[359,360] The relative intensity of the

signal decreases at 2 keV suggesting that the nitride contaminant is localised to the top 10 nm of the native layer. A peak at 401 eV has been reported for lithium hyponitrite (LiN_2O_2) as a decomposition product of $LiNO_3$ of the surface of lithium metal electrodes.[346,347,348] It is feasible that a similar contaminant has formed as part of the native layer on lithium foil, through contact with moisture and air. Two other peaks were observed in the N 1s (1 keV) spectra at 398.2 and 399.56 eV which could possibly be linked to imine and amine species as Li_3N is known to decompose to form ammonia on contact with water which could subsequently react with the lithium metal.[345,361,362,363] The presence of a strong LiOH signal indicates that the lithium foil has been in contact with water vapour.

The nitridation of battery-grade lithium foil was carried out by the procedure outlined in **Section 4.22**. The direct reaction of lithium with nitrogen gas should induce a colour change of the metallic lithium surface to a dark red/black.[364,365,366]

$$6Li + N_2 = 2Li_3N \qquad \textbf{Equation 51}$$

No obvious colour change was observed after 2 hours of flowing nitrogen (50 cm^3/min) over the lithium foil at 90 °C (**Figure 4.5**).

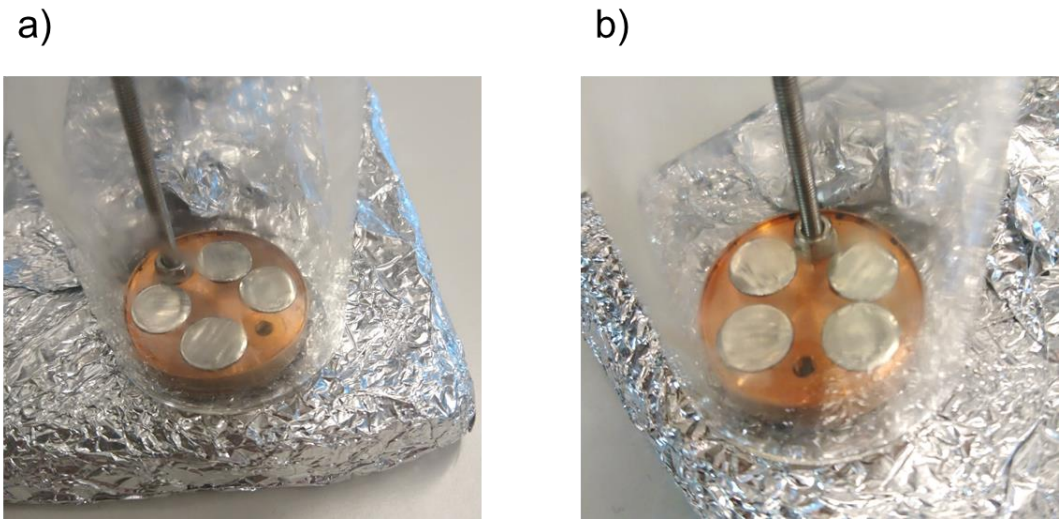

Figure 4.5 – Battery-grade lithium foil inside the portable reaction vessel before (**a**), and after (**b**), 2 hours nitridation.

One possible explanation is the native layer on the lithium metal surface has prevented the diffusion of nitrogen gas to the lithium surface. The strong contribution of Li_2O determined from XPS analysis of the pristine lithium foil (**Figures 4.3** and **4.4**) could have reduced the reactivity of the foil to the formation of a defined Li_3N layer.

To improve the reactivity of N_2 with the lithium metal surface, lithium foil was replaced by electrodeposited lithium as the target for Li_3N formation. In the absence of a native surface film with a strong oxide layer, the electrodeposited lithium metal surface could be more reactive towards lithium nitride formation. Lithium was electrodeposited onto a nickel current collector (**Section 4.21**) to produce lithium metal electrodes for nitrogen treatment. **Figure 4.4** presents voltage profiles typical of the electrodeposition process to forming plated lithium electrodes.

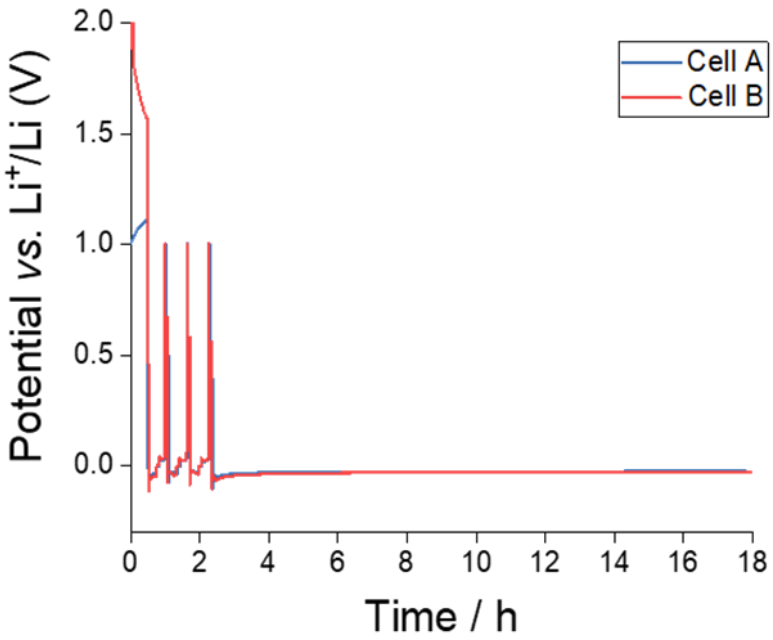

Figure 4.6 – Voltage profiles of the electrodeposition process for two identical cells in forming plated lithium electrodes on Ni current collectors.

The initial plate/strip steps allow for the treatment of the current collector, aiding the uniform plating of lithium during the final step. The voltage plots for lithium plating onto nickel discs in two identical cells demonstrate good reproducibility with the evolution of lithium plating.

Scanning electron microscopy (SEM) images reveal that lithium has been successfully electrodeposited onto the current collector (**Figure 4.7**).

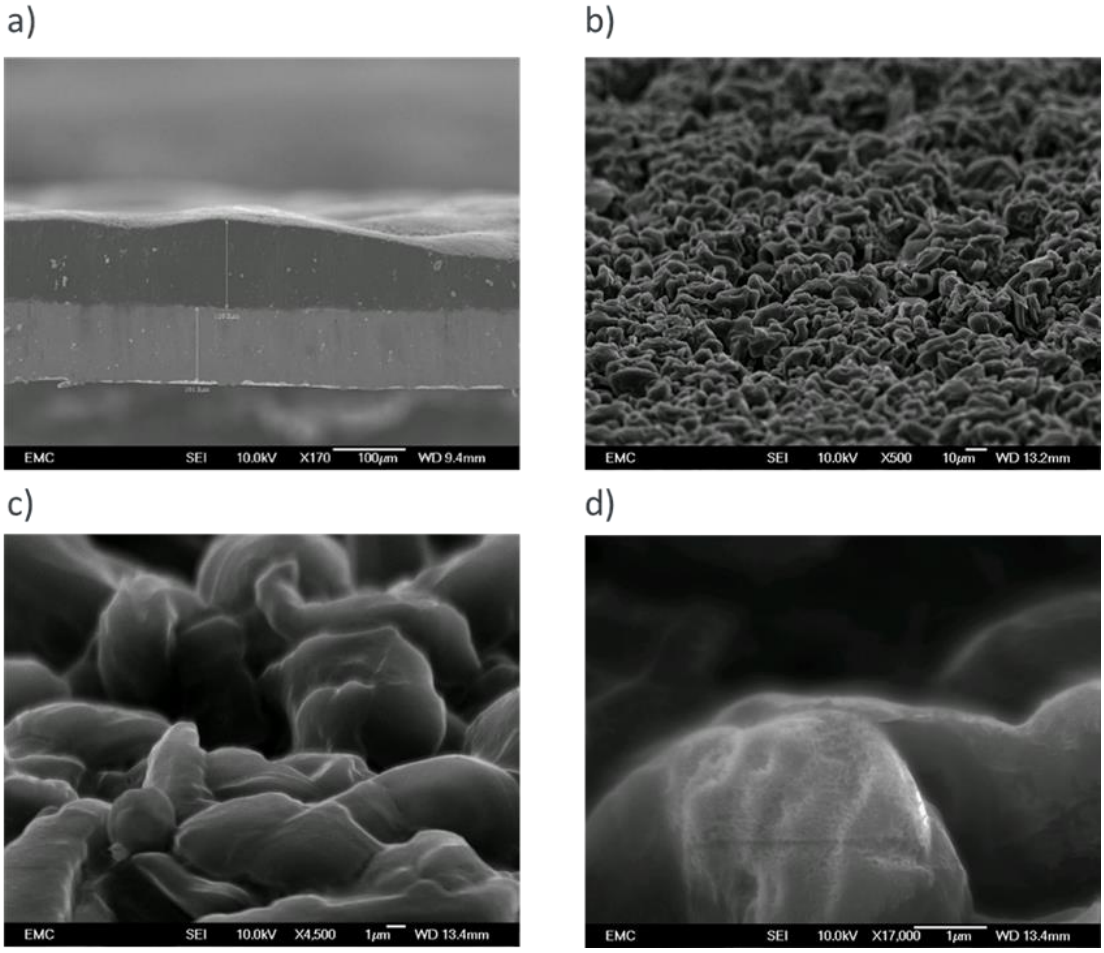

Figure 4.7 - (**a**) Cross-section SEM image of unmodified electrodeposited lithium onto a nickel current collector, 170x. SEM top surface images of unmodified electrodeposited lithium onto a nickel current collector at: (**b**), 500x magnification (**c**), 4500x magnification and (**d**), 17,000x magnification.

The lithium deposits have smooth, rounded edges, which is typical of lithium electrodeposition in ether-based electrolyte systems, when compared to needle-like lithium deposits electrodeposited in carbonate-based electrolyte systems.[165,168,187,367] This nodule-like morphology has a lower surface area and should be less reactive to the electrolyte when forming a stable SEI. The thickness of the electrodeposited lithium was approximately 120 µm with complete coverage of the current collector.

After establishing an effective and reproducible route for electrodepositing lithium onto current collectors, the plated lithium electrodes were nitrided for 2 hours at 90 °C.

A visible colour change was observed during nitridation from a metallic grey of the electrodeposited lithium to a brown-red colour indicative of Li_3N formation on the surface of the lithium electrode (**Figure 4.8**).

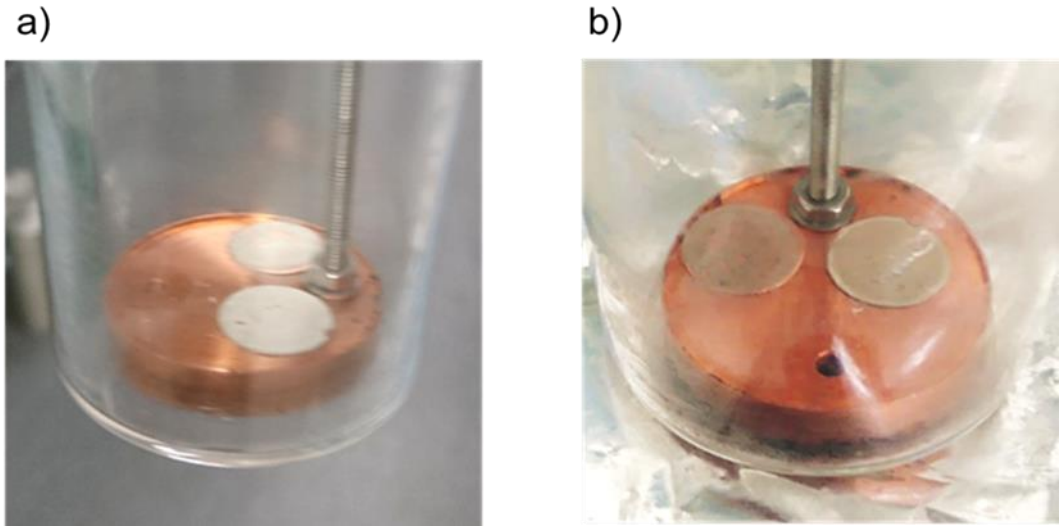

Figure 4.8 - Electrodeposited lithium inside the portable reaction vessel before (**a**), and after (**b**), 2 hours nitridation at 90 °C.

SEM images were also taken after nitriding the electrodeposited lithium electrodes for 2 hours at 90 °C. **Figure 4.9** presents SEM images of the nitrided electrodeposited lithium. The cross-section SEM image reveals the thickness of the electrode (**a**), 120 µm), which demonstrates good reproducibility of the plating process when compared with **Figure 4.7**. At lower magnification (500x) there was no obvious change to the morphology when compared to SEM images of the unmodified electrodeposited lithium (**Figure 4.7**).

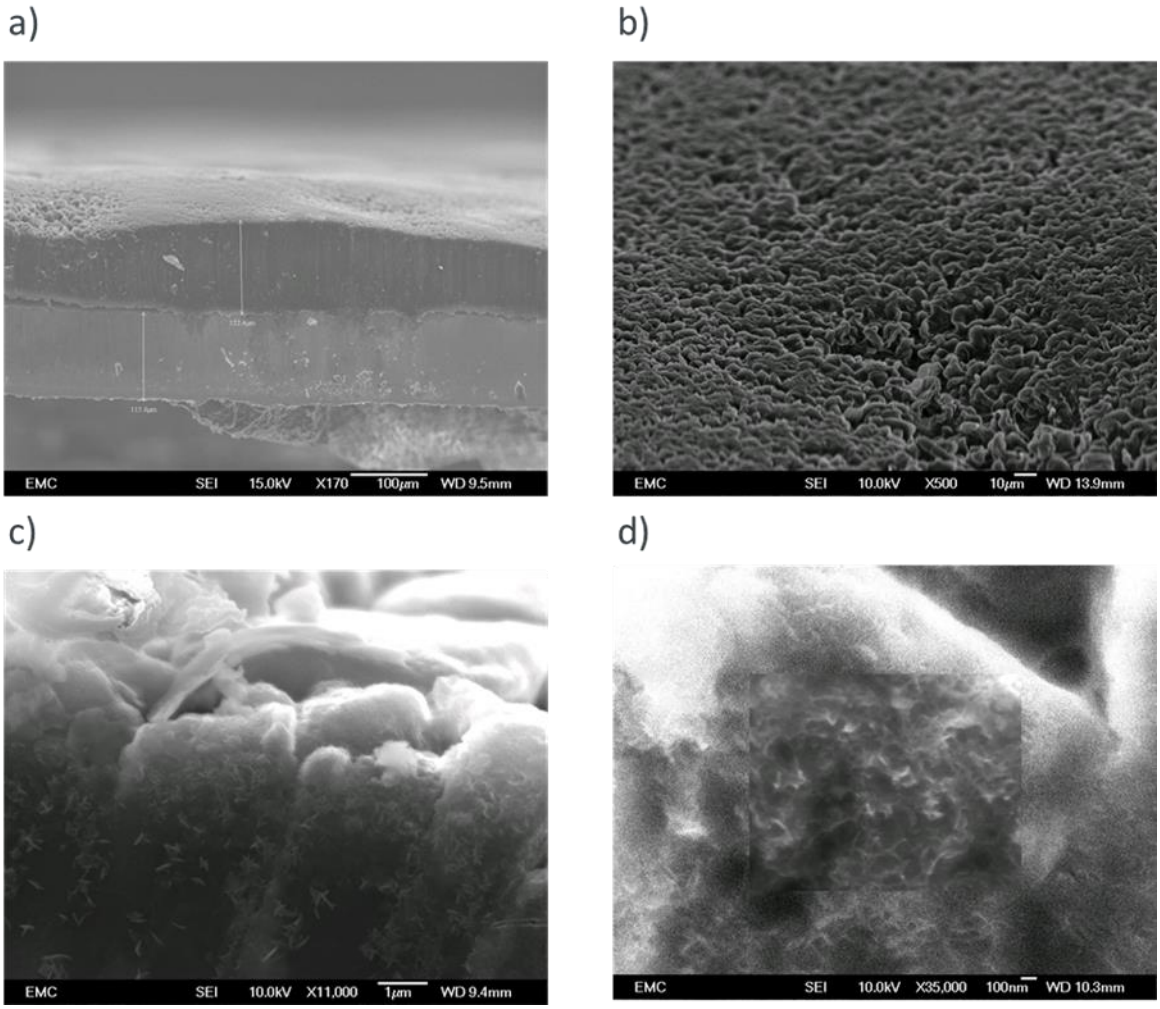

Figure 4.9 - (**a**), Cross-section SEM image of nitrided (2 hours at 90 °C) electrodeposited lithium on a nickel current collector, 170x. SEM top surface images of nitrided electrodeposited lithium onto a nickel current collector at: (**b**), 500x magnification, (**c**), 11,000x magnification and (**d**), 35,000x magnification.

Higher magnification reveals a scaffold like-structure that covers the surface of the electrode which is attributed to the formation of lithium nitride. The images were also considerably brighter than the SEM images of the unmodified electrodeposited lithium electrode, which could be due to an accumulation of charges on the electronically insulating Li_3N layer under the electron beam.[365]

Herein, this report refers to electrodeposited lithium that has not been nitrogen treated as the unmodified lithium electrode and the electrodeposited lithium exposed to N_2 for 2 hours at 90 °C as the nitrided lithium electrode.

Chemical analysis of the unmodified and nitrided electrodeposited lithium was carried out by scanning transmission X-ray microscopy (STXM) and X-ray photoelectron spectroscopy (XPS). STXM allows for spatially resolved spectroscopy of bulk lithium structures, whereas XPS investigates the chemical composition of the lithium surfaces and interfaces.

For STXM, samples were prepared by electrodepositing lithium structures onto nickel TEM grids under the same electrochemical conditions as described previously (**Section 3.22, Figure 4.6**). To allow for suitable STXM measurements to be collected, the final plating time was reduced to 15 minutes. This decrease in plating time led to lithium structures that were ~10-50 µm in diameter (**Figure 4.10**).

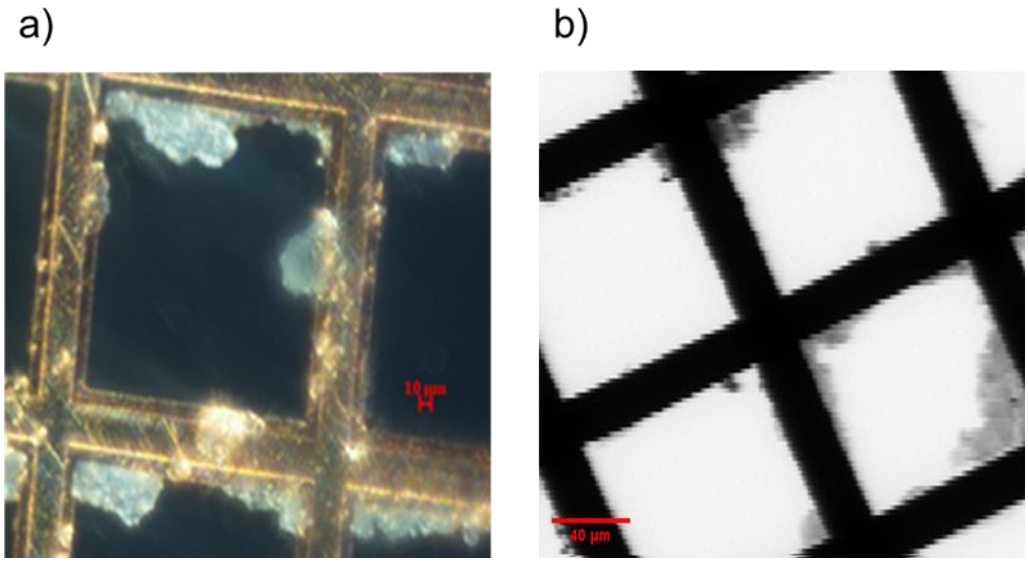

Figure 4.10 - (**a**), Optical microscope image at 20x magnification of unmodified electrodeposited lithium structures on a nickel TEM grid. Scale bar = 10 µm. (**b**), 200 x 200 µm (pixel size = 500 nm) STXM image of electrodeposited lithium on a copper TEM grid. Scale bar = 40 µm.

A number of challenges arose due to the small size and reactive nature of the lithium sample. Firstly, the TEM grid had to be placed centrally on top of a Cu current collector inside the Swagelok cell, to ensure good Li plating occurred on the grid. After plating, the cell was taken apart inside a glovebox, the grid was washed with 1,3 dioxolane to remove any salt that had precipitated out on the grid, as it would be difficult to distinguish Li structures from salt in the STXM images. The samples were stored in a

modified TEM holder to prevent the lithium structures coming into contact with any surface during storage and transfer.

For the unmodified electrodeposited lithium samples, the TEM grids were washed with 1,3 DOL after electrodeposition and stored for chemical analysis. STXM data acquisition and processing was carried out following the procedure described in **Section 2.81**. Multi-energy image scans (stacks) over the O K-edge (528-545 eV), C K-edge (282-310 eV) and N K- edge (392-420 eV) were measured on an unmodified electrodeposited lithium structure. **Figure 4.11** presents an STXM image taken at the C K-edge (290 eV) of the unmodified electrodeposited lithium structure chosen for chemical analysis.

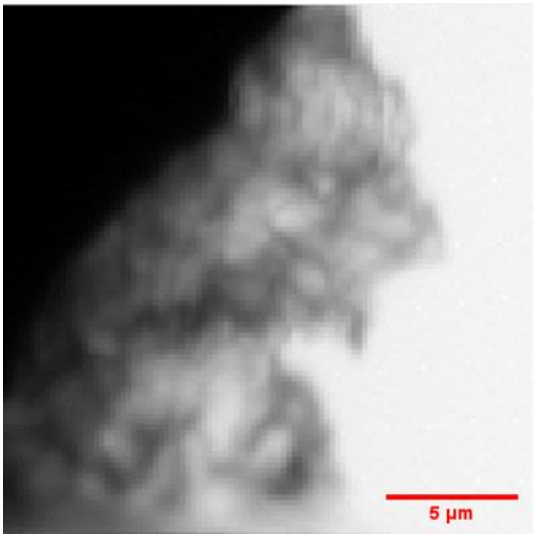

Figure 4.11 - 15 x 15 µm (290 eV, pixel size = 50 nm) STXM image of unmodified electrodeposited lithium structure chosen for chemical analysis. Scale bar = 5 µm.

Figure 4.12 presents the NEXAFS spectra generated from the STXM stacks over the O, C and N K-edge energies for the unmodified electrodeposited lithium structure and the corresponding regions within the sample generated for each stack. **Table 4.2** summarises the NEXAFS analysis and species assignments for the observed absorptions.

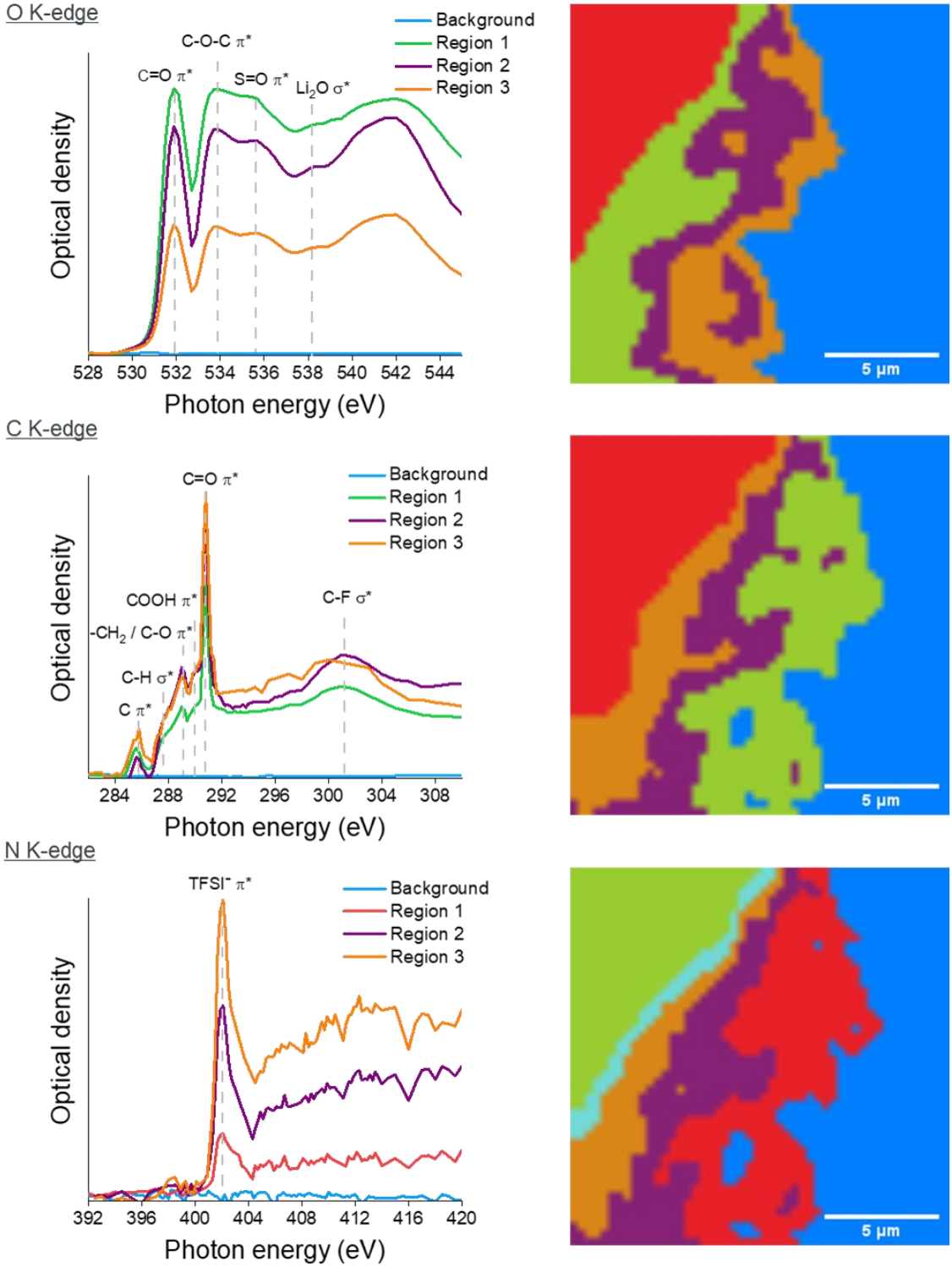

Figure 4.12 - NEXAFS spectra of the O, C and N K-edge energies and the corresponding cluster map for the unmodified electrodeposited lithium structure from **Figure 4.11**.

Table 4.2 – Summary of NEXAFS analysis and assignments for the unmodified electrodeposited lithium structure.

Element	Photon energy (eV)	Assignment
O K-edge	532	C=O (O 1s to C=O π^*)[368,369,370]
	534	C-O/OH (O 1s to C-O/C-OH π^*) standard and:[371,372,373]
	~536	S=O (O 1s to S=O π^*) from standard
	~538	Li_2O (O 1s to Li-O σ^*)[369,374]
C K-edge	285	C-C (C 1s to C-C π^*)[372,375,376]
	288.5	CH_2/CO (C 1s to C-H/C-O π^*)[372,375,376]
	289	COOH (C 1s to C-OO^- π^*)[375,376]
	290.5	C=O (290.6 eV, C 1s to C-=O π^*)[372,375,376]
	~301	CF_3 (C 1s to C-F σ^*)[377]
N K-edge	402	LiTFSI (N 1s to N-S) standard and: [373]
	408	Li_3N

To aid in the interpretation of the spectra, an O and N K-edge stack was recorded on a LiTFSI salt standard (**Figure 4.13**). The standard was produced by dispersing 4 molal LiTFSI in 1,3 DOL solution on a TEM grid, the solvent is then allowed to evaporate leaving salt deposits across the grid. The O K-edge of the LiTFSI salt standard (**a**) contains two prominent absorptions. The defined absorption at ~536.5 eV is assigned to the S=O (O 1s to S=O π^*) group of the LiTFSI salt. The initial absorption at 534 eV is assigned to the unreacted ether group (O 1s to C-O π^*) of 1,3 DOL residue, as the solvent was used to prepare the salt standard.[371,372,373]

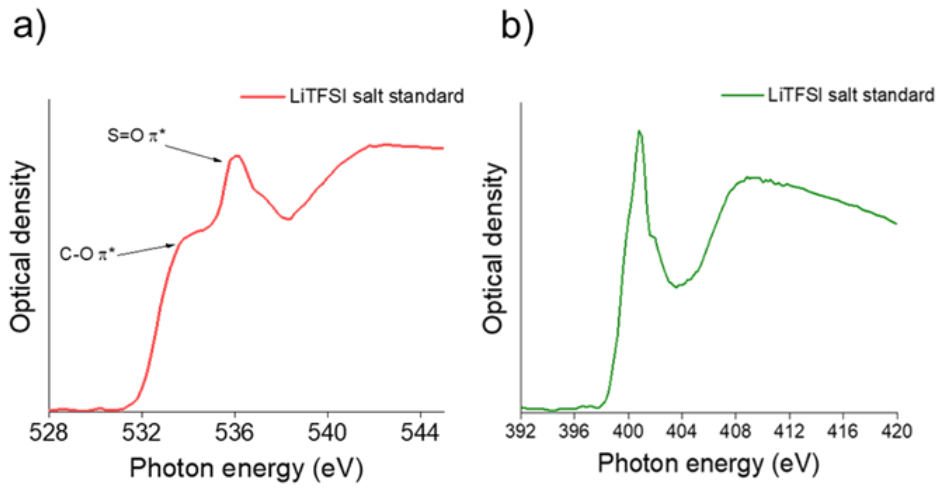

Figure 4.13 - NEXAFS spectrum of the (**a**), O K-edge and (**b),** N K-edge energy for the LiTFSI salt standard.

4 different regions were determined from the cluster analysis of the stacked STXM images corresponding to the O K-edge NEXAFS spectra for the unmodified electrodeposited lithium structure (**Figure 4.12**). The background (blue) shows no absorption. Regions 1 (green), 2 (purple) and 3 (orange) represent the bulk and surface of the lithium deposit.

The absorption at 532 eV is due to the presence of lithium carbonate and is assigned to the transition from O 1s to the C=O π^* states of CO_3. Lithium carbonate is a well-described decomposition product in an SEI formed on lithium metal electrodes that have been in contact with 1,3 DOL.[184,185,350,378] As the lithium is continuously electrodeposited onto the nickel TEM grid, it is likely to reduce the electrolyte (4 M LiTFSI in 1,3 DOL) after a sufficient lithium structure has formed. The unmodified electrodeposited lithium structure will have an SEI formed from the lithium plating process. The peak at 534 eV is assigned to either the unreacted ether groups from 1,3 DOL (O 1s to C-O π^*) or lithium alkoxide (O 1s to C- OH π^*). Lithium alkoxide has been reported as a reduction compound of 1,3 DOL on the surface of the lithium metal electrode as part of an SEI.[158,375,379] The shoulder at ~538 eV is ascribed to the presence of Li_2O, however the signal's relative intensity is small compared to the rest of the O K-edge spectrum.[369,374]

A similar cluster analysis and spectral response was observed for stacked STXM images collected on the lithium deposit over the C K-edge **(Figure 4.12**). Again, 4 different regions were determined by cluster analysis which contain organic species that are typical of electrodes that have been in contact with 1,3 DOL-based electrolyte solutions.[187,372,375] Peaks for C-C (285 eV, C 1s to C-C π^*) C-O (288.5 eV, C 1s to C-O π^*) COOH (289 eV, C 1s to C-OO^- π^*) and C=O (290.6 eV, C 1s to C-=O π^*) are observed and are related to the presence of 1,3 DOL and the reduction products of the cyclic ether.[158,372,375,380] These species can also be described as forming an SEI on the unmodified electrodeposited lithium structure during the lithium plating process. Region 1 (green) is away from the bulk of the lithium structure and presents the weakest spectral response for lithium carbonate (C=O), again implying the reduction of 1,3 DOL is concentrated towards the bulk of the unmodified lithium. A broad signal appears at ~301 eV which is attributed to the C-F group (C 1s to C-F σ^*) of the LiTFSI salt.[381] The absorption is weaker in region 1 (green) compared to 2 (purple) and 3 (orange), suggesting that the presence of the imide salt and any decomposition products are located closer to the bulk of the lithium.

The N K-edge NEXAFS spectra reveal one strong absorption at 402 eV (**Figure 4.12**). To aid in the interpretation of the spectra, the N K-edge stack was also collected on a LiTFSI salt standard (**Figure 4.13**). The strong absorption at 402 eV is attributed to the N 1s to N-S π^* transition in the imide salt. The broad shoulder observed ~408 eV is due to delocalised interactions between the Li^+ and N^-.[377]

Scanning transmission X-ray microscopy was also performed on nitrided electrodeposited lithium. To prepare the nitrided lithium samples, lithium structures were again electrodeposited onto a nickel TEM grid under the same conditions described for the unmodified electrodeposited samples. After electrodeposition, the lithium structures were washed with 1,3 DOL and then nitrided under the same conditions as described in **Section 4.22** before storage for chemical analysis. **Figure 4.14** presents an STXM image taken at the C K-edge (290 eV) of the nitrided electrodeposited lithium structure chosen for STXM-NEXAFS analysis.

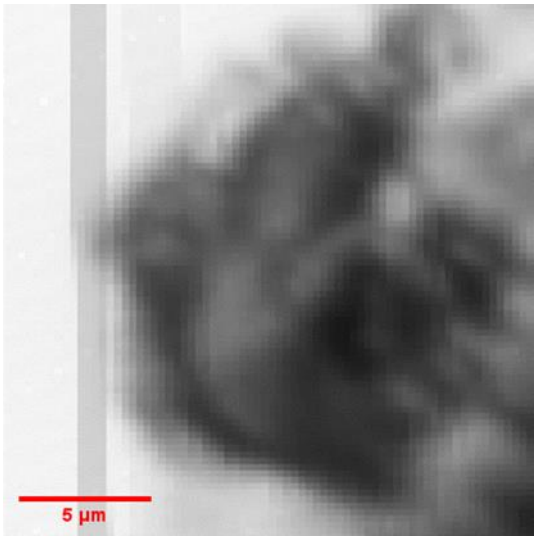

Figure 4.14 -15 x 15 µm (290 eV, pixel size = 50 nm) STXM image of nitrided electrodeposited lithium on a nickel TEM grid.

Figure 4.15 presents the NEXAFS spectra generated from the stacks over the O K-edge, C K-edge and N K-edge for the nitrided electrodeposited lithium structure. The corresponding regions within the sample generated for each stack are also shown.

The O and C K-edge stacks demonstrate a similar spectral response to the unmodified electrodeposited lithium **(Figure 4.12)**, with a slight increase in the Li_2O signal of the O K-edge spectra. This increase could be due to a contaminant from the nitridation process, despite procedures put in place to minimise exposure to air. 4 different regions were determined from the cluster analysis of the stacked STXM images corresponding to the N K-edge NEXAFS spectra for the 2 hour nitrided electrodeposited lithium sample. The background (blue) shows no absorption. Regions 1 (red), 2 (green) and 3 (purple) represent the nitrided electrodeposited lithium deposit.

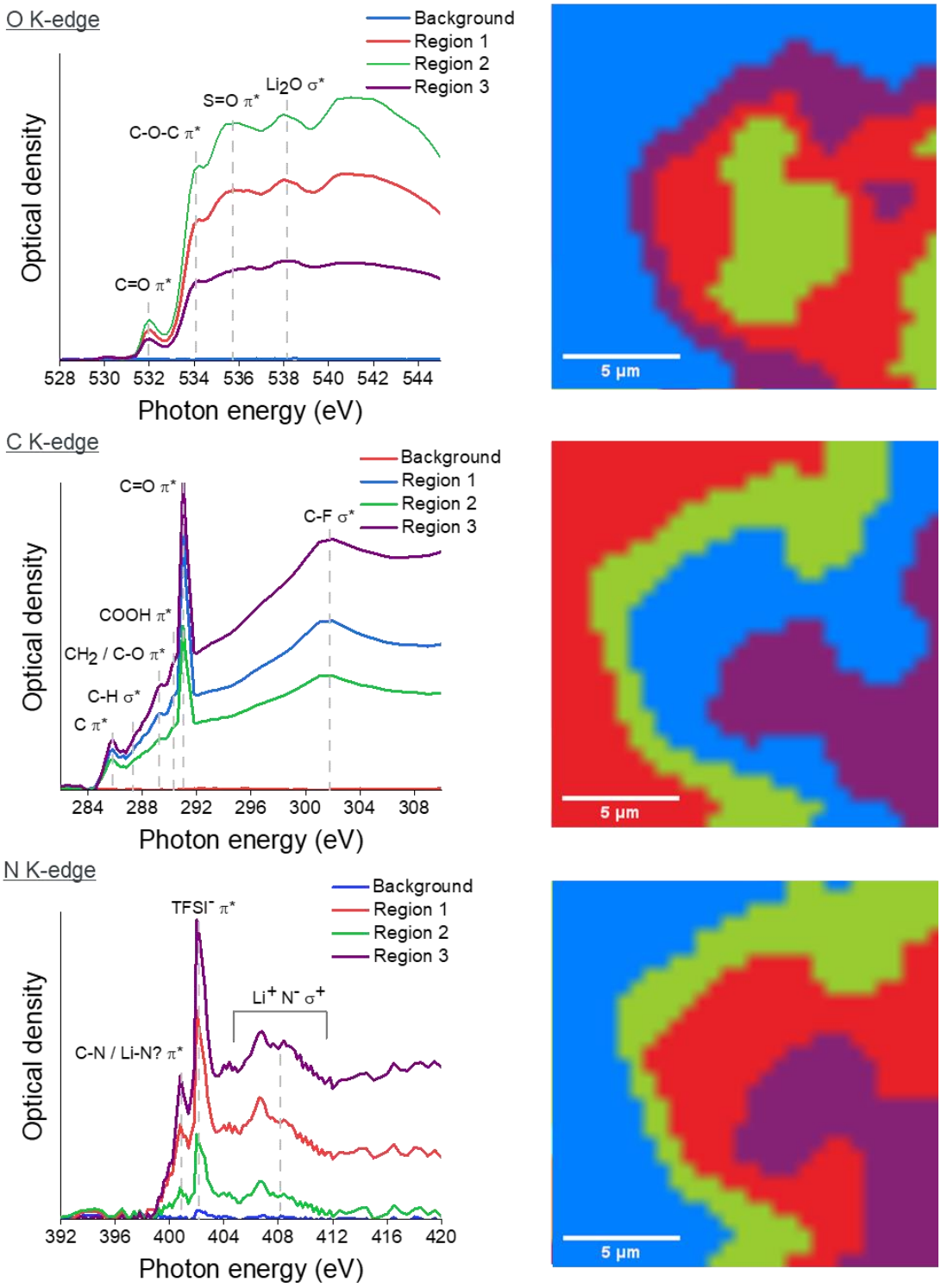

Figure 4.15 - NEXAFS spectra for the O, C and N K-edge energies and corresponding cluster map for the nitrided electrodeposited lithium structure from **Figure 4.14**.

To the best of our knowledge there has been no reported NEXAFS/XAS data collected on the N K-edge for Li_3N under ambient pressure. An additional absorption was observed at 401 eV that was not observed in the electrodeposited unmodified lithium (**Figure 4.12**) or LiTFSI salt standard (**Figure 4.13**). This absorption has been reported in XAS data for other metal nitride systems (N 1s to N-M π^*, where M = Cu,Fe,Te) as-well as C-N bonds (N 1s to N-C π^*)[382,383,384,385] It is reasonable to assume the absorption could be assigned to the Li-N species (N 1s to N-Li π^*) within the Li_3N layered structure. The structure also reveals a broad feature ~408 eV. This region is dominated by Li^+ N^- interactions as observed in the LiTFSI salt standard, however this region is more pronounced when compared to the electrodeposited unmodified lithium N K-edge region which could be the result of additional Li^+ N^- interactions from the ionic Li_3N structure.

Analysis of unmodified and nitrided electrodeposited lithium by STXM gave detailed information about the chemical environments of each sample, with a notable change in the N K-edge spectral response on nitridation of the electrodeposited lithium material. However, the surface chemistry cannot be sufficiently determined below 50 nm due to the spatial resolution limitations of STXM.

To analyse the surface of these materials, XPS was carried out on the I09 beamline at DLS to determine any additional chemical changes that are exclusive at the interface of unmodified and nitrided electrodeposited lithium electrodes. As XPS measures ejected photoelectrons from specific escape depths from the surface of materials, there is no restrictions on the thickness of the unmodified and nitrided electrodeposited lithium samples. Consequently, samples were prepared that best represent working electrodes for lithium metal batteries.

For the unmodified electrodeposited lithium electrode, lithium was electrodeposited onto a 4 mm diameter nickel disc following the same plating procedure detailed in **Section 4.2.1**, with a final plating time of 16 hours. Data acquisition and processing was carried out following the procedures described in **Section 2.9.1**.

Figure 4.16 presents the O 1s, C 1s, N 1s and Li 1s XPS spectra for the unmodified electrodeposited lithium electrode at increasing incident photon energies. The analysis and interpretation of the spectra is similar to that of battery-grade lithium foil (**Figure 4.3**). However, the assignments of peaks will differ to the battery grade lithium foil, as this sample was prepared from electrodeposited lithium and consequently new environments will form from the electrodeposition process (salt, solvent, SEI formation). Further, the pristine battery grade lithium foil contains unique environments that were specific to the extraction process of processing lithium.

Again, the Li^0 signal can be used as a reference-point to the depths each incident photon energy is probing into the SEI with respect to the electrodeposited lithium metal surface. A weak Li^0 signal is present at 6 keV (~38 nm) which suggests that the thickness of the SEI formed after lithium plating is greater than that of the native layer on the battery-grade lithium foil.

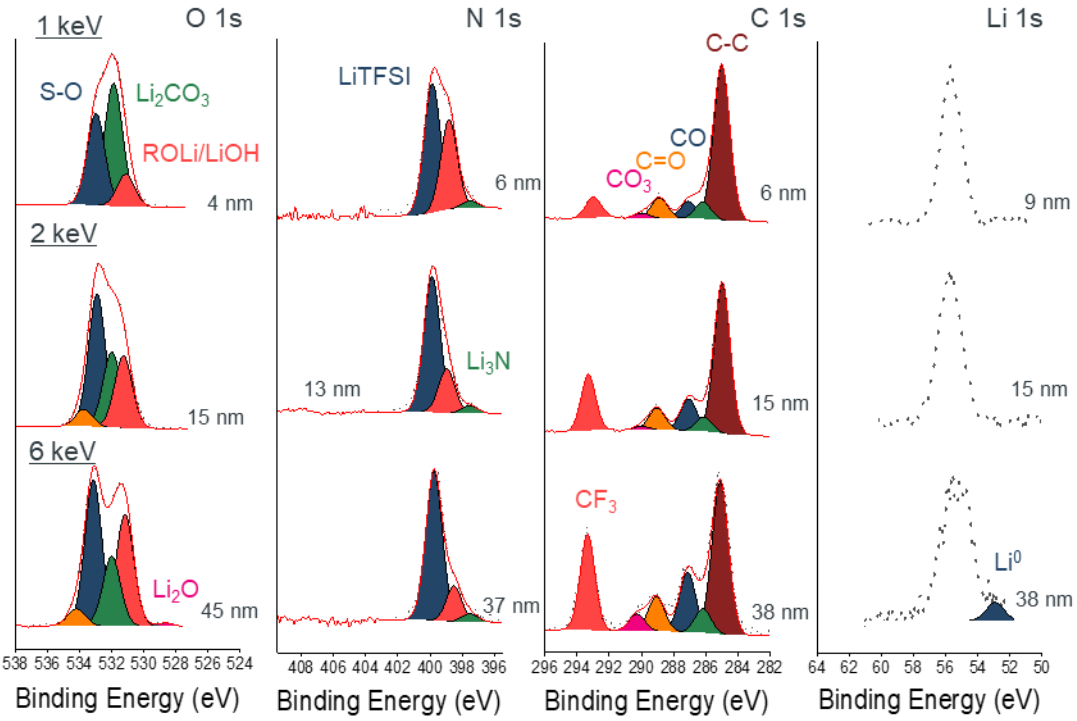

Figure 4.16 - XPS spectra for the O 1s, N 1s, C 1s and Li 1s regions of the unmodified electrodeposited lithium electrode as a function of increasing excitation energies, with the resulting probing depth calculated for each element.

Table 4.3 – Summary of XPS analysis and assignments for the surface characterisation of the unmodified electrodeposited lithium electrode.

Orbital	Binding energy (eV)	FWHM (eV)	Peak assignments
O 1s	528.3	1.2	Li_2O[325,330,331]
	530.8	1.3	ROLi/LiOH[325,332,333,386]
	531.9	1.3	Li_2CO_3[325,333,334]
	532.9	1.3	S-O / C-O[333,335,336,337,387]
	533.9	1.3	$LiTFSI_{decomp}$
N 1s	397.5	1.3	Li_3N[332,340,341,342]
	398.8	1.3	$LiTFSI_{decomp}$[340]
	399.8	1.3	LiTFSI[332,340,388,389]
C 1s	285	1.2	C-C[168,330]
	285.9	1.2	CH[155]
	286.8	1.2	C-O[155,168,351,352]
	288.3	1.2	C=O[168,330,351]
	289.4	1.2	CO_3[155,168,330,352]
	293.3	1.1	CF_3[175,350,390,391]
Li 1s	54.5	0.8	Li^0 [353,354,355,356]

At 1 keV, the O 1s spectra have a broad convoluted peak with defined shoulders that represent S-O groups from the LiTFSI salt (532.9 eV), Li_2CO_3 (531.9 eV) and an additional peak at 530.8 eV that has been assigned to LiOH and lithium alkoxides (ROLi). The presence of LiOH has been highlighted in previous characterisation studies of the SEI on lithium metal electrodes.[175,178,350,392,393] The hydroxide is attributed to reactions with water and whilst every precaution has been made during plating, storage and characterisation of the unmodified electrodeposited lithium sample, exposure to trace amounts of water in the electrolyte, glovebox and during sample transfer to the I09 beamline is still possible. However, there is no obvious absorption recorded for LiOH in the NEXAFS spectra of the O K-edge for unmodified electrodeposited lithium (**Figure 4.12**), suggesting that any contribution of lithium hydroxide to the signal at 530.8 eV is localised to the surface of the material. The signal is also likely to have a strong contribution from lithium alkoxides, especially at greater depths into the SEI which is the result of 1,3 DOL reduction on the metal electrode, as reported in previous studies of the

solvents' reaction pathway with Li.[350,394,395] The increase of the C-O signal (286.8 eV) in the C 1s spectra at 6 keV also supports the formation of ROLi species in the buried interface.

The increase of the CF_3 signal (293.3 eV) in the C 1s spectra at higher incident photon energies is attributed to the reduction products of the LiTFSI salt on contact with the metallic lithium surface. The decomposition signal is also highlighted in the N 1s spectra, as a weak signal of Li_3N which is an additional decomposition product of the imide salt.[390]

$$LiN(SO_2CF_3)_2 + ne^- + nLi^+ \rightarrow Li3N + Li_2S_2O_4 + LiF + LiCF_3 \qquad \textbf{Equation 52}$$

Figure 4.17 graphically summaries the XPS interpretation of the SEI formed during lithium plating on the unmodified electrodeposited lithium electrode.

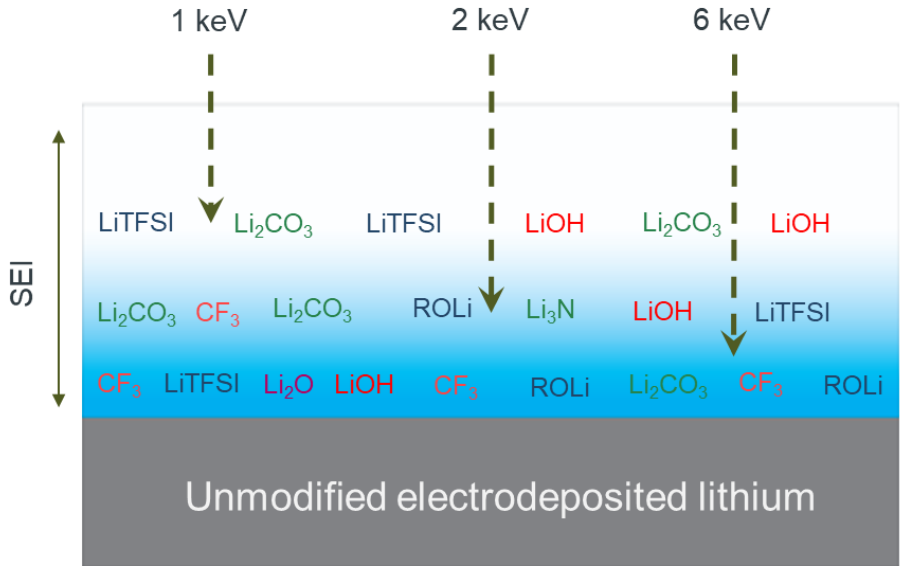

Figure 4.17 - Resulting schematic from the interpretation of XPS analysis of the unmodified electrodeposited lithium surface.

Figure 4.18 presents the O 1s, C 1s, N 1s and Li 1s XPS spectra for the nitrided electrodeposited lithium electrode at increasing incident photon energies.

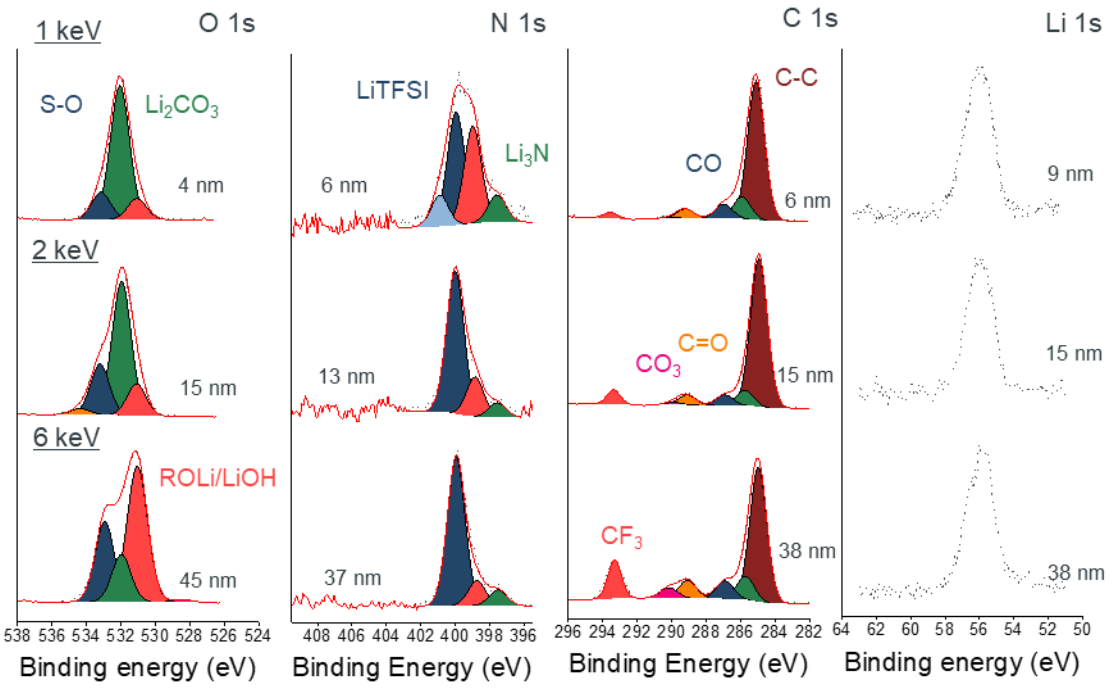

Figure 4.18 - XPS spectra for the O 1s, N 1s, C 1s and Li 1s regions of the nitrided electrodeposited lithium electrode as a function of increasing excitation energies, with the resulting probing depth calculated for each element.

There is an increase in the relative intensity of the Li_3N signal in the N 1s spectra for all three incident photon energies when compared to the unmodified electrodeposited lithium, suggesting that the nitrogen treatment has successfully formed a nitride layer on the electrodeposited lithium metal's surface. The formation of a nitride layer in addition to the SEI could explain the absence of the Li^0 signal at 6 keV, as the distance to the electrodeposited metallic lithium has increased on nitridation.

The N 1s spectra have an additional peak at 1 keV that has been previously assigned to lithium hyponitrite ($Li_2N_2O_2$). As this species is absent in the N 1s spectra of the unmodified electrodeposited lithium, it is possible that it could have formed during the nitridation process where trace amounts of oxygen/water have also reacted with the lithium surface. The species is not present at lower energies and so is confined to the outermost region of the nitrided electrodeposited lithium surface. Exposure to water

during the nitridation process could also explain the increase in the relative intensity of the LiOH/ROLi peak at 6 keV.

Figure 4.19 graphically summaries the XPS interpretation of the SEI/Li_3N layer for the surface of the nitrided electrodeposited lithium electrode.

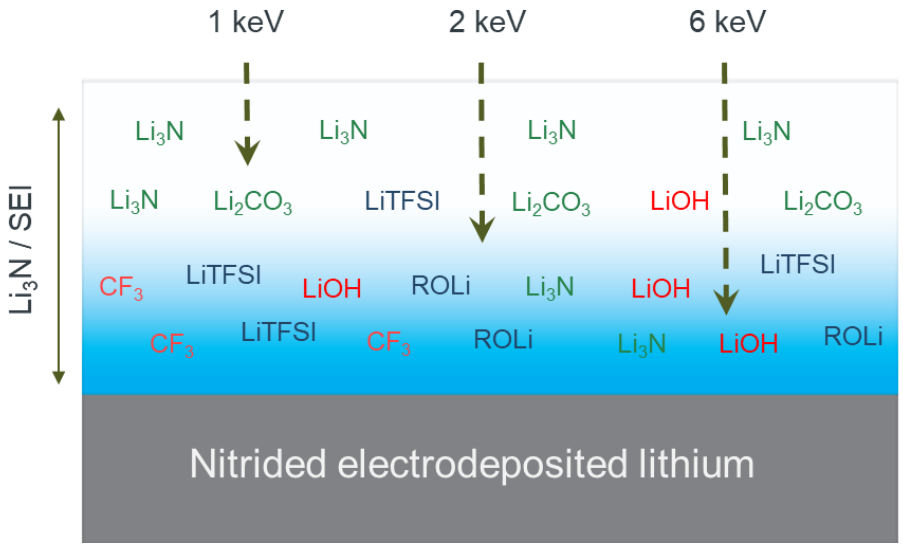

Figure 4.19 - Resulting schematic from the interpretation of XPS analysis of the nitrided electrodeposited lithium surface.

4.3.2 Electrochemistry of lithium nitride as a protective layer for lithium metal batteries

To determine whether the formed Li_3N layer affects the electrochemical performance of the lithium metal electrode, unidirectional galvanostatic polarisation and plate/strip measurements were carried out on both the unmodified and nitrided electrodeposited lithium electrodes.

4.3.2.1 Unidirectional galvanostatic polarisation of unmodified and nitrided lithium

Unidirectonal galvanostatic polarisation is an aggressive technique for assessing the failure mechanisms of lithium dendrite formation for lithium metal batteries.[396,397,398,399] Lithium is continuously stripped from one lithium metal electrode and plated onto the other at a fixed current density in symmetric cells. The benefit of testing the cells under these conditions means there is no break in the deposition (reversed during plate/strip during galvanostatic cycling). This electrochemical measurement, coupled with a high current density, produces a fast, convenient assessment of the stability of lithium metal electrodes during electrodeposition (plating).

To improve the reproducibility of the experiment, cells were constructed without a separator between the lithium metal electrodes. In the absence of a physical barrier, plated lithium/dendritic lithium growth can proceed without restriction between the two electrodes, which emphasises the electrode's plating behaviour. To promote the growth of lithium in these measurements, gaskets were produced with a 1 mm hole in the centre (**Figure 4.20**).

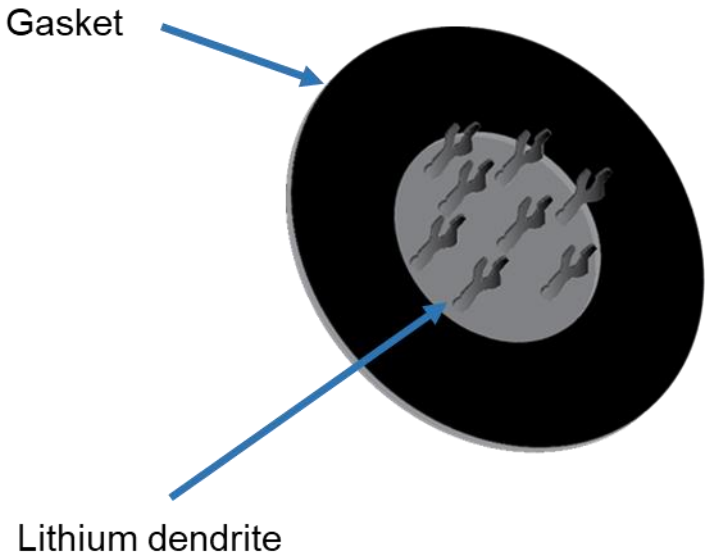

Figure 4.20 – Schematic illustration for the dendritic growth of lithium through the hole of a gasket.

By using a gasket in place of conventional cell separators, the physical barrier of the separator is removed, allowing plated lithium/dendrite growth to occur in the electrolyte filled hole, whilst still preventing the two electrodes touching. Viton rubber (fluoropolymer elastomer), Celguard 2400 and Kapton (polyimide film) were chosen as potential candidates for the gasket material. The material itself should be chemically resistant, have a greater Young's modulus to physically prevent the penetration of lithium dendrites and be elastic enough to accommodate the electrode expansion during plating. Gaskets were produced by sandwiching the individual materials between pre-cut brass plates and drilling through the centre. The resulting gaskets are presented in **Figure 4.21**.

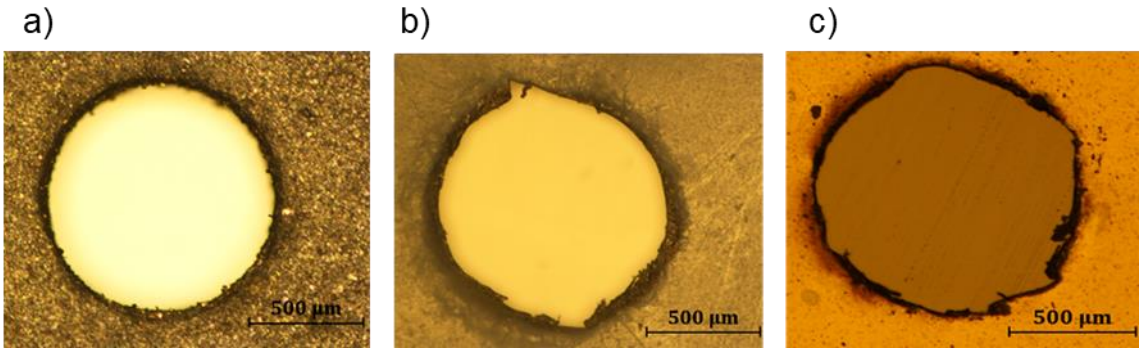

Figure 4.21 - Optical Microscopy images of the 1 mm gaskets at 100x magnification for: (**a**), Viton®. (**b**), Celgard® 2400. (**c**), Kapton®.

The images highlight deformities in the holes following drilling of the Celgard and Kapton gaskets. These materials were discarded as suitable materials as any deformities could act as favoured nucleation sites during lithium deposition. The Viton gasket was chosen for these experiments as the material produced the cleanest hole and has all the relevant chemical/physical properties.

An electrolyte solution of 1M $LiAsF_6$ in 1,3 DOL was chosen for these studies. Previous work by Aurbach et al. noted the smooth morphology of the lithium deposits formed during lithium plate/stripping which was attributed to this electrolyte solution.[400] One drawback of this electrolyte solution is the unavoidable presence of arsenic pentafluoride (AsF_5), formed from the decomposition of the $LiAsF_6$ salt.[185] AsF_5 is a Lewis acid and can readily polymerise cyclic ethers such as 1,3 dioxolane. To stabilise these electrolyte solutions, trace amounts of tributylamine (TBA) are added to the solutions as a base to neutralise the Lewis acid in solution. This stabilised electrolyte solution was employed in commercial cells by Tadiran, Ltd in the 1990's. The AA batteries were comprised of a Li_xMnO_2 cathode and a lithium metal negative electrode. The battery displayed a good cycle life (300 cycles at 100% depth of discharge, (DOD) with an energy density > 140 Wh kg^{-1}).[401] However the slow charging rates (0.5 mA cm^{-2}) required to achieve the full DOD over 100's of discharge cycles meant the cells could not compete in performance with the introduction of lithium-ion batteries.

For this work, 100 ppm of TBA was added to the 1M $LiAsF_6$/1,3-DOL electrolyte solution, as the tertiary amine should not interact with the lithium surface chemistry at this concentration.[185] Cell setup and unidirectional galvanostatic polarisation measurements were carried out following the procedure described in **Section 4.2.3**. The unmodified electrodeposited lithium working electrodes were prepared by electrodepositing lithium onto nickel foil as described in **Section 4.3.1**. These were compared with the nitrided electrodeposited lithium working electrodes (2 hours nitridation at 90 °C).

Figure 4.22 presents the evolution of voltage plots with time during unidirectional galvanostatic polarisation of unmodified and nitrided electrodeposited lithium working electrodes. Eight measurements were recorded for both unmodified and nitrided

electrodeposited electrodes at a fixed current density of 5 mA cm^{-2}. 1 M $LiAsF_6$/1,3-DOL electrolyte solution stabilised with 100 ppm of tributyl-amine (TBA) filled the 1 mm Viton gasket between the working electrode and battery-grade lithium foil counter-electrode.

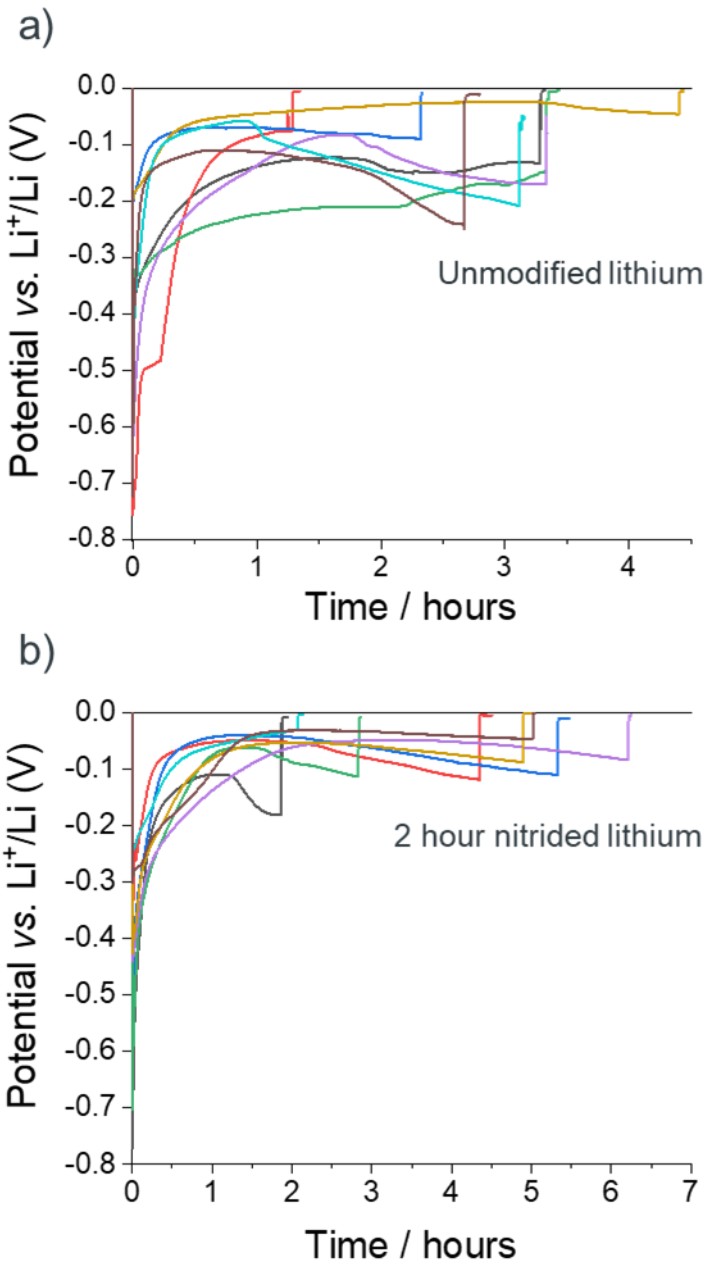

Figure 4.22 - Voltage vs. time plots for the unidirectional galvanostatic polarisation of: (**a**), unmodified electrodeposited lithium working electrodes and (**b**), nitrided electrodeposited lithium working electrodes at a fixed current density of 5 mA cm^{-2}.

Time to short circuit of the unmodified electrodeposited lithium electrodes varied from 1.3 to 4.4 h with a mean and standard error short-circuit time of 2.9 ± 0.9 h (**Figure 4.22**). Variations in the voltage profiles suggest there are differences with how the electrodeposition of Li proceeds between the unmodified electrodeposited lithium electrodes.

The mean time to short circuit with standard error increased to 4.0 ± 1.6 h for the nitrided electrodeposited lithium electrodes, suggesting that the nitride layer facilitated the even electrodeposition of lithium onto the electrode surface before a short circuit occurred. The voltage plots generally followed a similar profile, with flatter plating plateaus which could result from even electrodeposition of lithium over the Li_3N layer. However, there was greater variation within the times recorded for short circuit of nitrided electrodeposited lithium electrodes (**Figure 4.23**).

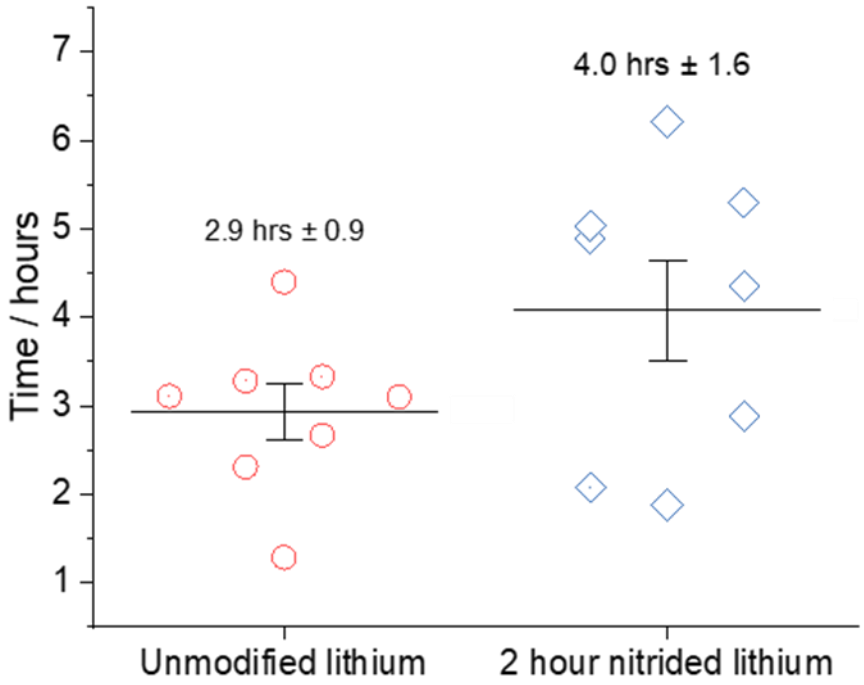

Figure 4.23 – Scatter plot with standard error for the short-circuit times during unidirectional galvanostatic polarisation of unmodified electrodeposited and nitrided electrodeposited lithium electrodes.

Galvanostatic cycling of unmodified and nitrided lithium

Unmodified and nitrided electrodeposited lithium electrodes were also investigated by galvanostatic cycling in two-electrode symmetric cells. The lithium plating/stripping processes over charge/discharge intervals were performed at a fixed current density (2 mA cm^{-2}). The conditions were chosen to "mimic" the operation of working lithium metal electrodes in LMBs. Electrochemical impedance spectroscopy was performed before and after plate/strip cycles to monitor the development of cell resistance and comment on the status of the electrode's interface.

The cell setup, galvanostatic plate/strip and PEIS measurements were carried out following the procedures described in **Section 4.2.3**. The voltage profile of the unmodified electrodeposited lithium metal working electrode during constant current plating and stripping in a Li||Li symmetric cell (cell 1) is presented in **Figure 4.24**.

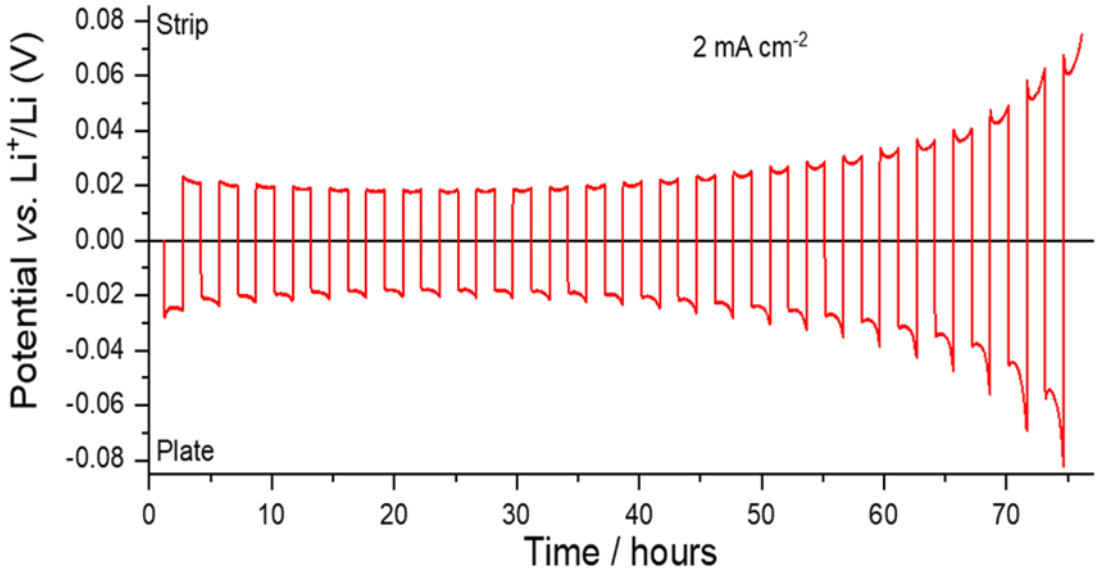

Figure 4.24 - Voltage vs. time profiles for the plating/stripping processes of unmodified electrodeposited lithium at a current density of 2 mA cm^{-2}. Measurements were collected in a Li||Li symmetric cell containing 1 M $LiAsF_6$ in 1,3-DOL electrolyte (cell 1).

The average polarisation increased in the voltage profile for both the plating and stripping processes over 25 cycles. The overpotential is determined by kinetic hindrances in the cell. In lithium plating and stripping processes, this may include concentration

limited mass transport of lithium ions in the electrolyte and at the solid electrolyte interphase; evolving morphology of the lithium metal surface during operation and the kinetic hindrance of the lithium ion reduction (plating) and oxidation (stripping) reactions at the electrode surface itself (charge-transfer resistance).[402,403,404,405] The sum of these processes may affect the overall cell resistance which can be identified by electrochemical impedance spectroscopy.

Interpreting impedance spectra for electrode materials is complex, there are many considerations that have to be made for lithium electrodes due to the dynamic nature of the plating/stripping processes and the evolution of the lithium surface. However, qualitative analysis of EIS can still provide meaningful insights into the cell behaviour. **Figure 4.25** presents the corresponding Nyquist plots of the impedance spectra for the unmodified electrodeposited Li||Li symmetric cell (cell 1) on assembly and after 25 cycles.

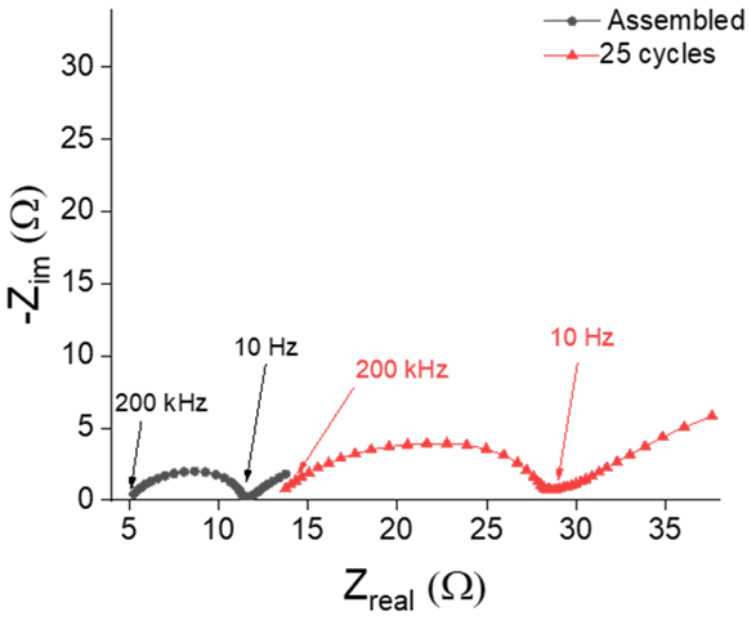

Figure 4.25 - Nyquist plots of the impedance spectra for the unmodified electrodeposited Li||Li symmetric cell containing 1M $LiAsF_6$ in 1,3-DOL as the electrolyte on assembly and after 25 plating/stripping cycles at 2 mA cm^{-2} (cell 1).

Impedance spectra presented as Nyquist plots start with the ohmic resistance at higher frequencies (200 kHz), which is determined by the ionic conductivity of the electrolyte ($R_{electrolyte}$), the following semi-circle visually contains information about

the interfacial resistance and the charge/transfer resistance at the electrode-electrolyte interphase ($R_{surface}$).[403,406,407,408]

After 25 cycles there was an increase in the solution resistance and the charge-transfer/interfacial resistance at the electrode-electrolyte interface in the unmodified electrodeposited Li||Li symmetric cell (cell 1). During the initial cycles there is the formation of a compact solid electrolyte interphase on the metal electrode surface along with the deposition/dissolution of mossy lithium. After multiple cycles, the lithium electrode surface is subjected to large volumetric changes which can dramatically affect the Li-ion mobility across the interface. Firstly, the thickness of the SEI layer can be increased as volume changes form stresses and cracks in the layer which can allow for further electrolyte decomposition (**Figure 4.26**).[169,405,409,410,411]

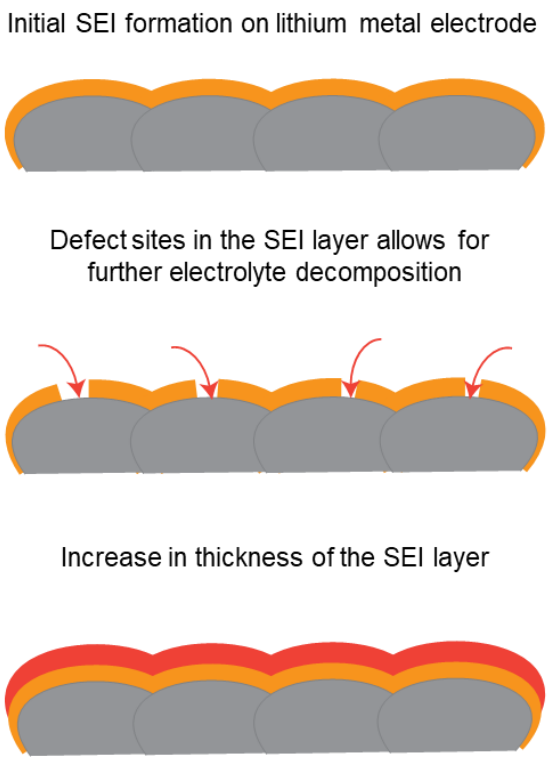

Figure 4.26 – Schematic illustration for the formation of a thick SEI layer on lithium metal electrodes.

Secondly, mossy lithium can mechanically detach from the bulk lithium surface and become electrically isolated.[402,404,412,413] A layer of inactive "dead lithium" can form on the surface of the electrode which greatly impedes Li-ion diffusion to the electrochemically active lithium metal surface (**Figure 4.27**).

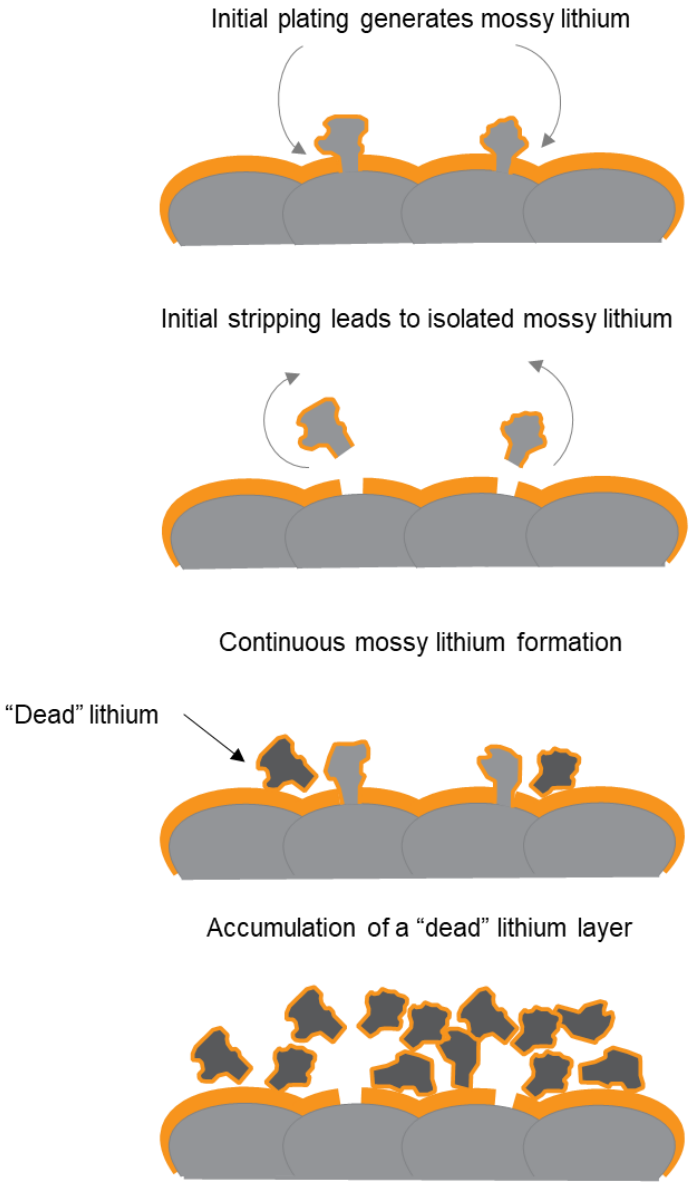

Figure 4.27 – Schematic illustration for the formation of a "dead" lithium layer over multiple cycles. Adapted from reference.[402]

The extent of these unwanted surface processes could explain the increase in the interfacial/charge-transfer resistance from the impedance spectra of the unmodified electrodeposited Li||Li symmetric cell (**Figure 4.25**), whilst also providing an explanation for the increase in the polarisation of the plating/stripping processes observed during galvanostatic cycling (**Figure 4.24**).

Figure 4.28 presents the voltage profile for a repeat unmodified electrodeposited lithium cell (cell 2), during constant current plating and stripping in an unmodified electrodeposited Li||Li symmetric cell.

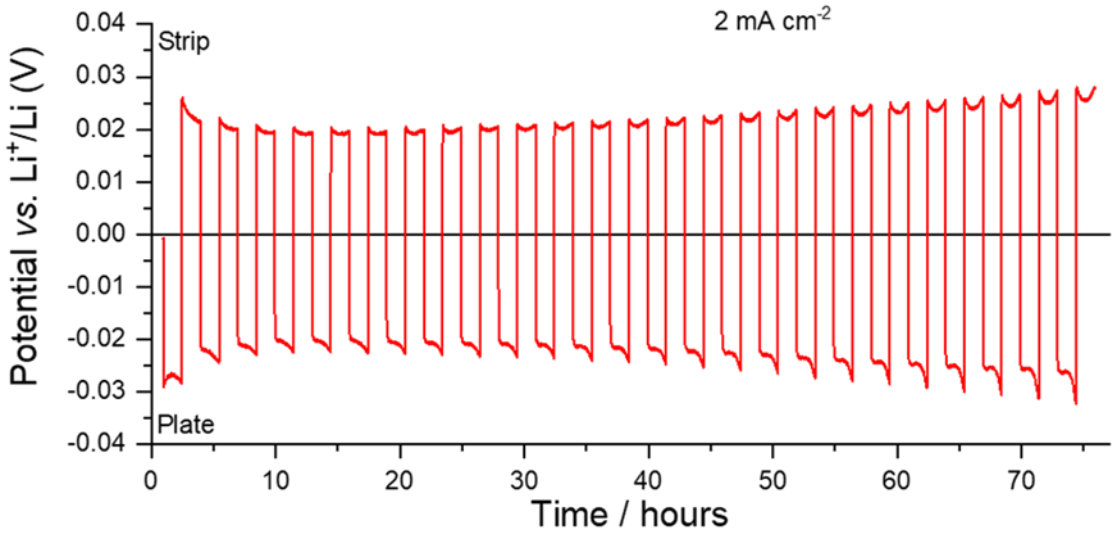

Figure 4.28 - Voltage vs. time profiles for the plating/stripping processes of unmodified electrodeposited lithium at a current density of 2 mA cm^{-2}. Measurements were collected in a Li||Li symmetric cell containing 1M $LiAsF_6$ in 1,3-DOL electrolyte (cell 2).

The overall polarisation remains constant over the 25 plating/stripping cycles, suggesting more uniform deposition and dissolution of the lithium has taken place when compared to cell 1. There is an increase in the semicircle representing the interfacial/charge-transfer resistance when comparing the Nyquist plots of the impedance spectra for cell 2 (**Figure 4.29**), however in comparison to cell 1 this is minimal. The difference in the plating/stripping behaviours of two identical cells represents the uncertainty of cycling unmodified electrodeposited lithium electrodes. Slight variations to the surface or plating/stripping behaviours can have an adverse effect on the overall cell performance.

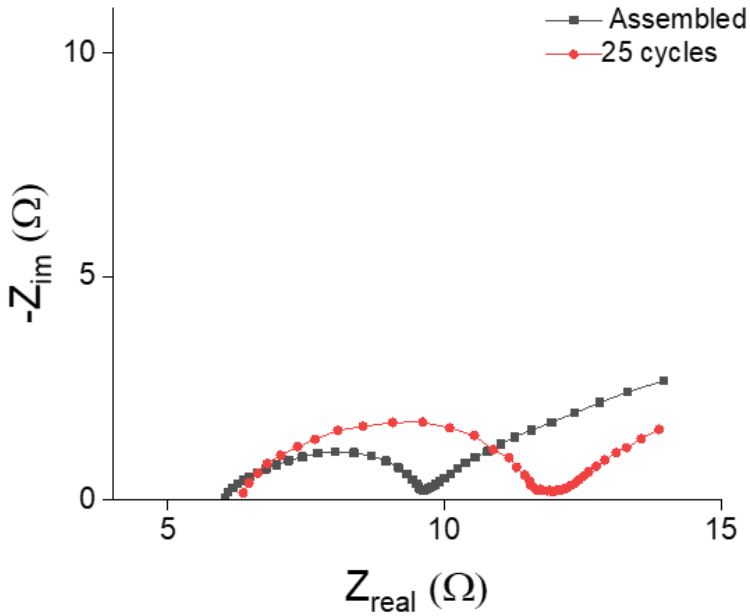

Figure 4.29 - Nyquist plots of the impedance spectra for the unmodified electrodeposited Li||Li symmetric cell containing 1M $LiAsF_6$ in 1,3-DOL as the electrolyte on assembly and after 25 plating/stripping cycles at 2 mA cm^{-2} (cell 2).

Figure 4.30 presents the voltage profile for another repeat unmodified electrodeposited lithium cell (cell 3) during constant current plating and stripping in a Li||Li symmetric cell. There was a significant increase in the cell polarisation after the 20th cycle indicating cell failure has occurred.[392,401]

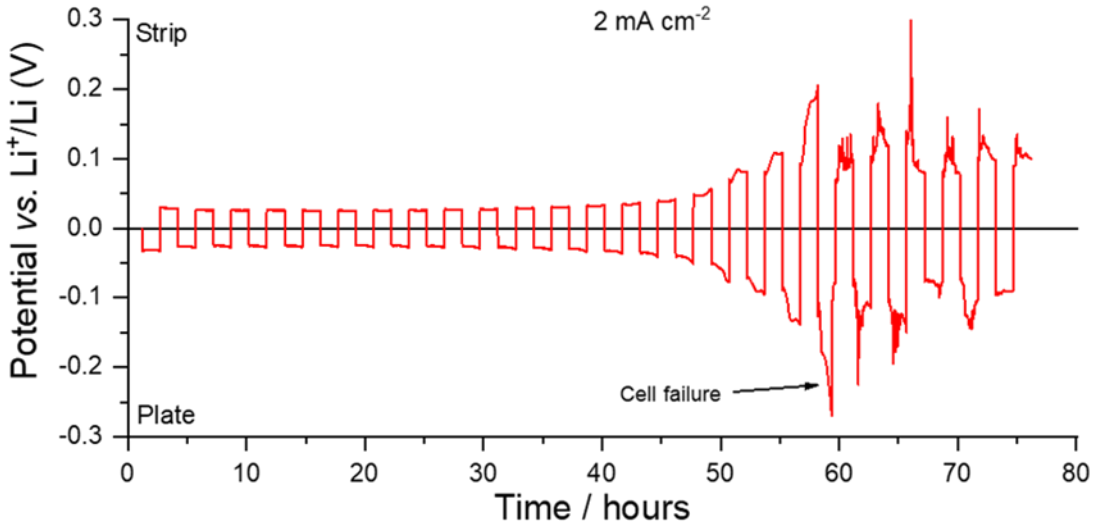

Figure 4.30 - Voltage vs. time profiles for the plating/stripping processes of unmodified electrodeposited lithium at a current density of 2 mA cm^{-2}. Measurements were collected in a Li||Li symmetric cell containing 1M $LiAsF_6$ in 1,3-DOL electrolyte (cell 3).

The corresponding Nyquist plots for the impedance spectra of cell 3 (**Figure 4.31**) after 25 cycles suggest there has been a severe change to the lithium surface as evidenced by the absence of a distinguished semicircle.

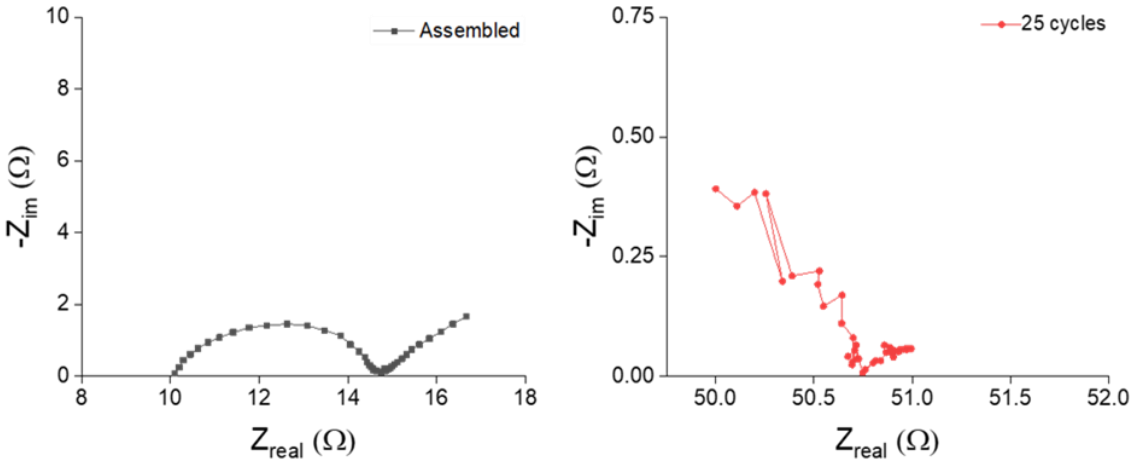

Figure 4.31 - Nyquist plots of the impedance spectra for the unmodified electrodeposited Li||Li symmetric cell containing 1M $LiAsF_6$ in 1,3-DOL as the electrolyte on assembly (left) and after 25 plating/stripping cycles (right) at 2 mA cm^{-2} (cell 3).

Possible explanations for this drastic change in cell behaviour include; the unfavourable plating/stripping of lithium could have contributed to irreversible pulverisation of the lithium electrode; accumulation of a substantially thick layer of "dead" lithium that dramatically affects Li-ion transport and continuous SEI breakdown/reformation which will greatly impede the Li-ion diffusion across the electrode-electrolyte interphase.

Galvanostatic cycling of the unmodified electrodeposited lithium in Li||Li symmetric cells displayed large variations in the plating/stripping behaviors of the electrode. To determine if the nitride layer of nitrided (2 hours at 90 °C) electrodeposited lithium can facilitate the plating/stripping of lithium, galvanostatic cycling was repeated for nitrided electrodeposited lithium Li_3N-Li||Li_3N-Li symmetric cells under the same electrochemical conditions as the unmodified electrodeposited lithium.

The voltage profile of the nitrided electrodeposited lithium metal working electrode during constant current plating and stripping in a Li_3N-Li||Li_3N-Li symmetric cell (cell 4) is presented in **Figure 4.32**.

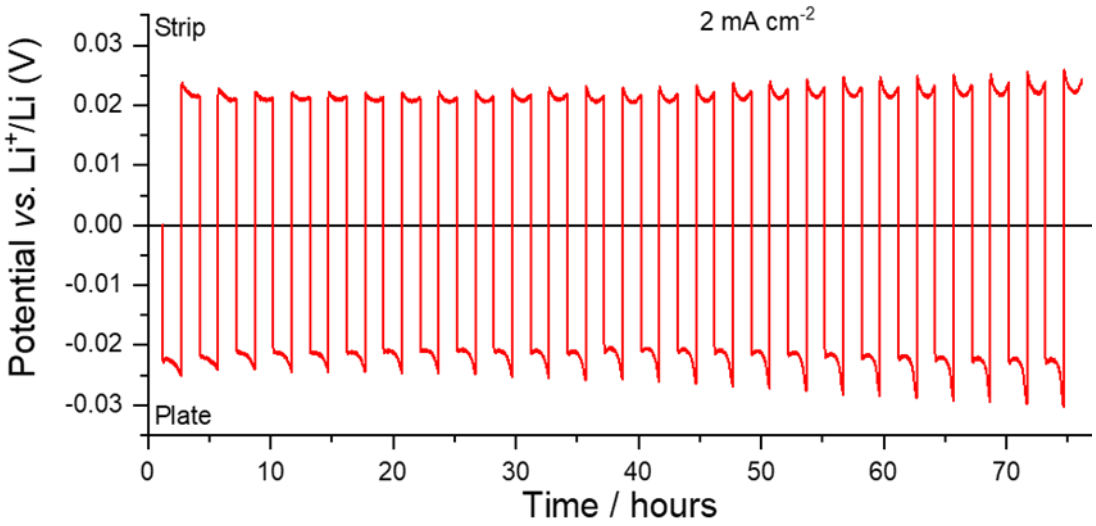

Figure 4.32 - Voltage vs. time profiles for the plating/stripping processes of nitrided electrodeposited lithium at a current density of 2 mA cm^{-2}. Measurements were collected in a Li_3N-Li||Li_3N-Li symmetric cell containing 1M $LiAsF_6$ in 1,3-DOL electrolyte (cell 4).

The average polarisation remains relatively constant in the voltage profile for both the plating and stripping processes over 25 cycles, indicating that the plating/stripping processes at the nitrided electrodeposited lithium surface were consistent throughout cycling. To determine whether any significant change to the interfacial /charge-transfer resistance has occurred to the nitrided lithium electrode, impedance spectra was collected before and after 25 plating/stripping cycles.

Figure 4.33 presents the corresponding Nyquist plots for the impedance spectra of the nitrided electrodeposited Li_3N-Li||Li_3N-Li symmetric cell (cell 4) on assembly and after 25 cycles.

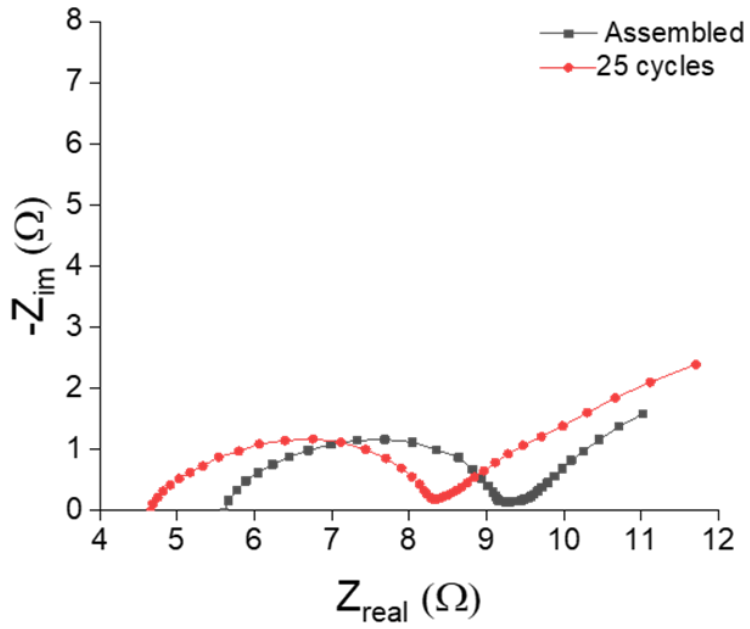

Figure 4.33 - Nyquist plots of the impedance spectra for the nitrided electrodeposited Li_3N-Li||Li_3N-Li symmetric cell containing 1M $LiAsF_6$ in 1,3-DOL as the electrolyte on assembly and after 25 plating/stripping cycles at 2 mA cm^{-2} (cell 4).

The size of the semicircle which corresponds to the interfacial/charge-transfer resistance remains the same when comparing the Nyquist plots of the impedance spectra on the assembled cell and after 25 cycles. This suggests that the interfacial chemistry and morphology has remained relatively constant though-out the plate/strip cycles. This stability could well be attributed to the nitride layer facilitating lithium deposition/stripping on the metal surface.

Figure 4.34 presents the voltage profile for a repeat nitrided lithium cell (cell 5) during constant current plating and stripping in a Li-Li_3N||Li-Li_3N symmetric cell. There was a slight increase in the cell polarisation over the 25 cycles.

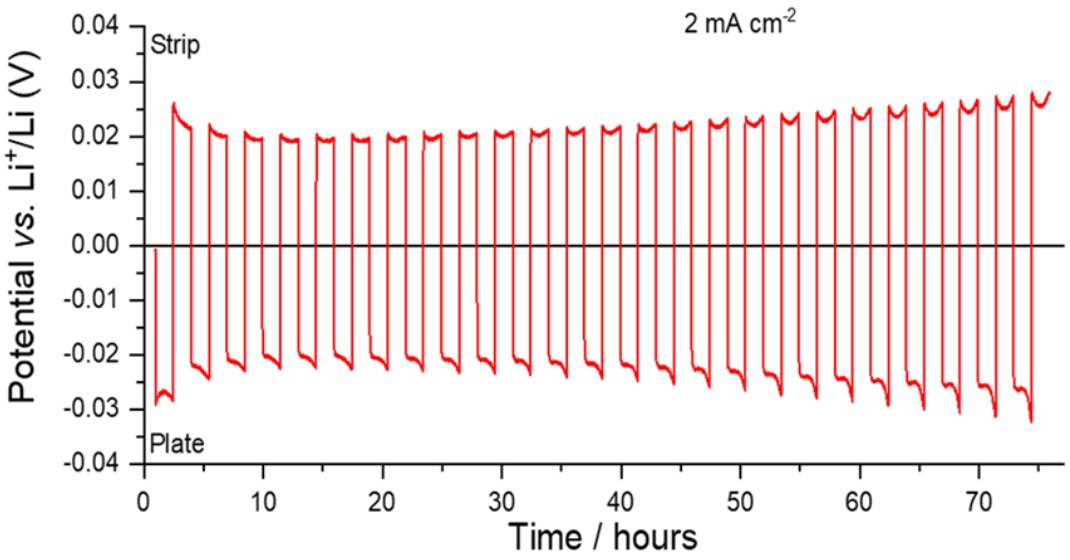

Figure 4.34 - Voltage vs. time profiles for the plating/stripping processes of nitrided electrodeposited lithium at a current density of 2 mA cm^{-2}. Measurements were collected in a Li_3N-Li||Li_3N-Li symmetric cell containing 1M LiAsF6 in 1,3-DOL electrolyte (cell 5).

The corresponding Nyquist plots for the impedance spectra of cell 5 (**Figure 4.35**) after 25 cycles suggests there has been a slight change to the lithium surface due to the small increase in size of the semicircle that represents the charge-transfer/interfacial resistance.

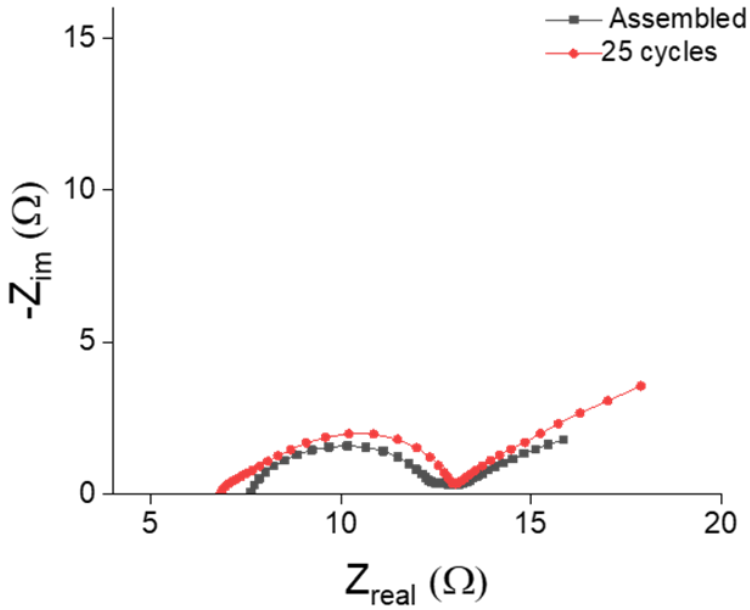

Figure 4.35 - Nyquist plots of the impedance spectra for the nitrided electrodeposited Li_3N-Li||Li_3N-Li symmetric cell containing 1M LiAsF6 in 1,3-DOL as the electrolyte on assembly and after 25 plating/stripping cycles at 2 mA cm^{-2} (cell 5).

Figure 4.36 presents the voltage profile for a repeat nitrided electrodeposited lithium cell (cell 6) during constant current plating and stripping in a Li-Li_3N||Li-Li_3N symmetric cell.

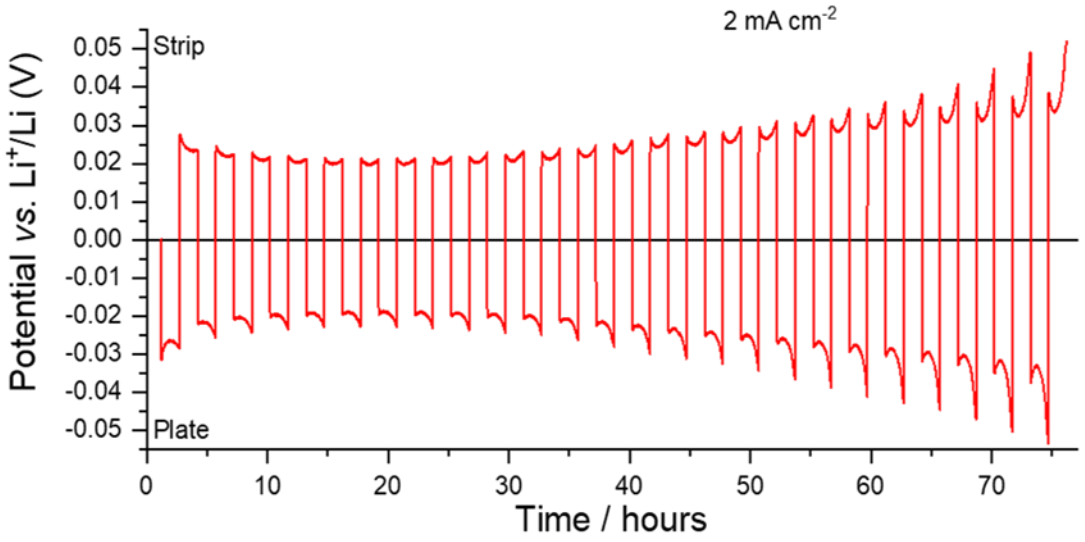

Figure 4.36 - Voltage vs. time profiles for the plating/stripping processes of nitrided lithium at a current density of 2 mA cm^{-2}. Measurements were collected in a Li_3N-Li||Li_3N-Li symmetric cell containing 1M LiAsF6 in 1,3-DOL electrolyte (cell 6).

The average polarisation increased in the voltage profile for both the plating and stripping processes over 25 cycles when compared to the previous 2 nitrided lithium cells (cells 4 and 5). Whilst no short circuit was recorded over the 25 cycles, the stability of the cell is still likely to be impacted. The corresponding Nyquist plots for cell 6 (**Figure 4.37**) confirm an increase in the interfacial / charge-transfer resistance has occurred after 25 cycles.

`

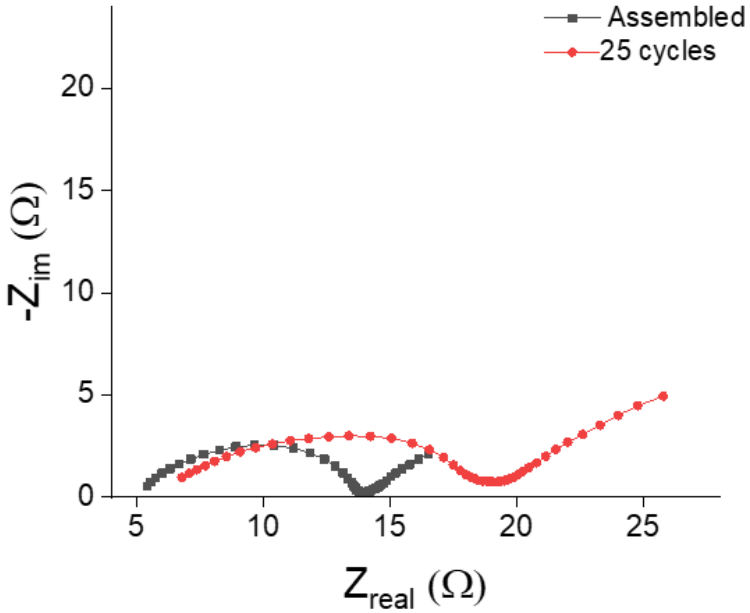

Figure 4.37 - Nyquist plots of the impedance spectra for the nitrided electrodeposited Li_3N-Li||Li_3N-Li symmetric cell containing 1M LiAsF6 in 1,3-DOL as the electrolyte on assembly and after 25 plating/stripping cycles at 2 mA cm^{-2} (cell 6).

4.4 Conclusions

A reproducible method for electrodepositing lithium onto current collectors has been developed for nitridation studies. The use of a highly concentrated electrolyte solution (4 M LiTFSI in 1,3 DOL) resulted in the even electrodeposition of smooth lithium metal deposits (**Figure 4.7**). The unmodified electrodeposited lithium can also be considered as representing lithium electrodes that have been plated and stripped, as the morphology and chemical environment will evolve from uniform to electrodeposited lithium.

Electrodeposited lithium electrodes were successfully nitrided using a modified Schlenk-line that minimised exposure to air and moisture.

Characterisation of the unmodified and nitrided electrodeposited lithium electrodes was carried out by scanning transmission X-ray microscopy and X-ray photoelectron spectroscopy, utilising synchrotron radiation from the Diamond Light source facility. STXM of the O, C and N K-edge revealed the presence of typical electrolyte decomposition species on the unmodified electrodeposited lithium as part of an SEI which had formed from the electrodeposition process (**Figure 4.12**). A unique absorption was recorded for the N K-edge of the nitrided lithium structure, which was assigned to the formation of lithium nitride on the lithium metal (**Figure 4.15**).

Analysis of unmodified and nitrided electrodeposited lithium structures by STXM gave detailed information about the chemical environments of each sample, with a notable change in the N K-edge spectral response on nitridation of the electrodeposited lithium material. However, the surface chemistry cannot be sufficiently determined below 50 nm due to the spatial resolution limitations of STXM.

To analyse the surface of these materials, XPS was carried out on the I09 beamline at DLS to determine any additional chemical changes that are exclusive at the interface of unmodified and nitrided electrodeposited lithium electrodes. XPS of the N 1s revealed a stronger signal for Li_3N in the nitrided lithium compared to the unmodified electrodeposited lithium electrode. The Li^0 signal was not recorded at 6 keV in the Li 1s XPS spectra of the nitrided electrodeposited lithium which could suggest that the formed lithium nitride layer is substantial and has contributed to the thickness of the surface layer.

Unidirectional galvanostatic polarisation measurements showed an increased time to short circuit during constant plating on nitrided electrodeposited lithium electrodes (2.9 ± 0.9 h for unmodified electrodeposited and 4.0 ± 1.6 h for nitrided electrodeposited lithium electrodes, **Figure 4.23**), suggesting that the nitride layer facilitated the even electrodeposition of lithium onto the electrode surface before a short circuit occurred. However, there was greater variation within the times recorded for short circuit of nitrided electrodeposited lithium electrodes.

Galvanostatic cyling (plate/strip) of unmodified and nitrided electrodeposited lithium electrodes was also explored. In general, the voltage profiles of the nitrided electrodeposited lithium electrodes demonstrated stable cycling, with one cell recording an increase in the polarisation of the plating/stripping processes. The plating of unmodified electrodeposited lithium electrodes varied greatly between repeat measurements with one cell demonstrating serious cell failure (**Figure 4.30**). Qualitative interpretation of the EIS spectra also showed greater changes in the electrode-electrolyte features of the unmodified electrodeposited lithium electrodes before and after cycling compared to the EIS recorded on the nitrided electrodeposited lithium electrodes.

.

Chapter 5 Evaluation of lithum nitride as a protective layer for lithium-sulfur batteries

5.1 Introduction

In addition to the issues of low Coulombic efficiency and dendritic growth, lithium metal negative electrodes encounter further challenges in lithium-sulfur cells through the corrosive reactions of polysulfides on the surface of the metal electrode. In Li-S batteries, polysulfide species, formed at the sulfur electrode, can diffuse through the porous separator towards the lithium metal negative electrode where they can be reduced to Li_2S or soluble shorter-chain polysulfides via a chemical reaction that consumes lithium active material:[414]

$$Li_2S_n + 2Li \rightarrow Li_2S_{n-1} + Li_2S \qquad \textbf{Equation 53}$$

Figure 5.1 graphically illustrates the chemical reactions of polysulfides with lithium metal.

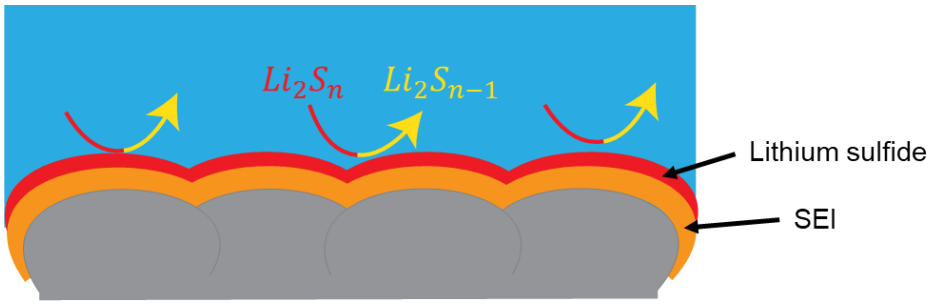

Figure 5.1 - Schematic of the chemical reactions between polsyulfides and the lithium metal electrode.

The development of effective lithium protection approaches to suppress the reaction of polysulfides with lithium metal is crucial to improve the performance of Li-S batteries. Lithium nitride has been reported as a protective coating for the lithium metal electrode in Li-S applications.

Armand et al. assessed an in situ method for forming the Li_3N on the lithium metal surface for Li-S batteries.[364] Azido-trimethyl silane [$(CH_3)_3SiN_3$] was used as an electrolyte additive which was expected to decompose to Li_3N on contact with the Li metal electrode. They noted an increase in discharge capacity when increasing the concentration of the azide additive from 0.01 to 0.1 M. After 20 cycles there was a decrease in capacity which was comparable to cells cycled without the additive. This behaviour was ascribed to the non-uniform deposition of Li_3N from the in-situ approach. Ma et al. reported the performance of a Li_3N protective layer in Li-S cells using a conventional method of flowing N_2 gas over lithium foil for 2 hours.[415] The resulting Li_3N layer was 200-300 nm thick. AC impedance measurements suggested that the protected lithium metal electrode showed greater stability towards the Li-S electrolyte (1 M LiTFSI in 1,3 DOL:DME (1:1)) when compared to the as-received lithium foil which was attributed to the reduced reactivity of Li_3N. There was a noticeable improvement in the cyclability of Li_3N protected lithium metal electrodes in Li-S cells. A discharge capacity of 956 mA h g^{-1} was passed after 200 cycles at 0.2 C with a Coulombic efficiency of 79.7%. In comparison the unmodified lithium electrode passed 452 mA h g^{-1} after 200 cycles with a capacity retention of 37.2%. It was determined that a Li_3N protective layer of ~ 100 nm can minimise the reduction of polysulfides and consumption of active lithium metal material (**Figure 5.2**).

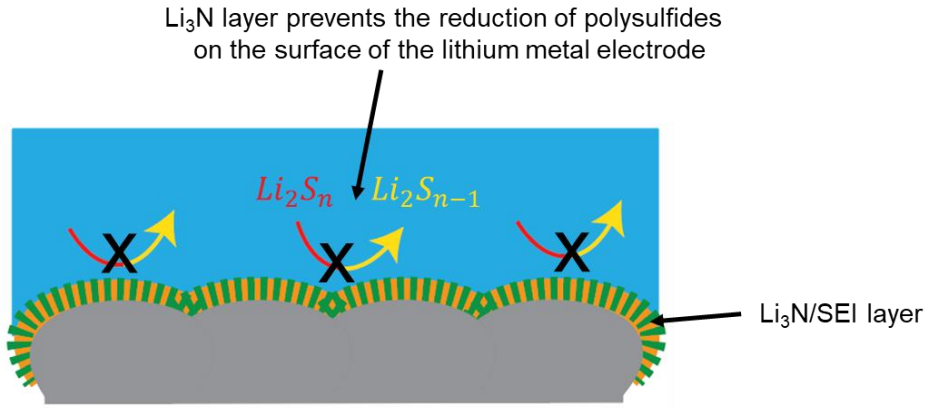

Figure 5.2 – Schematic illustration of lithium nitride protecting the lithium metal electrode from reactions with polysulfides.

Chapter 4 demonstrated a method for producing well-ordered Li_3N layers by flowing high purity nitrogen at an elevated temperature over a reactive electrodeposited lithium metal electrode. The nitrided electrodeposited lithium demonstrated reasonable plating/stripping behaviour as a secondary electrode. This chapter assesses the nitrided electrodeposited lithium electrodes reported in **Chapter 4** as a protective layer against polysulfide-containing solutions. The stability of the Li_3N layers was determined by STXM and XPS.

5.2 Experimental

5.2.1 Preparation of lithium polysulfide electrolyte solutions

The preparation of lithium polysulfide electrolyte blends follows a procedure previously reported within the group.[416] In an argon-filled glovebox, lithium sulfide (99.98%, Sigma-Aldrich) and sulfur (S_8, 100 mesh, sublimed, Sigma-Aldrich, dried at r.t under vacuum over 72 h) were added into a vial in ratios to give the desired Li_2S_n composition based on **Equation 54**, followed by adding the electrolyte solution (1 M LiTFSI in 1,3 DOL:DME (1:1 by vol.) or 1 M LiTFSI in 1,3 DOL:DME (1:1 by vol.) with 2% $LiNO_3$). The solution was allowed to stir at 60 °C for 10 days to ensure full dissolution. After 10 days of stirring, a clear ruby-red polysulfide solution is obtained with an average chain length of Li_2S_6.

$$Li_2S + \left(\frac{n-1}{8}\right) S_8 \rightarrow Li_2S_n \qquad \textbf{Equation 54}$$

Preparation of Li_2S_n where the average chain length n can be varied.

5.3 Results and discussion

5.3.1 Stability of unmodified and nitrided lithium towards polysulfide-containing electrolyte solutions

To understand any improvements in behaviour of the Li_3N protected electrodeposited lithium electrode within a Li-S cell, it is necessary to understand the stability of the nitride layer towards polysulfide species formed on cycling. Our research group has developed a method for determining solution composition and solid formation in sulfur-Li_2S-electrolyte systems.[417] From this work, solutions with known polysulfide composition can be analysed. For the purpose of these experiments a polysulfide solution containing Li_2S_6 was prepared in a common Li-S electrolyte solution (1 M LiTFSI in 1,3 DOl:DME (1:1 by vol.).

To determine the stability of unmodified electrodeposited lithium towards the 1 M Li_2S_6, 1 M LiTFSI 1,3 DOL: DME (1:1 by vol.), polysulfide solution was assessed via in situ optical imaging. Unmodified electrodeposited lithium structures were electrodeposited onto a nickel TEM grid under the same conditions as described in **Chapter 4**. Optical images were recorded following the procedure described in **Section 2.3**, where a lithiated TEM grid is placed into a glass cell and covered with 20 µL of the 1 M LiTFSI, Li_2S_6 polysulfide-electrolyte solution before sealing with a glass slide. The glass cell is transferred to the microscope stage and a series of dark-field optical microscopy images are acquired with 15 minute intervals **(Figure 5.3**).

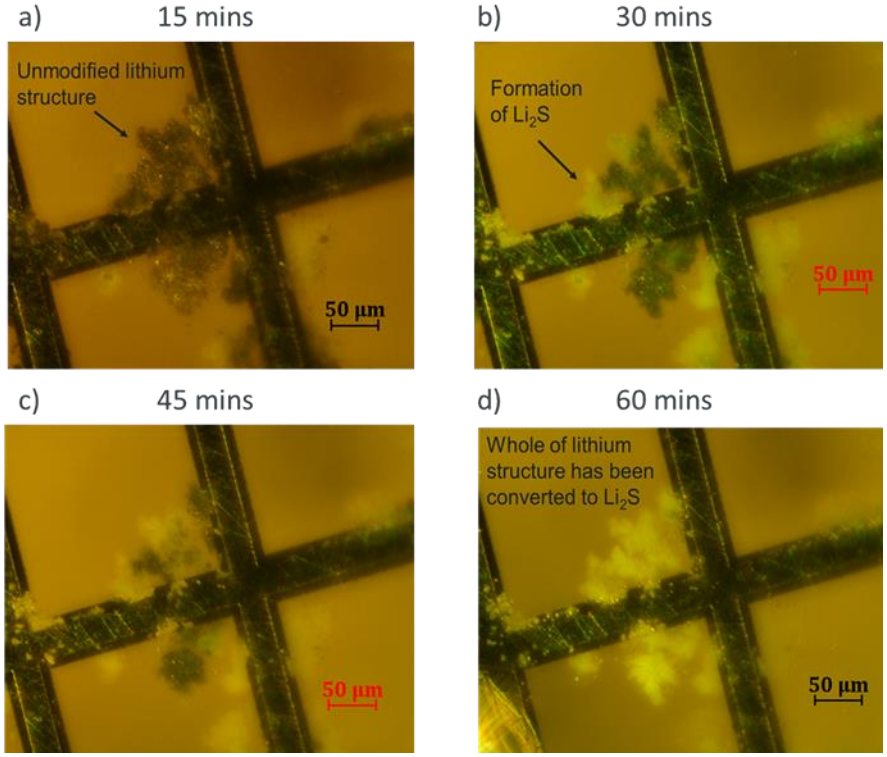

Figure 5.3 - Series of dark-field optical microscope images of a unmodified electrodeposited lithium structure exposed to 1 M Li_2S_6 in 1M LiTFSI 1,3 DOL:DME polysulfide solution at increasing times of exposure.

Figure 5.3 (**a**) presents the unmodified electrodeposited lithium structure on the nickel TEM grid after 15 minutes' exposure to the 1 M Li_2S_6, 1 M LiTFSI polysulfide solution. The bulk of the lithium structure has remained intact to Li_2S formation. After 30 minutes (**b**), there are signs of initial Li_2S formation, as white deposits are observed on the lithium structure where the lithium metal has chemically reacted with the Li_2S_6 solution. After 60 minutes (**d**), the entire unmodified electrodeposited lithium structure has been converted to Li_2S. The white deposits were confirmed to be Li_2S by STXM later in the chapter.

The chemical stability of unmodified electrodeposited lithium in contact with the Li_2S_6 polysulfide solution was limited to ~15 minutes before Li_2S was observed. To determine whether a Li_3N layer can effectively suppress Li_2S formation, lithium structures were electrodeposited onto a nickel TEM grid and nitrided for 2 hours under the same conditions described in **Chapter 4**. The nitrided TEM grid is then placed into a

glass cell and covered with 20 µL of the 1 M LiTFSI, 1 M Li_2S_6 polysulfide-electrolyte solution before sealing with a glass slide. The glass cell is transferred to the microscope stage where a series of dark-field optical microscopy images are taken with 15 minute intervals (**Figure 5.4**).

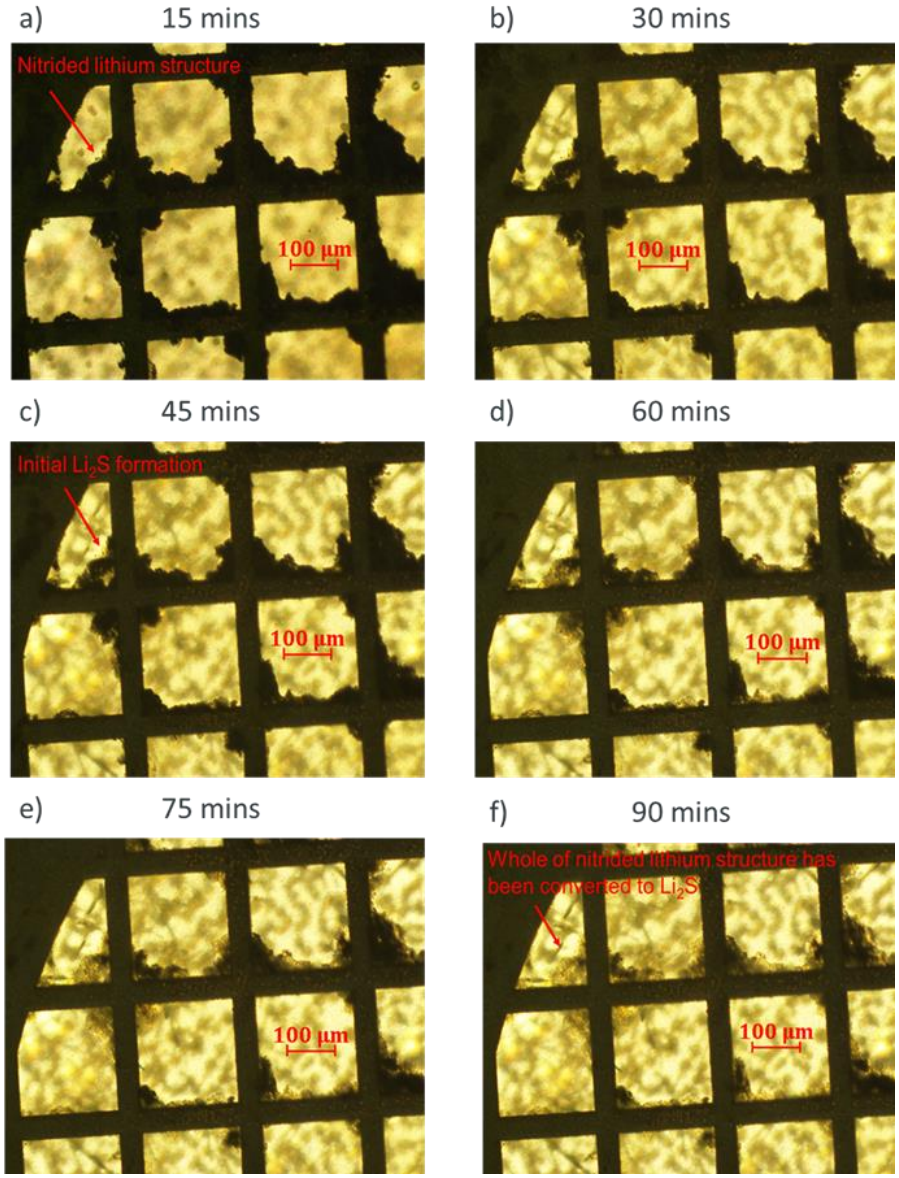

Figure 5.4 - Series of dark-field optical microscope images of a nitrided electrodeposited lithium structure exposed to 1 M Li_2S_6 in 1M LiTFSI 1,3 DOL polysulfide solution at increasing times of exposure.

Figure 5.4 (**a**) presents the nitrided electrodeposited lithium structure on the nickel TEM grid after 15 minutes' exposure to the polysulfide-electrolyte solution. The bulk of the lithium structure remains intact to Li_2S formation after 30 minutes (**b**). After 45 minutes (**c**), there are signs of initial Li_2S formation, as white deposits are observed on the nitrided electrodeposited lithium structure where the lithium metal has chemically reacted with the Li_2S_6 solution. After 90 minutes (**f**), the entire nitrided lithium structure has been converted to Li_2S. Optical images reveal that total lithium conversion to Li_2S has still occurred in the presence of a Li_3N protective layer. However, the time for complete conversion to Li_2S has increased from 60 minutes for the unmodified electrodeposited lithium structure to 90 minutes for the nitrided electrodeposited lithium structure, suggesting the Li_3N layer had initially suppressed the reaction between Li_2S_6 electrolyte solution and the lithium surface.

Chemical analysis of the unmodified and nitrided electrodeposited lithium was carried out by scanning transmission X-ray microscopy (STXM) and XPS, to better understand the reactions between the polysulfide-electrolyte solutions and unmodified and nitrided lithium electrodes.

For STXM measurements, samples were prepared by electrodepositing lithium structures onto nickel TEM grids under the same electrochemical conditions as described previously (**Section 3.22, Figure 4.6**). To allow for suitable STXM measurements to be collected, the final plating time was reduced 15 minutes. This decrease in plating time led to lithium structures that were ~5-50 µm in diameter.

For the unmodified electrodeposited lithium samples, the TEM grids were washed with 1,3 DOL after electrodeposition and were then exposed to 20 µL 1M Li_2S_6, 1 M LiTFSI in 1,3 DOL:DME (1:1 by vol.) electrolyte solution for 30 minutes which was the onset for the initial formation of Li_2S that was observed by optical microscopy (**Figure 5.3**). After 30 minutes, the TEM grid is further washed with 1,3 DOL to prevent further reactions before being stored for chemical analysis. STXM data acquisition and processing was carried out following the procedure described in **Section 2.9.1**. Multi-energy image scans (stacks) over the S K-edge (2460-2495 eV) were collected.

To better understand the sulfur chemical environments that are present on the unmodified electrodeposited lithium structure, multi-energy image scans (stacks) over the S K-edge (2460-2495 eV) were collected on a LiTFSI and Li_2S_6 standard (**Figure 5.5**).

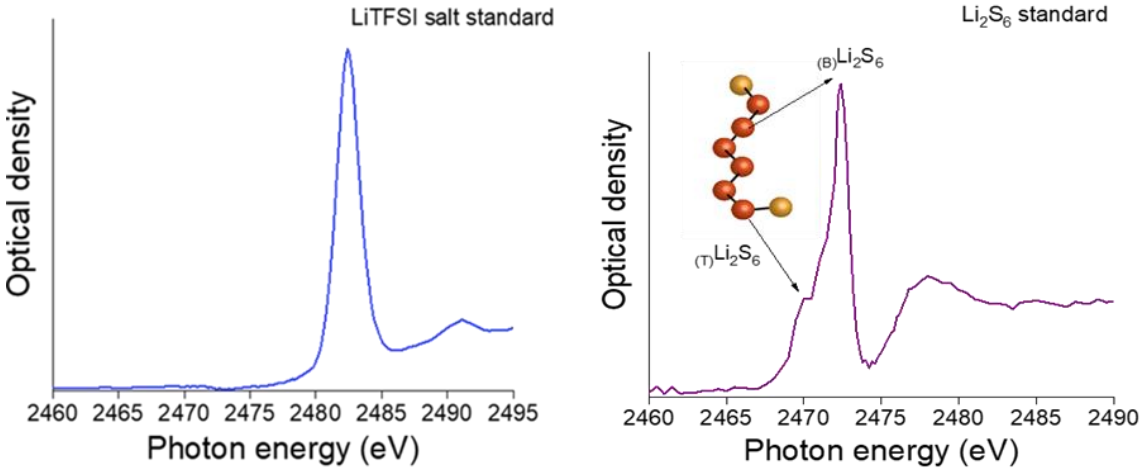

Figure 5.5 - NEXAFS spectrum of the S K-edge energy for the (left) LiTFSI salt standard and (right) Li_2S_6 standard.

The S K-edge NEXAFS spectrum for the LiTFSI standard (**Figure 5.5**) reveal one strong absorption at 2482.5 eV which is attributed to the S 1s to S=O π^* transition in the imide salt.[372,418] In the Li_2S_6 standard, there is a distinct shoulder to the main absorbing peak at 2470 eV. This pre-edge feature is attributed to the charged terminal sulfur environment (end of polysulfide dianion chain) of the Li_2S_6 species (S 1s to Li-S σ^*) with the main absorbing peak (2472 eV) assigned to the neutral bridging S-S (S 1s to S-S π^*) environment within the polysulfide species.[419,420,421]

Figure 5.6 presents an STXM image taken of the unmodified electrodeposited lithium structure (sample 1) exposed to Li_2S_6 polysulfide-electrolyte solution for 30 minutes.

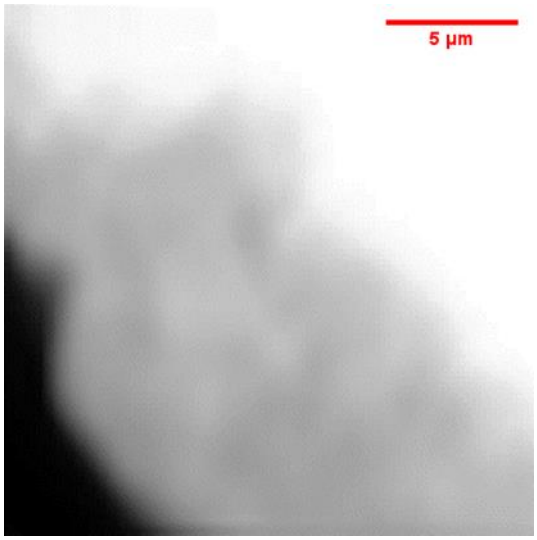

Figure 5.6 - 15 x 15 µm (2460 eV, pixel size = 150 nm) STXM image of the unmodified electrodeposited lithium on a Ni TEM grid after exposure to Li_2S_6 solution (sample 1).

Multi-energy image stacks over the S K-edge (2460-2495 eV) were measured on the 15 x 15 µm sample of unmodified electrodeposited lithium on a Ni TEM grid after exposure to the Li_2S_6 electrolyte solution for 30 minutes (sample 1). The sample area included a region without lithium to allow for processing of the data. The stack images were aligned and converted from transmission intensity to optical density as described in (**Section 2.9.1**).

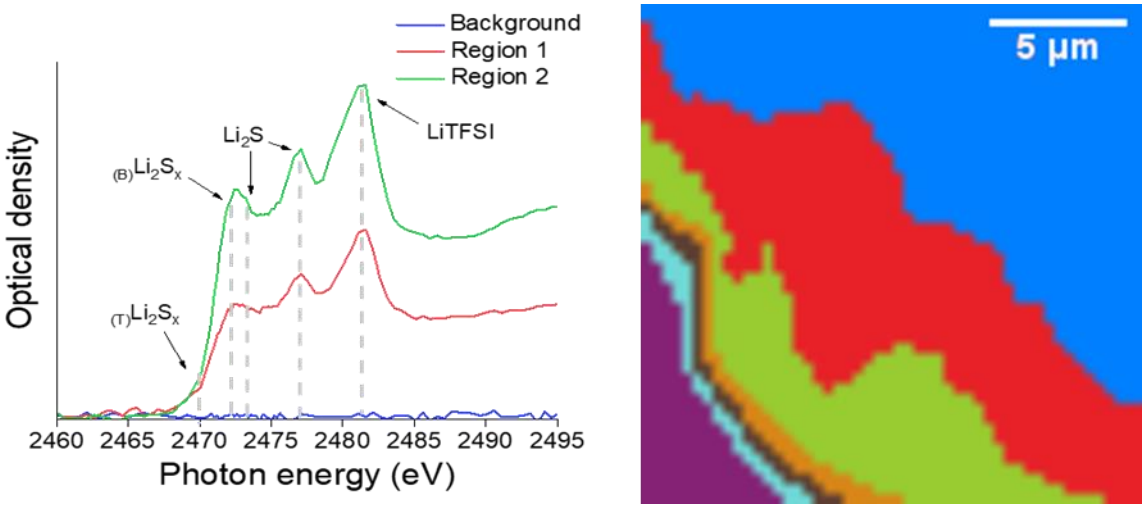

Figure 5.7 - NEXAFS spectra of the S K-edge energies and the corresponding cluster map for the unmodified electrodeposited lithium structure exposed to Li_2S_6 solution (sample 1).

3 different regions were determined from the cluster analysis of the stacked STXM images corresponding to the S K-edge NEXAFS spectra for the unmodified electrodeposited lithium structure exposed to the Li_2S_6 electrolyte solution (sample 1). The background (blue) shows no absorption. Regions 1 (red) and 2 (green) represent the bulk of the lithium structure. Absorption for polysulfide species (Li_2S_x) was observed at 2470 eV (pre-edge) and 2472 eV for the terminal (S1s to Li-S σ^*) and bridging (S1s to S-S π^*) Li_2S_x environments respectively. A strong absorption at 2476.5 eV is due to the presence of lithium sulfide (Li_2S) and is assigned to the S 1s to Li_2S σ* transition.[422,423,424] The absorption at 2482.5 eV is attributed to the S 1s to S=O π^* transition in the imide salt as recorded from the imide salt standard (**Figure 5.5**). The relative intensities between the polysulfide species and Li_2S remains constant through-out the structure.

Multi-energy image stacks over the S K-edge were repeated on a different unmodified electrodeposited structure exposed to the Li_2S_6 solution**. Figure 5.8** presents the STXM image of a 15 x 15 µm sample of unmodified electrodeposited lithium on a Ni TEM grid after exposure to the Li_2S_6 solution for 30 minutes (sample 2).

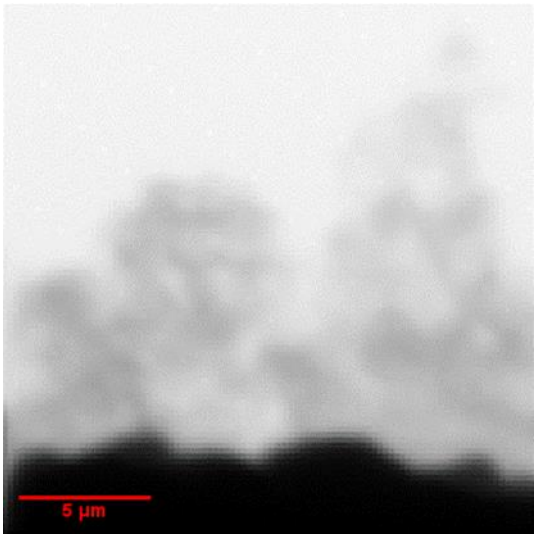

Figure 5.8 - 15 x 15 µm (2460 eV, pixel size = 150 nm) STXM image of the unmodified electrodeposited lithium on a Ni TEM grid after exposure to Li_2S_6 solution (sample 2).

Figure 5.9 presents the NEXAFS spectra generated from the stack over the S K-edge for the unmodified electrodeposited lithium exposed to Li_2S_6 polysulfide solution

for 30 minutes on a Ni TEM grid (sample 2), with the corresponding regions within the sample generated for each stack.

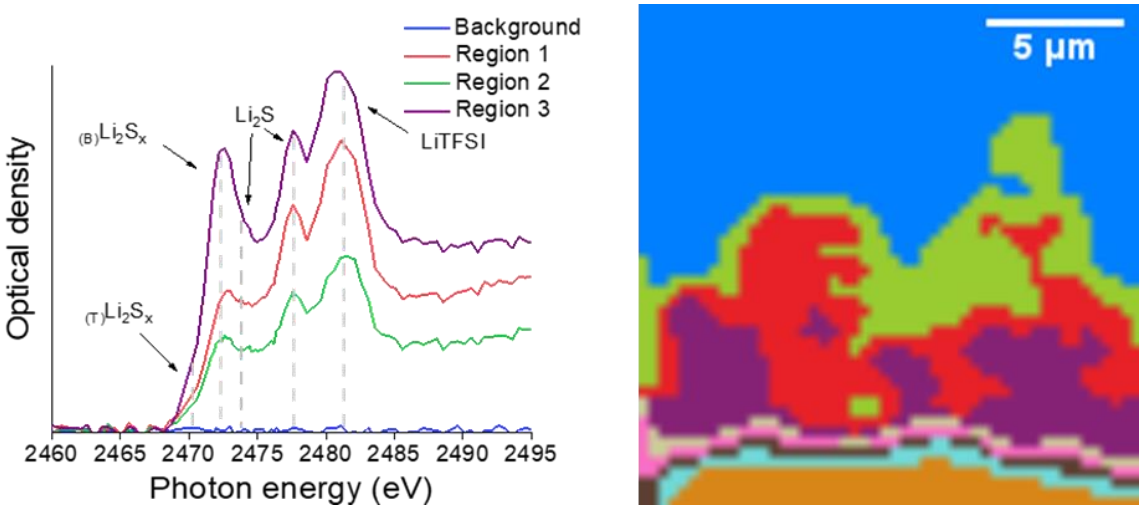

Figure 5.9 - NEXAFS spectra of the S K-edge energies and the corresponding cluster map for the unmodified electrodeposited lithium structure exposed to Li_2S_6 solution (sample 2).

The S K-edge stacks demonstrate a similar spectral response to sample 1, however there was a change in the relative ratios of the absorbing peaks for the polysulfide species and lithium sulfide. Region 1 (red) contains the strongest Li_2S contribution with respect to Li_2S_x, in reference to the cluster map, this region represents an area from the interface (region 2, green) towards the bulk of the lithium structure (region 3, purple) suggesting the reaction between Li_2S_6 and lithium metal has proceeded through the interface and continues through the bulk of the structure.

Scanning transmission X-ray microscopy was also performed on nitrided lithium exposed to Li_2S_6 polysulfide solution for 30 minutes. To produce the sample, lithium structures were electrodeposited onto a TEM grid as discussed previously. The nitrided lithium structures on the TEM grid are then exposed to 20 µL of 1 M Li_2S_6 in 1 M LiTFSI 1,3 DOL solution for 30 minutes, to stop the reaction. The TEM grid is rinsed with 1,3 DOL before storage for data collection.

The corresponding STXM image of nitrided electrodeposited lithium exposed to Li_2S_6 solution for 30 minutes is presented in **Figure 5.10** (sample 3).

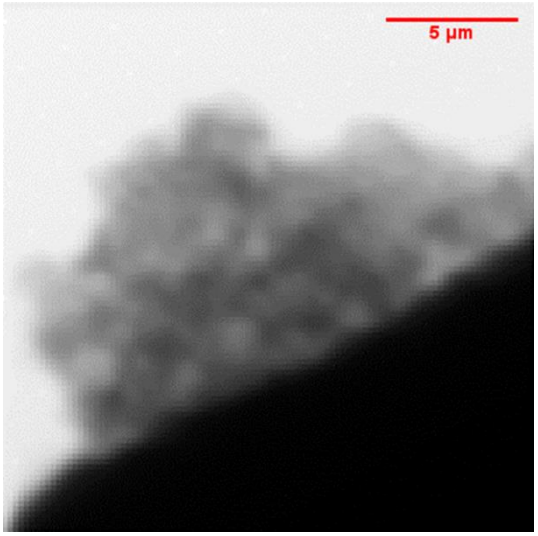

Figure 5.10 - 15 x 15 µm (2460 eV, pixel size = 150 nm) STXM image of the nitrided electrodeposited lithium on a Ni TEM grid after exposure to Li_2S_6 solution (sample 3).

NEXAFS spectra generated from the stacks over the S K-edge and the corresponding regions for nitrided electrodeposited lithium exposed to Li_2S_6 solution (sample 3) are presented in **Figure 5.11**.

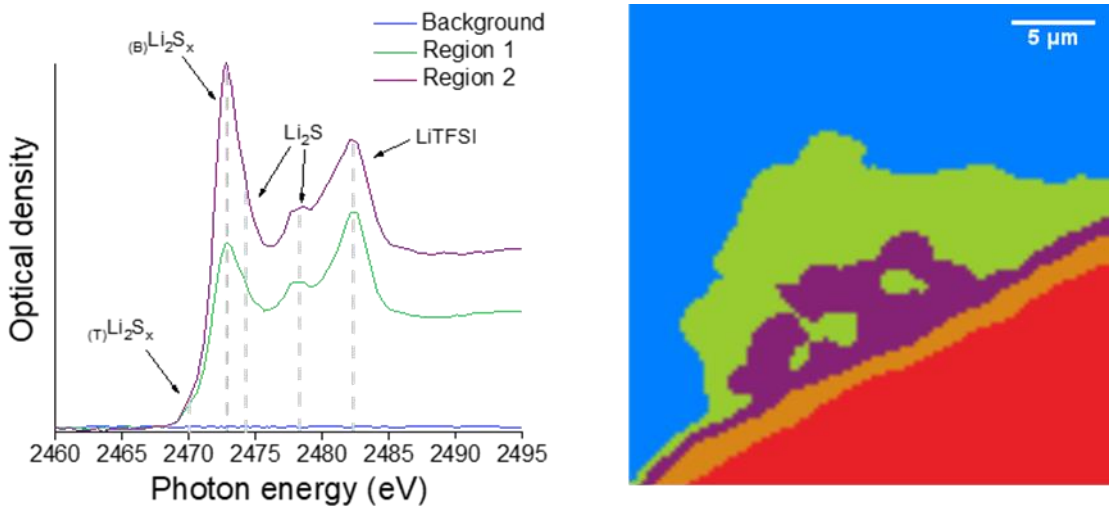

Figure 5.11 - NEXAFS spectra of the S K-edge energies and the corresponding cluster map for the nitrided electrodeposited lithium structure exposed to Li_2S_6 solution (sample 3).

3 different regions were generated from the cluster analysis of the stacked STXM images corresponding to the S K-edge NEXAFS spectra for sample 3 (**Figure 5.11**). The background (blue) shows no absorption. Regions 1 (green), and 2 (purple) represent the

nitrided electrodeposited lithium structure. Li_2S was observed in both regions however the relative intensity was lower with respect to the polysulfide species (Li_2S_x), when compared to the unmodified electrodeposited structures (samples 2 and 3). The inner-most region (region 2, purple) contains a strong absorption with respect to Li_2S_x suggesting Li_2S formation had not proceeded as the same rate compared with the unmodified electrodeposited samples.

NEXAFS spectra obtained from stacks over the S K-edge was repeated for nitrided electrodeposited lithium exposed to Li_2S_6 solution for 30 minutes (sample 4). **Figure 5.12** presents the STXM image of sample 4.

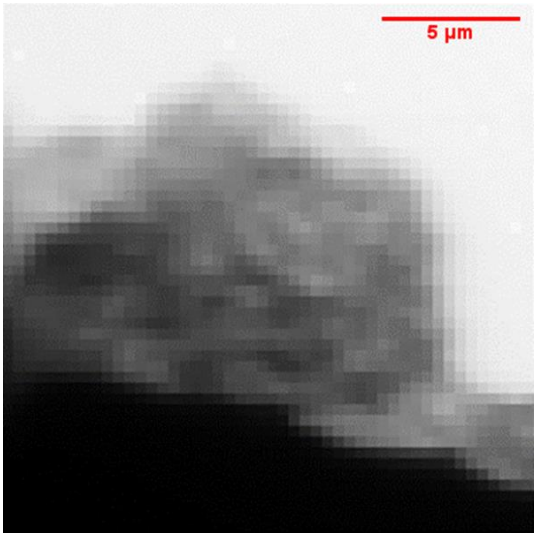

Figure 5.12 - 15 x 15 µm (2460 eV, pixel size = 150 nm) STXM image of the nitrided electrodeposited lithium on a Ni TEM grid after exposure to Li_2S_6 solution (sample 4).

NEXAFS spectra generated from the stacks over the S K-edge and the corresponding regions for nitrided electrodeposited lithium exposed to Li_2S_6 solution (sample 4) are presented in **Figure 5.13**.

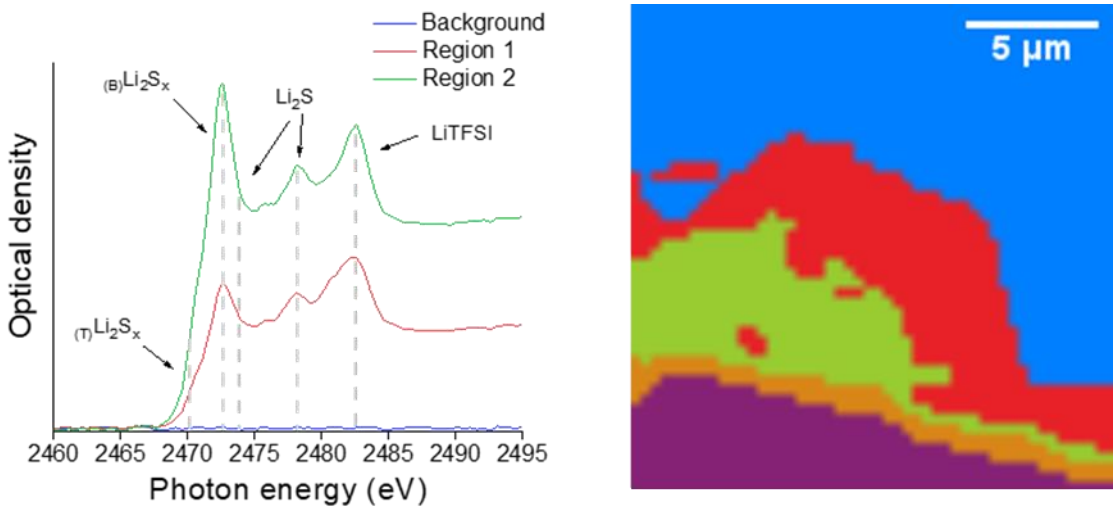

Figure 5.13 - NEXAFS spectra of the S K-edge energies and the corresponding cluster map for the nitrided electrodeposited lithium structure exposed to Li_2S_6 solution (sample 4).

A similar spectral response and cluster analysis was observed in the repeat nitrided electrodeposited lithium structure exposed to Li_2S_6 (sample 4). As was determined in sample 3, the inner-most region of the nitrided lithium structure (region 2, green) contains a strong absorption for Li_2S_x with a greater overall contribution of polysulfide species observed with respect to Li_2S.

Chemical analysis of unmodified and nitrided electrodeposited lithium electrodes exposed to the polysulfide-electrolyte solution was also carried out by XPS. As previously discussed in **Chapter 4**, XPS can be performed on larger materials, so samples were prepared that best represent working electrodes for lithium-sulfur batteries.

For the unmodified electrodeposited lithium electrode, lithium was electrodeposited onto 4 mm diameter nickel discs following the same plating procedure detailed in **Section 4.2.1**, with a final plating time of 16 hours. After plating, the unmodified electrodeposited lithium electrode was exposed to 80 µL of 1M Li_2S_6, 1 M LiTFSI in 1,3 DOL: DME (1:1 by vol.)) electrolyte solution for 30 minutes, (the same time length as for the STXM study). After 30 minutes, the TEM grid is again washed with 1,3 DOL to stop further reactions and then stored for chemical analysis. Data acquisition and processing was carried out following the procedures described in **Section 2.9.1**.

Figure 5.14 presents the N 1s and S 2p XPS spectra for the unmodified electrodeposited lithium electrode exposed to the polysulfide-electrolyte solution for 30 minutes at increasing incident photon energies.

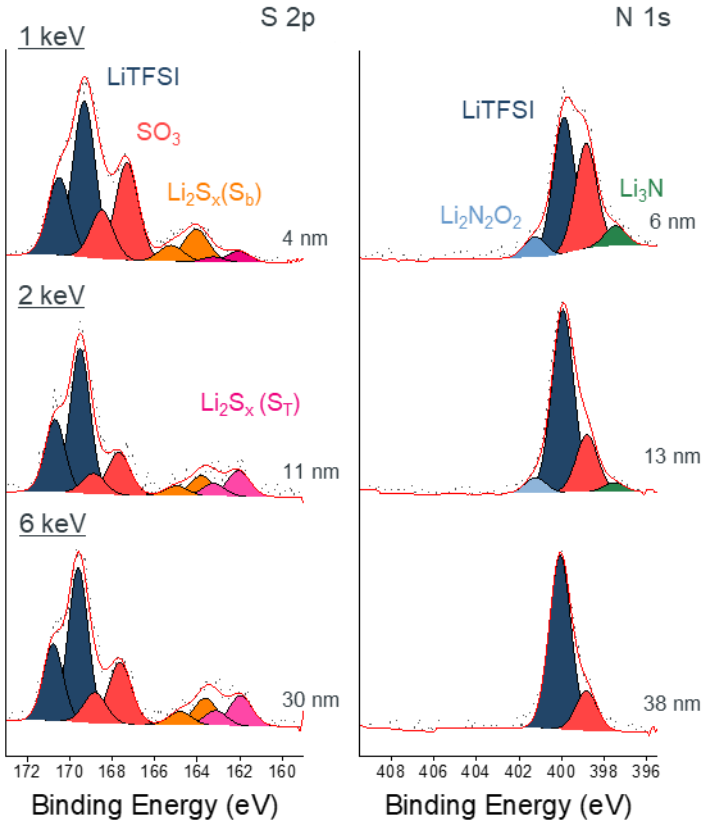

Figure 5.14 - XPS spectra for the S 2p, and N 1s regions of the unmodified electrodeposited lithium electrode exposed to 1 M Li_2S_6, 1 M LiTFSI in 1,3 DOL:DME as a function of increasing excitation energies, with the resulting probing depth calculated for each element.

Table 5.1 – Summary of XPS analysis and assignements for the surface characterisation of unmodified lithium exposed to polysulfide-electrolyte solution.

Orbital	Binding energy (eV)	FWHM	Peak assignments
N 1s	397.5	1.3	Li_3N[332,340,341,342]
	398.8	1.3	$LiTFSI_{decomp}$[340]
	399.8	1.3	LiTFSI[332,340,350,388,389]
	401	1.3	$Li_2N_2O_2$[346,347,348.349]
S 2p	169.2	1.2	LiTFSI (SO_4)[387,425,426 421,422]
	167.2	1.2	(SO_3)[143,387,425,426]
	164	1.3	Metastable Li_2S_x (S_B) [143,387,425,426,427,428]
	162	1.3	Metastable Li_2S_x (S_T) [143,387,425,426,427,428]

The N 1s spectra is very similar to the XPS recorded on the surface of the unmodified electrodeposited lithium electrode reported in **Chapter 4** (**Figure 4.16**) with the major species being attributed to the LiTFSI salt and decomposition products.

Figure 5.14 also presents the XPS spectra of the S 2p core level. The strongest emission at 169.2 eV is attributed to the binding energy of the sulfate ($[SO_4]^{2-}$) group in the LiTFSI salt. As 4 molal LiTFSI was used to electrodeposit the lithium and is also present in the polysulfide-electrolyte solution, it is not surprising that it has a strong XPS signal.

The peak at 167.2 eV has been reported as the sulphite species ($[SO_3]^{2-}$), formed from the decomposition of the LiTFSI salt. The peak at 164 eV is assigned to the bridging sulfur (S_B) of metastable polysulfide species (Li_2S_x) with an additional peak at 162 eV relating to the terminal sulfur (S_T) environment of the polysulfides. At 1 keV, the signal for bridging sulfur species (S_B) is stronger in intensity that of the terminal sulfur species (S_T). This can be attributed to a greater presence of higher-order polysulfide chains that contain multiple S-S covalent bonds.[143,427,429] At increasing photon energies, the relative intensity of the bridging sulfur (S_B), decreases and the peak for the terminal sulfur environment (S_B) of polysulfides (Li_2S_x) increases. The change in relative intensities can be ascribed to the reduction of higher-order polysulfides to lower-order polysulfides at depths closer to the reactive lithium surface.[143,387,427]

Figure 5.15 presents the XPS spectra N 1S and S 2p core energies of the nitrided electrodeposited lithium electrode exposed to the polysulfide-electrolyte solution.

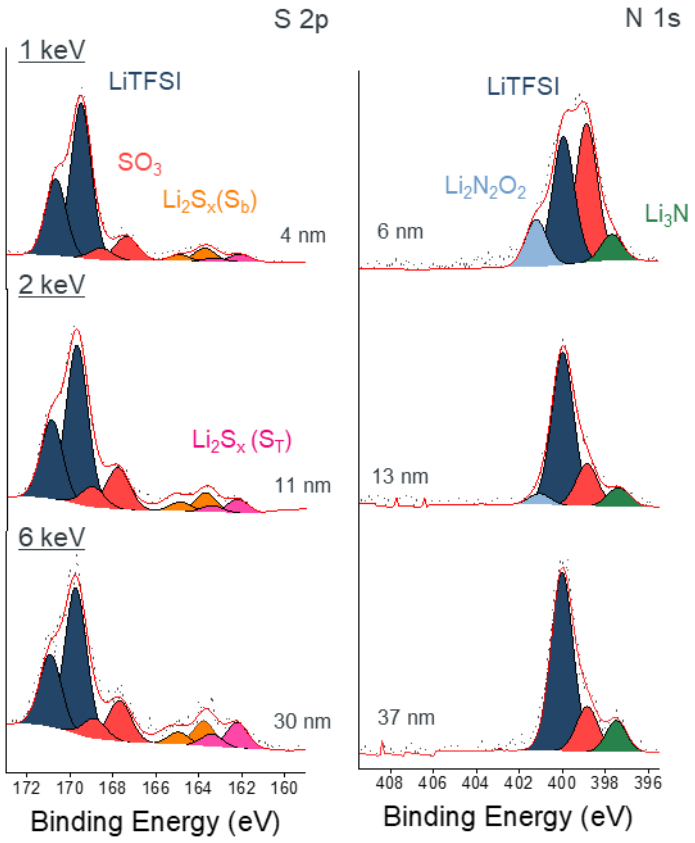

Figure 5.15 - XPS spectra for the S 2p, and N 1s regions of the nitrided electrodeposited lithium electrode exposed to 1 M Li_2S_6, 1 M LiTFSI in 1,3 DOL with 2% $LiNO_3$ as a function of increasing excitation energies, with the resulting probing depth calculated for each element.

The N 1s spectra contains the same nitrogen species that were recorded in the XPS spectra of the nitrided electrodeposited lithium electrode in **Chapter 4** (**Figure 4.18**). The Li_3N signal is retained after exposure to the polysulfide-electrolyte solution, suggesting no chemical change has occurred to the Li_3N layer. At 1 keV there is a weak signal for the bridging and terminal sulfur environments of polysulfide species, with a slightly stronger signal for the bridging environment (higher-order Li_2S_x). At 2 keV, the intensity of the bridging sulfur (S_B) environments is still greater that the terminal environment (S_T) suggesting that the reactivity of the electrode has been suppressed by the nitride layer in comparison with the unmodified electrodeposited lithium. At 6 keV there is an increase

in the terminal environment signal but it is still reduced on comparison to the unmodified electrodeposited lithium electrode.

5.4 Conclusions

Unmodified and nitrided electrodeposited lithium electrodes were exposed to a polysulfide-electrolyte solution (1M Li_2S_6, 1 M LiTFSI in 1,3 DOL/DME (1:1 by vol.)), to determine the stability towards polysulfides that would form during the cycling of a Li-S battery.

In the optical microscopy study, the time taken for the complete conversion of the lithium to Li_2S increased from 60 to 90 minutes between the unmodified and nitrided electrodeposited samples. STXM confirmed there was an increase in the Li_2S absorption for unmodified electrodeposited lithium structures after a 30-minute exposure to the polysulfide-electrolyte solution.

Chemical analysis of unmodified and nitrided electrodeposited lithium electrodes exposed to the polysulfide-electrolyte solution was also carried out by XPS. The unmodified electrodeposited lithium electrode was more reactive towards the polysulfide species in the solution, as the intensity of the bridging sulfur environments (S_B) which represent higher-order polysulfide species, decreased at higher incident photon energies as they are converted to shorter-chained polysulfides. This was confirmed by an increase in the terminal sulfur signal (S_T).

Chapter 6 Conclusions and future work

This doctoral work investigated some promising nitride materials as negative electrodes for sodium-ion and lithium metal battery applications.

A new simple and scalable method to synthesise spinel-structured Sn_3N_4 has been developed using $SnCl_4$ and $LiNH_2$ precursors under solvothermal conditions. Nanocrystalline Sn_3N_4 with a crystallite size < 10 nm was produced and tested as a negative electrode material in sodium half-cells, demonstrating a very high reversible (de-sodiation) capacity of ~850 mA h g^{-1} measured over 50 cycles. Ex situ X-ray absorption spectroscopy and X-ray diffraction show that the electrochemical reactions are reversible and that Sn_3N_4 is recovered upon re-oxidation. X-ray diffraction shows that the peaks associated with Sn_3N_4 reflections become narrower during discharge (reduction), evidencing that the smaller Sn_3N_4 particles are primarily involved in the electrochemical reactions, and broadening of the peaks is reversibly recovered upon oxidation. The analysis of the near edge X-ray absorption data (XANES) shows that the Sn oxidation state decreases during reduction and nearly recovers the initial value during oxidation. Extended X-ray absorption fine-structure (EXAFS) measurements of reduced electrodes suggest that the electrochemical reactions proceed by insertion of Na ions into the Sn_3N_4 structure followed by substitution of tetrahedral Sn, as evidenced by the reduction of tetrahedral the Sn site. The EXAFS measurements of reduced electrodes, also show the recovery of the pristine structure at the end of oxidation.

Further work could see nanocrystalline Sn_3N_4 incorporated into a highly structured carbon architecture structure (graphene sheets, carbon spheres etc.) which could improve the conductivity and perhaps increase the amount of Sn_3N_4 material that could be electrochemically accessible during cycling.

The nitridation of electrodeposited lithium offers a unique perspective for designing protective layers for lithium metal battery applications. This work developed a reproducible method to electrodeposit lithium onto current collectors that formed the basis of these studies. The reactivity of as-received battery-grade lithium foil differs

dramatically compared to the unmodified electrodeposited lithium, as evidenced by the lack of reaction on exposure to flowing N_2 gas (2 hours at 90 °C). Conversely, the unmodified electrodeposited lithium showed a visual colour change on exposure to N_2 as STXM and XPS confirmed the formation of lithium nitride during the nitridation process. The lack of reactivity of the battery-grade lithium foil was attributed to the native layer consisting of a high content of Li_2O as reported by XPS. Unidirectional galvanostatic polarisation measurements showed an increased time to short circuit-during constant plating on nitrided electrodeposited lithium electrodes (2.9 ± 0.9 h for unmodified electrodeposited and 4.0 ± 1.6 h for nitrided electrodeposited lithium electrodes), at a high current of 5 mA cm^{-2} suggesting the Li_3N layers facilitated the even deposition of lithium before a short-circuit occurs. Improvements in plating/stripping behaviours were also evidenced in galvanostatic cycling of nitrided electrodeposited lithium electrodes. Where generally stable plating/stripping plateaus were recorded in the voltage profiles of nitrided electrode Li_3N-Li||Li_3N-Li symmetric cells cycled at a moderate current of 2 mA cm^{-2}. There was a larger variation in the cycling behaviour of unmodified electrodeposited Li||Li symmetric cells, with one cell showing serious signs of cell failure.

Future work for nitrided electrodeposited lithium electrodes for secondary lithium metal battery applications, could include validating the electrochemical measurements in more commercially accepted electrolytes (1 M LiTFSI, 0.25 M $LiNO_3$ in DOL,DME) which move away from arsenic-containing electrolyte solutions. Improvements in the nitridation experimental setup could further reduce the exposure of the electrodeposited lithium electrodes to moisture, as XPS revealed a significant increase in intensity of LiOH on the surface of the nitrided electrodeposited electrodes (**Figure 4.18**). The improved chemical stability of nitrided electrodeposited lithium electrodes towards polysulfide containing electrolyte solution, could be investigated further by performing galvanostatic measurements of the protected electrode in Li-S cells. By protecting the lithium metal electrode, it is likely to improve the cyclability of the cell, improving the capacity retention and Coulombic efficiency over multiple cycles.

Chapter 7 References

1 P. K. Nayak, E. M. Erickson, F. Schipper, T. R. Penki, N. Munichandraiah, P. Adelhelm, H. Sclar, F. Amalraj, B. Markovsky and D. Aurbach, *Adv. Energy Mater.*, 2018, **8**, 1702397.

2 L. Lu, X. Han, J. Li, J. Hua and M. Ouyang, *J. Power Sources.*, 2013, **226**, 272–288.

3 A. Volta, *Abstr. Pap. Print. Phil. Trans. R. Soc Lond.*, 1800, **1**, 27–29.

4 F. A. J. L. James, *J. Am. Chem. Soc.*, 1989, vol. 390, pp. 32–49.

5 A. Boulabiar, K. Bouraoui, M. Chastrette and M. Abderrabba, *J. Chem. Educ.*, 2004, **81**, 754.

6 V. S. Bagotsky, *J. Solid State Electrochem.*, 2011, **15**, 1559–1562.

7 P. Kurzweil, *J. Power Sources*, 2010, **195**, 4424–4434.

8 B. Scrosati, *J. Solid State Electrochem.*, 2011, **15**, 1623–1630.

9 M. D. Bhatt and C. O'Dwyer, *Phys. Chem. Chem. Phys.*, 2015, **17**, 4799–4844.

10 D. Larcher, S. Beattie, M. Morcrette, K. Edström, J.-C. Jumas and J.-M. Tarascon, *J. Mater. Chem.*, 2007, **17**, 3759–3772.

11 M. Winter, B. Barnett and K. Xu, *Chem. Rev.*, 2018, **118**, 11433–11456.

12 J.-M. Tarascon and M. Armand, *Nat.*, 2001, **414**, 359–367.

13 T. M. Bandhauer, S. Garimella and T. F. Fuller, *J. Electrochem. Soc.*, 2011, **158**, R1.

14 P. G. Bruce, *Chem. Commun.,* 1997, **0**, 1817–1824.

15 J. B. Goodenough, *Nat. Electron.*, 2018, **1**, 204–204.

16 J. B. Goodenough and Y. Kim, *Chem. Mater.*, 2010, **22**, 587–603.

17 D. W. Murphy, F. J. Di Salvo, J. N. Carides and J. V. Waszczak, *Mater. Res. Bull.*, 1978, **13**, 1395–1402.

18 K. Brandt, *Solid State Ionics.*, 1994, **69**, 173–183.

19 Z.-I. Takehara and K. Kanamura, *Electrochim. Acta*, 1993, **38**, 1169–1177.

20 T. Ohzuku and R. J. Brodd, *J. Power Sources*, 2007, **174**, 449–456.

21 S. Goriparti, E. Miele, F. De Angelis, E. Di Fabrizio, R. Proietti Zaccaria and C. Capiglia, *J. Power Sources*, 2014, **257**, 421–443.

22 S. J. An, J. Li, C. Daniel, D. Mohanty, S. Nagpure and D. L. Wood, *Carbon*, 2016, **105**, 52–76.

23 P. Ganesh, P. R. C. Kent and D. Jiang, *J. Phys. Chem. C*, 2012, **116**, 24476–24481.

24 Y. F. Reynier, R. Yazami and B. Fultz, *J. Electrochem. Soc.*, 2004, **151**, A422.

25 R. Yazami and Ph. Touzain, *J. Power Sources*, 1983, **9**, 365–371.

26 B. C. Melot and J.-M. Tarascon, *Acc. Chem. Res.*, 2013, **46**, 1226–1238.

27 A. R. Armstrong, M. Holzapfel, P. Novák, C. S. Johnson, S.-H. Kang, M. M. Thackeray and P. G. Bruce, *J. Am. Chem. Soc.*, 2006, **128**, 8694–8698.

28 D. Aurbach, K. Gamolsky, B. Markovsky, G. Salitra, Y. Gofer, U. Heider, R. Oesten and M. Schmidt, *J. Electrochem. Soc.*, 2000, **147**, 1322.

29 K. Edström, T. Gustafsson and J. O. Thomas, *Electrochim. Acta*, 2004, **50**, 397–403.

30 N. Yabuuchi, K. Yoshii, S.-T. Myung, I. Nakai and S. Komaba, *J. Am. Chem. Soc.*, 2011, **133**, 4404–4419.

31 D. Aurbach, Y. Talyosef, B. Markovsky, E. Markevich, E. Zinigrad, L. Asraf, J. S. Gnanaraj and H.-J. Kim, *Electrochim. Acta*, 2004, **50**, 247–254.

32 Y. Wang, S. Nakamura, M. Ue and P. B. Balbuena, *J. Am. Chem. Soc.*, 2001, **123**, 11708–11718.

33 H. Zhang, I. Hasa and S. Passerini, *Adv. Energy Mater.*, 2018, **8**, 1870082.

34 C. Vaalma, D. Buchholz, M. Weil and S. Passerini, *Nat. Rev. Mater.*, 2018, **3**, 18013.

35 F. Li, Z. Wei, A. Manthiram, Y. Feng, J. Ma and L. Mai, *J. Mater. Chem. A*, 2019, **7**, 9406–9431.

36 X. Li, A. L. Hector, J. R. Owen and S. I. U. Shah, *J. Mater. Chem. A*, 2016, **4**, 5081–5087.

37 J.-Y. Hwang, S.-T. Myung and Y.-K. Sun, *Chem. Soc. Rev*, 2017, **46**, 3529–3614.

38 S. Y. Hong, Y. Kim, Y. Park, A. Choi, N.-S. Choi and K. T. Lee, *Energy Environ. Sci.*, 2013, **6**, 2067–2081.

39 Y. Lei, X. Li, L. Liu and G. Ceder, *Chem. Mat.*, 2014, **26**, 5288–5296.

40 Y. H. Jung, A. S. Christiansen, R. E. Johnsen, P. Norby and D. K. Kim, *Adv. Funct. Mater.*, 2015, **25**, 3227–3237.

41 P.-F. Wang, Y. You, Y.-X. Yin and Y.-G. Guo, *Adv. Energy Mater.*, 2018, **8**, 1701912.

42 B. Senthilkumar, C. Murugesan, L. Sharma, S. Lochab and P. Barpanda, *Small Methods*, 2019, **3**, 1800253.

43 S. Baskar, R. Angalakuthi, C. Murugesan, S. B. Krupanidhi and P. Barpanda, *Electrochem. Soc. Trans.*, 2018, **85**, 227–234.

44 X. Dou, I. Hasa, D. Saurel, C. Vaalma, L. Wu, D. Buchholz, D. Bresser, S. Komaba and S. Passerini, *Mater. Today*, 2019, **23**, 87–104.

45 B. Xiao, T. Rojo and X. Li, *ChemSusChem*, 2019, **12**, 133–144.

46 C. Matei Ghimbeu, J. Górka, V. Simone, L. Simonin, S. Martinet and C. Vix-Guterl, *Nano Energy*, 2018, **44**, 327–335.

47 D. A. Stevens and J. R. Dahn, *J. Electrochem. Soc.*, 2000, **147**, 1271–1273.

48 D. Li, L. Zhang, H. Chen, J. Wang, L.-X. Ding, S. Wang, P. J. Ashman and H. Wang, *J. Mater. Chem. A*, 2016, **4**, 8630–8635.

49 T. Chen, Y. Liu, L. Pan, T. Lu, Y. Yao, Z. Sun, D. H. C. Chua and Q. Chen, *J. Mater. Chem. A*, 2014, **2**, 4117–4121.

50 W. Tang, J. Wu, X. Wang, X. Xia and J. Tu, *Green Energy Environ.*, 2018, **3**, 50–55.

51 M. Anji Reddy, M. Helen, A. Groß, M. Fichtner and H. Euchner, *Am. Chem. Soc., Energy Lett.*, 2018, **3**, 2851–2857.

52 S. Alvin, D. Yoon, C. Chandra, H. S. Cahyadi, J.-H. Park, W. Chang, K. Y. Chung and J. Kim, *Carbon*, 2019, **145**, 67–81.

53 S. Qiu, L. Xiao, M. L. Sushko, K. S. Han, Y. Shao, M. Yan, X. Liang, L. Mai, J. Feng, Y. Cao, X. Ai, H. Yang and J. Liu, *Adv. Energy Mater.*, 2017, **7**, 1700403.

54 P. R. Abel, Y.-M. Lin, T. de Souza, C.-Y. Chou, A. Gupta, J. B. Goodenough, G. S. Hwang, A. Heller and C. B. Mullins, *J. Phys. Chem. C*, 2013, **117**, 18885–18890.

55 C.-H. Lim, T.-Y. Huang, P.-S. Shao, J.-H. Chien, Y.-T. Weng, H.-F. Huang, B. J. Hwang and N.-L. Wu, *Electrochim. Acta*, 2016, **211**, 265–272.

56 C. Wang, L. Wang, F. Li, F. Cheng and J. Chen, *Adv. Mater.*, 2017, **29**, 1702212.

57 Y. Rok Lim, F. Shojaei, K. Park, C. Su Jung, J. Park, W. Il Cho and H. Seok Kang, *Nanoscale*, 2018, **10**, 7047–7057.

58 S. Guo, X. Hu, W. Zhou, X. Liu, Y. Gao, S. Zhang, K. Zhang, Z. Zhu and H. Zeng, *J. Phys. Chem. C*, 2018, **122**, 29559–29566.

59 B. Farbod, K. Cui, W. P. Kalisvaart, M. Kupsta, B. Zahiri, A. Kohandehghan, E. M. Lotfabad, Z. Li, E. J. Luber and D. Mitlin, *Am. Chem. Soc. Nano*, 2014, **8**, 4415–4429.

60 J. Qian, X. Wu, Y. Cao, X. Ai and H. Yang, *Angew. Chem., Int. Ed.*, 2013, **52**, 4633–4636.

61 N. Yabuuchi, Y. Matsuura, T. Ishikawa, S. Kuze, J.-Y. Son, Y.-T. Cui, H. Oji and S. Komaba, *ChemElectroChem*, 2014, **1**, 580–589.

62 J. He, Y. Wei, T. Zhai and H. Li, *Mater. Chem. Front.*, 2018, **2**, 437–455.

63 H. Ying and W.-Q. Han, *Adv. Sci.*, 2017, **4**, 1700298.

64 Z. Li, J. Ding and D. Mitlin, *Acc. Chem. Res.*, 2015, **48**, 1657–1665.

65 L. D. Ellis, B. N. Wilkes, T. D. Hatchard and M. N. Obrovac, *J. Electrochem. Soc.*, 2014, **161**, A416–A421.

66 A. Darwiche, C. Marino, M. T. Sougrati, B. Fraisse, L. Stievano and L. Monconduit, *J. Am. Chem. Soc.*, 2012, **134**, 20805–20811.

67 Y. Zhu, X. Han, Y. Xu, Y. Liu, S. Zheng, K. Xu, L. Hu and C. Wang, *Am. Chem. Soc. Nano*, 2013, **7**, 6378–6386.

68 C. R. Becker, K. E. Strawhecker, Q. P. McAllister and C. A. Lundgren, *Am. Chem. Soc. Nano*, 2013, **7**, 9173–9182.

69 B. Scrosati, J. Hassoun and Y.-K. Sun, *Energy Environ. Sci.*, 2011, **4**, 3287–3295.

70 M. K. Datta, R. Epur, P. Saha, K. Kadakia, S. K. Park and P. N. Kumta, *J. Power Sources*, 2013, **225**, 316–322.

71 Q. Wang, C. Zhao, Y. Lu, Y. Li, Y. Zheng, Y. Qi, X. Rong, L. Jiang, X. Qi, Y. Shao, D. Pan, B. Li, Y.-S. Hu and L. Chen, *Small*, 2017, **13**, 1701835.

72 G.-L. Xu, Z. Chen, G.-M. Zhong, Y. Liu, Y. Yang, T. Ma, Y. Ren, X. Zuo, X.-H. Wu, X. Zhang and K. Amine, *Nano Lett.*, 2016, **16**, 3955–3965.

73 Y. Fang, X.-Y. Yu and X. W. (David) Lou, *Matter*, 2019, **1**, 90–114.

74 J. W. Wang, X. H. Liu, S. X. Mao and J. Y. Huang, *Nano Lett.*, 2012, **12**, 5897–5902.

75 P. Poizot, S. Laruelle, S. Grugeon, L. Dupont and J.-M. Tarascon, *Nat.*, 2000, **407**, 496–499.

76 A. Jahel, C. M. Ghimbeu, A. Darwiche, L. Vidal, S. Hajjar-Garreau, C. Vix-Guterl and L. Monconduit, *J. Mater. Chem. A*, 2015, **3**, 11960–11969.

77 J. Qin, N. Zhao, C. Shi, E. Liu, F. He, L. Ma, Q. Li, J. Li and C. He, *J. Mater. Chem. A*, 2017, **5**, 10946–10956.

78 Y. Ching Lu, C. Ma, J. Alvarado, N. Dimov, Y. Shirley Meng and S. Okada, *J. Mater. Chem. A*, 2015, **3**, 16971–16977.

79 C. Xia, F. Zhang, H. Liang and H. N. Alshareef, *Nano Res.*, 2017, **10**, 4368–4377.

80 Y. Kim, Y. Kim, A. Choi, S. Woo, D. Mok, N.-S. Choi, Y. S. Jung, J. H. Ryu, S. M. Oh and K. T. Lee, *Adv. Mater.*, **26**, 4139–4144.

81 J. Liu, P. Kopold, C. Wu, P. A. van Aken, J. Maier and Y. Yu, *Energy Environ. Sci.*, 2015, **8**, 3531–3538.

82 Y. Liu, X. Fang, M. Ge, J. Rong, C. Shen, A. Zhang, H. A. Enaya and C. Zhou, *Nano Energy*, 2015, **16**, 399–407.

83 Y. Wei, Z. Wang, H. Ye, J. Mou, D. Lei, Y. Liu, W. Lv, B. Li, F. Kang and Y.-B. He, *ChemistrySelect*, 2017, **2**, 11365–11369.

84 L. Liu, M. An, P. Yang and J. Zhang, *Sci. Rep.*, 2015, **5**, 9055.

85 J. S. Chen, Y. L. Cheah, Y. T. Chen, N. Jayaprakash, S. Madhavi, Y. H. Yang and X. W. Lou, *J. Phys. Chem. C*, 2009, **113**, 20504–20508.

86 R. Hu, D. Chen, G. Waller, Y. Ouyang, Y. Chen, B. Zhao, B. Rainwater, C. Yang, M. Zhu and M. Liu, *Energy Environ. Sci.*, 2016, **9**, 595–603.

87 J. Ding, Z. Li, H. Wang, K. Cui, A. Kohandehghan, X. Tan, D. Karpuzov and D. Mitlin, *J. Mater. Chem. A*, 2015, **3**, 7100–7111.

88 Y. Cheng, J. Huang, J. Li, Z. Xu, L. Cao and H. Qi, *J. Power Sources*, 2016, **324**, 447–454.

89 M. Gu, A. Kushima, Y. Shao, J.-G. Zhang, J. Liu, N. D. Browning, J. Li and C. Wang, *Nano Lett.*, 2013, **13**, 5203–5211.

90 J. Yue, W. Wang, N. Wang, X. Yang, J. Feng, J. Yang and Y. Qian, *J. Mater. Chem. A*, 2015, **3**, 23194–23200.

91 J. Cui, Z.-L. Xu, S. Yao, J. Huang, J.-Q. Huang, S. Abouali, M. A. Garakani, X. Ning and J.-K. Kim, *J. Mater. Chem. A*, 2016, **4**, 10964–10973.

92 Y.-X. Wang, Y.-G. Lim, M.-S. Park, S.-L. Chou, J. Ho Kim, H.-K. Liu, S.-X. Dou and Y.-J. Kim, *J. Mater. Chem. A*, 2014, **2**, 529–534.

93 Q. Wu, Q. Shao, Q. Li, Q. Duan, Y. Li and H. Wang, *ACS Appl. Mater. Interfaces*, 2018, **10**, 15642–15651.

94 J. Choi and E. G. Gillan, *J. Mater. Chem. A*, 2006, **16**, 3774–3784.

95 L. Ma, P. Yan, S. Wu, G. Zhu and Y. Shen, *J. Mater. Chem. A*, 2017, **5**, 16994–17000.

96 L. Baggetto, N. A. M. Verhaegh, R. A. H. Niessen, F. Roozeboom, J.-C. Jumas and P. H. L. Notten, *J. Electrochem. Soc.*, 2010, **157**, A340.

97 A. Manthiram, Y. Fu and Y.-S. Su, *Acc. Chem. Res.*, 2013, **46**, 1125–1134.

98 G. Xu, B. Ding, J. Pan, P. Nie, L. Shen and X. Zhang, *J. Mater Chem. A*, 2014, **2**, 12662–12676.

99 H. Yao, K. Yan, W. Li, G. Zheng, D. Kong, Z. Wei Seh, V. Kris Narasimhan, Z. Liang and Y. Cui, *Energy Environ. Sci.*, 2014, **7**, 3381–3390.

100 S. Ahmed, P. A. Nelson, K. G. Gallagher, N. Susarla and D. W. Dees, *J. Power Sources*, 2017, **342**, 733–740.

101 M. Hagen, S. Dörfler, P. Fanz, T. Berger, R. Speck, J. Tübke, H. Althues, M. J. Hoffmann, C. Scherr and S. Kaskel, *J. Power Sources*, 2013, **224**, 260–268.

102 Y. Song, W. Cai, L. Kong, J. Cai, Q. Zhang and J. Sun, *Adv. Energy Mater.*, 2020, **10**, 1901075.

103 M. Liu, N. Deng, J. Ju, L. Fan, L. Wang, Z. Li, H. Zhao, G. Yang, W. Kang, J. Yan and B. Cheng, *Adv. Funct. Mater.*, 2019, **29**, 1905467.

104 M. A. Pope and I. A. Aksay, *Adv. Energy Mater.*, 2015, **5**, 1500124.

105 M. U. M. Patel, R. Demir-Cakan, M. Morcrette, J.-M. Tarascon, M. Gaberscek and R. Dominko, *ChemSusChem*, 2013, **6**, 1177–1181.

106 Y.-C. Lu, Q. He and H. A. Gasteiger, *J. Phys. Chem. C*, 2014, **118**, 5733–5741.

107 M. U. M. Patel, I. Arčon, G. Aquilanti, L. Stievano, G. Mali and R. Dominko, *Chemphyschem*, 2014, **15**, 894–904.

108 M. Wild, L. O'Neill, T. Zhang, R. Purkayastha, G. Minton, M. Marinescu and G. J. Offer, *Energy Environ. Sci.*, 2015, **8**, 3477–3494.

109 J. Gao, M. A. Lowe, Y. Kiya and H. D. Abruña, *J. Phys. Chem. C*, 2011, **115**, 25132–25137.

110 X. Zhang, K. Chen, Z. Sun, G. Hu, R. Xiao, H.-M. Cheng and F. Li, *Energy Environ. Sci.*, 2020, **13**, 1076-1095

111 Y. Pan and W. M. Guan, *Inorg. Chem.*, 2018, **57**, 6617–6623.

112 Z. Liu, P. B. Balbuena and P. P. Mukherjee, *J. Phys. Chem. Lett.*, 2017, **8**, 1324–1330.

113 Z. Feng, C. Kim, A. Vijh, M. Armand, K. H. Bevan and K. Zaghib, *J. Power Sources*, 2014, **272**, 518–521.

114 R. D. Rauh, K. M. Abraham, G. F. Pearson, J. K. Surprenant and S. B. Brummer, *J. Electrochem. Soc.*, 1979, **126**, 523.

115 H. Yamin, A. Gorenshtein, J. Penciner, Y. Sternberg and E. Peled, *J. Electrochem. Soc.*, 1988, **135**, 1045.

116 Y. Jung and S. Kim, *Electrochem. Commun.*, 2007, **9**, 249–254.

117 X. Qiu, Q. Hua, L. Zheng and Z. Dai, *RSC Adv.*, 2020, **10**, 5283–5293.

118 L. Kong, J.-X. Chen, H.-J. Peng, J.-Q. Huang, W. Zhu, Q. Jin, B.-Q. Li, X.-T. Zhang and Q. Zhang, *Energy Environ. Sci.*, 2019, **12**, 2976–2982.

119 S. S. Zhang, *J. Power Sources*, 2013, **231**, 153–162.

120 M. A. Lowe, J. Gao and H. D. Abruña, *RSC Adv.*, 2014, **4**, 18347–18353.

121 M. Cuisinier, C. Hart, M. Balasubramanian, A. Garsuch and L. F. Nazar, *Adv. Energy Mater.*, 2015, **5**, 1401801.

122 Q. He, Y. Gorlin, M. U. M. Patel, H. A. Gasteiger and Y.-C. Lu, *J. Electrochem. Soc.*, 2018, **165**, A4027.

123 N. Angulakshmi and A. M. Stephan, *Front. Energy Res.*, 2015, **17**, 224–231

124 M. R. Busche, P. Adelhelm, H. Sommer, H. Schneider, K. Leitner and J. Janek, *J. Power Sources*, 2014, **259**, 289–299.

125 R. Fang, S. Zhao, Z. Sun, D.-W. Wang, H.-M. Cheng and F. Li, *Adv. Mater.*, 2017, **29**, 3221–3229.

126 A. Manthiram, Y. Fu, S.-H. Chung, C. Zu and Y.-S. Su, *Chem. Rev.*, 2014, **114**, 11751–11787.

127 L. Chen and L. L. Shaw, *J. Power Sources*, 2014, **267**, 770–783.

128 H.-J. Peng, J.-Q. Huang, X.-B. Cheng and Q. Zhang, *Adv. Energy Mater.*, 2017, **7**, 1700260.

129 M. Cuisinier, P.-E. Cabelguen, B. D. Adams, A. Garsuch, M. Balasubramanian and L. F. Nazar, *Energy Environ. Sci.*, 2014, **7**, 2697–2705.

130 M. J. Lacey, F. Jeschull, K. Edström and D. Brandell, *Chem. Commun.*, 2013, **49**, 8531–8533.

131 N. Nakamura, T. Yokoshima, H. Nara, T. Momma and T. Osaka, *J. Power Sources*, 2015, **274**, 1263–1266.

132 S. Evers and L. F. Nazar, *Acc. Chem. Res.*, 2013, **46**, 1135–1143.

133 L. Wang, J. Liu, S. Yuan, Y. Wang and Y. Xia, *Energy Environ. Sci.*, 2016, **9**, 224–231.

134 Y. Fan, Z. Niu, F. Zhang, R. Zhang, Y. Zhao and G. Lu, *Am. Chem. Soc. Omega*, 2019, **4**, 10328–10335.

135 X. Xiong, W. Yan, C. You, Y. Zhu, Y. Chen, L. Fu, Y. Zhang, N. Yu and Y. Wu, *Front. Chem.*, 2019, **27**, 827**.**

136 D. Bresser, S. Passerini and B. Scrosati, *Chem. Commun.*, 2013, **49**, 10545–10562.

137 S. Xiong, K. Xie, Y. Diao and X. Hong, *Ionics*, 2012, **18**, 867–872.

138 M. Ling, L. Zhang, T. Zheng, J. Feng, J. Guo, L. Mai and G. Liu, *Nano Energy*, 2017, **38**, 82–90.

139 Y. Liu, W. Yan, X. An, X. Du, Z. Wang, H. Fan, S. Liu, X. Hao and G. Guan, *Electrochimica Acta*, 2018, **271**, 67–76.

140 H. Hu, H. Cheng, Z. Liu, G. Li, Q. Zhu and Y. Yu, *Nano Lett.*, 2015, **15**, 5116–5123.

141 W. Yang, W. Yang, A. Song, G. Sun and G. Shao, *Nanoscale*, 2018, **10**, 816–824.

142 K. Zhang, K. Xie, K. Yuan, W. Lu, S. Hu, W. Wei, M. Bai and C. Shen, *J. Mater. Chem. A*, 2017, **5**, 7309–7315.

143 X. Liang, C. Hart, Q. Pang, A. Garsuch, T. Weiss and L. F. Nazar, *Nat. Commun.*, 2015, **6**, 1–8.

144 C. Zheng, S. Niu, W. Lv, G. Zhou, J. Li, S. Fan, Y. Deng, Z. Pan, B. Li, F. Kang and Q.-H. Yang, *Nano Energy*, 2017, **33**, 306–312.

145 Z. Yuan, H.-J. Peng, T.-Z. Hou, J.-Q. Huang, C.-M. Chen, D.-W. Wang, X.-B. Cheng, F. Wei and Q. Zhang, *Nano Lett.*, 2016, **16**, 519–527.

146 N. Mosavati, S. O. Salley and K. Y. S. Ng, *J. Power Sources*, 2017, **340**, 210–216.

147 C. Zu and A. Manthiram, *J. Phys. Chem. Lett.*, 2014, **5**, 2522–2527.

148 X. Luo, X. Lu, G. Zhou, X. Zhao, Y. Ouyang, X. Zhu, Y.-E. Miao and T. Liu, *Am. Chem. Soc. Appl. Mater. Interfaces*, 2018, **10**, 42198–42206.

149 X. Yu, S. Feng, M. J. Boyer, M. Lee, R. C. Ferrier, N. A. Lynd, G. S. Hwang, G. Wang, S. Swinnea and A. Manthiram, *Mater. Energy*, 2018, **7**, 98–104.

150 A. Gupta and S. Sivaram, *Energy Technol.*, 2019, **7**, 1800819.

151 S. Liu, G.-R. Li and X.-P. Gao, *ACS Appl. Mater. Interfaces*, 2016, **8**, 7783–7789.

152 S. Li, H. Dai, Y. Li, C. Lai, J. Wang, F. Huo and C. Wang, *Energy Storage Mater.*, 2019, **18**, 222–228.

153 G. Li, Q. Huang, X. He, Y. Gao, D. Wang, S. H. Kim and D. Wang, *Am. Chem. Soc. Nano*, 2018, **12**, 1500–1507.

154 X. Liu, T. Kong, J. Qu, C. Wang and C. Lai, *J. Electrochem. Soc.*, 2019, **166**, A3886.

155 S. Xiong, K. Xie, Y. Diao and X. Hong, *Electrochimica Acta*, 2012, **83**, 78–86.

156 X. Liang, Z. Wen, Y. Liu, M. Wu, J. Jin, H. Zhang and X. Wu, *J. Power Sources*, 2011, **196**, 9839–9843.

157 M. J. Lacey, A. Yalamanchili, J. Maibach, C. Tengstedt, K. Edström and D. Brandell, *RSC Adv.*, 2016, **6**, 3632–3641.

158 L. Zhang, M. Ling, J. Feng, L. Mai, G. Liu and J. Guo, *Energy Storage Mater.*, 2018, **11**, 24–29.

159 W. Wang, X. Yue, J. Meng, J. Wang, X. Wang, H. Chen, D. Shi, J. Fu, Y. Zhou, J. Chen and Z. Fu, *Energy Storage Mater.*, 2019, **18**, 414–422.

160 C. Yang, K. Fu, Y. Zhang, E. Hitz and L. Hu, *Adv. Mater.*, 2017, **29**, 1701169.

161 C.-F. Lin, Y. Qi, K. Gregorczyk, S. B. Lee and G. W. Rubloff, *Acc. Chem. Res.*, 2018, **51**, 97–106.

162 A. Zhamu, G. Chen, C. Liu, D. Neff, Q. Fang, Z. Yu, W. Xiong, Y. Wang, X. Wang and B. Z. Jang, *Energy Environ. Sci.*, 2012, **5**, 5701–5707.

163 C. Monroe and J. Newman, *J. Electrochem. Soc.*, 2005, **152**, A396.

164 C. Monroe and J. Newman, *J. Electrochem. Soc.*, 2004, **151**, A880.

165 P. Bai, J. Li, F. R. Brushett and M. Z. Bazant, *Energy Environ. Sci.*, 2016, **9**, 3221–3229.

166 A. Kushima, K. P. So, C. Su, P. Bai, N. Kuriyama, T. Maebashi, Y. Fujiwara, M. Z. Bazant and J. Li, *Nano Energy*, 2017, **32**, 271–279.

167 S.-I. Tobishima, K. Hayashi, Y. Nemoto and J.-I. Yamaki, *J. Appl. Electrochem.*, 1999, **29**, 789–796.

168 C. Fang, J. Li, M. Zhang, Y. Zhang, F. Yang, J. Z. Lee, M.-H. Lee, J. Alvarado, M. A. Schroeder, Y. Yang, B. Lu, N. Williams, M. Ceja, L. Yang, M. Cai, J. Gu, K. Xu, X. Wang and Y. S. Meng, *Nat.*, 2019, **572**, 511–515.

169 D. Lu, Y. Shao, T. Lozano, W. D. Bennett, G. L. Graff, B. Polzin, J. Zhang, M. H. Engelhard, N. T. Saenz, W. A. Henderson, P. Bhattacharya, J. Liu and J. Xiao, *Adv. Energy Mater.*, 2015, **5**, 1400993.

170 D. Aurbach, B. Markovsky, M. D. Levi, E. Levi, A. Schechter, M. Moshkovich and Y. Cohen, *J. Power Sources*, 1999, **81–82**, 95–111.

171 D. Aurbach, I. Weissman, A. Zaban and O. Chusid, *Electrochimica Acta*, 1994, **39**, 51–71.

172 E. Peled, D. Golodnitsky and G. Ardel, *J. Electrochem. Soc.*, 1997, **144**, L208.

173 K. Xu, *Chem. Rev.*, 2004, **104**, 4303–4418.

174 W. Xu, J. Wang, F. Ding, X. Chen, E. Nasybulin, Y. Zhang and J.-G. Zhang, *Energy Environ. Sci.*, 2014, **7**, 513–537.

175 D. Aurbach, *J. Power Sources*, 2000, **89**, 206–218.

176 X.-B. Cheng, C. Yan, H.-J. Peng, J.-Q. Huang, S.-T. Yang and Q. Zhang, *Energy Storage Mater.*, 2018, **10**, 199–205.

177 Y. S. Cohen, Y. Cohen and D. Aurbach, *J. Phys. Chem. B*, 2000, **104**, 12282–12291.

178 D. Aurbach, M. L. Daroux, P. W. Faguy and E. Yeager, *J. Electrochem. Soc.*, 1987, **134**, 1611.

179 Y. Merla, B. Wu, V. Yufit, N. P. Brandon, R. F. Martinez-Botas and G. J. Offer, *J. Power Sources*, 2016, **307**, 308–319.

180 K. Kanamura, H. Tamura, S. Shiraishi and Z. Takehara, *J. Electrochem. Soc.*, 1995, **142**, 340.

181 D. Aurbach, E. Zinigrad, Y. Cohen and H. Teller, *Solid State Ionics*, 2002, **148**, 405–416.

182 X.-B. Cheng, R. Zhang, C.-Z. Zhao, F. Wei, J.-G. Zhang and Q. Zhang, *Adv. Sci.*, 2016, **3**, 1500213.

183 A. C. Kozen, C.-F. Lin, O. Zhao, S. B. Lee, G. W. Rubloff and M. Noked, *Chem. Mater.*, 2017, **29**, 6298–6307.

184 D. Aurbach, O. Youngman, Y. Gofer and A. Meitav, *Electrochimica Acta*, 1990, **35**, 625–638.

185 Y. Gofer, M. Ben-Zion and D. Aurbach, *J. Power Sources*, 1992, **39**, 163–178.

186 S.-K. Jeong, H.-Y. Seo, D.-H. Kim, H.-K. Han, J.-G. Kim, Y. B. Lee, Y. Iriyama, T. Abe and Z. Ogumi, *Electrochem. Communi.*, 2008, **10**, 635–638.

187 J. Qian, W. A. Henderson, W. Xu, P. Bhattacharya, M. Engelhard, O. Borodin and J.-G. Zhang, *Nat. Commun.*, 2015, **6**, 6362.

188 F. Shen, F. Zhang, Y. Zheng, Z. Fan, Z. Li, Z. Sun, Y. Xuan, B. Zhao, Z. Lin, X. Gui, X. Han, Y. Cheng and C. Niu, *Energy Storage Mater.*, 2018, **13**, 323–328.

189 C.-P. Yang, Y.-X. Yin, S.-F. Zhang, N.-W. Li and Y.-G. Guo, *Nat. Commun.*, 2015, **6**, 1–9.

190 H. Zhao, D. Lei, Y.-B. He, Y. Yuan, Q. Yun, B. Ni, W. Lv, B. Li, Q.-H. Yang, F. Kang and J. Lu, *Adv. Energy Mater.*, 2018, **8**, 1800266.

191 F. Ding, W. Xu, G. L. Graff, J. Zhang, M. L. Sushko, X. Chen, Y. Shao, M. H. Engelhard, Z. Nie, J. Xiao, X. Liu, P. V. Sushko, J. Liu and J.-G. Zhang, *J. Am. Chem. Soc.*, 2013, **135**, 4450–4456.

192 Y. Zhang, J. Qian, W. Xu, S. M. Russell, X. Chen, E. Nasybulin, P. Bhattacharya, M. H. Engelhard, D. Mei, R. Cao, F. Ding, A. V. Cresce, K. Xu and J.-G. Zhang, *Nano Lett.*, 2014, **14**, 6889–6896.

193 G. Wang, X. Xiong, D. Xie, X. Fu, X. Ma, Y. Li, Y. Liu, Z. Lin, C. Yang and M. Liu, *Energy Storage Mater.*, 2019, **23**, 701–706.

194 J. Heine, P. Hilbig, X. Qi, P. Niehoff, M. Winter and P. Bieker, *J. Electrochem. Soc.*, 2015, **162**, A1094–A1101.

195 L. Zhang, K. Zhang, Z. Shi and S. Zhang, *Langmuir*, 2017, **33**, 11164–11169.

196 J. Qian, W. Xu, P. Bhattacharya, M. Engelhard, W. A. Henderson, Y. Zhang and J.-G. Zhang, *Nano Energy*, 2015, **15**, 135–144.

197 G. A. Umeda, E. Menke, M. Richard, K. L. Stamm, F. Wudl and B. Dunn, *J. Mater, Chem. A*, 2011, **21**, 1593–1599.

198 N.-W. Li, Y.-X. Yin, C.-P. Yang and Y.-G. Guo, *Adv. Mater.*, 2016, **28**, 1853–1858.

199 G. Hou, C. Ci, D. Salpekar, Q. Ai, Q. Chen, H. Guo, L. Chen, X. Zhang, J. Cheng, K. Kato, R. Vajtai, P. Si, G. Babu, L. Ci and P. M. Ajayan, *J. Power Sources*, 2020, **448**, 227547.

200 D. H. Gregory, *Chem. Rec.*, 2008, **8**, 229–239.

201 N. Kamaya, K. Homma, Y. Yamakawa, M. Hirayama, R. Kanno, M. Yonemura, T. Kamiyama, Y. Kato, S. Hama, K. Kawamoto and A. Mitsui, *Nat. Mater.*, 2011, **10**, 682–686.

202 W. Li, J. Chen and T. Wang, *Physica B: Condensed Matter*, 2010, **405**, 400–403.

203 Y. Li, M. Abdel-Monem, R. Gopalakrishnan, M. Berecibar, E. Nanini-Maury, N. Omar, P. van den Bossche and J. Van Mierlo, *J. Power Sources*, 2018, **373**, 40–53.

204 S. B. Sarmah, P. Kalita, A. Garg, X. Niu, X.-W. Zhang, X. Peng and D. Bhattacharjee, *J. Electrochem. En. Conv. Stor*,. 2019, **16**, 40801

205 E. Talaie, P. Bonnick, X. Sun, Q. Pang, X. Liang and L. F. Nazar, *Chem. Mater.*, 2017, **29**, 90–105.

206 B. Wu, V. Yufit, Y. Merla, R. F. Martinez-Botas, N. P. Brandon and G. J. Offer, *J. Power Sources*, 2015, **273**, 495–501.

207 X. Li, J. Jiang, L. Y. Wang, D. Chen, Y. Zhang and C. Zhang, *Appl. Energy*, 2016, **177**, 537–543.

208 P. W. Atkins, *Shriver & Atkins' inorganic chemistry*, Oxford University Press, Oxford; New York, 2010.

209 A. A. Bunaciu, E. gabriela Udriştioiu and H. Y. Aboul-Enein, *Crit. Rev. Anal. Chem.*, 2015, **45**, 289–299.

210 R. Guinebretière, *X-Ray Diffraction by Polycrystalline Materials*, John Wiley & Sons, 2013.

211 A. Jesche, M. Fix, A. Kreyssig, W. R. Meier and P. C. Canfield, *Philos. Mag.*, 2016, **96**, 2115–2124.

212 N. Scotti, W. Kockelmann, J. Senker, S. Traßel and H. Jacobs, *Z. Anorg. Allg. Chem*, 1999, **625**, 1435–1439.

213 M. Hellenbrandt, *Crystallogr. Rev.*, 2004, **10**, 17–22.

214 B. H. Toby, *J. Appl. Cryst.*, 2001, **34**, 210–213.

215 D. H. Bilderback, P. Elleaume and E. Weckert, *J. Phys. B: At. Mol. Opt. Phys.*, 2005, **38**, S773–S797.

216 S. Dierker, *NSLS-II Preliminary Design Report*, Brookhaven National Lab. (BNL), Upton, NY (United States), 2007.

217 K. Zhukovsky, *High Energy Short Pulse Lasers*, 2016 chapter 2

218 J. Yano and V. K. Yachandra, *Photosyn. Res.*, 2009, **102**, 241–254.

219 J. McBreen, *J. Solid State Electrochem*, 2009, **13**, 1051–1061.

220 X.-D. Wen, M. W. Löble, E. R. Batista, E. Bauer, K. S. Boland, A. K. Burrell, S. D. Conradson, S. R. Daly, S. A. Kozimor, S. G. Minasian, R. L. Martin, T. M. McCleskey, B. L. Scott, D. K. Shuh and T. Tyliszczak, *J. Electron Spectrosc.*, 2014, **194**, 81–87.

221 J. J. Rehr and R. C. Albers, *Rev. Mod. Phys.*, 2000, **72**, 621–654.

222 P. A. M. Dirac and N. H. D. Bohr, *Proc. R. Soc. Lond.,* 1927, **114**, 243–265.

223 L. Douillard, F. Jollet, C. Bellin, M. Gautier and J. P. Duraud, *J. Phys. Condens. Matter*, 1994, **6**, 5039–5052.

224 C. T. Dillon, *Aust. J. Chem.*, 2012, **65**, 204–217.

225 P. W. Atkins and J. De Paula, *Atkins' Physical chemistry*, Oxford University Press, Oxford; New York, 2010.

226 D. E. Sayers, E. A. Stern and F. W. Lytle, *Phys. Rev. Lett.*, 1971, **27**, 1204–1207.

227 F. Guérin and D. Richeson, *J. Chem. Soc., Chem. Commun.*, 1994, 2213–2214.

228 A. J. Dent, G. Cibin, S. Ramos, A. D. Smith, S. M. Scott, L. Varandas, M. R. Pearson, N. A. Krumpa, C. P. Jones and P. E. Robbins, *J. Phys. Conf. Ser.*, 2009, **190**, 012039.

229 B. Ravel and M. Newville, *J. Synchrotron Rad*, 2005, **12**, 537–541.

230 E. A. Stern, *Phys. Rev. B*, 1974, **10**, 3027–3037.

231 F. W. Lytle, D. E. Sayers and E. A. Stern, *Phys. Rev. B*, 1975, **11**, 4825–4835.

232 E. A. Stern, D. E. Sayers and F. W. Lytle, *Phys. Rev. B*, 1975, **11**, 4836–4846.

233 B. Kaulich, P. Thibault, A. Gianoncelli and M. Kiskinova, *J. Phys. Condens. Matter*, 2011, **23**, 083002.

234 D. Guay, J. Stewart-Ornstein, X. Zhang and A. P. Hitchcock, *Anal. Chem.*, 2005, **77**, 3479–3487..

235 P. Guttmann and C. Bittencourt, *Beilstein J. Nanotechnol.*, 2015, **6**, 595–604.

236 T. H. Yoon, *Appl. Spectroc. Rev.*, 2009, **44**, 91–122.

237 J. Kirz, *J. Opt. Soc. Am.,* 1974, **64**, 301–309.

238 R. C. Moffet, A. V. Tivanski and M. K. Gilles, *Scanning Transmission X-ray Microscopy: Applications in Atmospheric Aerosol Research*, Lawrence Berkeley National Lab. (LBNL), Berkeley, CA (United States), 2011.

239 H. Rarback, D. Shu, S. C. Feng, H. Ade, J. Kirz, I. McNulty, D. P. Kern, T. H. P. Chang, Y. Vladimirsky, N. Iskander, D. Attwood, K. McQuaid and S. Rothman, *Review of Scientific Instruments*, 1988, **59**, 52–59.

240 M. Lerotic, R. Mak, S. Wirick, F. Meirer and C. Jacobsen, *J. Synchrotron Radiat*, 2014, **21**, 1206–1212.

241 M. P. Seah, *Surf. Interface Anal.*, 1980, **2**, 222–239.

242 F. Reinert and S. Hüfner, *New J. Phys.*, 2005, **7**, 97–97.

243 H. Krieger, *Basics of radiation physics and radiation protection,* Springer Science and Business Media Inc., 4th edn., 2012.

244 G. Greczynski and L. Hultman, *Prog. Mater. Sci.*, 2020, **107**, 100591.

245 G. Greczynski and L. Hultman, *ChemPhysChem*, 2017, **18**, 1507–1512.

246 *An Introduction to Surface Analysis by XPS and AES*, John Wiley & Sons, Ltd, 1st edn., 2019.

247 In *An Introduction to Synchrotron Radiation*, John Wiley & Sons, Ltd, 2011, pp. 223–302.

248 H. Iwai, H. Namba, Y. Kido, M. Taguchi and R. Oiwa, *J. Synchrotron Rad*, 1998, **5**, 1020–1022.

249 T. J. M. Zouros and E. P. Benis, *J. Electron Spectrosc.*, 2002, **125**, 221–248.

250 W. A. M. Aarnink, A. Weishaupt and A. van Silfhout, *Appl. Surf. Sci.*, 1990, **45**, 37–48.

251 N. Grinberg, S. Rodriguez and S. Rodriguez, *Ewing's Analytical Instrumentation Handbook,* 4th edn., 2019.

252 M. P. Seah, *Surf. Interface Anal.*, 1993, **20**, 865–875.

253 J. C. Arnault, *Diam. Relat. Mater.*, 2018, **84**, 157–168.

254 T.-L. Lee and D. A. Duncan, *Synchrotron Radiat. News*, 2018, **31**, 16–22.

255 M. B. Trzhaskovskaya, V. K. Nikulin, V. I. Nefedov and V. G. Yarzhemsky, *At. Data Nucl. Data Tables*, 2006, **92**, 245–304.

256 Magnuson, M. and Butorin, S. M. and Guo, J.-H. and Agui, A. and Nordgren, J. and Ogasawara, H. and Kotani, A. and Takahashi, T. and Kunii, S., *Phys. Rev. B.,* 2001, **63**, 75-101

257 S. Tanuma, C. J. Powell and D. R. Penn, *Surf. Interface Anal.*, 2003, **35**, 268–275.

258 B. D. Ratner and D. G. Castner, in *Surface Analysis – The Principal Techniques*, John Wiley & Sons, Ltd, 2009, pp. 47–112.

259 N. Nitta, F. Wu, J. T. Lee and G. Yushin, *Mater. Today*, 2015, **18**, 252–264.

260 H. Zhang, I. Hasa and S. Passerini, *Adv. Energy Mater.*, 2018, **8**, 1870082.

261 S. Roberts and E. Kendrick, *Nanotechnol. Sci. Appl.*, 2018, **11**, 23–33.

262 N. Sun, H. Liu and B. Xu, *J. Mater. Chem. A*, 2015, **3**, 20560–20566.

263 V. Simone, A. Boulineau, A. de Geyer, D. Rouchon, L. Simonin and S. Martinet, *J. Energy Chem.*, 2016, **25**, 761–768.

264 H. Hou, X. Qiu, W. Wei, Y. Zhang and X. Ji, *Adv. Energy Mater.*, 2017, **7**, 1602898.

265 A. Ruderman, S. Smrekar, M. V. Bracamonte, E. N. Primo, G. L. Luque, J. Thomas, E. Leiva, G. A. Monti, D. E. Barraco and F. V. Chávez, *Phys. Chem. Chem. Phys.*, 2021, **23**, 3281–3289.

266 L. Wu, H. Lu, L. Xiao, J. Qian, X. Ai, H. Yang and Y. Cao, *J. Mater. Chem. A*, 2014, **2**, 16424–16428.

267 Q. Li, Z. Li, Z. Zhang, C. Li, J. Ma, C. Wang, X. Ge, S. Dong and L. Yin, *Adv. Energy Mater.*, 2016, **6**, 1600376.

268 J. S. C. Kearney, M. Graužinytė, D. Smith, D. Sneed, C. Childs, J. Hinton, C. Park, J. S. Smith, E. Kim, S. D. S. Fitch, A. L. Hector, C. J. Pickard, J. A. Flores-Livas and A. Salamat, *Angew. Chem., Int. Ed.*, 2018, **57**, 11623–11628.

269 T. Lindgren, M. Larsson and S.-E. Lindquist, *Sol. Energy Mater. Sol. Cells*, 2002, **73**, 377–389.

270 F. Qu, Y. Yuan and M. Yang, *Chem. Mater.*, 2017, **29**, 969–974.

271 N. Scotti, W. Kockelmann, J. Senker, S. Trassel and H. Jacobs, *Z. Anorg. Allg. Chem*., 1999, **625**, 1435–1439.

272 F. Fischer and G. Ilicvici, *Ber. Dtsch. Chem. Ges.*, 1909, **42**, 527–537.

273 L. Maya, *Inorg. Chem.*, 1992, **31**, 1958–1960.

274 R. S. Lima, P. H. Dionisio, W. H. Schreiner and C. Achete, *Solid State Commun.*, 1991, **79**, 395–398.

275 M. P. Shemkunas, G. H. Wolf, K. Leinenweber and W. T. Petuskey, *J. Am. Ceram. Soc.*, 2002, **85**, 101–104.

276 A. C. Larson and R. B. Von Dreele*, Generalized Structure Analysis System* (*GSAS*), Los Alamos National Laboratory Report LAUR, 2004, pp. 86–748; B. H. Toby, *J. Appl. Crystallogr*., 2001, **34**, 210–213

277 R. B. Von Dreele and A. C. Larson, *GSAS manual, LANSCE MSH805*, Los Alamos National Laboratory, NM87545, 2000

278 N. Scotti, W. Kockelmann, J. Senker, S. Traßel and H. Jacobs, *Z. Anorg. Allg. Chem.*, 1999, **625**, 1435–1439.

279 P. Chirico, A. L. Hector and B. Mazumder, *Dalton Trans.*, 2010, **39**, 6092–6097.

280 P. Xi, Z. Xu, D. Gao, F. Chen, D. Xue, C.-L. Tao and Z.-N. Chen, *RSC Adv.*, 2014, **4**, 14206–14209.

281 B. Mazumder, P. Chirico and A. L. Hector, *Inorg. Chem.*, 2008, **47**, 9684–9690.

282 B. Mazumder and A. L. Hector, *J. Mater. Chem.*, 2008, **18**, 1392–1398.

283 S. I. U. Shah, A. L. Hector, X. Li and J. R. Owen, *J. Mater. Chem. A*, 2015, **3**, 3612–3619.

284 J. Choi and E. G. Gillan, *Inorg. Chem.*, 2005, **44**, 7385–7393.

285 L. Lei, W. Yin, X. Jiang, S. Lin and D. He, *Inorg. Chem.*, 2013, **52**, 13356–13362.

286 Y. Gu, F. Guo, Y. Qian, H. Zheng and Z. Yang, *Mater. Lett.,* 2003, **57**, 1679–1682.

287 P. Maneechakr, S. Karnjanakom and J. Samerjit, *RSC Adv.*, 2016, **6**, 73947–73952.

288 I. AlShibane, J. S. J. Hargreaves, A. L. Hector, W. Levason and A. McFarlane, *Dalton Trans.*, 2017, **46**, 8782–8787.

289 P. Kumar Dutta, U. Kumar Sen and S. Mitra, *RSC Adv.*, 2014, **4**, 43155–43159.

290 I. Kovalenko, B. Zdyrko, A. Magasinski, B. Hertzberg, Z. Milicev, R. Burtovyy, I. Luzinov and G. Yushin, *Sci.*, 2011, **334**, 75–79.

291 L. Ling, Y. Bai, Z. Wang, Q. Ni, G. Chen, Z. Zhou and C. Wu, *Am. Chem. Soc. Appl. Mater. Interfaces*, 2018, **10**, 5560–5568.

292 Z. Yang, A. A. Gewirth and L. Trahey, *Am. Chem. Soc. Appl. Mater. Interfaces*, 2015, **7**, 6557–6566.

293 H. Kim, J. Kim, H. Kim, Y. Kim, J. H. Ryu, S. M. Oh and S. Yoon, *J. Electroanal. Chem.*, 2018, **808**, 137–140.

294 C. Bommier and X. Ji, *Small*, 2018, **14**, 1703576.

295 P. Zhang, X. Zhao, Z. Liu, F. Wang, Y. Huang, H. Li, Y. Li, J. Wang, Z. Su, G. Wei, Y. Zhu, L. Fu, Y. Wu and W. Huang, *NPG Asia Mater.*, 2018, **10**, 429–440.

296 D. Chao, C. Zhu, P. Yang, X. Xia, J. Liu, J. Wang, X. Fan, S. V. Savilov, J. Lin, H. J. Fan and Z. X. Shen, *Nat. Commun.*, 2016, **7**, 12122.

297 Y. Fang, X.-Y. Yu and X. W. (David) Lou, *Angew. Chem., Int. Ed.*, 2018, **57**, 9859–9863.

298 Y. Wang, Y. Jin, C. Zhao, Y. Duan, X. He and M. Jia, *Mater. Lett.*, 2017, **191**, 169–172.

299 S.-H. Yu, A. Jin, X. Huang, Y. Yang, R. Huang, J. D. Brock, Y.-E. Sung and H. D. Abruña, *RSC Adv.*, 2018, **8**, 23847–23853.

300 D. Ma, Y. Li, H. Mi, S. Luo, P. Zhang, Z. Lin, J. Li and H. Zhang, *Angew. Chem., Int. Ed.*, 2018, **57**, 8901–8905.

301 J. Qian, Y. Xiong, Y. Cao, X. Ai and H. Yang, *Nano Lett.*, 2014, **14**, 1865–1869.

302 Y. Cheng, A. Nie, L.-Y. Gan, Q. Zhang and U. Schwingenschlögl, *J. Mater. Chem. A*, 2015, **3**, 19483–19489.

303 V. L. Chevrier and G. Ceder, *J. Electrochem. Soc.*, 2011, **158**, A1011–A1014.

304 L. D. Ellis, T. D. Hatchard and M. N. Obrovac, *J. Electrochem. Soc.*, 2012, **159**, A1801–A1805.

305 S. Komaba, Y. Matsuura, T. Ishikawa, N. Yabuuchi, W. Murata and S. Kuze, *Electrochem. Commun.*, 2012, **21**, 65–68.

306 J. M. Stratford, M. Mayo, P. K. Allan, O. Pecher, O. J. Borkiewicz, K. M. Wiaderek, K. W. Chapman, C. J. Pickard, A. J. Morris and C. P. Grey, *J. Am. Chem. Soc.*, 2017, **139**, 7273–7286.

307 S. Li, Y. Wang, J. Qiu, M. Ling, H. Wang, W. Martens and S. Zhang, *RSC Adv.*, 2014, **4**, 50148–50152.

308 H. Bian, J. Zhang, M.-F. Yuen, W. Kang, Y. Zhan, D. Y. W. Yu, Z. Xu and Y. Y. Li, *J. Power Sources*, 2016, **307**, 634–640.

309 L. Baggetto, J.-C. Jumas, H. T. (Bert) Hintzen and P. H. L. Notten, *Electrochim. Acta*, 2010, **55**, 6617–6631.

310 Y. Xu, B. Peng and F. M. Mulder, *Adv. Energy Mater.*, 2018, **8**, 1701847.

311 M. Dahbi, N. Yabuuchi, M. Fukunishi, K. Kubota, K. Chihara, K. Tokiwa, X. Yu, H. Ushiyama, K. Yamashita, J.-Y. Son, Y.-T. Cui, H. Oji and S. Komaba, *Chem. Mater.*, 2016, **28**, 1625–1635.

312 A. Rabenau, *Solid State Ionics*, 1982, **6**, 277–293.

313 C. Vinod Chandran and P. Heitjans, in *Annual Reports on NMR Spectroscopy*, ed. G. A. Webb, Academic Press, 2016, vol. 89, pp. 1–102.

314 B. A. Boukamp and R. A. Huggins, *Phys. Lett. A*, 1976, **58**, 231–233.

315 T. Lapp, S. Skaarup and A. Hooper, *Solid State Ionics*, 1983, **11**, 97–103.

316 M. Wu, Z. Wen, Y. Liu, X. Wang and L. Huang, *J. Power Sources*, 2011, **196**, 8091–8097.

317 D. W. Osborne and H. E. Flotow, *The J. Chem. Thermodyn.*, 1978, **10**, 675–682.

318 D. H. Gregory, P. M. O'Meara, A. G. Gordon, J. P. Hodges, S. Short and J. D. Jorgensen, *Chem. Mater.*, 2002, **14**, 2063–2070.

319 D. Fauteux and R. Koksbang, *J. Appl. Electrochem.*, 1993, **23**, 1–10.

320 Y. J. Zhang, W. Wang, H. Tang, W. Q. Bai, X. Ge, X. L. Wang, C. D. Gu and J. P. Tu, *J. Power Sources*, 2015, **277**, 304–311.

321 Y. Li, Y. Sun, A. Pei, K. Chen, A. Vailionis, Y. Li, G. Zheng, J. Sun and Y. Cui, *Am. Chem. Soc. Cent. Sci.*, 2018, **4**, 97–104.

322 United States, US4738716A, 1988.

323 R. R. Rogers and G. E. Viens, *J. Electrochem. Soc.*, 1951, **98**, 483–487.

324 P. H. Schmidt, *J. Electrochem. Soc.*, 1966, **113**, 201–204.

325 J. Becking, A. Gröbmeyer, M. Kolek, U. Rodehorst, S. Schulze, M. Winter, P. Bieker and M. C. Stan, *Adv. Mater. Interfaces*, 2017, **4**, 1700166.

326 R. Schmitz, R. Müller, S. Krüger, R. W. Schmitz, S. Nowak, S. Passerini, M. Winter and C. Schreiner, *J. Power Sources*, 2012, **217**, 98–101.

327 C. Naudin, J. L. Bruneel, M. Chami, B. Desbat, J. Grondin, J. C. Lassègues and L. Servant, *J. Power Sources*, 2003, **124**, 518–525.

328 K. Morigaki and A. Ohta, *J. Power Sources*, 1998, **76**, 159–166.

329 D. Ensling, A. Thissen and W. Jaegermann, *Appl. Surf. Sci.*, 2008, **255**, 2517–2523.

330 S. Xiong, K. Xie, Y. Diao and X. Hong, *J. Power Sources*, 2014, **246**, 840–845.

331 I. Ismail, A. Noda, A. Nishimoto and M. Watanabe, *Electrochim. Acta*, 2001, **46**, 1595–1603.

332 C. Xu, B. Sun, T. Gustafsson, K. Edström, D. Brandell and M. Hahlin, *J. Mater. Chem. A*, 2014, **2**, 7256–7264.

333 S. Malmgren, K. Ciosek, R. Lindblad, S. Plogmaker, J. Kühn, H. Rensmo, K. Edström and M. Hahlin, *Electrochim. Acta*, 2013, **105**, 83–91.

334 B. Deng, H. Wang, W. Ge, X. Li, X. Yan, T. Chen, M. Qu and G. Peng, *Electrochim. Acta*, 2017, **236**, 61–71.

335 X. Wang, Z. Sun, Y. Zhao, J. Li, Y. Zhang and Z. Zhang, *J. Solid State Electrochem.*, 2020, **24**, 111–119.

336 D. Farhat, F. Ghamouss, J. Maibach, K. Edström and D. Lemordant, *ChemPhysChem*, 2017, **18**, 1333–1344.

337 X. Li, Z. Yin, X. Li and C. Wang, *Ionics*, 2014, **20**, 795–801.

338 Y. Miura, H. Kusano, T. Nanba and S. Matsumoto, *J. Non-Cryst. Solids*, 2001, **290**, 1–14.

339 L. Baggetto, P. Ganesh, C.-N. Sun, R. A. Meisner, T. A. Zawodzinski and G. M. Veith, *J. Mater. Chem. A*, 2013, **1**, 7985–7994.

340 R. Grissa, V. Fernandez, N. Fairley, J. Hamon, N. Stephant, J. Rolland, R. Bouchet, M. Lecuyer, M. Deschamps, D. Guyomard and P. Moreau, *Am. Chem. Soc. Appl. Energy Mater.*, 2018, **1**, 5694–5702.

341 C.-Z. Zhao, X.-B. Cheng, R. Zhang, H.-J. Peng, J.-Q. Huang, R. Ran, Z.-H. Huang, F. Wei and Q. Zhang, *Energy Storage Mater.*, 2016, **3**, 77–84.

342 C. Xue, X. Zhang, S. Wang, L. Li and C.-W. Nan, *Am. Chem. Soc. Appl. Mater. Interfaces*, 2020, **12**, 24837–24844.

343 A. Al-Ani, H. Pingle, N. P Reynolds, P.-Y. Wang and P. Kingshott, *Polymers*, 2017, **9**, 343.

344 S. Ravi, S. Zhang, Y.-R. Lee, K.-K. Kang, J.-M. Kim, J.-W. Ahn and W.-S. Ahn, *J. Ind. Eng Chem.*, 2018, **67**, 210–218.

345 Y. Xie, L. Fang, H. Cheng, C. Hu, H. Zhao, J. Xu, J. Fang, X. Lu and J. Zhang, *J. Mater. Chem. A*, 2016, **4**, 15612–15620.

346 A. Zhang, X. Fang, C. Shen, Y. Liu and C. Zhou, *Nano Res.*, 2016, **9**, 3428–3436.

347 X. Chen, T.-Z. Hou, B. Li, C. Yan, L. Zhu, C. Guan, X.-B. Cheng, H.-J. Peng, J.-Q. Huang and Q. Zhang, *Energy Storage Mater.*, 2017, **8**, 194–201.

348 X. Xing, Y. Li, X. Wang, V. Petrova, H. Liu and P. Liu, *Energy Storage Mater.*, 2019, **21**, 474–480.

349 S. Liu, X. Xia, S. Deng, D. Xie, Z. Yao, L. Zhang, S. Zhang, X. Wang and J. Tu, *Adv. Mater.*, 2019, **31**, 1806470.

350 C. Fiedler, B. Luerssen, M. Rohnke, J. Sann and J. Janek, *J. Electrochem. Soc.*, 2017, **164**, A3742–A3749.

351 X.-B. Cheng, C. Yan, X. Chen, C. Guan, J.-Q. Huang, H.-J. Peng, R. Zhang, S.-T. Yang and Q. Zhang, *Chem*, 2017, **2**, 258–270.

352 S. Xiong, K. Xie, Y. Diao and X. Hong, *J. Power Sources*, 2013, **236**, 181–187.

353 K. N. Wood, K. X. Steirer, S. E. Hafner, C. Ban, S. Santhanagopalan, S.-H. Lee and G. Teeter, *Nat. Commun.*, 2018, **9**, 1–10.

354 C. F. Mallinson, J. E. Castle and J. F. Watts, *Surf. Sci. Spectra*, 2013, **20**, 113–127.

355 Y. Zhang, X. Xia, D. Wang, X. Wang, C. Gu and J. Tu, *RSC Adv.*, 2016, **6**, 11657–11664.

356 S. Oswald, F. Thoss, M. Zier, M. Hoffmann, T. Jaumann, M. Herklotz, K. Nikolowski, F. Scheiba, M. Kohl, L. Giebeler, D. Mikhailova and H. Ehrenberg, *Batteries*, 2018, **4**, 36.

357 E. P. Kamphaus, S. Angarita-Gomez, X. Qin, M. Shao, M. Engelhard, K. T. Mueller, V. Murugesan and P. B. Balbuena, *Am. Chem. Soc. Appl. Mater. Interfaces*, 2019, **11**, 31467–31476.

358 K. Kanamura, *J. Electrochem. Soc.*, 1994, **141**, 2379.

359 J. Zheng, M. Gu, H. Chen, P. Meduri, M. H. Engelhard, J.-G. Zhang, J. Liu and J. Xiao, *J. Mater. Chem. A*, 2013, **1**, 8464–8470.

360 X.-B. Cheng, R. Zhang, C.-Z. Zhao and Q. Zhang, *Chem. Rev.*, 2017, **117**, 10403–10473.

361 J. Chen, Y. Xu, M. Cao, C. Zhu, X. Liu, Y. Li and S. Zhong, *J. Power Sources*, 2019, **426**, 169–177.

362 J. M. McEnaney, A. R. Singh, J. A. Schwalbe, J. Kibsgaard, J. C. Lin, M. Cargnello, T. F. Jaramillo and J. K. Nørskov, *Energy Environ. Sci.*, 2017, **10**, 1621–1630.

363 J.-L. Ma, D. Bao, M.-M. Shi, J.-M. Yan and X.-B. Zhang, *Chem*, 2017, **2**, 525–532.

364 M. Baloch, D. Shanmukaraj, O. Bondarchuk, E. Bekaert, T. Rojo and M. Armand, *Energy Storage Mater.*, 2017, **9**, 141–149.

365 K. Chen, R. Pathak, A. Gurung, E. A. Adhamash, B. Bahrami, Q. He, H. Qiao, A. L. Smirnova, J. J. Wu, Q. Qiao and Y. Zhou, *Energy Storage Mater.*, 2019, **18**, 389–396.

366 W. Li, G. Wu, C. M. Araújo, R. H. Scheicher, A. Blomqvist, R. Ahuja, Z. Xiong, Y. Feng and P. Chen, *Energy Environ. Sci.*, 2010, **3**, 1524–1530.

367 J. Zhou, Y. Guo, C. Liang, L. Cao, H. Pan, J. Yang and J. Wang, *Chem. Commun.*, 2018, **54**, 5478–5481.

368 C. Yogi, D. Takamatsu, K. Yamanaka, H. Arai, Y. Uchimoto, K. Kojima, I. Watanabe, T. Ohta and Z. Ogumi, *J. Power Sources*, 2014, **248**, 994–999.

369 T. T. Fister, M. Schmidt, P. Fenter, C. S. Johnson, M. D. Slater, M. K. Y. Chan and E. L. Shirley, *J. Chem. Phys.*, 2011, **135**, 224513.

370 L. Cheng, E. J. Crumlin, W. Chen, R. Qiao, H. Hou, S. F. Lux, V. Zorba, R. Russo, R. Kostecki, Z. Liu, K. Persson, W. Yang, J. Cabana, T. Richardson, G. Chen and M. Doeff, *Phys. Chem. Chem. Phys.*, 2014, **16**, 18294–18300.

371 M. Uesugi, M. Ito, H. Yabuta, H. Naraoka, F. Kitajima, Y. Takano, H. Mita, Y. Kebukawa, A. Nakato and Y. Karouji, *Meteorit. Planet. Sci.*, 2019, **54**, 638–666.

372 X. Feng, M.-K. Song, W. C. Stolte, D. Gardenghi, D. Zhang, X. Sun, J. Zhu, E. J. Cairns and J. Guo, *Phys. Chem. Chem. Phys.*, 2014, **16**, 16931–16940.

373 H. W. Kim, M. B. Ross, N. Kornienko, L. Zhang, J. Guo, P. Yang and B. D. McCloskey, *Nat. Catal.*, 2018, **1**, 282–290.

374 M. J. Zachman, Z. Tu, S. Choudhury, L. A. Archer and L. F. Kourkoutis, *Nat.*, 2018, **560**, 345–349.

375 Y. Ye, A. Kawase, M.-K. Song, B. Feng, Y.-S. Liu, M. Marcus, J. Feng, E. Cairns, J. Guo and J. Zhu, *Nanomater.*, 2016, **6**, 14.

376 Y. Ye, M.-K. Song, Y. Xu, K. Nie, Y. Liu, J. Feng, X. Sun, E. J. Cairns, Y. Zhang and J. Guo, *Energy Storage Mater.*, 2019, **16**, 498–504.

377 F. Rodrigues, D. Galante, G. M. do Nascimento and P. S. Santos, *J. Phys Chem. B*, 2012, **116**, 1491–1498.

378 Y. Zhong, F. Lin, M. Wang, Y. Zhang, Q. Ma, J. Lin, Z. Feng and H. Wang, *Adv. Funct. Mater.*, 2020, **30**, 1907579.

379 B. J. Schultz, R. V. Dennis, J. P. Aldinger, C. Jaye, X. Wang, D. A. Fischer, A. N. Cartwright and S. Banerjee, *RSC Adv.*, 2013, **4**, 634–644.

380 S.-M. Bak, R. Qiao, W. Yang, S. Lee, X. Yu, B. Anasori, H. Lee, Y. Gogotsi and X.-Q. Yang, *Adv. Energy Mate.*, 2017, **7**, 1700959.

381 C. A. da Silva Moura, G. Kretzmann Belmonte, P. Guruprasad Reddy, K. E. Gonslaves and D. Eduardo Weibel, *RSC Adv.*, 2018, **8**, 10930–10938.

382 A. Tayal, M. Gupta, A. Gupta, P. Rajput and J. Stahn, *Phys. Rev. B*, 2015, **92**, 054109.

383 Y. Gorlin, B. Lassalle-Kaiser, J. D. Benck, S. Gul, S. M. Webb, V. K. Yachandra, J. Yano and T. F. Jaramillo, *J. Am. Chem. Soc.*, 2013, **135**, 8525-8534

384 M. Krbal, A. V. Kolobov, P. Fons, K. V. Mitrofanov, Y. Tamenori, B. Hyot, B. Andre and J. Tominaga, *J. Alloys and Compd.*, 2017, **704**, 254–259.

385 Y. K. Chang, H. H. Hsieh, W. F. Pong, M.-H. Tsai, T. E. Dann, F. Z. Chien, P. K. Tseng, L. C. Chen, S. L. Wei, K. H. Chen, J.-J. Wu and Y. F. Chen, *J. Appl. Phys.*, 1999, **86**, 5609–5613.

386 S. Jiao, X. Ren, R. Cao, M. H. Engelhard, Y. Liu, D. Hu, D. Mei, J. Zheng, W. Zhao, Q. Li, N. Liu, B. D. Adams, C. Ma, J. Liu, J.-G. Zhang and W. Xu, *Nat. Energy*, 2018, **3**, 739–746.

387 M. I. Nandasiri, L. E. Camacho-Forero, A. M. Schwarz, V. Shutthanandan, S. Thevuthasan, P. B. Balbuena, K. T. Mueller and V. Murugesan, *Chem. Mater.*, 2017, **29**, 4728–4737.

388 R. Dedryvère, S. Leroy, H. Martinez, F. Blanchard, D. Lemordant and D. Gonbeau, *J. Phys. Chem. B*, 2006, **110**, 12986–12992.

389 M. R. Busche, T. Drossel, T. Leichtweiss, D. A. Weber, M. Falk, M. Schneider, M.-L. Reich, H. Sommer, P. Adelhelm and J. Janek, *Nat. Chem.*, 2016, **8**, 426–434.

390 D. Aurbach, E. Pollak, R. Elazari, G. Salitra, C. S. Kelley and J. Affinito, *J. Electrochem. Soc.*, 2009, **156**, A694.

391 V. Nilsson, R. Younesi, D. Brandell, K. Edström and P. Johansson, *J. Power Sources*, 2018, **384**, 334–341.

392 E. Peled, *J. Power Sources*, 1983, **9**, 253–266.

393 A. Kominato, E. Yasukawa, N. Sato, T. Ijuuin, H. Asahina and S. Mori, *J. Power Sources*, 1997, **68**, 471–475.

394 S. Duangdangchote, A. Krittayavathananon, N. Phattharasupakun, N. Joraleechanchai and M. Sawangphruk, *Chem. Commun.*, 2019, **55**, 13951–13954.

395 F. Ding, Y. Liu and X. Hu, *Rare Met.*, 2006, **25**, 297–302.

396 Y. Lu, Z. Tu and L. A. Archer, *Nat. Mater*, 2014, **13**, 961–969.

397 M. Rosso, C. Brissot, A. Teyssot, M. Dollé, L. Sannier, J.-M. Tarascon, R. Bouchet and S. Lascaud, *Electrochim. Acta*, 2006, **51**, 5334–5340.

398 Y. Lu, Z. Tu, J. Shu and L. A. Archer, *J. Power Sources*, 2015, **279**, 413–418.

399 P. Zhang, J. Zhu, M. Wang, N. Imanishi and O. Yamamoto, *Electrochem Commun*, 2018, **87**, 27–30.

400 D. Aurbach, I. Weissman, H. Yamin and E. Elster, *J. Electrochem. Soc.*, 1998, **145**, 1421–1426.

401 P. Dan, E. Mengeritsky, D. Aurbach, I. Weissman and E. Zinigrad, *J. Power Sources*, 1997, **68**, 443–447.

402 K.-H. Chen, K. N. Wood, E. Kazyak, W. S. LePage, A. L. Davis, A. J. Sanchez and N. P. Dasgupta, *J. Mater. Chem. A*, 2017, **5**, 11671–11681.

403 G. Bieker, M. Winter and P. Bieker, *PhysChemChemPhys.*, 2015, **17**, 8670–8679.

404 K. N. Wood, E. Kazyak, A. F. Chadwick, K.-H. Chen, J.-G. Zhang, K. Thornton and N. P. Dasgupta, *Am. Chem. Soc. Cent. Sci.*, 2016, **2**, 790–801.

405 X. Liang, Q. Pang, I. R. Kochetkov, M. S. Sempere, H. Huang, X. Sun and L. F. Nazar, *Nat. Energy*, 2017, **2**, 1–7.

406 D. Koo, B. Kwon, J. Lee and K. T. Lee, *Chem. Commun.*, 2019, **55**, 9637–9640.

407 F. Orsini, M. Dollé and J.-M. Tarascon, *Solid State Ionics*, 2000, **135**, 213–221.

408 W. Zhang, H. L. Zhuang, L. Fan, L. Gao and Y. Lu, *Sci. Adv.*, 2018, **4**, eaar4410.

409 E. Peled and S. Menkin, *J. Electrochem. Soc.*, 2017, **164**, A1703–A1719.

410 C. M. López, J. T. Vaughey and D. W. Dees, *J. Electrochem. Soc.*, 2009, **156**, A726–A729.

411 F. Shi, A. Pei, D. T. Boyle, J. Xie, X. Yu, X. Zhang and Y. Cui, *PNAS*, 2018, **115**, 8529–8534.

412 J. Zheng, P. Yan, D. Mei, M. H. Engelhard, S. S. Cartmell, B. J. Polzin, C. Wang, J.-G. Zhang and W. Xu, *Adv. Energy Mater.*, 2016, **6**, 1502151.

413 S. Lv, T. Verhallen, A. Vasileiadis, F. Ooms, Y. Xu, Z. Li, Z. Li and M. Wagemaker, *Nat. Commun*., 2018, **9** 2152

414 Y. V. Mikhaylik and J. R. Akridge, *J. Electrochem. Soc.*, 2004, **151**, A1969.

415 G. Ma, Z. Wen, M. Wu, C. Shen, Q. Wang, J. Jin and X. Wu, *Chem. Commun.*, 2014, **50**, 14209–14212.

416 J. W. Dibden, J. W. Smith, N. Zhou, N. Garcia-Araez and J. R. Owen, *Chem. Commun.*, 2016, **52**, 12885–12888.

417 J. W. Dibden, N. Meddings, J. R. Owen and N. Garcia-Araez, *ChemElectroChem*, 2018, **5**, 445–454.

418 S. Drvarič Talian, S. Jeschke, A. Vizintin, K. Pirnat, I. Arčon, G. Aquilanti, P. Johansson and R. Dominko, *Chem. Mater.*, 2017, **29**, 10037–10044.

419 K. H. Wujcik, T. A. Pascal, C. D. Pemmaraju, D. Devaux, W. C. Stolte, N. P. Balsara and D. Prendergast, *Adv. Energy Mater.*, 2015, **5**, 1500285.

420 E. Zhao, J. Wang, F. Li, Z. Jiang, X.-Q. Yang, F. Wang, H. Li and X. Yu, *Chem. Commun.*, 2019, **55**, 4993–4996.

421 T. A. Pascal, C. D. Pemmaraju and D. Prendergast, *Phys. Chem. Chem. Phys.*, 2015, **17**, 7743–7753.

422 Y. Gorlin, M. U. M. Patel, A. Freiberg, Q. He, M. Piana, M. Tromp and H. A. Gasteiger, *J. Electrochem. Soc.*, 2016, **163**, A930–A939.

423 R. Dominko, A. Vizintin, G. Aquilanti, L. Stievano, M. J. Helen, A. R. Munnangi, M. Fichtner and I. Arcon, *J. Electrochem. Soc.*, 2018, **165**, A5014–A5019.

424 T. Takeuchi, H. Kageyama, K. Nakanishi, Y. Inada, M. Katayama, T. Ohta, H. Senoh, H. Sakaebe, T. Sakai, K. Tatsumi and H. Kobayashi, *J. Electrochem. Soc.*, 2011, **159**, A75–A84.

425 C. Zu, N. Azimi, Z. Zhang and A. Manthiram, *J. Mater. Chem. A*, 2015, **3**, 14864–14870.

426 X. Liang, C. Y. Kwok, F. Lodi-Marzano, Q. Pang, M. Cuisinier, H. Huang, C. J. Hart, D. Houtarde, K. Kaup, H. Sommer, T. Brezesinski, J. Janek and L. F. Nazar, *Adv. Energy Mater.*, 2016, **6**, 1501636.

427 M. J. Klein, K. Goossens, C. W. Bielawski and A. Manthiram, *J. Electrochem. Soc.*, 2016, **163**, A2109.

428 M. Fantauzzi, B. Elsener, D. Atzei, A. Rigoldi and A. Rossi, *RSC Adv.*, 2015, **5**, 75953–75963.

429 K. Sun, Q. Wu, X. Tong and H. Gan, *Am. Chem. Soc. Appl. Energy Mater.*, 2018, **1**, 2608–2618.

Chapter 8 Appendices

8.1 Repeat galvanostatic cycling data of tin nitride in sodium half-cells

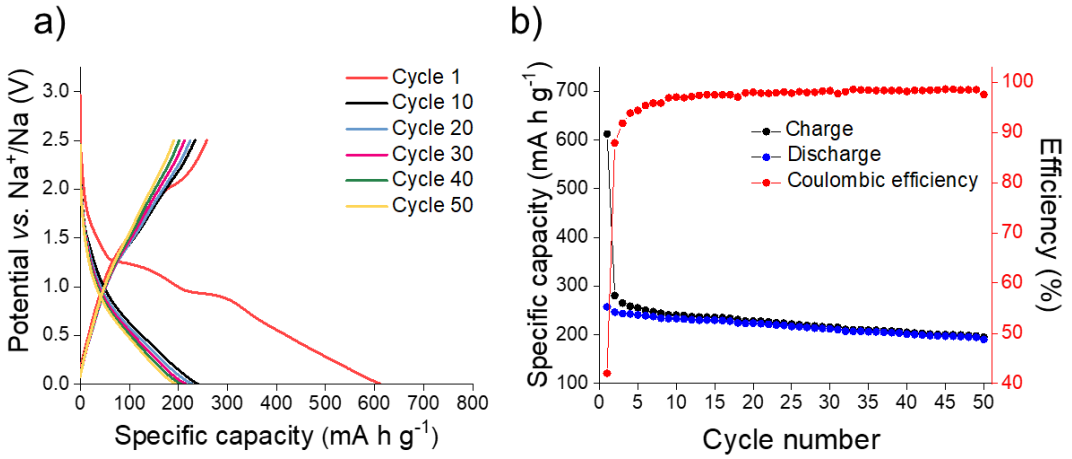

Figure 8.1 – (**a**), Galvanostatic cycling of Sn_3N_4 (micro) vs. Na^+/Na (V) with 5% FEC at 200 mA g^{-1} between 2.5 V and 10 mV, over 50 cycles. (b), Corresponding specific capacity of Sn3N4 vs. cycle number. (Repeat cell).

Table 8.1 - Specific capacity values obtained from galvanostatic cycling of microcrystalline Sn_3N_4 at 200 mA g^{-1} with 5% FEC and the corresponding Coulombic efficiency (Repeat cell).

Cycle number	Capacity-Reduction (mA h g^{-1})	Capacity-Oxidation (mA h g^{-1})	Coulombic efficiency (%)
1	612	257	42
10	240	233	97
20	228	224	97
30	215	212	98
40	205	201	98
50	195	190	98

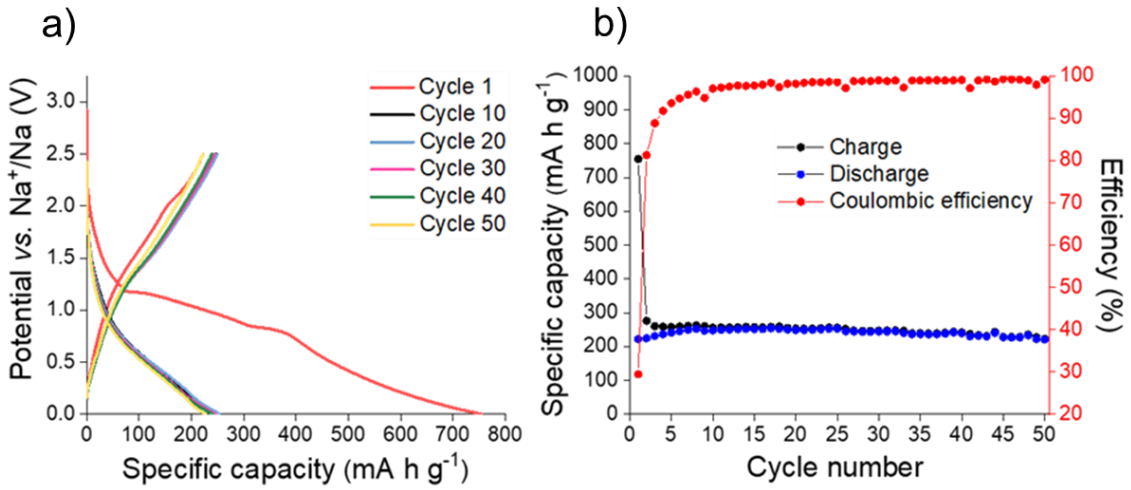

Figure 8.2 - (**a**), Galvanostatic cycling of Sn_3N_4 (micro) vs. Na^+/Na (V) with 5% FEC at 50 mA g^{-1} between 2.5 V and 10 mV, over 50 cycles. (**b**), Corresponding specific capacity of Sn_3N_4 vs. cycle number. (Repeat cell).

Table 8.2 – Specific capacity values obtained from galvanostatic cycling of microcrystalline Sn_3N_4 at 50 mA g^{-1} with 5% FEC and the corresponding Coulombic efficiency.

Cycle number	Capacity-Reduction (mA h g^{-1})	Capacity-Oxidation (mA h g^{-1})	Coulombic efficiency (%)
1	754	222	30
10	255	248	97
20	253	249	98
30	247	244	99
40	241	239	99
50	223	221	99

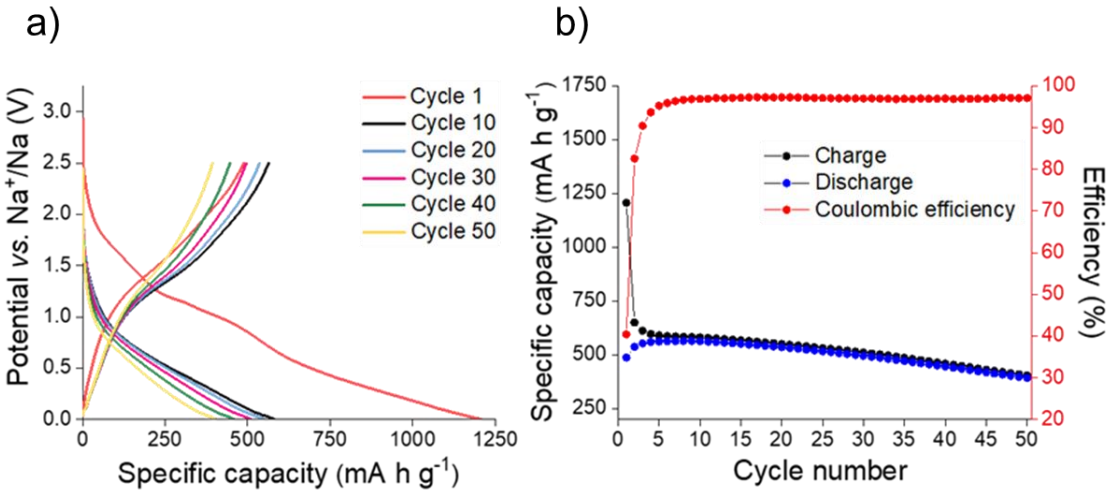

Figure 8.3 – (**a**), Galvanostatic cycling of Sn_3N_4 (nano) vs. Na^+/Na (V) with 5% FEC at 200 mA g^{-1} over 50 cycles. (**b**), Corresponding specific capacity of Sn_3N_4 vs. cycle number. (Repeat cell).

Table 8.3 - Specific capacity values obtained from galvanostatic cycling of nanocrystalline Sn_3N_4 at 200 mA g^{-1} with 5% FEC and the corresponding Coulombic efficiency

Cycle number	Capacity-Reduction (mA h g^{-1})	Capacity-Oxidation (mA h g^{-1})	Coulombic efficiency (%)
1	1207	488	40.3
10	581	563	97
20	551	536	97
30	511	496	97
40	460	446	97
50	405	393	97